



# Politecnico di Bari

Repository Istituzionale dei Prodotti della Ricerca del Politecnico di Bari

## Application Of Thermal Methods Based On Infrared Thermography For The Mechanical Characterisation Of Materials

This is a PhD Thesis

*Original Citation:*

Application Of Thermal Methods Based On Infrared Thermography For The Mechanical Characterisation Of Materials / De Finis, Rosa. - STAMPA. - (2017). [10.60576/poliba/iris/de-finis-rosa\_phd2017]

*Availability:*

This version is available at <http://hdl.handle.net/11589/123456> since: 2018-02-28

*Published version*

DOI:10.60576/poliba/iris/de-finis-rosa\_phd2017

Publisher: Politecnico di Bari

*Terms of use:*

(Article begins on next page)



Department of Mechanics, Mathematics and Management  
MECHANICAL AND MANAGEMENT ENGINEERING

Ph.D. Program

SSD: ING-IND/14—MECHANICAL DESIGN AND  
MACHINE CONSTRUCTION

**Final Dissertation**

---

# Application Of Thermal Methods Based On Infrared Thermography For The Mechanical Characterisation Of Materials

---

by  
(*Rosa De Finis*):

Supervisors:

Prof. U. Galietti

*Coordinator of Ph.D Program:*

*Prof. G.P. Demelio*

---

*Course n°30, 01/11/2014-31/10/2017*



Politecnico  
di Bari

Department of Mechanics, Mathematics and Management  
MECHANICAL AND MANAGEMENT ENGINEERING

Ph.D. Program

SSD: ING-IND/14—MECHANICAL DESIGN AND  
MACHINE CONSTRUCTION

**Final Dissertation**

---

# Application Of Thermal Methods Based On Infrared Thermography For The Mechanical Characterisation Of Materials

---

by  
(Rosa De Finis):

---

*Firma leggibile e per esteso*

Referees:

Prof. V. Dattoma

Prof. G. Pitarresi

Supervisor:

Prof. U. Galietti

\_\_\_\_\_ *firma*

*Coordinator of Ph.D Program:*

*Prof. G.P. Demelio*

\_\_\_\_\_ *firma*

---

*Course n°30, 01/11/2014-31/10/2017*

# PhD Thesis



*Applicazione Dei Metodi Termici Basati Sulla Termografia Ad Infrarossi Per La Caratterizzazione Dei Materiali*

*Application Of Thermal Methods Based On Infrared Thermography For The Mechanical Characterisation Of Materials*

*Rosa De Finis*



Galaxies appear quite different in infrared light than they do in visible light.

The visible-light image of galaxy M101 (left) is dominated by the glow of stars.

The infrared view (right) brings out the skeletal dust lanes where new stars can form

[<http://hubble25th.org/science/7>]

Credits: [Left] NASA, ESA, K. Kuntz (JHU), F. Bresolin (University of Hawaii), J. Trauger (Jet Propulsion Laboratory), J. Mould (NOAO), Y.-H. Chu (University of Illinois, Urbana), and STScI; [Right] NASA, Jet Propulsion Laboratory/Caltech, and K. Gordon (STScI)

Rosa De Finis

Politecnico di Bari – Dipartimento di Ingegneria Meccanica Matematica e Management.

Bari, 2017.

*I hereby declare that this submission is my own work and that, to the best of my knowledge and belief, it contains nor material previously published or written by another person nor material which has been accepted for the award of any other degree or diploma of the university or other institute of higher learning, except where due acknowledgment has been made in the text.*

*Rosa De Finis*

---

## *Abstract*

---

**T**hermography is a full-field, non-contact, non-destructive technique which provides the temperature map from a body at temperature higher than 0K, by detecting its infrared radiation. The most important characteristic making thermography a useful Non Destructive technique is the possibility to inspect any kind of body without any contact with it; this allows high temperature measurements or critical environment inspections without any material/sensor contaminations.

Since the age of its discovery by Sir William Herschel, 1800, the technique undergone a great deal of improvements, in fact recent IR detectors benefit of high accuracy (resolution is roughly in the order of centigrade) and wide operating temperature range (from -20°C to 1000 °C). However, even if the techniques based on thermography are widely diffused in academic field, in the last 20 years a significant delay is observed due to the higher costs of IR equipment and mostly due to the absence of Standards which discipline such the technique. In this sense, difficulties arises from the difficult collocation of thermography in a specific field of application due to its great versatility.

In fact, the feasibility of the Thermography extends from medical to many industrial applications.

In the field of Medicine, the great interest of scientific community for the prevention of breast cancer and neurological diseases involves the research of more accurate methods for early diagnosis.

In this sense, thermography is useful for measuring the surface temperatures from the body as related to the heat produced by the organism passing through the skin and tissues. In recent years, medical researchers developed accurate algorithms for 2-dimension imaging analysis to detect the presence of tumours, as well to evaluate changes in blood circulation in order to localise the presence of any ischemic lesion.

On the other hand, in the industrial framework, the keywords which lead the researcher to find new techniques being introduced in the manufacturing process were Time-to-Market and Quality.

Nowadays entrepreneurs are interested in reducing the time between the product is manufactured and sold, as it determines their profits. The reduction of the time to market is coupled with increasing the quality of products. The continuous demand of the quality in the

industrial products, allows integrating the quality control in the manufacturing process. To do this, a technique providing in-situ, non-destructive tests during or at the end of the process with fast performing and data processing, is required.

In particular, by introducing Thermography in the manufacturing process, Industry takes advantage from the possibility of using a technique which does not require any production downtime, allows predicting maintenance as well as fast and focused actions on machines and finally to reduce the risk of accident and catastrophes. For example, Thermography with respect Ultrasound technique does not need of acoustic coupling, and it is not important if the detectors are located far away or near the sample being investigate, since the contact is not required.

Another interesting aspect related to the use of Infrared radiation by materials is the possibility to set up a technique that, somehow allows mechanical characterisation, as well. In fact, a part from the process controlling and non-destructive tests for assessing the quality of the products, thermography can be adopted for evaluating the fatigue limit, the yield strength of samples undergoing dynamic loading. The standard test method to evaluate fatigue properties of materials requires extremely long lasting test procedure, great number of material testes, and wide number of operating time of machines while by using an IR detector, by following a specific test procedure it is possible to study fatigue and the damage of the material, whatever the material is.

This novel way to perform fatigue tests is consistent with the spirit of ensuring a little time to market of products together with an economic saving.

In this thesis, it will be showed the capabilities of the Thermography to the fatigue characterisation of materials (stainless steels, composites). In particular, the first part (chapter 1 and 2) will be focused on providing the basic concepts on the physics of heat exchange phenomena as well as an understanding on the theory of Thermoelastic Stress Analysis (TSA) approach. This latter, as will be showed, is empirical and provides two methods (temperature variation of first order and thermoelastic phase shift) for studying the behaviour of material undergoing dynamic loading. In chapter 2, together with TSA approach, energetic approaches will be presented capable to provide more information on dissipative heat sources producing damage in the materials. These approaches are focused on the assessment of irreversible phenomena from materials by measuring temperature variations or by assessing the energy dissipated during the hysteresis loop.

In chapter 3, the attempt to unify the approaches is provided by presenting the adopted model of temperature variations. The model presents the measured temperature evolution, as separated in its components of first and second order and relatively phase shifts.

In effect, literature lacks of a unified theory that assesses and uses in the same time both

thermoelastic reversible and dissipative irreversible heat sources.

Due to the adopted model, a single temperature variation can be associated with relative physically explanation, with the advantage that by a single test/thermographic acquisition/analysis it is possible to assess complementary information on behaviour of the material being tested.

An appropriate study of energy dissipation determining the macroscopic physical phenomena related to the fatigue loading, has been setup before building all the models. In fact, the understanding of the fatigue processes (dissipative viscous and plastic phenomena) represents the basis for explaining the temperature variations.

After initial chapters on the theory and physics of heat exchanges, the adopted 'energetic' approach will be shown and the methods and algorithms will be accurately presented. Such the part incorporates all the details of experimental campaigns.

Results, will interest both the aspect of Fatigue: fatigue of smooth samples and fracture mechanics.

In chapter 4, all the aspect of fatigue of smoothed samples will be discussed in sight of viscous and plastic behaviour of material. It will showed the effect of loading ratio or the microstructure on the temperature variation by the sample undergoing cyclic loadings.

The result will focus on different types of materials: stainless steels and composites. The procedure to estimate the fatigue limit will be presented together with the damage phenomena localisation by observing the parameter provided by the adopted model. This feature is very important in case of random loading of operating components for detecting the onset of damage.

Moreover, the procedure setup for evaluating the fatigue limit involves non-destructive fatigue tests, as it is possible to stop the test when a threshold value of temperature variation has been achieved. This could be used for a new generation of fatigue testing by means of thermal methods.

Chapter 5 will be focused on the assessment of fatigue behaviour of composites materials by using all the parameters presented for metals analysis. One of the most important achievements refers to the possibility of separating the behaviour of fiber and matrix in order to study damage phenomena online in situ.

Chapter 6, will present the application of presented approach on fracture mechanics. In this case, when the crack is just developed it is interesting to observe that the thermography can support in assessing otherwise the Paris's law. So that, for real operating components, it is possible to make prediction live on the crack growth and prevent catastrophic failures.

By using the presented model, becomes simple to determine the crack tip position and the plastic area, and distinguish also between static plastic area and the area of crack closure

effect.

Apart from to present the strong impact of Thermography-based approaches in the field of mechanical characterisation, the whole dissertations presented in this work, is addressed to gather all the theories on the study of fatigue by using thermal methods, in order to make more information on damage by a single test.

On the point of view of the market, the presented methods and techniques, will not only reduce time-to-market of products, but also include and increase the quality in the manufacturing process.



To my husband Antonio and my family

To Franco Conticchio, my grandfather.  
No matter how far you are,  
You will remain here, where my heart is.

To all the 'Alice in Wonderland' like me,  
because all the things that happen do not always have a rational explanation,  
but they can be great.  
Be free like a butterfly and strong like a flower.  
Be like yourself.  
Be a natural woman, a gutsy natural woman.

## INDEX

### **1. Chapter 1: Infrared Thermography: Physics, Applications, Potential of development**

*1.1. Heat Exchange: Radiation*

*1.2. Accounting For The Importance Of Thermal Radiation*

*1.3. Basic Concepts*

*1.3.1. Solid angle*

*1.3.2. Spectral or monochromatic radiation intensity  $I_{\lambda,e}$*

*1.3.3. Spectral hemispherical emissive power  $E_b(\lambda)$*

*1.3.4. Relationship between the intensity  $I$  and temperature  $T$*

*1.4. Radiation from Black Body*

*1.5. Radiation from Real Bodies*

*1.6. Atmospheric Radiation*

*1.7. Infrared Detectors*

*1.7.1. Historical Aspects*

*1.7.2. Classification*

*1.7.3. Physical Characteristics*

*1.8. Bolometers*

*1.8.1. Thermistors*

*1.8.2. Liquid Crystals*

*1.9. Photonic Detectors*

*1.9.1. Photo emissive photonic detectors*

*1.9.2. Quantum Detectors*

*1.10. Infrared Imaging Devices*

*1.10.1. Pyroelectric Detectors*

*1.10.2. Infrared Focal Plane Array*

*1.11. Cooling systems*

*1.12. Thermography*

*Conclusions*

*References*

### **2. Thermography Based Approaches**

*2.1. Thermoelastic Stress Analysis*

*2.1.1. Teory, Hystory and Practice*

*2.1.2. First Order Thermoelastic Temperature Variations*

*2.1.3. Cyclic Testing and High Order Temperature Variations*

*2.1.4. Thermoelastic Phase Analysis*

*2.1.5. Application of TSA on cracked specimens*

*2.1.6. Application of TSA on orthotropic materials*

*2.2. Thermal Methods*

*Conclusions*

*References*

### **3. *Toward a Unified Approach: Thermographic Signal Analysis***

*3.1. Evaluation of dissipated energy  $E_d$  in form of heat*

*3.2. Temperature Changes Provided by Energy Variations*

*3.3. The Components Of Thermal Signal: The Temperature Model*

*3.4. Experimental Campaign*

*3.4.1. Emissivity*

*3.4.2. Materials*

*3.4.3. Self-Heating Test And Specific Loading Tables*

*3.4.4. Fracture Mechanics Tests*

*3.4.5. Sample Geometries*

*3.4.6. Machines and Layout*

*3.5. Processing procedures*

*3.5.1. Linear temperature variation ( $T_0$  parameter)*

*3.5.2. Thermoelastic temperature variation ( $T_{the}$  parameter)*

*3.5.3. Thermoelastic phase variation ( $\phi$  parameter)*

*3.5.4. Temperature variation of second order ( $T_d$  parameter)*

*Conclusions*

*References*

### **4. *On The Application of Thermographic Signal Analysis to Fatigue of smoothed samples***

*4.1. Multi-signal analysis for fatigue life estimations*

*4.1.1. The Threshold Method*

*4.1.1.1. Application on Martensitic Stainless Steels*

*4.1.1.2. Comparison between Austenitic and Martensitic Stainless Steels*

*4.1.1.3. Application on Duplex Stainless Steels*

*4.1.2. The Slope Method*

*4.2. Fatigue Damage and Fatigue regimes on Metals: Stress Ratio Influence and Graphic Analysis of Intrinsic Dissipations*

*4.3. Influence of Microstructure of Metals on Thermal Signal*

*Conclusions*

*References*

### **5. *Thermographic Signal Analysis for Composites***

*5.1. Thermographic Signal Approach for studying fatigue in Composites*

*5.1.1. Introduction*

*5.1.2. Recall of basic concepts of TSA applied to Orthotropic Materials*

*5.1.3. Experimental Campaign*

*5.1.4. Method and Data Analysis*

*5.2. A new rapid thermographic method to assess the fatigue limit in GFRP Composites.*

*5.3. Study of damage evolution in composite materials based on the Thermoelastic Phase Analysis (TPA) method*

*Conclusions*

*References*

## **6. *Thermographic Signal Analysis for Fracture Mechanics***

*6.1. TSA for Fracture Mechanics: SIF and Crack Length*

*6.2. Temperature Variation for Assessing Dissipative Effects in the Plastic Zones*

*6.3. On the Use of TPA for Crack Tip Measurement*

*6.3.1. Development of an Automatic Procedure for Paris Law Estimations*

*6.3.2. On the Use of Phase Shift of Second Harmonic for Crack Growth Length Assessment*

*6.4. Development of a Different Form of Paris' Law Based on Dissipative Temperature Components.*

*Conclusions*

*References*

## ***Conclusions***

***Appendix A: Loading Tables***

***Appendix B. Matlab Routines***



---

## ***Chapter 1: Infrared Thermography: Physics, Applications, Potential of development***

---

The common opinion on the concept of '*Heat Transfer*' is that represents the energy interaction that occurs solely due to the temperature difference between a system and its surroundings, in the presence or absence of an intervening medium. In general, the term Heat Transfer can refer also to the different modes of energy exchange: conduction, convection and radiation.

Conduction occurs in presence of a medium without any flow of the medium, when thermal energy is passed from atom to atom through the interatomic forces which tend to maintain the interatomic spacing [1].

The conduction heat transfer, described by Fourier's law of heat diffusion, states that the local heat flux  $\dot{Q}_{cond}$  [W/m<sup>2</sup>] can be related to the local temperature gradient  $\nabla T$  [°C/m] with a proportional relation through  $k$  [W/m °C] which is the thermal conductivity. The minus sign indicates the spontaneous heat transfer occurring between higher to lower temperatures, or down the temperature gradient, according to the Second Law of Thermodynamics. The conduction heat transfer equation is:

$$\dot{Q}_{cond} = -k\nabla T \quad (1.1)$$

Figure 1.1 describes the different phases of conduction heat exchanges in metals: firstly, the particles at the heated end vibrate vigorously, secondly they increase their kinetic energy and collide with neighboring particles and transfer their energy.

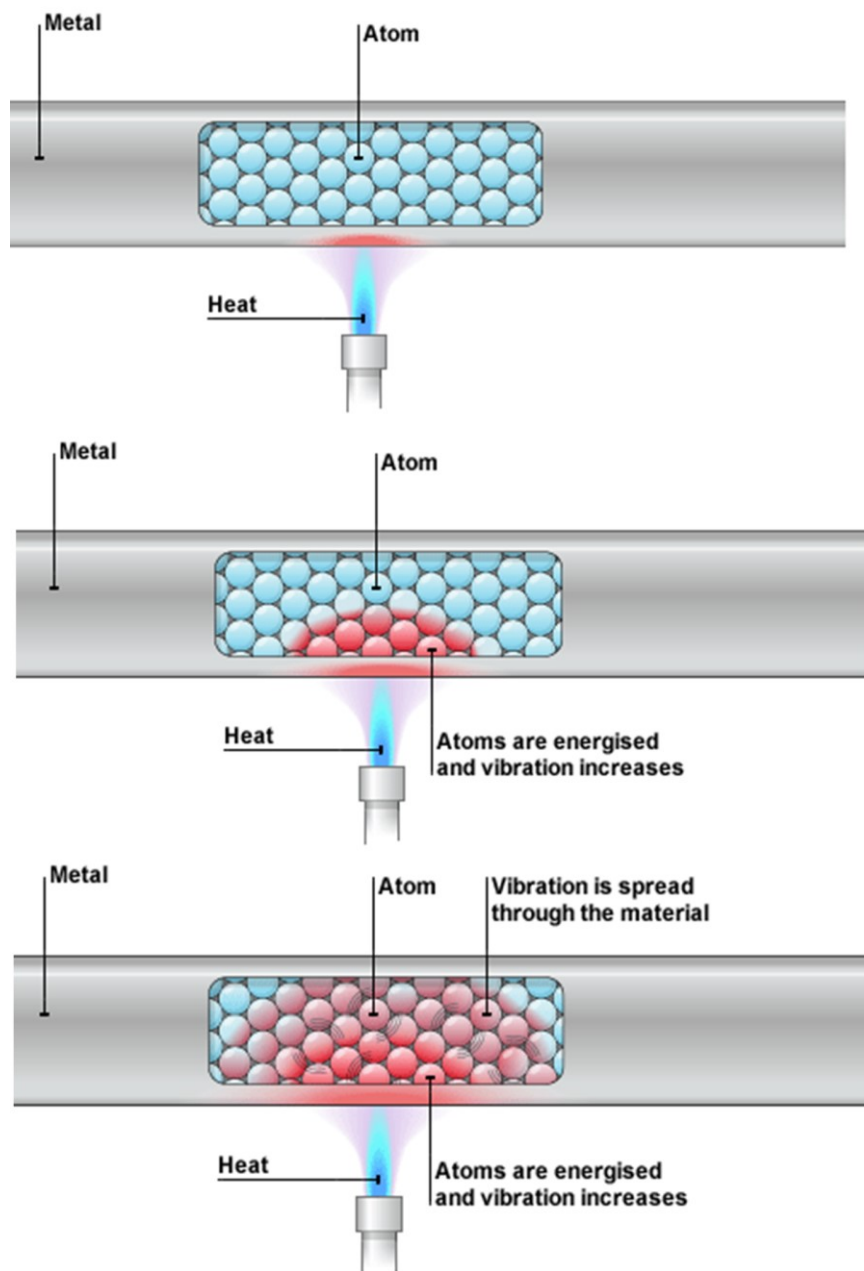


Figure 1.1. Heat conduction in three phases: up) Heat from the source as causing the atoms of the solid to vibrate and gain kinetic energy, middle) Heat from the source as causing the atoms of the solid to vibrate and gain kinetic energy, down) Heat energy is conducted through the solid in this way. As the atoms of the solid gain kinetic energy the temperature of the solid increases [2].

In all solids, thermal energy is transferred through the vibration and collision of particles, in metals, due to the presence of free electrons, thermal energy is also spread through electron diffusion.

Electrons gain kinetic energy and move more rapidly. They collide with atoms in the cooler parts of the metal and pass on their energy in the process [3].

Convection heat transfer requires the presence of an intervening physical medium between

the system object of study and its surroundings. In this case, the medium is the fluid that flows between the system being heated/cooled and its surroundings.

Mathematically Newton's law of cooling governs the phenomenon by stating that the heat flux from a surface at  $T_s$  [°C] temperature to a surrounding fluid, whose temperature far from the surface is  $T_\infty$  [°C], is proportional to temperature difference  $T_s - T_f$ . This relation is expressed by the following equation:

$$\dot{Q}_{conv} = h(T_s - T_f) \quad (1.2)$$

where  $h$  is the heat transfer coefficient [W/m<sup>2</sup>°C].

Since it is an aerodynamic quantity its value depends on the details of the boundary layer flow across the surface being heated/cooled [1]. A schematically representation of the phenomenon is depicted in Figure 1.2.

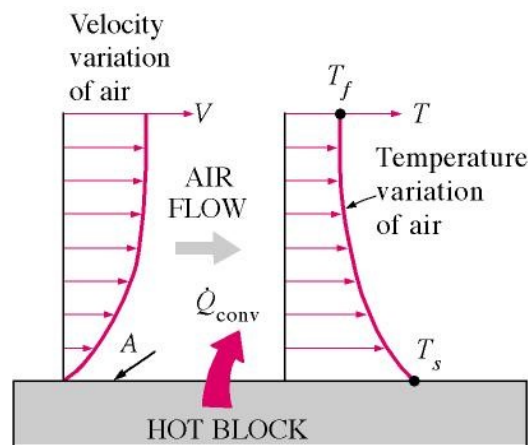


Figure 1.2. Convection heat transfer is the mode of energy transfer between a solid surface and the adjacent liquid or gas that is in motion, and it involves the combined effects of conduction and fluid motion [4].

## 1.1 Heat Exchange: Radiation

Radiation is the transfer of thermal energy in the form of electromagnetic waves, in this case, there is not the aid of a medium: solar energy, X-rays, Cosmic rays represent examples on how energy propagates by means of radiation.

A schematic representation of the electromagnetic spectrum is provided by Figure 1.3.

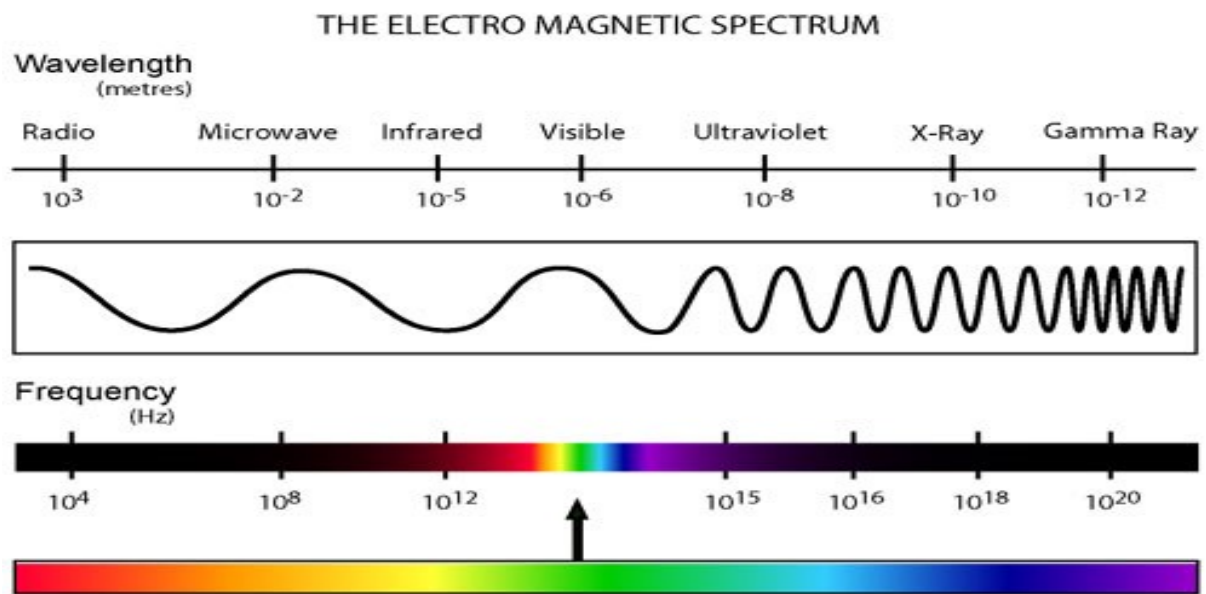


Figure 1.3. The electromagnetic spectrum, the part of the spectrum 'visible' by humans occupies only  $0.3 \mu\text{m}$  of the spectrum![2].

Generally, the frequency of a radiation  $\nu$  (Hz), is related to its wavelength  $\lambda$  (m), according to the relation:

$$\nu = c / \lambda \quad (1.3)$$

where  $c$  (m/s) is light speed in the medium through which the light is passing. In those cases in which effect of polarization, diffraction and interference must be considered this is the best approach to radiation.

Radiant energy propagation can be considered from another viewpoint, in fact, in field of physics is noteworthy to know that electromagnetic radiation has a dual wave-particle nature. In 1924, De Broglie proposed his idea on atomic particles which could exhibit wave properties just as a photon can be assigned mass. By using the Planck's constant  $h$  ( $6.6237 \times 10^{-34} \text{ J s}$ ) and the statement particle momentum ( $p = mc$ ), the wavelength of the de Broglie can be defined as:

$$\lambda = h/p \quad (1.4)$$

Equation 1.4 establishes that radiation has dual wave-particle nature, in some cases it is convenient to consider that light emitted and propagates as a stream of energy packets (photons) [1] in other cases it is convenient to refer to light as a wave.

The dual wave-particle nature of radiation represent both the basis of Einstein's theory of Relativity and the basis of science of spectroscopy. In fact, as a consequence of de Broglie principle, when an electron moves from one energy level to another within an atom, a corresponding amount (quantum) of energy be absorbed or emitted from the atom.

These concepts make a rough idea of the nature of electromagnetic radiation.

In particular, thermal radiation is the part of electromagnetic radiation emitted by a material substance solely due to its temperature. All bodies at temperature higher than 0K emit a radiation in the band of Infrared wavelengths.

At such the temperature particles (electrons, ions, atoms, molecules) oscillate producing heating. The related heat transfer is provided by electromagnetic waves capable of carrying energy from one location to another, especially under vacuum conditions [5].

The model adopted for studying the radiation heat transfer is Stefan-Boltzman's model represented by equation:

$$\dot{Q}_{\text{rad}} = \sigma(T_b)^4 \quad (1.5)$$

The model presented by equation 1.5 refers the heat flux emitted from a blackbody at absolute temperature  $T_b$ . The quantity  $\sigma$  represents the Stefan-Boltzman constant. Since the equation refers to an ideal condition, it has to be modified in case of 'real' surfaces and bodies. The correcting factor is called emissivity  $\varepsilon$ . The role of emissivity is to multiply the Stefan-Boltzman constant, it is a non-dimensional factor, its meaning will be furtherly explained.

## **1.2 Accounting For The Importance Of Thermal Radiation**

The factor, which determines the importance of thermal radiation in some applications, is the manner in which radiant emission depends on temperature. The heat transfer by thermal radiation, according to equation 1.5, has a fourth power dependence from temperature. Convection and conduction have a first power dependence from temperature variations. This lead to the considerations that, especially when the absolute temperature are high in value, radiation heat exchange assumes a great importance. For instance, some devices for space applications are designed to operate at high temperature levels to achieve high thermal efficiency, hence radiation must be considered in calculating thermal effects in components of Aerospace Industry.

The importance of Radiation is also due to the absence of medium between the two locations for radiant exchange, that is, the thermal radiation passes through a vacuum. This is in contrast with the physics of convection and conduction heat transfers, as previously said. This leads to develop a technique which allows measuring the heat contribution from a body without contact [6].

Moreover, the double wave-particle nature of thermal radiation involves also the development of two types detectors based on: photon emission (zero mass particles with quantum energy) or electromagnetic wave emission with own frequency and wavelength. This allows different ways to study radiative phenomena.



## 1.3 Basic Concepts

### 1.3. 1 Solid angle

Consider Figure 1.5, the elemental plane angle shown here is  $d\alpha = dl/r$ . Consider the elemental area  $dA_n$  which subtends an elemental solid angle  $d\omega_n$  as shown in Figure 1.5. The elemental solid angle  $d\omega_n$  is given by

$$d\omega_n = \frac{dA_n}{r^2} \text{ [steradians]} \quad (1.6)$$

where  $A_n$  is the normal area.

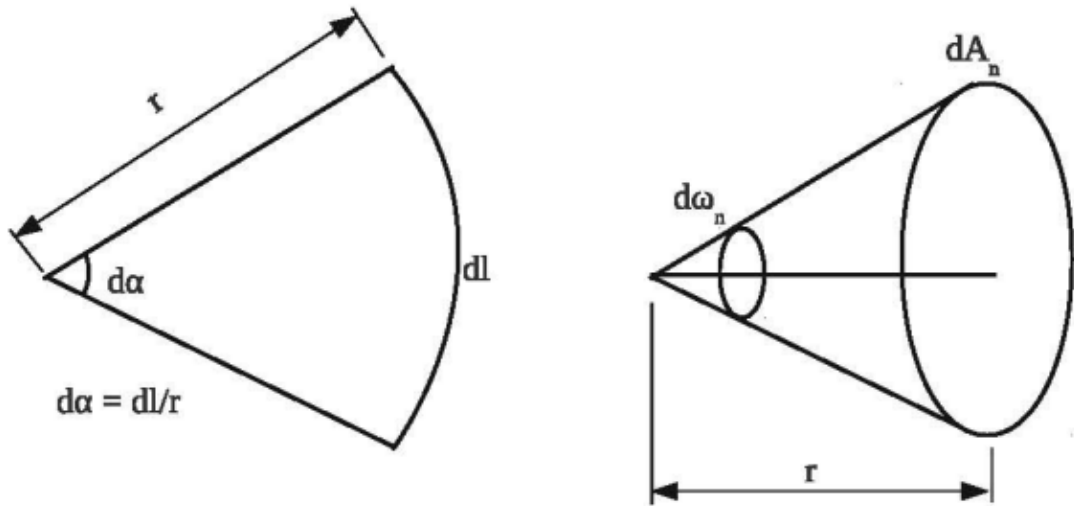


Figure 1.5. Plane (a) and solid (b) angles.

Consider Figure 1.6, and suppose that  $dA_l$  is the emitting surface and radiation is spreading from this surface in all the directions. Among all the directions, we are taking a small elemental area  $dA_n$  and are trying finding out how much radiation this area intercepts and try and work this out in terms of the fundamental coordinates.

The solid angle is the angle subtended by an elemental area  $dA_n$  at a point on  $dA_l$  where  $dA_l$  is the area emitting the radiation and  $dA_n$  is the elemental area which is receiving the radiation.

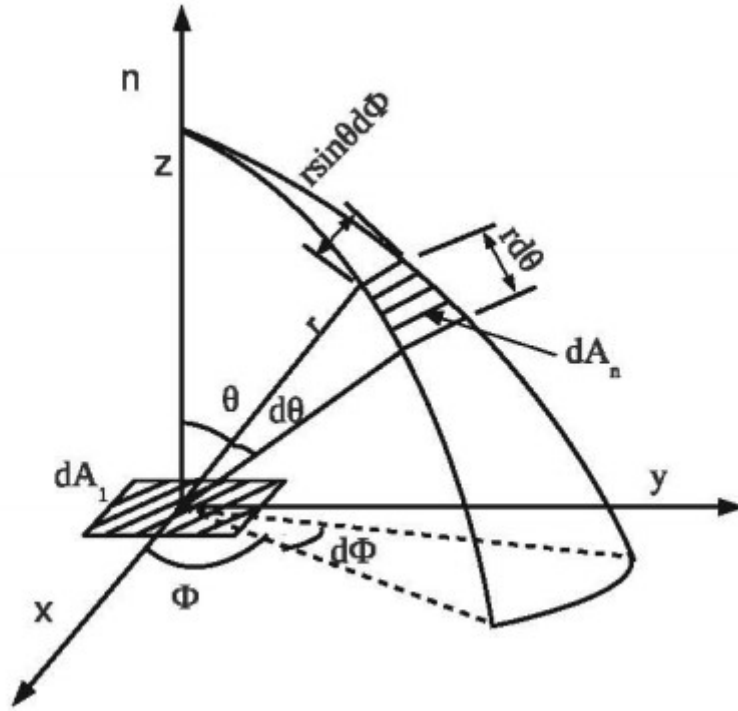


Figure 1.6. Solid angle subtended by  $dA_n$  about  $dA_1$  in the spherical coordinate system

By using the definition of solid angle shown in equation 1.7, the solid angle become:

$$d\omega = \frac{r^2 \sin\theta d\theta d\phi}{r^2} \quad (1.7)$$

Therefore, the total solid angle associated with the elemental area  $dA_1$ , if radiation is falling on a hypothetical hemisphere above it, is given by

$$\omega = 2\pi r \quad (1.8)$$

Therefore the total solid angle associated with the hemisphere is  $2\pi$  steradians. The solid angle associated with a sphere will be  $4\pi$  steradians. The solid angle is a very important concept in radiative heat transfer because we are finally interested in the radiation heat transfer between surfaces [7].

Therefore, it is interested in heat transfer between surfaces and these surfaces are of finite area, because radiation has a tendency to spread in all the directions, it is important to know the directional orientation of one surface with respect to the other surface.

In order to do this, not only is the spherical coordinate system useful, the definition of the solid angle also becomes imperative and essential.

### 1.3. 2 Spectral or monochromatic radiation intensity $I_{\lambda,e}$

In order to understand the meaning of  $I_{\lambda,e}$ , it is very important to refer to Figure 1.6 where  $dA_I$  is the emitting surface or the surface that emits the radiation and the shaded region represents the elemental area  $dA_n$  that intercepts the radiation from  $dA_I$ . The centers of  $dA_I$  and  $dA_n$  are joined, and the distance between them is denoted by radius  $r$ . In principle, if we join any point on  $dA_I$  with any point on  $dA_n$ , that should also be  $r$  because  $dA_I$  and  $dA_n$  are infinitesimally small surfaces. The zenith angle and the azimuthal angle are also marked on the Figure 1.6. The zenith angle  $\theta$  varies from 0 to  $\pi/2$  for the hemisphere while the azimuthal angle  $\phi$  varies from 0 to  $2\pi$ .

The spectral radiation intensity  $I_{\lambda,e}$  ( $\lambda$  stands for a spectral quantity and the subscript  $e$  denotes that emission is under consideration) is the rate at which radiant energy is emitted by a surface, per unit area normal to the surface, in the direction  $\theta$ , per unit solid angle  $d\omega$  about  $(\theta, \phi, \lambda)$  in the unit wavelength  $d\lambda$  about  $\lambda$ , given by:

$$I_{\lambda,e}(\theta, \phi, \lambda) = \frac{dQ}{dA_I \cos\theta d\omega d\lambda} \text{ [W/m}^2 \text{ } \mu\text{m steradians]} \quad (1.9)$$

The reason for in the equation the spectral radiation intensity is indicated in function of wavelength is such that the radiation, whether emission or reflection, in general, will be a function of wavelengths. The radiation emitted by a surface can also be in all possible directions or wavelength. Therefore, it is important that the directional and spectral nature of the intensity of radiation be taken into account.

### 1.3. 3 Spectral hemispherical emissive power $E_b(\lambda)$

The spectral emissive power from a black body  $E_b(\lambda)$  is

$$E_b(\lambda) = \int_0^{\pi/2} \int_0^{2\pi} I_{\lambda,e} \cos\theta \sin\theta d\phi \text{ [W/m}^2 \text{ } \mu\text{m]} \quad (1.10)$$

This is called the spectral hemispherical emissive power. It is spectral because it is still a function of  $\lambda$  as we have not integrated it with respect to  $\lambda$ . and it is hemispherical because we have integrated it with respect to a hypothetical hemisphere by doing two integrations, one with respect to  $\theta$  and the other with respect to  $\phi$ .

The total hemispherical emissive power is  $E_b(T)$ , where total means that the integration is

with respect to the wavelength, hemispherical means that the integration is with respect to the angle. The equation representing  $E_b(T)$  is:

$$E_b(T) = \pi I_{\lambda,e}(T) \quad (1.11)$$

Where  $E_b(T)$  depends on:

$$E_b(T) = \int_0^\infty E_b(\lambda) d\lambda \quad (1.12)$$

with the appropriate substitutions and by considering as a black body is diffuse,  $I_{\lambda,e}(\theta, \phi, \lambda)$  can be pulled out of the integral and retained while performing the integration with respect to the direction, and it becomes  $I_b(T)$ .

Finally, equation 1.12, represents the emissive power of a black body integrated for all the wavelengths and over the hemisphere.

### 1.3. 4 Relationship between the intensity I and temperature T

Right now the considered quantities have been of wavelength domain, the question is if is possible to assess the same relationships by using thermodynamic quantities.

Consider a gas occupying a volume  $V$ , with pressure  $P$ , at temperature  $T$ .

The total internal energy  $U$  is equal to the product of the specific internal energy  $u$  and the volume  $V$ . The specific internal energy is defined as energy per unit volume.

$$U = uV \quad (1.13)$$

From the second Law of Thermodynamics relations:

$$TdS = dU + PdV \quad (1.14)$$

$$TdS = d(uV) + PdV \quad (1.15)$$

$$TdS = u dV + V du + PdV \quad (1.16)$$

By considering that  $p = u/3$

$$TdS = u dV + V du + u/3 dV \quad (1.17)$$

$$TdS = V du + 4/3 u dV \quad (1.18)$$

$$dS = \frac{V}{T} du + \frac{4}{3T} u dV \quad (1.19)$$

The quantity  $S$ , here is entropy, a property and hence it is a point function. As a consequence,  $dS$  is an exact differential. So that by differentiating equation 1.19:

$$\frac{du}{u} = 4 \frac{dT}{T} \quad (1.20)$$

And integrating both sides:

$$\ln(u) = 4\ln(T) + \ln(c_1) \quad (1.21)$$

the follow equation is obtained:

$$u = aT^4 \quad (1.22)$$

the quantity ' $u$ ', for a black body is defined as:

$$u_b = \frac{4\pi I_b}{c} \quad (1.23)$$

Equation 1.22, becomes:

$$\frac{4\pi I_b}{c} = aT^4 \quad (1.24)$$

For a blackbody, the emissive power is:

$$E_b = \pi I_b \quad (1.25)$$

And then

$$E_b = \frac{ac}{4} T^4 \quad (1.26)$$

Stefan-Boltzmann arrived at this independently, in this equation  $c$  is the velocity of light in vacuum ( $2.998 \times 10^8$  m/s), and however the constant ' $a$ ' is not known. To get a value of ' $a$ ',

this expression has to be matched with the values got through experiments. By doing this, it is now known that  $ac/4 = 5.67 \times 10^{-8} \text{ W/m}^2\text{K}^4$  that can be referred as Stefan-Boltzmann constant  $\sigma$ :

$$E_b = \sigma T^4 \quad (1.27)$$

It still does not know what " $I$ " is. But with the help of thermodynamics, without knowing  $I$ , it is possible to establish that the black body radiation is proportional to the fourth power of temperature. Many questions are still unanswered such as, for a given temperature, how does  $I_b$  vary with  $\lambda$ .

Wien (1864 - 1928), a German, was the first scientist who proposed a distribution in 1886 as follows:

$$I_{b,\lambda}(\lambda, T) = \frac{c_1 \lambda^{-5}}{e^{c_2/\lambda T}} \quad (1.28)$$

Where  $c_1$  and  $c_2$  values are respectively  $1.19 \times 10^{-8} [\text{W}\mu\text{m}^4/\text{m}^2]$  and  $14388 [\mu\text{mK}]$ .

For a black body at 6000 K (the temperature of the sun), while the Wien's distribution holds good for short wavelengths, it deviates from the experimentally obtained distribution at higher values of  $\lambda$ , see Figure 1.7.

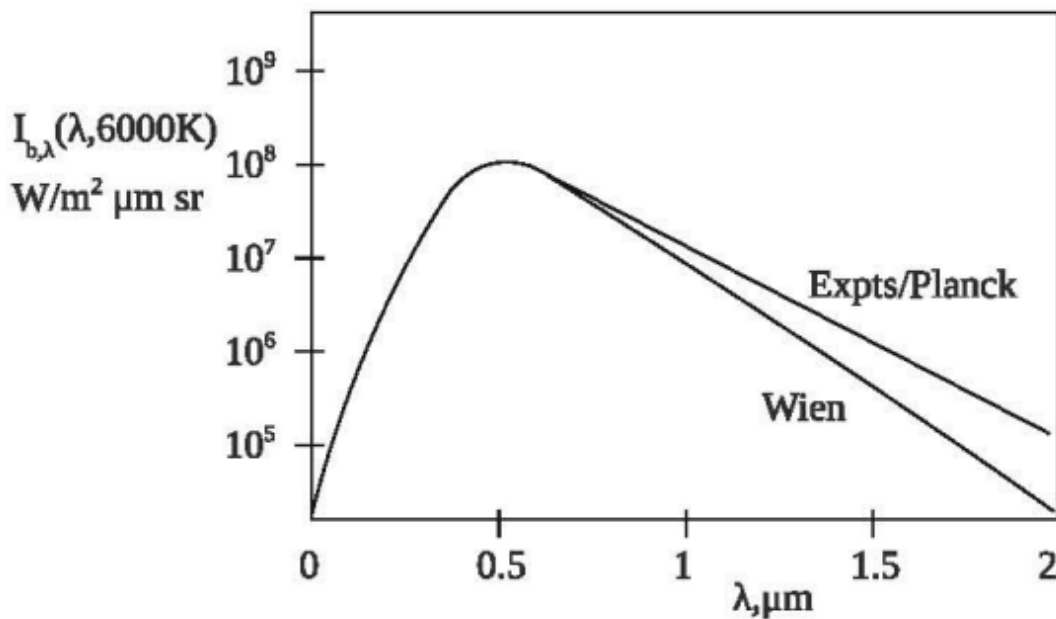


Figure 1.7. Wien's distribution and comparison with experiments

The second distribution was proposed by the two scientists Lord Rayleigh (1842 - 1919) in



1900 and Sir Jeans (1877 - 1946) in 1905. They both independently worked out yet another incorrect distribution for  $I_{b,\lambda}$  as follows:

$$I_{b,\lambda}(\lambda, T) = \frac{c_1 \lambda^{-5}}{c_2 / \lambda T} \quad (1.29)$$

Referring to Wien's distribution, the numerator together with the constants  $c_1$  and  $c_2$  of equation 1.28 are the same, both the distributions at shorter wavelengths  $I_{b,\lambda}(\lambda, T) \rightarrow \infty$  that is not true. So at ultraviolet wavelengths, there is a significant deviation from measured values and this dramatic failure of classical physics in the hands of two greatest physicists was called as the ultraviolet catastrophe!

In 1901 (four years before the publication of the incorrect Rayleigh-Jeans distribution), Max Planck proposed a distribution for  $I_{b,\lambda}(\lambda, T)$ , by only putting the term  $(-1)$  at the denominator of the Wien's distribution:

$$I_{b,\lambda}(\lambda, T) = \frac{c_1 \lambda^{-5}}{e^{\frac{c_2}{\lambda T}} - 1} \quad (1.30)$$

The distribution represented in equation 1.30, proposed by Planck agreed perfectly with experimental data obtained.

The correct distribution was proposed by Planck and for proposing this correct quantum hypothesis, he was awarded the Nobel prize in 1918 at the age of 60. The logic is more or less the same as what Rayleigh Jean proposed, but there is a modification in terms of the average energy, the  $C_1$  ( $1.198 \times 10^8 \text{ W}\mu\text{m}^4/\text{m}^2$ ) is called the first radiation constant and  $C_2$  ( $14388 \mu\text{mK}$ ) is called the second radiation constant. A representation of the distribution is presented in Figure 1.8.

As depicted in Figure 1.8 the following points emerge:

- $I_{b,\lambda}$  is a continuous function of  $\lambda$ , for every value of  $\lambda$ , just unique value for  $I_{b,\lambda}$ ,
- For every temperature there is a peak,
- For a given  $\lambda$ ,  $I_{b,\lambda}$  increases with temperature, as stated by second law of thermodynamics,
- The peak of  $I_{b,\lambda}$  is shifted to the left for increasing temperatures.

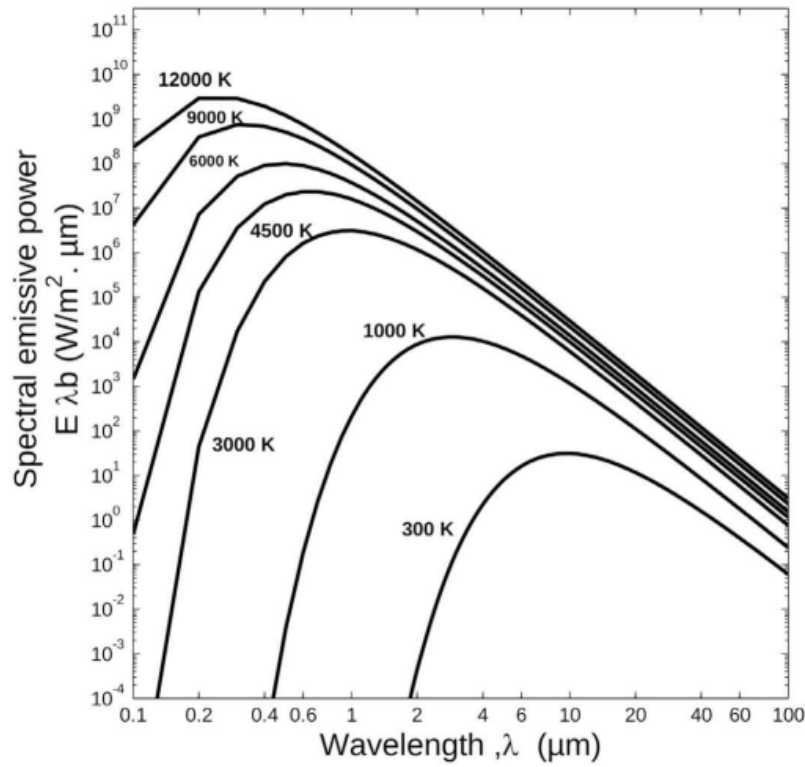


Figure 1.8. Planck's distribution.

The equation 1.30 is valid under the hypothesis that energy transfer must take place only in discrete multiples of ' $h\nu$ ': it was the beginning of quantum mechanics, [7].

An interesting result regarding the black body can be assessed by dividing equation 1.30 by the quantity  $T^5$ :

$$\frac{I_{b\lambda}(\lambda, T)}{T^5} = \frac{1}{T^5} \frac{c_1 \lambda^{-5}}{e^{\frac{c_2}{\lambda T}} - 1} = f(\lambda T) \quad (1.31)$$

By dividing  $I_{b\lambda}$  by a simple quantity  $T^5$  it is possible to assess a term which is function only of  $\lambda T$ , the relative curve for the temperature of 2898  $\mu\text{mK}$  represents the universal black body distribution function. The area under this curve, between two fixed wavelength indicates the fraction that is emitted in a particular band.

In other words, all Planck blackbody radiation distribution curves for all temperature and all wavelengths collapse onto a single curve under the change of variable operated by equation 1.31, as possible to see in figure 1.9, [1].

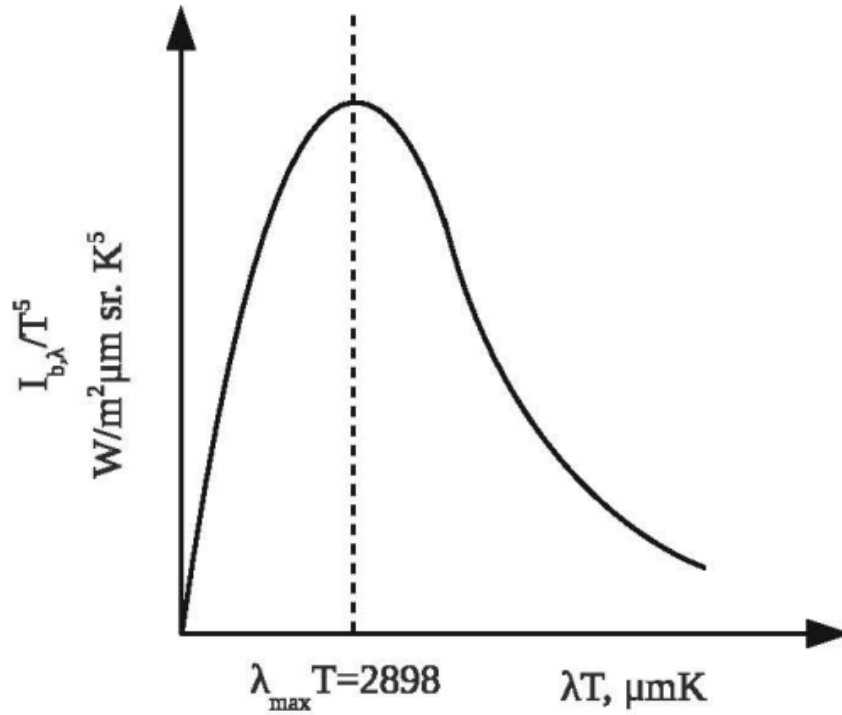


Figure 1.9. Universal black body distribution function.

By integrating several times the equation 1.30, and opportunely operating a change of variable it is possible to obtain the formula  $E_b = \sigma T^4$  and also make several points:

- For the limit that  $c_2/\lambda T$  is very small, the Rayleigh-Jeans law is assessed
- When  $c_2/\lambda T$  is very large, Wien's equation is assessed,
- By integrating the Planck's distribution, the Stefan-Boltzmann law is assessed.

It is also interesting to know the wavelength at which the blackbody radiation distribution function peaks for a given temperature. In other word, the question is :”for what value of  $\lambda T$  is the function maximum?”.

Wien's attempted to answer to this question by setting the Wien's displacement law in its more general form:

$$I_{b,\lambda}(\lambda, T) = T^5 f(\lambda, T) \quad (1.32)$$

This equation is very important since it means that whatever the form of the function  $f(\lambda, T)$ , the successful radiation distribution function for blackbodies at all temperatures mus have the property that, when divided by  $T^5$ , the result is a function only of the product  $\lambda T$  [1].

## 1.4 Radiation From Black Body

Blackbody can be referred as an instrument that absorbs radiations from any direction and wavelength [5].

The concept of blackbody is an idealisation which allows studying the radiation phenomena. When radiation is incident on a homogeneous body, the results is that a part of it is reflected, another part penetrates into the body. A certain amount of energy could be also absorbed by the medium. Moreover, depending on the thickness of the material, a portion of incident energy can be also transmitted through the body. If, on the other hand the material is a strong internal absorber, the radiation that is not reflected from the body will be converted into internal energy within a thin layer adjacent to the surface. Depending on the material properties, the body can be a good absorber, if the ability to internally absorb the radiation after is passed into the material or vice versa the material could let the radiation pass through its surface. To be a good absorber for incident energy, a body must have a low surface reflectivity and internal absorption sufficiently high to prevent the radiation for passing through. Blackbody must have zero surface reflection and complete internal absorption [6]

This lead to make a definition for blackbody: A black body is one that allows all incident radiation and internally absorbs all of it [7].

The blackbody is a perfect radiator, the radiation emitted in function of the blackbody temperature, its magnitude depends on the wavelength. The blackbody moreover, isotropically diffuse its radiation since the radiation does not depend on the direction [8].

A schematization of the laboratory blackbody is depicted in Figure 1.10.

Therefore, for a given wavelength and in a given incident direction, there can be no body which absorbs more radiation than a black body. Any real body has to absorb a radiation which is lower than that of the black body.

Even if, basically, blackbody is a mathematical concept, in nature real examples of blackbodies do exist such as: cavity with small aperture, or a flat surface with perfect absorbing coating. However, real blackbodies are different from perfect blackbody, in fact for example the radiation is not isotropically diffused [5].

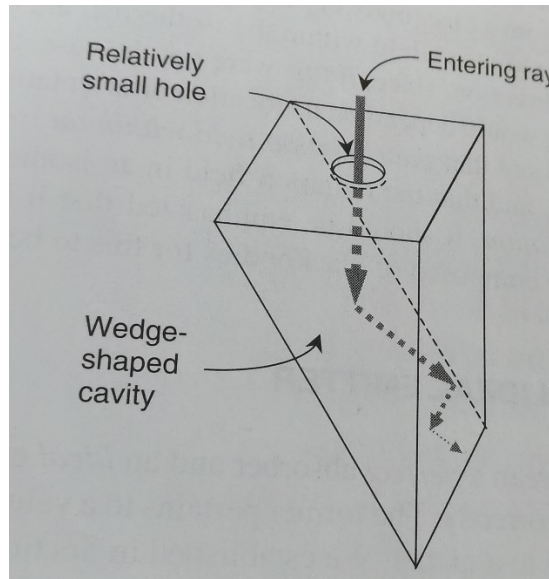


Figure1.10. example of practical laboratory blackbody (temperature is controlled to a uniform value, the wall coating absorbs more than 90% of all incident radiation , reflection are mostly mirror like [1].

A part from its characteristics, the blackbody presents different important properties, in fact as a perfect absorber and perfect emitter, the properties of a blackbody as an ideal emitter are here presented:

- **Ideal emitter:**

Because the blackbody is by definition absorbing the maximum possible radiation incident from an enclosure at each wavelength and from each direction, it must also be emitting the maximum total amount of radiation.

- **Radiation isotropy in a black enclosure**

This property is due to the evidence that it is an ideal emitter. Because the black radiation filling the enclosure is isotropic, the radiation received and hence emitted in any direction by the enclosed black surface, per unit projected area normal to that direction must be the same as that in any other direction.

- **Perfect emitter at every wavelength**

The total radiant energy emitted by a blackbody in vacuum is a function only of its temperature.

- **Total radiation into vacuum is a function only of temperature**

The total radiant energy emitted by a blackbody in vacuum is a function only of its temperature.

## 1.5 Radiation From Real Bodies

In reality, it is almost impossible to encounter a black body. Real bodies are neither perfect absorbers nor perfect emitters. So there is a deviation from black body behaviour in fact the totality of cases, the surfaces are real surfaces that are not black bodies.

Therefore, the concept of radiation surface properties have to be introduced. The goal of this characterization is to be able to quantify the departure of real bodies from black body behaviour, Figure 1.11. This departure manifests itself as incomplete absorption and imperfect emission.

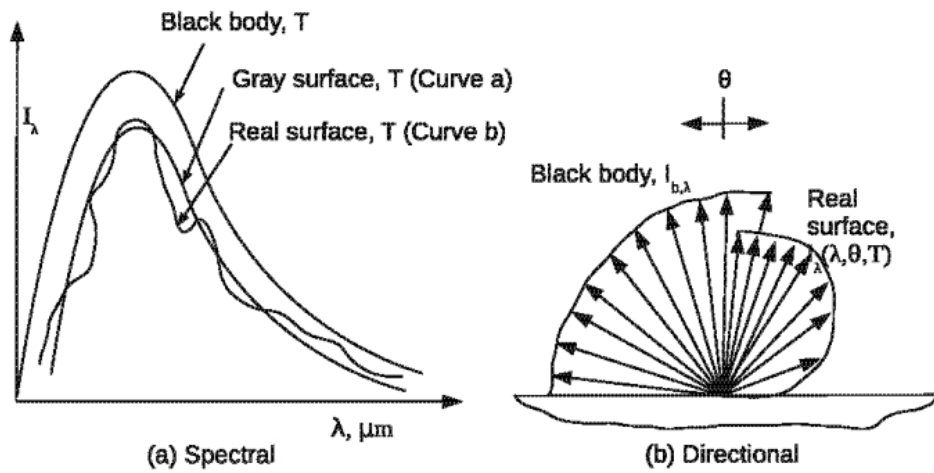


Figure 1.11. Typical distribution of  $I_{b,\lambda}$  for real surfaces

By Considering Figure 1.11, that presents the typical variation of spectral intensity of emission with wavelength for a black body at 1073 K (about 800 °C), a temperature normally encountered in engineering. Using the Planck's distribution, we can plot the curve of  $I_{b,\lambda}$  versus  $\lambda$  and the peak of the distribution is around 2.8  $\mu\text{m}$ . We can have a body corresponding to curve 'a' which is called a gray body at 1073 K, whose ratio of emission at a particular wavelength to that by a blackbody is fixed. Mathematically for a gray body/surface the relation representing  $I_{b,\lambda}$  is:

$$\frac{I_{\lambda}}{I_{b,\lambda}} \neq f(\lambda) \quad (1.33)$$

The gray body is an idealization, which we use because it helps us to simplify calculations in radiative heat transfer.

Why is it used? Because, for most surfaces,  $I_{b,\lambda}$  versus  $\lambda$  is not known. The ratio given above

is called emissivity and when it is a function of wavelength, it is called spectral emissivity and this is unknown for most surfaces and therefore we go in for gray body behavior. The other reason is that even if the spectral emissivity is known, often we do not know how to incorporate this information into our analysis, which is generally the case. So, because of these two reasons, namely, either the spectral emissivity is not known or if known, we do not have the competence or wherewithal to use this information, people go in for a simple assumption where  $\frac{I_\lambda}{I_{b,\lambda}}$  is not a function of  $\lambda$ . This is called the gray body assumption.

Let consider now the properties of non-blackbodies as emitter:

- **Emissivity**

- **Spectral directional emissivity  $\epsilon'_\lambda(\lambda, T, \theta, \phi)$**

The spectral directional emissivity given by  $\epsilon'_\lambda$  is the ratio of the spectral directional intensity of emission of a real surface to the spectral radiation intensity of a black body at that wavelength, at that temperature in the same direction. It can be defined as:

$$\epsilon'_\lambda (\lambda, T, \theta, \phi) = \frac{I_{\lambda,e}(\lambda, T, \theta, \phi)}{I_{b,\lambda}(\lambda, T)} \quad (1.34)$$

So, as expected, it is a dimensionless ratio, which varies between 0 and 1. It is a non dimensional way of declaring the efficiency of emission of a surface. To say how efficient a surface is, the benchmark is the black body. Corresponding to a black body, how efficiently the surface is emitting is what this number conveys.

For a diffuse surface the following relations hold,

$$\epsilon'_\lambda (\lambda, T, \theta, \phi) = \epsilon'_\lambda (\lambda, T) \quad (1.35)$$

The term "diffuse" is with respect to angle and "gray" is with respect to wavelength. For a gray, diffuse surface, then is only function of the temperature:

$$\epsilon'_\lambda (\lambda, T, \theta, \phi) = f(T) \quad (1.36)$$

- **Hemispherical spectral emissivity  $\epsilon_\lambda(\lambda, T)$**

The mathematically hemispherical spectral emissivity,  $\epsilon_\lambda(\lambda, T)$  is expressed by

$$\epsilon_\lambda(\lambda, T) = \frac{E_\lambda(\lambda, T)}{E_b(\lambda, T)} \quad (1.37)$$

- **Directional total emissivity,  $\epsilon'(T, \theta, \phi)$**

The prime in the symbol denotes that it is still a directional quantity, but we got rid of the  $\lambda$  and hence it is a total emissivity. Mathematically, is provided by:

$$\epsilon'(T, \theta, \phi) = \frac{E'(T, \theta, \phi)}{E_b(T, \theta, \phi)} \quad (1.38)$$

- **Hemispherical total emissivity,  $\epsilon(T)$**

However, sometimes the dependence is weak and in which, we assume that the emissivity is independent of temperature. The hemispherical, total emissivity denoted by  $\epsilon(T)$  is given by the emissive power of a real surface at a given temperature  $T$  divided by the emissive power of a black body at the same temperature.

The mathematical expression is:

$$\epsilon(T) = \frac{E(T)}{E_b(T)} \quad (1.39)$$

By resuming, the emissivity is function of the direction of emission of energy from the surface. This is an important statement since it depends on the quality and surface finishing. In case the roughness is accentuated, inter-reflection phenomena occur, and consequently multiple absorptions are present, hence the surface properties change.



## ▪ Absorptivity, Reflectivity, Transmissivity

By considering an incident radiation on a surface (Figure 1.12), it is possible to see that this radiation can be absorbed, reflected or transmitted. If we apply the first law of thermodynamics to this system, mathematically we can state that at steady state:

$$Q_{inc} = Q_{abs} + Q_{ref} + Q_{trans} \quad (1.40)$$

Where  $Q_{inc}$  is the quantity of incident energy,  $Q_{abs}$  is the quantity of absorbed energy,  $Q_{ref}$  is the quantity of reflected energy and  $Q_{trans}$  is the quantity of transmitted energy.

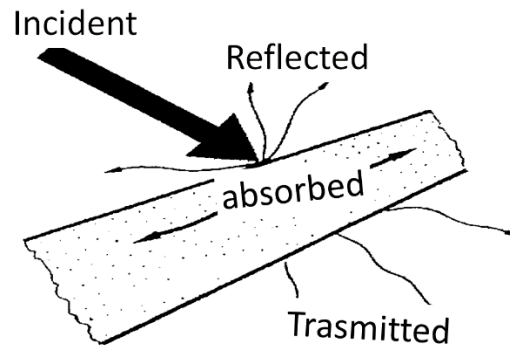


Figure 1.12. Breakdown of incident waveform.

Dividing by  $Q_{inc}$  all the terms of equation 1.40, it is possible to assess three dimensionless ratios, none of which individually greater than 1. Such the quantities are also measures of the efficiency with which a surface absorbs, reflects or transmits, in particular the ratio  $Q_{abs}/Q_{inc}$  is called the *absorptivity* denoted by  $\alpha$ , the term  $Q_{refl}/Q_{inc}$  is called *reflectivity* and denoted by  $\rho$ , the term  $Q_{trans}/Q_{inc}$  is called *transmissivity* and denoted by  $\tau$ .

Hence the equation 1.40, can be rewritten as :

$$\alpha + \rho + \tau = 1 \quad (1.41)$$

or referring to a specific wavelength :

$$\alpha_{\lambda} + \rho_{\lambda} + \tau_{\lambda} = 1 \quad (1.42)$$

In case the body has an opaque surface, being  $\tau=0$ , the equation 1.41, becomes:

$$\alpha + \rho = 1 \quad (1.43)$$

Let focus on the properties of non-blackbodies as absorber, hence the characteristic being considered is absorptivity.

A body which is heated by incoming solar radiation to a temperature of 80°C or 100°C, will emit in the infrared part of the spectrum. Now, if we have a surface that emits very poorly in the infrared part of the spectrum, but absorbs very well in the visible part of the spectrum, we have a good solar collector. By the same token, if we have a surface that absorbs very poorly in the visible part of the spectrum, but emits very well in the infrared part of the spectrum, it may be a good candidate for insulation.

Referring to absorptivity, several can be made:

- The spectral directional absorptivity is equal to the spectral directional emissivity :  $\alpha'(\lambda, T, \theta, \varphi) = \epsilon'(\lambda, T, \theta, \varphi)$  which represents the Kirchoff's law which is always true and holds good without any constraints.
- For a gray diffuse surface, the emissivity is equal to the absorptivity which is also equal to the total hemispherical emissivity and the total hemispherical absorptivity:  $\alpha = \epsilon$ .

Radiation coming on to a surface can come from one particular direction or from the hemisphere above the surface. By the same token, it is possible to look at the reflected radiation as going out in a particular direction or as going out in the hemispherical space above the surface; so there are four possibilities:

- 1) If incident radiation is from a particular direction, reflected radiation can go out in a particular direction.
- 2) The incoming radiation can be from a particular direction while the radiation going out is into the hemispherical space.
- 3) The incoming radiation can come from the hemispherical space and the outgoing radiation can be in a particular direction.
- 4) The radiation can come from the hemispherical space and also go out in to the hemispherical space.

The spectral dependence, in these cases have to be considered.

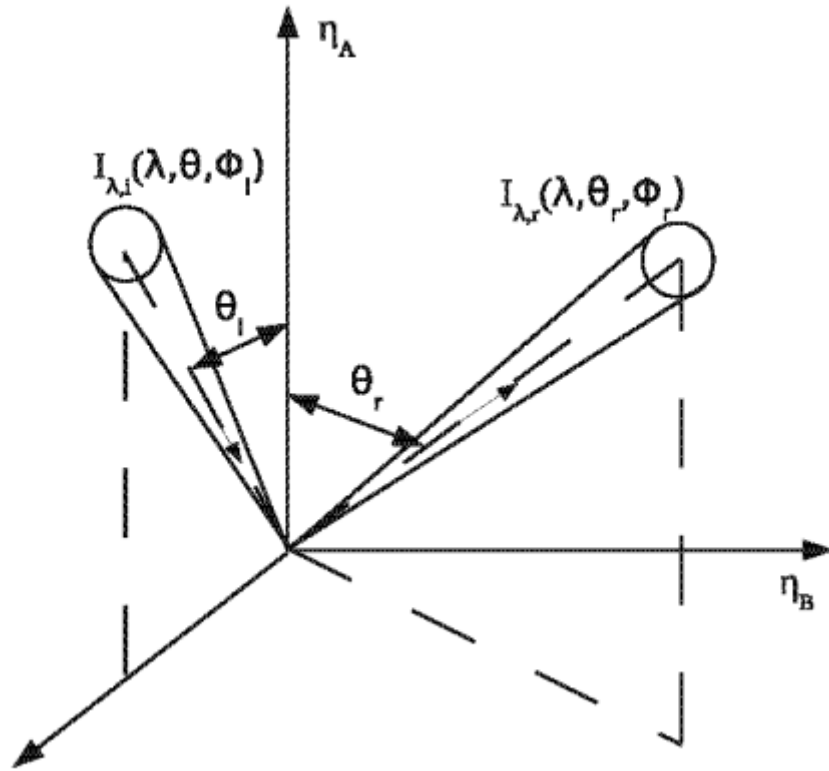


Figure 1.13. Bi-directional reflectivity

In the Figure 1.13 it is possible to observe the incident radiation  $I_{\lambda,i}$  as a function of  $\lambda, \theta_i, \phi_i$  while outgoing radiation  $I_{\lambda,r}$  is a function of more and more quantities:  $T, \lambda, \theta_i, \phi_i, \theta_r, \phi_r$ . The reflection can take place in any direction, by focusing on the specific direction defined by the angles  $\theta_r, \phi_r$ , it is possible to observe at first sight, that with respect to absorptivity the reflectivity depends of two more quantities  $\theta_r, \phi_r$ , in case of bi-hemispherical total reflectivity  $\rho$  is given by :

$$\rho = \frac{\int_{\lambda=0}^{\infty} \rho_{\lambda} I_{\lambda,i} d\lambda}{\int_{\lambda=0}^{\infty} I_{\lambda,i} d\lambda} \quad (1.44)$$

Another property is the transmission of the radiation, particularly important in those cases (i.e. glass), in which the incident radiation can penetrate the medium (a non-opaque body). In case the radiation passing through the medium (absorbed or scattered) the medium can referred as participating medium [5].

A medium that can absorb, scatter and transmit is called a participating medium, by indicating the thickness of the participating medium with ' $t$ ', then the spectral transmissivity is:

$$\tau_{\lambda}(\lambda, t) = \frac{I_{\lambda, tr}(\lambda)}{I_{\lambda, i}(\lambda)} \quad (1.45)$$

The total transmissivity  $\tau$  is given by:

$$\tau(t) = \frac{\int_{\lambda=0}^{\infty} \tau_{\lambda} I_{\lambda, i} d\lambda}{\int_{\lambda=0}^{\infty} I_{\lambda, i} d\lambda} \quad (1.46)$$

The basic difference between a participating medium and the surfaces so far considered is that reflection, absorption, happen in the first few micrometers of the surface. In the atmosphere, the radiation penetrates deep inside, agitates all the molecules within it, which may absorb, scatter or reflect the radiation or the atmosphere itself may emit volumetrically. This is different from the emission of a surface. In the case of the atmosphere, the whole gas volume emits. It may scatter differently in different directions (anisotropic scattering).

In participating media, there can be emission, absorption and also scattering. Scattering is basically reflection, but is from the volume. This scattering could be a function of wavelength and also a function of the angle, otherwise, the medium is called as isotropic. Scattering also depends on the size of the particle, like in the case of the atmosphere. Scattering by a dust particle will be different from the scattering by a water molecule, which will be different from the scattering by an ice particle. When the ice particle is oblique and non-spherical, the scattering phenomena can get very involved [7].

## 1.6 Atmospheric Radiation

In the major part of scientific research, the medium lying beyond the surface is assumed to be the vacuum. This is acceptable for different engineering situations, but in those applications in which the atmosphere is present between surfaces exchanging radiation, it is necessary to consider the radiation emitted, scattered and absorbed atmospheric gases. Atmosphere in fact is the principal participating medium involved in heat exchange between surfaces or between a surface and a lens. Even though the effect of radiation from and to atmosphere has to be considered in the analysis, there are specific intervals of wavelengths, called '*atmospheric windows*', in which the atmosphere is considered transparent, Figure 1.14. In these spectra is suitable to make infrared measurements, since in these intervals of wavelengths the properties of atmosphere do not 'participate' to the measurements [6], Figure 1.14.

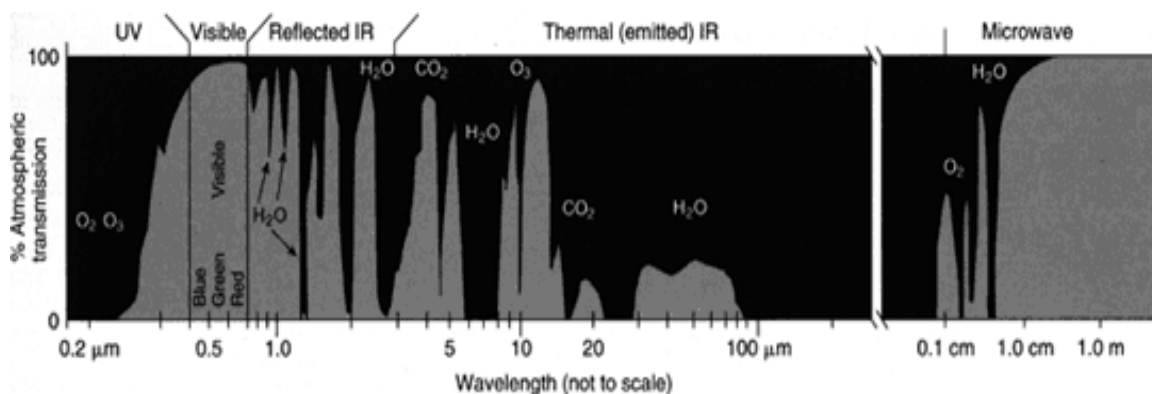


Figure 1.14. Diagram of atmospheric windows—wavelengths at which electromagnetic radiation will penetrate the Earth's atmosphere. Chemical notation (CO<sub>2</sub>, O<sub>3</sub>) indicates the gas responsible for blocking sunlight at a particular wavelength.. Image credit: NASA [9].

An atmospheric window is a range of electromagnetic wavelengths to which Earth's atmosphere is largely or partially transparent. All spectral regions are affected to some extent by absorption in the atmosphere but there are two nearly transparent ranges, the optical window and the radio window, and several narrow, partial infrared windows.

The optical window allows through visible light, from red, as far as the band of molecular oxygen (O<sub>2</sub>) at 7600 Å, to violet and a little beyond, as far as at the ozone (O<sub>3</sub>) cut-off at 2950 Å. Shorter wavelengths are blocked by atoms and molecules of oxygen, nitrogen, and other gases, and by geo-coronal hydrogen and helium.

The radio window spans a wavelength range from about one millimeter to about 30 meters. Lower wavelengths are reflected by the ionosphere, while shorter wavelengths suffer

increasing amounts of molecular absorption.

Several narrow infrared windows exist at micrometer wavelengths, the photometric designations of which are J (1.25 microns), H (1.6 microns), K (2.2 microns), L (3.6 microns), M (5.0 microns), N (10.2 microns), and Q (21 microns). There are also small but usable windows at 350 and 460 microns. Because water vapor is one of the main absorbers of infrared, observatories for studying infrared must be sited in particularly dry or mountainous regions where the effect of water vapor is reduced and/or the atmosphere is thinner [10].

Most remote sensing instruments on aircraft or space-based platforms operate in one or more of these windows by making their measurements with detectors tuned to specific frequencies (wavelengths) that pass through the atmosphere. When a remote sensing instrument has a line-of-sight with an object that is reflecting sunlight or emitting heat, the instrument collects and records the radiant energy. The atmosphere is nearly opaque to EM radiation in part of the mid-IR and all of the far-IR regions. In the microwave region, by contrast, most of this radiation moves through unimpeded, so radar waves reach the surface (although weather radars are able to detect clouds and precipitation because they are tuned to observe backscattered radiation from liquid and ice particles) [9].

By supposing the range of wavelength in which atmosphere is transparent to thermal radiation, all thermographical investigations involve some kind of thermal detector. In the next paragraph will be showed an overview of infrared detectors, the essential component of InfraRed devices.

Whatever the device is, the role of the infrared detector is to convert the incident energy (to the detector lens) in an electrical signal (tension or current).

## 1.7 Infrared Detectors

### 1.7.1 Historical Aspects

*“All physical phenomena in the range of about 0.1–1 eV can be proposed for InfraRed detectors”*. In effect, many materials have been investigated in the IR field [11].

The first detector, provided by Herschel's experiment, consisted of a liquid in a glass thermometer with a specially blackened bulb to absorb radiation. Herschel built a crude monochromator that used a thermometer as a detector so that he could measure the distribution of energy in sunlight.

The most important steps in the development of IR detectors are the following [12]:

- In 1821 Seebeck discovered the thermoelectric effect and soon thereafter demonstrated the first thermocouple.
- In 1829 Nobili constructed the first thermopile by connecting a number of thermocouples in series.
- In 1833 Melloni modified the thermocouple and used bismuth and antimony for its design.

Langley's bolometer appeared in 1880. Langley used two thin ribbons of platinum foil, connected to form two arms of a Wheatstone bridge. It took twenty years to develop a bolometer four hundreds times more sensitive than his first efforts appeared in 1880. His latest bolometer could detect the heat from a cow at a distance of a quarter of a mile.

Smith in 1873 discovered the photoconductive effect when he experimented with selenium as an insulator for submarine cables.

Twentieth century observed the development of photon detectors. The first IR photoconductor was developed by Case in 1917, which discovered the photoconductivity of a substance composed of thallium and sulfur. Later he found that the addition of oxygen greatly enhanced the response. However, instability of resistance in the presence of light or polarizing voltage, loss of responsivity due to overexposure to light, high noise, sluggish response, and lack of reproducibility seemed to be inherent weaknesses. Since about 1930 the development of IR technology has been dominated by the photon detectors [11-13].

In 1933, Kutzscher at the University of Berlin, discovered that lead sulphide (from natural galena found in Sardinia) was photoconductive and had response to about 3  $\mu\text{m}$ . The research was used only for war applications. In 1941, Cashman improved the technology of thallous sulfide detectors, which led to successful production and after the second World War, found that other semiconductors of the lead salt family (PbSe and PbTe) showed promise as IR detectors [13-16].

The effect studied in these approach are: thermoelectric power (thermocouples), change in electrical conductivity (bolometers), gas expansion (Golay cell), pyroelectricity (pyroelectric detectors), photon drag, Josephson effect (Josephson junctions, SQUIDs), internal emission (PtSi Schottky barriers), fundamental absorption (intrinsic photodetectors), impurity absorption (extrinsic photodetectors), [14].

During the ninetieth IR detectors were built using a single-element-cooled lead salt detectors that were polycrystalline and were produced by vacuum evaporation and chemical deposition from a solution, followed by a post-growth sensitization process. Extrinsic photoconductive response from copper, zinc, and gold impurity levels in germanium gave rise to devices using in the 8 to 14 micrometers very long wavelength IR region. The must be operated at lower temperatures to achieve performance similar to that of intrinsic detectors, but the limitation is found in quantum efficiency required to avoid thick detectors.

In 1973, Shepherd and Yang proposed the metal-silicide/silicon Schottky-barrier detectors. For the first time it became possible to have much more sophisticated readout schemes-both detection and readout could be implemented in one common silicon chip [17].

In the late 1970s and through the 1980s, HgCdTe technology efforts focused almost exclusively on photovoltaic device development because of the need for low power dissipation and high impedance in large arrays to interface to readout input circuits. This effort is finally paying off with the birth of HgCdTe second-generation IR systems that provide large 2-D arrays in both linear formats with TDI for scanning imagers, and in square and rectangular formats for staring arrays. The  $1024 \times 1024$  hybrid HgCdTe focal plane arrays (FPAs) have been produced recently.

However, present HgCdTe FPAs are limited by the yield of arrays, which increases their cost. In such a situation, alternative alloy systems for infrared detectors, such as quantum well infrared photodetectors (QWIPs) and type II superlattices, are investigated [18-22].

The trend of increasing pixel numbers is likely to continue in the area of large format arrays. This increasing will be continued using close-buttet mosaic of several SCAs. Raytheon manufactured a  $4 \times 4$  mosaic of  $2K \times 2K$  HgCdTe SCAs and assisted in assembling it into the final focalplane configuration to survey the entire sky in the Southern Hemisphere at four IR wavelengths. With 67 million pixels, this is currently the world's largest IR focal plane. Although there are currently limitations to reducing the size of the gaps between active detectors on adjacent SCAs, many of these can be overcome. It is predicted that a focal plane of 100 megapixels and larger will be possible, constrained only by budgets but not by technology.

A negative aspect of support by defense agencies has been the associated secrecy requirements that inhibit meaningful collaborations among research teams on a national and



especially on an international level. In addition, the primary focus has been on FPA demonstration and much less on establishing the knowledge base. Nevertheless, significant progress has been made over four decades. At present, HgCdTe is the most widely used variable gap semiconductor for IR photodetectors [23-24]. Much recent research has focused on both hybrid and monolithic uncooled arrays and has yielded significant improvements in the detectivity of both bolometric and pyroelectric detector arrays. Honeywell has licensed bolometer technology to several companies for the development and production of uncooled FPAs for commercial and military systems. At present, the compact  $640 \times 480$  microbolometer cameras are produced by Raytheon, Boeing, and Lockheed-Martin in the United States. In recent years, several countries, including the United Kingdom, France, Japan, and Korea, have picked up the ball, determined to develop their own uncooled imaging systems [25-28].

### **1.7.2 Classification**

Interest has centered mainly on the wavelengths of the two atmospheric windows 3–5  $\mu\text{m}$  [middle wavelength IR (MWIR)] and 8–14  $\mu\text{m}$  (LWIR region; atmospheric transmission is the highest in these bands and the emissivity maximum of the objects at  $T \approx 300\text{ K}$  is at the wavelength  $\lambda \approx 10\text{ micron}$ ), though in recent years there has been increasing interest in longer wavelengths stimulated by space applications.

Progress in IR detector technology is connected with semiconductor IR detectors, which are included in the class of photon detectors. In this class of detectors the radiation is absorbed within the material by interaction with electrons either bound to lattice atoms or to impurity atoms or with free electrons. The observed electrical output signal results from the changed electronic energy distribution. The fundamental optical excitation processes in semiconductors are illustrated in Figure 1.15, [29-31].

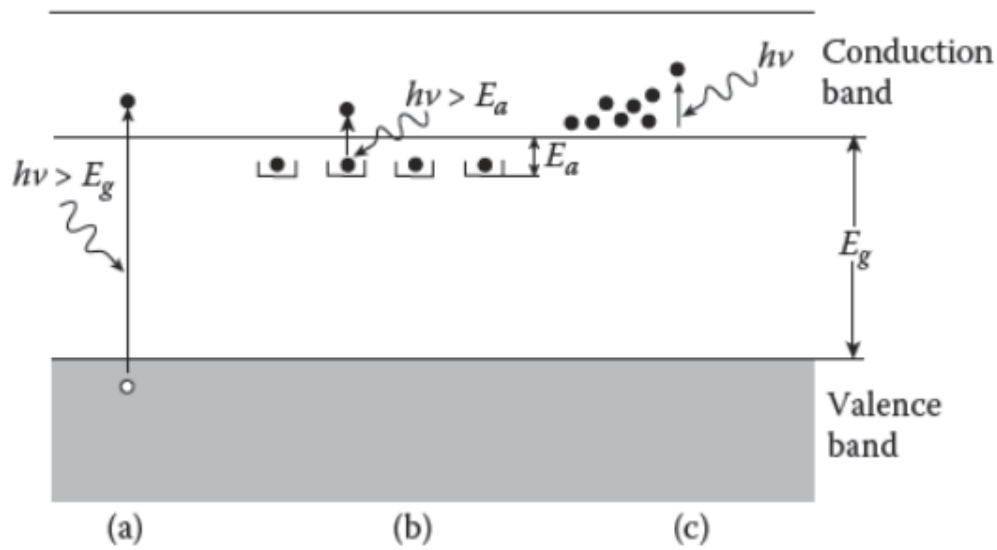


Figure 1.15. Fundamental optical excitation processes in semiconductors (a) intrinsic absorption, (b) extrinsic absorption, (c) free carrier absorption [32].

The photon detectors show a selective wavelength dependence of response per unit incident radiation power. They exhibit both perfect signal-to-noise performance and a very fast response. But to achieve this, the photon detectors require cryogenic cooling. Photon detectors having long wavelength limits above about 3  $\mu\text{m}$  are generally cooled. This is necessary to prevent the thermal generation of charge carriers. The thermal transitions compete with the optical ones, making noncooled devices very noisy.

Depending on the nature of the interaction, the class of photon detectors is further subdivided into different types, in particular, the most important are: intrinsic detectors, extrinsic detectors, photoemissive (metal silicide Schottky barriers) detectors, and QW detectors.

Depending on how the electric or magnetic fields are developed, there are various modes such as photoconductive, photovoltaic, photoelectromagnetic (PEM), and photoemissive ones. Each material system can be used for different modes of operation.

However, in thermal detectors, the incident radiation heats the surface, and the heating affects a property of the heated material such as the electrical conductivity which in turn translates into variation of the signal output.

One of interesting aspect of the infrared detector, is such that the response is independent of the wavelength. Thus if a specific wavelength band is desired for a given application, an interference filter rejecting the unwanted radiations will have to be placed in front of the detector to restrict the response [5],[14].

In the following paragraph the attention will be focused on the infrared thermal detectors, whose Table I presents an overview.

Table I. Infrared Thermal Detectors

Detector	Method of Operation
<b>BOLOMETER</b>	change in electrical conductivity
<i>metal</i>	
<i>semiconductor</i>	
<i>superconductor</i>	
<i>ferroelectric</i>	
<i>hot electron</i>	
<b>THERMOCOUPLE</b>	voltage generation caused by change in temperature of the junction of two dissimilar materials
<b>PYROELECTRIC</b>	changes in spontaneous electrical polarization
<b>GOLAY CELL/GAS MICROPHONE</b>	optical transmission of a semiconductor
<b>ABSORPTION EDGE</b>	changes in magnetic properties
<b>PYROMAGNETIC</b>	changes of optical properties

### 1.7.3 Physical Characteristics

An infrared detector is a device that converts the radiant infrared energy into a measurable signal, generally electrical in nature, as previously said.

One of electrical characteristic is the detector impedance ( $Z=dV/dI$ ) since determine the maximum power that can be extracted from such a detector, that is achieved when 'Z' achieves the value  $Z_a$  that is the input impedance of the preamplifier to which the detector is connected. A correct impedance match is important to maximize the output signal since electric signal sat the detector output are generally small.

Another property is represented by the time constant ' $\tau=1/2\pi f_c$ ' which specifies the response time of a detector.

Referring to the merit for detectors the noise equivalent power (NEP) has to be considered that is the amount of power induced by an optical signal whose amplitude is equivalent to the intrinsic noi power present at the detector output (without signal) due to thermal agitation and optical radiation granularity [5], [26-27]. The correlated energy flow is called : noise equivalent flow  $F_{NEP}$ . Otherwise, NETD, noise equivalent temperature difference is adopted instead of NEP. NETD corresponds to the change in temperature of a large blackbody in the observed scene, causing a change in the signal-to-noise ratio of unity in the output of the detector. The NETD value is: 50 mK for microbolometer arrays, <20mK for large arrays of InSb (indium-antimonide). Generally, this value depends on the F-number of a lens given by its focal distance divided by its effective diameter aperture.

Sometimes to specify a detector it is used the inverse of  $F_{NEP}$ , a parameter called detectivity ( $D=1/ F_{NEP}$ ), which has to be high to obtain a reasonable signal-to-noise ratio. Generally, in

order to compare different detectors, the specific detectivity is introduced ( $D^*$ ), that is  $D$  scaled to the unit-sensitive detector area and unit of bandwidth.

The smallest temperature difference observable by an operator when the range is constituted by a repetitive bar pattern over a uniform background (thermal range). Such the parameter is called MRTD and it is useful to characterize either a detector or a thermal imaging system.

Finally, the fundamental limit of all system is the noise. In particular, electronic noise and optical noise are the types more likely to occur in any thermal imaging system or detector, and which determine a degradation of the signal. An in depth analysis of the kind of the noises involves the:

- Shot noise: that is the ultimate limit for radiation detection. It is caused by the arrival of random and discrete photons in the incident radiation.
- Thermal noise: that is caused by random motion of electrons in resistive materials.
- Flicker noise: due to the trapping charge carriers near the sensing surface of semiconductor detectors, and it depends on the observation frequency (it is provided by  $1/f_n$ ) where  $f$  is the signal frequency and  $n$  is typically between 0.9 and 1.35 [33].

## 1.8 Bolometers

The bolometer is a resistive element constructed from a material with a very small thermal capacity and large temperature coefficient so that the absorbed radiation produces a large change in resistance. In contrast to the thermocouple, the device is operated by passing an accurately controlled bias current through the detector and monitoring the output voltage. The change in resistance is like to the photoconductor, however, the basic detection mechanisms are different. In the case of a bolometer, radiant power produces heat within the material, which in turn produces the resistance change. There is no direct photon-electron interaction.

For bolometers such as thermistors the physical property affected is the electrical conductivity. Consequently, a current must cross the element for signal generation. For example, a bridge circuit can be used for signal pickup. This current is characterised by its own fluctuations and add noise to the detector measurements.

Typical materials used for metal bolometers are nickel, bismuth, platinum, or antimony. These metals are in use where their high, long-term stability is an essential requirement. Being made from metal, these bolometers need to be small so that the heat capacity is low enough to allow reasonable sensitivity. Most metal bolometers are formed as film strips, about 100–500 Å thick, via vacuum evaporation or sputtering. They are often coated with a black absorber such as evaporated gold or platinum black.

A typical value of temperature coefficient is positive for metals and is equal about 0.3%/°C. The metal bolometers operate at room temperature and have detectivities of the order  $1 \times 10^8$  cmHz<sup>1/2</sup>W<sup>-1</sup>, with response times of approximately 10 msec.

Unfortunately, they are generally rather fragile, thus limiting their use in certain applications. The technology of these devices is generally limited to small arrays due to power consumption and amplifier design constraints associated with matching to the low detector impedance [14-16], [34]. The representation and schematisation of a type of bolometer is provided by Figure 1.16.

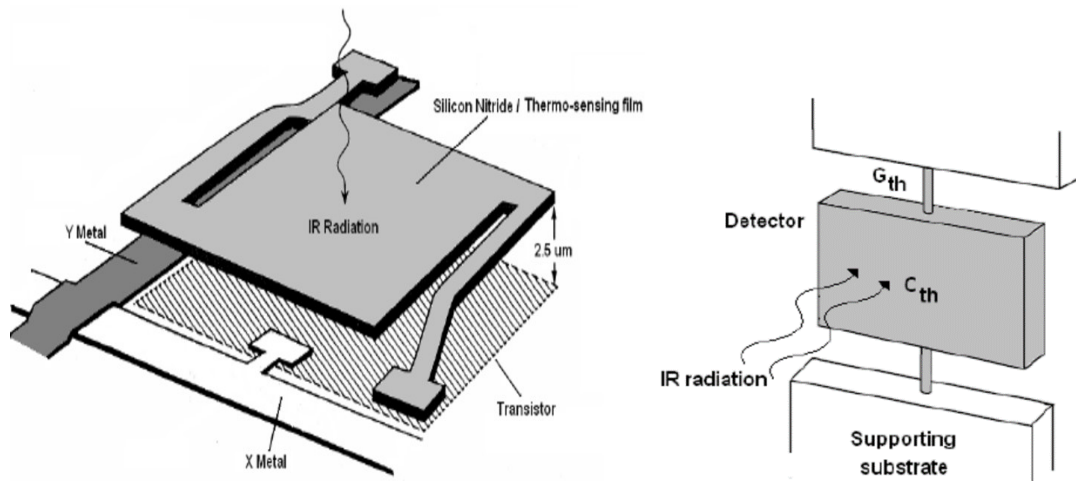


Figure 1.16. Typical microbolometer (a) scheme and (b) representation. [15]

### 1.8.1 Thermistors

Thermistor bolometers are constructed from a sintered mixture of various semiconducting oxides that have a higher TCR than metals (2–4% °C), and are generally much more rugged. They crystallize in the spinel structure. In their final form they are semiconductor flakes 10 μm thick.

The negative temperature coefficient depends on the band gap, the impurity states, and the dominant conduction mechanism. This coefficient is not constant but varies as  $T^{-2}$ , which is a result of exponential dependence of semiconductor resistivity. The sensitive material in a thermistor bolometer is typically made of wafers of manganese, cobalt, and nickel oxides sintered together and mounted on electrically insulating but thermally conducting material such as sapphire.

The sapphire is then mounted on a metallic heat sink, to control the time constant of the device.

The sensitive area is blackened to improve its radiation absorption characteristics. Typical room temperature resistivity of a thermistor changes between 250 and 2500 Ωcm. They can be made in sizes ranging from 0.05 to 5 mm square. The principal material investigated is  $(\text{MnNiCo})_3\text{O}_4$ , which has a negative TCR of about 0.04/°C at room temperature.

The usual construction uses a matched pair of devices for a single unit. One of the pair of thermistors is shielded from radiation and fitted into a bridge such that it acts as the load resistor. This arrangement allows one to optimize the signal from the active element by compensating for any ambient temperature changes. The result can be a dynamic range of a million to one. The device sensitivity and response time cannot both be optimized as improved heat sinking, to reduce the time constant, prevents the detector from reaching its maximum temperature, thus reducing the responsivity.

Since the thermistor is Johnson noise limited, an improvement in detectivity can be realized by placing a hemispherical or hyperhemispherical lens over its surface. This procedure would not improve the signal-to-noise ratio if the detector is photon noise limited. The detector must be optically coupled with the lens, which can be accomplished by depositing the detector directly on the plane of the lens [21-22].

The thermistor detectors are mainly fabricated by bonding thin flakes of the thermistor material to a substrate. Device performance parameters such as responsivity, noise, and response time are very dependent on operator skill and experience, and processing conditions. To overcome these drawbacks and reduce the cost of thermistors the possibility of evaporated films has been investigated. As an example of the thermistor circuit

The thermistor spectral responsivity is essentially flat with an upper wavelength determined by the transmission of the window that encapsulates the chip. Because they exhibit a large amount of  $1/f$  noise arising at grain boundaries, thermistor thin films have not been found to be useful in uncooled bolometer thermal imaging arrays [17].

### **1.8.2 Liquid Crystals**

Liquid crystals are cholesterol esters which, under a temperature effect, change orientation and reflect coloured light from red to violet when illuminated with white light. Depending on their composition, 0.01°C resolution can be obtained. As advantages, they are not expensive, they are sensitive to slight thermal variations, and they make surface measurement possible. The main problem is represented by contact measurement, the restricted sensitivity span (5°C to 10 °C), the necessity to prepare the surface before the application, and the necessity to clean up after the measurement to remove the crystals [14][35].

## 1.9 Photonic Detectors

In 1973, thanks to Shepherd and Yang of Rome Air Development Center (Rome, New York) it became possible to have much more sophisticated readout schemes by implementing both detection and readout in one common silicon chip.

Since then, the development of the Schottky-barrier technology has progressed continuously and currently offers large IR image sensor format [17],[23].

### 1.9.1 Photoemissive Photonic Detectors

For photo-emissive photonic detectors the signal observed is constituted by the measurement of the electron flow (i.e measurement of a current ' $i$ '), pulled away from the photocathode under the effect of both the incident photons and static polarization. The spectral sensitivity depends on the properties of both the material used for the photocathode the outer envelope infrared transmission, Figure 1.17.

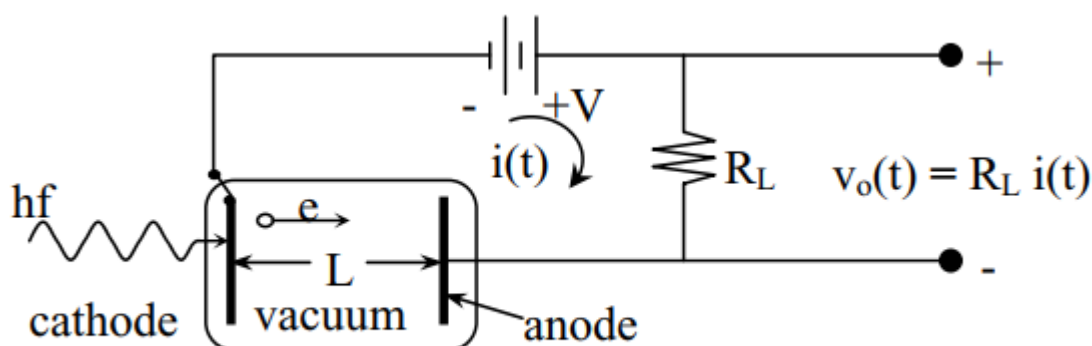


Figure 1.17. Schematic diagram of a photoemissive detector: phototube detect circuit [36].

In the circuit of Figure 1.17, a typical photon may release an electron with a probability equal to the quantum efficiency (typically less than 30 percent for germanium or silicon cathodes). The released electron then accelerates linearly toward the anode where it is intercepted. The current pulse in the anode circuit associated with this moving electron increases linearly with time as the image charge on the anode increases, and ends when the electron impacts the positively charged anode, neutralizing that image charge. This current can be characterized by the electron charge times the electron velocity divided by the cathode-anode gap. If photon arrival times are rare compared to the transit time of the electrons, then the anode current is a Poisson-distributed series of triangle waves for which the integrated current is one electron



charge. A practical problem with such detectors is that these weak currents and the voltages are typically small compared to the Johnson noise produced by the load resistor  $R_L$  showed in Figure 1.17.

### 1.9.2 Quantum Detectors

Quantum detectors are solid-state detectors in which photon interactions either change conductivity (photoconductor) or generate voltage (photoelectric). Since no heating phenomenon is needed as for a thermal detector, the response time is short while the solid-state structure made these detectors compact, reliable and robust. For photoconductive detectors an external current is necessary to measure conductivity change while photoelectric detectors acts as a power generator, supplying a signal without need for polarization. Since biasing current is needed for photoconductor detectors, high charge capacity alkaline batteries can be used to induce minimum noise and ripple. This is essential to achieve stable results. In this regard, since photovoltaic detectors supply a signal by themselves, they are much more attractive than photoconductor detectors, requiring less complex readout circuits. Common materials used in photoelectric are Si, InAs, InSb and CMT (cadmium-mercury telluride), [1], [5].

HgCdTe photoconductive detectors operating at 77 K in the 8–14  $\mu\text{m}$  range are widely used in the first generation thermal imaging systems in linear arrays of up to 200 elements, although custom 2-D arrays up to  $10 \times 10$  have been made for unique applications. The material used is n-type with an extrinsic carrier density of about  $1 \times 10^{14} \text{ cm}^{-3}$ . The low hole diffusion coefficient makes n-type devices less vulnerable to contact and surface recombination. In addition, n-type materials exhibit a lower concentration of SR centers and there are good methods of surface passivation [14].

## 1.10 Infrared Imaging Devices

The presented detectors allow by themselves and without mechanical scanning operation to imaging applications that is to the production of an array of points (pixels) in one or two dimension. Although infrared films (such as liquid crystals) made from specific dyes sensitive in the range 1 to 3 microns are available, they are not really of practical use in those application in which is required a real-time imaging. In these applications, the output of detector produces a 2D image by means of two main image-forming processes: direct image formation (pyroelectric detectors) and detectors associated with electromechanical scanning of the scene.

### 1.10.1 Pyroelectric Detectors

Whenever a pyroelectric crystal undergoes a change of temperature, surface charge is produced in a particular direction as a result of the change in its spontaneous polarization with temperature. This effect has been known as a physically observable phenomenon for many centuries. Its name “pyroelectricity” was introduced by Brewster [37]. The concept of using the pyroelectric effect for detecting radiation was proposed very early by Ta [38]. The importance of the pyroelectric effect in infrared detection was becoming obvious about 50 years ago, due to scientific activity from different authors [39-42].

Pyroelectric materials are those with a temperature dependent spontaneous electrical polarization. There are 32 known crystal classes. Twenty-one are non-centrosymmetric and 10 of these exhibit temperature-dependent spontaneous polarization. Under equilibrium conditions the electrical asymmetry is compensated by the presence of free charges. If, however, the temperature of the material is changed at a rate faster than these compensating charges can redistribute themselves, an electrical signal can be observed. This means that the pyroelectric detector is an AC device, unlike other thermal detectors that detect temperature levels rather than temperature changes. This generally limits the low frequency operation, and for a maximum output signal the rate of change of the input radiation should be comparable to the electrical time constant of the element. Among the single crystals, the most notable success has been achieved with TGS [triglycine sulphate,  $(\text{NH}_2\text{CH}_2\text{COOH})_3\text{H}_2\text{SO}_4$ ]. It possesses attractive properties, a high pyroelectric coefficient, a reasonably low dielectric constant and thermal conductivity (high value of  $F_v$ ). However, this material is rather hygroscopic, difficult to handle, and show poor long-term stability, both chemically and electrically. Its low Curie temperature is a major disadvantage, particularly for detectors that

are required to meet military specifications.

Several variants on pure TGS have been developed to overcome the problem of the low Curie temperature. The alane and arsenic acid doped materials (ATGSAs) are particularly interesting because of their low dielectric losses and high pyroelectric coefficients [43-48].

### **1.10.2 Infrared Focal Plane Array**

Traditionally, IR technologies are connected with controlling functions and night vision problems with earlier applications connected simply with detection of IR radiation, and later by forming IR images from temperature and emissivity differences (systems for recognition and surveillance, tank sight systems, anti-tank missiles, air-air missiles).

In the last five decades, different types of detectors are combined with electronic readouts to make detector arrays. The progress in integrated circuit design and fabrication techniques has resulted in continued rapid growth in the size and performance of these solid state arrays. In the infrared technique, these devices are based on a combination of a readout array connected to an array of detectors. The term “focal plane array” (FPA) refers to an assemblage of individual detector picture elements (“pixels”) located at the focal plane of an imaging system. Although the definition could include one-dimensional (“linear”) arrays as well as two-dimensional (2-D) arrays, it is frequently applied to the latter. Usually, the optics part of an optoelectronic images device is limited only to focusing of the image onto the detectors array. These so-called staring arrays are scanned electronically usually using circuits integrated with the arrays. The architecture of detector-readout assemblies has assumed a number of forms that are discussed below [49-50]

Two families of multi-element detectors can be considered; one used for scanning systems and the other used for staring systems. The simplest scanning linear FPA consists of a row of detectors (Figure 1.18 (a)). An image is generated by scanning the scene across the strip using, as a rule, a mechanical scanner. At standard video frame rates, at each pixel (detector) a short integration time has been applied and the total charges are accommodated. A staring array is a 2-D array of detector pixels that are scanned electronically (Figure 1.18(b)). These types of arrays can provide enhanced sensitivity and gain in camera weight.

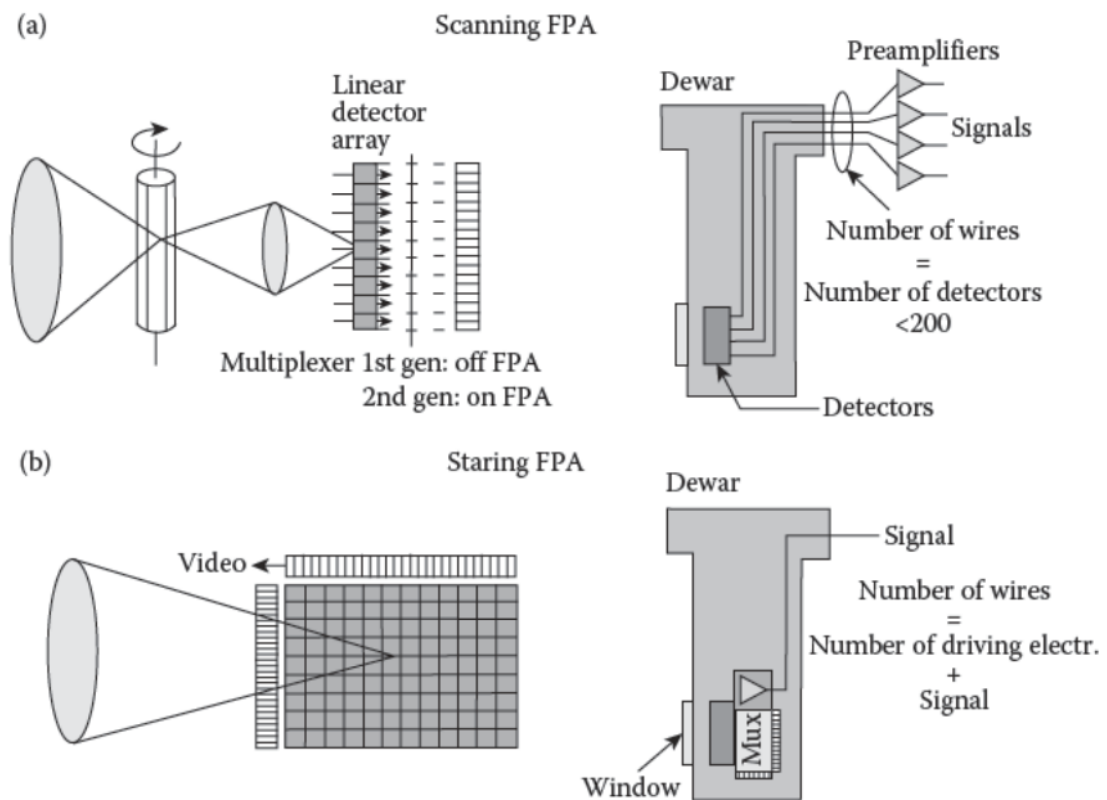


Figure 1.18. Scanning focal plane array (a), staring focal plane arrays (b).

However, actual systems (full framing systems), which represent the second generation of systems, have at least three orders of magnitude more elements ( $>10^6$ ) on the focal plane than first generation systems and the detectors elements are configured in a 2D array. These staring arrays are scanned electronically by circuits integrated with the arrays. These readout integrated circuits include for example pixel deselecting, antiblooming on each pixel, subframe imaging, output preamplifiers and other features [51-53].

Development of large format, high sensitivity, mosaic IR sensors for ground-based astronomy is the goal of many observatories around the world (large arrays dramatically multiply the data output of a telescope system). This is somewhat surprising given the comparative budgets of the defense market and the astronomical community. While the size of individual arrays continues to grow, the very large focal plane arrays (FPAs) required for many space missions by mosaicking a large number of individual arrays. An example of a large mosaic developed by Teledyne Imaging Sensors, is a 147 megapixel FPA that is comprised of 35 arrays, each with  $2048 \times 2048$  pixels. This is currently the world's largest IR focal plane. Although there are currently limitations to reducing the size of the gaps between active detectors on adjacent SCAs, many of these can be overcome. It is predicted that focal plane of 100 megapixels and larger will be possible, constrained only by budgets but not technology [54].

## 1.11 Cooling Systems

The method of cooling varies according to the operating temperature and the system's logistical requirements. Various types of cooling systems have been developed including dewars with cryogenic liquids or solids, Joule–Thompson open cycle, Stirling closed cycle, and thermoelectric coolers, Figure 1.19.

Most of 8-14 micrometers detectors operate at approximately 77K and can be cooled by liquid nitrogen. Cryogenic liquid pour-filled dewars are frequently used for detector cooling in laboratory. Their limit is represented by the fact that liquid nitrogen every few hours need to be refilled [55].

The Joule-Thompson coolers is based on the fact that as a high-pressure gas expands upon leaving a throttle valve, it cools and liquefies. The coolers require a high-pressure gas supply from bottles and compressors. By using the compressed air, temperature on the order of 80 K can be achieved in one or little more minutes. The gas used must be purified to remove water vapor and carbon dioxide that could freeze and block the throttle valve.

Stirling cycle coolers are refrigerators designed to produce operating temperature of 77 K directly from DC power. The manufacturing technique born in the late 1970s is actually refined.

Stirling engines require several minutes of cooldown time and the working fluid is helium. Closed-cycle coolers offer the ultimate detector performance without the need for bulk liquid nitrogen. Temperature as low as 15 K can be obtained. The limit of these cooling instruments is represented by high initial cost and large input power.

The Peltier coolers exploit the thermoelectric cooling of detectors which is simpler and less costly than closed-cycle cooling. In this case, the detectors are usually mounted in a hermetic encapsulation with a base designed to make good contact with a heat sink. These coolers can achieve to 200K and have roughly twenty years operating life and low input power, they are also small and rugged [56-57].

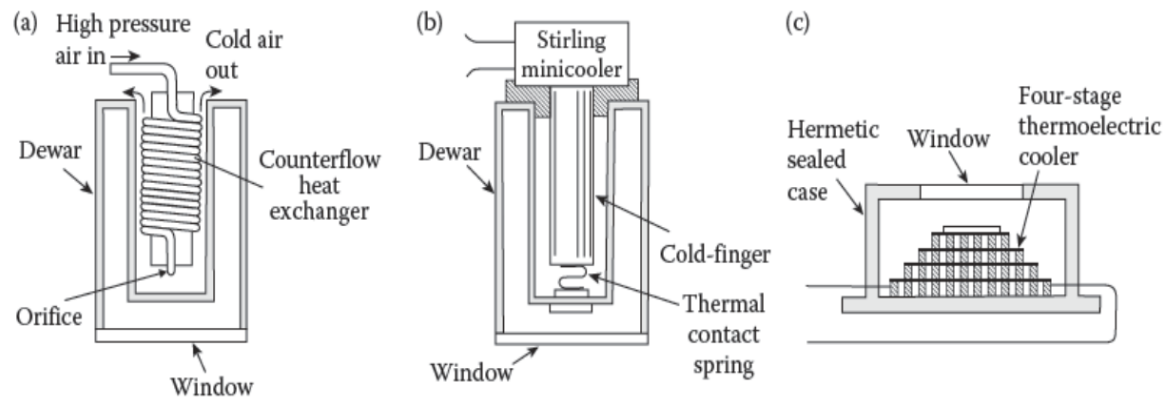


Figure 1.19. Three ways of cooling IR detectors (a) Joule-Thompson cooler, (b) Stirling cycle engine (c) Peltier effect four-stage thermoelectric cooler.

## 1.12 Thermography

All objects with surface temperatures above absolute zero emit electromagnetic radiation. The physical principles that allow calculation of the surface temperatures of objects from the wavelength and intensity of electromagnetic radiation emitted in the in-fared region of the spectrum is called Infrared Thermography.

The intensity of the infrared radiation emitted by objects is mainly a function of their temperature. In infrared thermography, this feature is used for multiple purposes: as a health indicator in medical applications, as a sign of malfunction in mechanical and electrical maintenance or as an indicator of heat loss in buildings.

The difference between a visible image and an infrared image is that the visible image is a representation of the reflected light on the scene, whereas in the infrared image, the scene is the source and can be observed by an infrared camera without light. Images acquired using infrared cameras are converted into visible images by assigning a color to each infrared energy level. The result is a false-color image called a thermogram [58-59].

IRT has many advantages over other technologies [60]. In general, the main advantages of IRT are the following:

- IRT is a non-contact technology: the devices used are not in contact with the source of heat, i.e., they are non-contact thermometers. In this way, the temperature of extremely hot objects or dangerous products, such as acids, can be measured safely, keeping the user out of danger.
- IRT provides two-dimensional thermal images, which make a comparison between areas of the target possible.
- IRT is in real time, which enables not only high-speed scanning of stationary targets, but also acquisition from fast-moving targets and from fast-changing thermal patterns.
- IRT has none of the harmful radiation effects of technologies, such as X-ray imaging. Thus, it is suitable for prolonged and repeated use.
- IRT is a non-invasive technique. Thus, it does not intrude upon or affect the target in any way.

The fact that IRT is a non-contact technique is very important in this field, because this means that it is a painless procedure. Moreover, as the instrument is non-contact, it does not affect the result of the measurement and can be carried out remotely. Other alternatives can be painful, and when the sensor is in contact with the animal, it can affect the measurement. Therefore, IRT is very effective, not only for measuring the temperature of the animal, but other variables, such as stress [61]. Due to all of these advantages, thermography has been established as an effective tool in many different applications.

In the present Thesis, a Thermography based approach has been developed in order to study quantitatively and more accurately the fatigue and damage behaviour of materials.

In this regard, the developed approach allows considering and separating different thermal contribution occurring at both the mechanical frequency and its multiples, related to dissipative heat sources involved in damage processes.

## **Conclusions**

This chapter provides the basic knowledge on the physics of heat exchanges with particular regard to radiation heat transfer. The most important equations and their derivation referring to the thermal radiation are presented just to give an overview of the phenomena involved in the twice particle-wave light nature.

This chapter, also presents the ideal black body emitter and absorber behaviours, and subsequently the discussion shifts to real gray/non-black bodies, which behaviours are far from the one provided by the black body. In this regard, different properties have been showed: emissivity, absorption, transmissivity and reflectivity which, can be assessed by considering the energy conservation law applied to an incident radiation wave on a surface. All the formulas and the quantities have been demonstrated or explained from a practical point of view, in order to understand the global meaning and the general physics of the phenomena.

Another section of the present chapter refers to the infrared detectors: from the first bolometers to novel focal full-frame plane array which determine nowadays a copious increment of the infrared thermal cameras demand. In addition, the section speaks about the most relevant characteristics as well as the features of detectors.

The knowledge of the basics concepts of infrared detectors is very important in designing the research appropriately, as an example the choice of the spectral range or cooled/bolometric detectors, discriminates the kind of the test and then affects the results.

The following chapter will show a technique based on Thermography, the Thermoelastic Stress Analysis (TSA) and its important applications.

Such the technique, provides an immediate relation between temperature and surface stress (the first invariant) of the body undergoing fatigue test.

The role of the detector in this case is essential for assessing the temperature variations.



## References

- [1] R.Mahan. Radiation Heat Transfer, John Wiley & Sons, N.Y, 2002.
- [2] P. Kombucha Mushroom, Goliath National Bank (GNB), teaching material, 2014, available on: <https://www.slideshare.net/kombuchamushroom>, assessed 14/08/2017.
- [3] J. Walker, D. Halliday, R. Resnick. Fundamentals of Physics, Wiley, USA, 2014.
- [4] McGrawHill Education Online, website: <http://www.mcgraw-hill.it/>, assessed 31/08/2017.
- [5] X. P.V. Maldague. Theory and Practice of Infrared Technology for Nondestructive Testing, Wiley&Sons, N.Y., 2001)
- [6] R. Siegel, J.R. Howell. Thermal Radiation Heat Transfer, Hemisphere Publishing Group, 1992)
- [7] C. Balaji. Essential of Radiation Heat Transfer, J. Wiley & Sons, RoW, 2014)
- [8] M. Kaviany. Heat Transfer Physics. Cambridge University Press, 2008.
- [9] Earth observatory, NASA:  
[https://earthobservatory.nasa.gov/Features/RemoteSensing/remote\\_04.php](https://earthobservatory.nasa.gov/Features/RemoteSensing/remote_04.php)
- [10] D. Darling. The Universal Book of Astronomy ,Wiley 2003.
- [11] A. Manissadjian, D. Gohier, E. Costard, and A. Nedelcu. Single Color and Dual Band QWIP Production Results,In: Proceedings of SPIE 6206, 62060E, 2006.
- [12] E. S. Barr. The Infrared Pioneers—III. Samuel Pierpont Langley. Infrared Physics 3, 195–206,1963.
- [13] R. D. Hudson, J. W. Hudson, Infrared Detectors, Dowden, Hutchinson & Ross, Stroudsburg,, PA, 1975.
- [14] A. Rogalski. Infrared Detectors, CRP PRESS Taylor & Francis Group 2011.
- [15] M. Moreno, A. Torres, R. Ambrosio, A. Kosarev. Un-Cooled Microbolometers with Amorphous Germanium-Silicon (a-GexSiy:H) Thermo-Sensing Films. Chapter in book: Bolometers 2012.
- [16] G. Sarusi. QWIP or Other Alternatives for Third Generation Infrared Systems. Infrared Physics & Technology 44, 439-44, 2003.
- [17] A. Rogalski. Third Generation Photon Detectors. Optical Engineering 42, 3498–3516, 2003.
- [18] J. T. Caulfield. Next Generation IR Focal Plane Arrays and Applications. Proceedings of 32<sup>nd</sup> Applied Imagery Pattern Recognition Workshop, IEEE, New York, 2003.
- [19] E. P. G. Smith, L. T. Pham, G. M. Venzor, E. M. Norton, M. D. Newton, P. M. Goetz, V. K. Randall, et al. HgCdTe Focal Plane Arrays for Dual-Color Mid- and Long-Wavelength Infrared Detection. Journal of Electronic Materials 33, 509–16, 2004.
- [20] W. A. Radford, E. A. Patten, D. F. King, G. K. Pierce, J. Vodicka, P. Goetz, G. Venzor, et al. Third Generation FPA Development Status at Raytheon Vision Systems. In: Proceedings of SPIE 5783, 331-39, 2005.

- [21] G. Destefanis, J. Baylet, P. Ballet, P. Castelein, F. Rothan, O. Gravrand, J. Rothman, J. P. Chamonal, and A. Million. Status of HgCdTe Bicolor and Dual-Band Infrared Focal Plane Arrays at LETI. *Journal of Electronic Materials* 36, 1031–44, 2007.
- [22] P. D. Dreiske. Development of Two-Color Focal-Plane Arrays Based on HDVIP. In: *Proceedings of SPIE* 5783, 325–30, 2005.
- [23] G. Kazanskii, P. L. Richards, and E. E. Haller. Far-Infrared Photoconductivity of Uniaxially Stressed Germanium,” *Applied Physics Letters* 31, 496–97, 1977.
- [24] H.-W. Hübers, S. G. Pavlov, K. Holldack, U. Schade, and G. Wüstefeld. Long Wavelength Response of Unstressed and Stressed Ge:Ga Detectors,” *Proceedings of SPIE* 6275, 627505, 2008.
- [25] A. Rogalski, *Infrared Detectors*. Gordon and Breach, Amsterdam, 2000.
- [26] J. T. Houghton and S. D. Smith, *Infra-Red Physics*, Oxford University Press, Oxford, 1966.
- [27] E. L. Dereniak and G. D. Boreman, *Infrared Detectors and Systems*, Wiley, New York, 1996.
- [28] J. Piotrowski. Breakthrough in Infrared Technology; The Micromachined Thermal Detector Arrays. *Opto-Electronics Review* 3, 3–8, 1995.
- [29] P. H. Siegel. Terahertz Technology. *IEEE Transactions on Microwave Theory Technology* 50, 910–28, 2002.
- [30] P. H. Siegel and R. J. Dengler. Terahertz Heterodyne Imaging Part I: Introduction and Techniques. *International Journal of Infrared Millimeter Waves* 27, 465–80, 2006.
- [31] P. H. Siegel and R. J. Dengler. Terahertz Heterodyne Imaging Part II: Instruments. *International Journal of Infrared Millimeter Waves* 27, 631–55, 2006.
- [32] C.T. Elliot, N.T. Gordon. *Handbook on semiconductors*, Vol. 4, 841–936, Elsevier 1993.
- [33] A. Van Der Ziel. Flicker Noise in Electronic Devices. *Advances in Electronics and Electron Physics*, 49, 225–97, 1979.
- [34] V. N. Leonov, Y. Creten, P. De Moor, B. Du Bois, C. Goessens, B. Grietens, P. Merken, et al. Small Two-Dimensional and Linear Arrays of Polycrystalline SiGe Microbolometers at IMEC-XenICs. In: *Proceedings of SPIE* 5074, 446–57, 2003.
- [35] A. Hadni, Y. Henninger, R. Thomas, P. Vergnat, and B. Wyncke. Investigation of Pyroelectric Properties of Certain Crystals and Their Utilization for Detection of Radiation. *Comptes Rendus* 260, 4186, 1965.
- [36] Website: <https://ocw.mit.edu/courses/electrical-engineering-and-computer-science/6-661-receivers-antennas-and-signals-spring-2003/readings/ch2new.pdf> ).
- [37] D. Brewster. Observation of Pyroelectricity of Minerals. *Edinburg Journal of Science* 1, 208–14, 1824.
- [38] Y. Ta. Action of Radiations on Pyroelectric Crystals. *Comptes Rendus* 207, 1042–44, 1938.
- [39] G. Chynoweth. Dynamic Method of Measuring the Pyroelectric Effect with Special Reference to Barium Titanate. *Journal of Applied Physics* 27, 78–84, 1956.
- [40] J. Cooper. A Fast-Response Pyroelectric Thermal Detector. *Journal of Scientific Instruments* 39, 467–72, 1962.

- [41] J. Cooper. Minimum Detectable Power of a Pyroelectric Thermal Receiver. *Review of Scientific Instruments* 33, 92–95, 1962.
- [42] G. A. Burdick and R. T. Arnold. Theoretical Expression for the Noise Equivalent Power of Pyroelectric Detectors. *Journal of Applied Physics* 37, 3223–26, 1966.
- [43] P. W. Kruse, L. D. McGlauchlin, and R. B. McQuistan, *Elements of Infrared Technology*, Wiley 1962.
- [44] J. H. Ludlow, W. H. Mitchell, E. H. Putley, and N. Shaw. Infrared Radiation Detection by Pyroelectric Effect. *Journal of Scientific Instruments* 44, 694–96, 1967.
- [45] H. P. Beerman. Pyroelectric Infrared Radiation Detector. *American Ceramic Society Bulletin* 46, 737, 1967.
- [46] M. Glass. Ferroelectric Strontium-Barium-Niobate as a Fast and Sensitive Detector of Infrared Radiation. *Applied Physics Letters* 13, 147–49, 1968.
- [47] R. W. Astheimer and F. Schwarz. Thermal Imaging Using Pyroelectric Detectors: Mylar Supported TGS. *Applied Optics* 7, 1687–95, 1968.
- [48] R. J. Phelan, Jr., R. J. Mahler, and A. R. Cook. High D\* Pyroelectric Polyvinylfluoride Detectors. *Applied Physics Letters* 19, 337–38, 1971.
- [49] G. Destefanis, P. Ballet, J. Baylet, P. Castelein, O. Gravrand, J. Rothman, F. Rothan, et al., “Bi-Color and Dual-Band HgCdTe Infrared Focal Plane Arrays at DEFIR. In: *Proceedings of SPIE* 6206, 62060R, 2006.
- [50] N. T. Gordon, P. Abbott, J. Giess, A. Graham, J. E. Hails, D. J. Hall, L. Hipwood, C. L. Lones, C. D. Maxeh, and J. Price. Design and Assessment of Metal-Organic Vapour Phase Epitaxy–Grown Dual Wavelength Infrared Detectors. *Journal of Electronic Materials* 36, 931–36, 2007.
- [51] P. Norton, J. Campbell, S. Horn, and D. Reago. Third-Generation Infrared Imagers. In: *Proceedings of SPIE* 4130, 226–36, 2000
- [52] M. Z. Tidrow, W. A. Beck, W. W. Clark, H. K. Pollehn, J. W. Little, N. K. Dhar, P. R. Leavitt, et al. Device Physics and Focal Plane Applications of QWIP and MCT. *Opto-Electronics Review* 7, 283–96, 1999.
- [53] M. N. Abedin, T. F. Refaat, I. Bhat, Y. Xiao, S. Bandara, and S. D. Gunapala. Progress of Multicolor Single Detector to Detector Array Development for Remote Sensing. In: *Proceedings of SPIE* 5543, 239–47, 2004.
- [54] R. A. Smith, F. E. Jones, and R. P. Chasmar. *The Detection and Measurement of Infrared Radiation*, Clarendon, Oxford, 1958.
- [55] U. Mizrahi, A. Fraenkel, L. Bykov, A. Giladi, A. Adin, E. Ilan, N. Shiloah, et al. “Uncooled Detektor Development Program at SCD. In: *Proceedings of SPIE* 5783, 551–58, 2005.
- [56] P. Tribolet. M. Vuillermet, and G. Destefanis. The Third Generation Cooled IR Detector Approach in France. *Proceedings of SPIE* 5964, 49–60, 2005.
- [57] D. F. King, W. A. Radford, E. A. Patten, R. W. Graham, T. F. McEwan, J. G. Vodicka, R. F. Bornfreund, P. M. Goetz, G. M. Venzor, and S. M. Johnson. 3rd-Generation 1280 × 720 FPA

Development Status at Raytheon Vision Systems. In: Proceedings of SPIE 6206, 62060W, 2006.

- [58] R. Usamentiaga, P. Venegas , J. Guerediaga, L. Vega , J. Molleda, F. G. Bulnes. Infrared Thermography for Temperature Measurement and Non-Destructive Testing. *Sensors* 14, 12305-12348, 2014; doi:10.3390/s140712305.
- [59] G. Gaussorgues. Infrared Thermography; Springer: Berlin/Heidelberg, Germany, 1994.
- [60] R. Gade, T.B. Moeslund. Thermal cameras and applications: A survey. *Machines Vision Application*. 25, 245–262, 2014.
- [61] M. Stewart, J. Webster, A. Schaefer, N. Cook, S. Scott . Infrared thermography as a non-invasive tool to study animal welfare. *Anim. Welf.* 2005, 14, 319–325.

---

## *Chapter 2: Thermography Based Approaches*

---

Despite the development over recent years of advanced finite element and computer aided design programs, designer and engineer are still faced with uncertainties when predicting the strength or durability of a component structure, particularly for complex geometries. In fact, no matter how sophisticated the theoretical analysis software may be, a lack of precision in the representation of the geometry, boundary conditions, physical properties, etc. produce a finite uncertainty in the result, and may lead to considerable inaccuracies in the predicted assessed stresses. On the other hand, the reduction of time-to-market of final product leads to refer more and more to the software analysis.

However, the fact that the demands and expectations placed upon theoretical methods have steadily increased and that relatively good predictions on complex structure require considerable user expertise has led to the growing acceptance that experimental techniques fulfils a necessary and integrated complementary role in enhancing product quality and reliability.

The scientific panorama is observing, nowadays, a continuous ‘osmosis’ of information between experimental and numerical / theoretical approaches due to the significant time and cost reduction of experimental campaigns provided by the advances in modern instrumentations.

In this sense, the use of thermography is very interesting, not only as non-destructive test but also to set up a technique to estimate stress from experimental measurements, in order to support engineers in satisfactory designs in terms of strength, safety and reliability.

Thermoelastic Stress Analysis (TSA), provides the experimental estimation of the stresses produced by the application of dynamic loading to a structure, by only measuring the surface temperature. Its capability ranges from theoretical model validation applicable to a wide range of engineering fields to non-destructive evaluation of stress concentration zones of real operating components.

The previous understanding of Chapter 1, referring to radiation heat exchanges and infrared detectors will be suitable to discuss the TSA setup since the use of efficient data acquisition and signal processing techniques is of critical importance.

Thanks to the development and advances in infrared detector technology, another strong

point is such that, due to the fine spatial resolution and non –contacting nature of the TSA technology, it has considerable potential for experimental studies of the localised and high-gradients elastic-stress distribution around the crack tip.

Moreover, by following the engineering design demand which encourages the weight saving of materials, thermoelastic theory can be extended to such anisotropic materials.

Beside to the whole advantages of using TSA technique, it is worth mentioning that its applicability is submitted to several hypothesis, in particular, the adiabaticity nature of the test. In case, adiabatic conditions are lost, some parameters lose validity.

For this reason and in order to better study the temperature variations correlated with the dissipative phenomena (occurring in case adiabatic conditions are lost) other approaches have been developed.

However, these approaches do not disregard the TSA technique, but provide an in depth understanding of the dissipative-irreversible phenomena.

They associate to the thermoelastic reversible temperature variations, other terms representing the irreversible temperature variations. Some of them directly evaluate the energy from fatigue hysteresis loop and associate it with the thermal contribution of the body. The introduction of thermal methods involving an energetic approach is very interesting since these approaches provide more information on damage and are free from geometrical aspects.

These information can be adopted to build or to validate mathematical models and then this can support numerical methods in predicting damage of structures.

## **2.1 Thermoelastic Stress Analysis**

### **2.1.1 Theory, History and Practice**

Thermoelastic stress analysis refers to the estimation of the state of stress in a structure by the measurement of the thermal response resulting from the application of a load within the elastic range of the material. The phenomenon of gases changing temperature when subjected to changes of pressure is well known. What is much less familiar, however is that similar principles apply to solid materials, although the temperature changes are much smaller: temperature changes in mild steel rapidly loaded to just below the yield point produces a temperature change of approximately 0.2 °C.

The relationship between applied stresses and the corresponding temperature changes in solid materials is known as the thermoelastic effect. Since the heat transfer causes these temperature changes to be transitory under the application of static loads, the analysis of

thermoelastic response is usually performed under dynamic load condition of a sufficient frequency to maintain an essentially adiabatic state in the material.

The interest in thermoelastic stress analysis has increased greatly over past decades due to the appearance on the market of an infra-red (IR) scanning system known as SPATE (Stress Pattern Analysis by measurement of Thermal Emission), [1], represented in Figure 2.1 and Figure 2.2 (a), which is a system providing sufficient sensitivity that is capable of estimating full-field stress patterns from dynamically loaded structures. The feature of the SPATE is to measure load-correlated temperature variations on the surface of the material.

A modern apparatus for stress pattern assessing is represented in figure 2.2 (b).

The hypothesis that governs the measurements is the ‘adiabatic condition’ achieved. In this condition in fact, the temperature changes at a point in a component are proportional to changes in volume at that position. Since the changes in volume are in turn proportional to the first stress invariant (the sum of the principal stresses) at that point, the measured temperature changes can be converted to stress values on the surface of the structure. The estimated stresses are scalar values proportional to the hydrostatic component of the stress tensor.

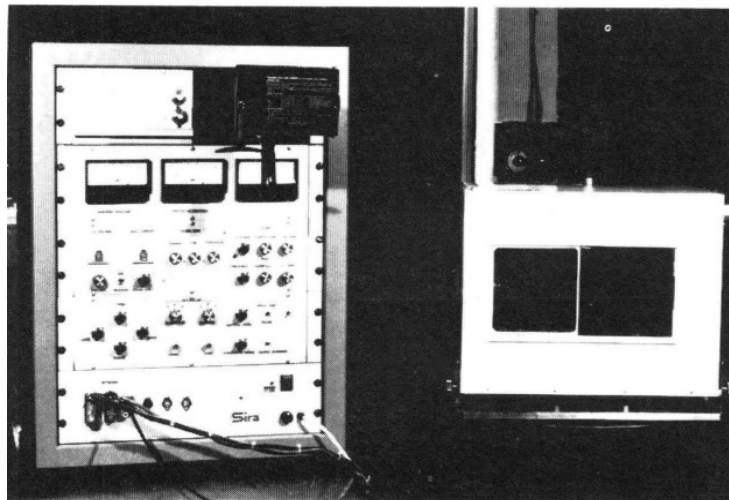
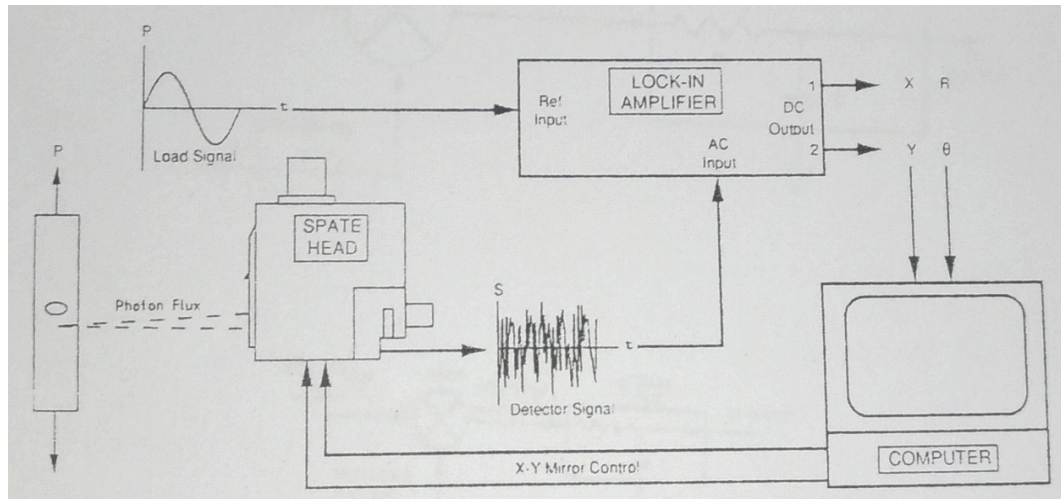
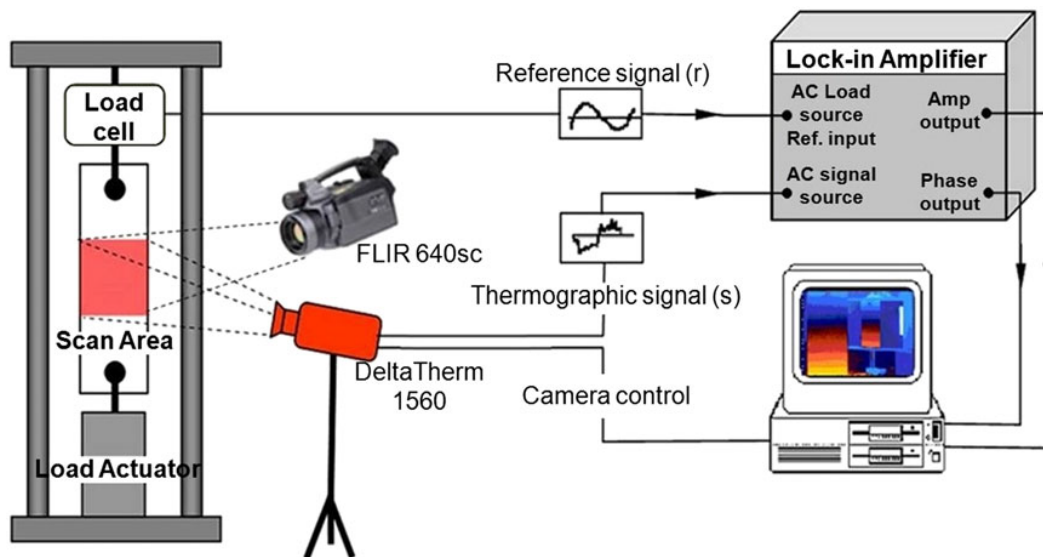


Figure 2.1. SPATE 8000 equipment



(a)



(b)

Figure 2.2. (a) SPATE 9000 block diagram system [1], (b) modern TSA system.

Thermodynamics theory predicts that, for the great majority of structural materials, tension produces a controlling effect, whereas compressive stresses produce an increase in temperature. This phenomenon can be used to determine the sign of estimated stress values. The phenomenon of material changing temperature when it is stretched was first noted by Gough in 1805 who performed a series of simple experiments using strands of india-rubber. Such elastomers do not of course behave like metals, but the first observation of the thermoelastic effect was performed by Weber in 1830 [2]. At this point, no scientific understanding of the physics basis of the results was provided, until the theory proposed by Lord Kelvin, the key figure of the thermoelasticity.

After Lord Kelvin, other scientists focused on the validation of the theory for a wide range of materials [3]. Tamman and Warrentrup in 1937 showed that the thermoelastic effect and



the reversal in the direction of the temperature change as energy was suddenly released by plastic strain could be used to indicate yield point in nickel and carbon steel. In 1938, Zener developed a theory which showed that thermoelasticity is an important factor in the damping of vibrations in polycrystalline materials while Rocca [4], some years later, found that the thermoelastic effect reduces close to Curie temperature in ferromagnetic materials. The following advances in the theory and practice have been provided by Biot [5].

By the developing of the SPATE system, many papers on applications of TSA have been presented [6-9].

Generally, to acquire the temperature changes the SPATE setup (figure 2.2(a)) or a modern system (figure 2.2 (b)) require, a system composed by a computer-controlled, non-contacting instrument which may be used to estimate full-field stress patterns in the form of coloured contour maps showing the distribution of the sum of the principal stress over optically accessible surfaces on structure subjected to dynamic loading. The dynamic loading have to be applied with frequency high enough to ensure that the thermodynamic condition in the component material can be considered to be adiabatic. In this way the reversibility is maintained between mechanical and thermal forms of energy [2].

As an example, the minimum frequency for an essentially adiabatic state depends on the thermal conductivity of the material and the gradients of the stress fields generated by the loading conditions. For most part of metallic components, it would not be advisable to use a mechanical frequency of less than 3 Hz unless corrections could be made for attenuation due to thermal conduction.

The waveform of the applied cyclic stress could be sinusoidal, which is the mostly preferred condition, since noise rejection is more efficient when all the energy of interest is concentrated at a single frequency [9].

For setting up the TSA technique, highly sensitive detector (equipped with a germanium lens i.e.) and amplifier/analyser which generates a signal in response to the thermoelastic infrared flux emitted from a spot on the surface of a structure which is undergoing uniform cyclic loading.

The detector has to operate in the bandwidth of the electromagnetic spectrum between 3 and 14 microns which contains the maximum photon and energy emission for bodies at room temperature. Since this bandwidth lies in the IR region of the light spectrum, sensors which operate within this bandwidth are known as IR detectors. The IR sensors are basically of two types, as previously explained, thermal detectors or photon detectors.

The first responds to incident radiation by changing its temperature, which in turn produces a change in resistance (bolometer), optical properties (e.g liquid crystals), or electrical field (e.g. pyroelectric devices) across the detector. Pyroelectric detectors may be used in thermal

imaging systems where they have the advantage of not requiring to be cooled, but their relatively poor sensitivities make them unsuitable for thermoelastic stress analysis. The alternative is represented by the photon detector made from a semiconductor material in which carriers may be excited from a valence energy band into a mobile conduction band by interaction with incident photons of sufficient energy. Such the detectors have a fairly abrupt upper cut-off in wavelength to which they respond, since long-wavelength photons are unable to supply sufficient energy to enable particles to cross the energy gap between the bound and mobile states. Particles are excited in proportion to the intensity of the incident radiation. These detectors requires to be cooled down. Materials used for building these detectors are Indium-antimonide (InSb) and the staring arrays have a 512\*512 element matrix of sensors.

The system requires also a clean reference signal taken from a function generator, a load cell or a strain gauge connected to the test structure, in this condition the noise may be rejected-out of the measured thermoelastic response and to allow the phase relationship between the reference and response signals to be determined [11-15].

Another parameter which has to be taken into account for measurements is the emissivity of the surface of the target, higher 0.9 in order to enhance the measured response and reduce thermal reflections from surrounding objects.

The last procedure for set up the technique involves the calibration of thermoelastic data from isotropic-homogeneous materials. The first type of calibration leads to compare the analytical solution for the stress distribution for an identical material to that one of the test and loaded at the same frequency [2]. Another procedure involves in using a strain gauge rosette bonded to the structure and used to assess a calibration factor relating the sum of the principal stresses to the amplitude of the thermoelastic response signal measured adjacent to the strain gauges. Finally, another method of calibration is to substitute values in the theoretical equation for the sum of the principal stresses and values of IR detection techniques resulting from the following working equation:

$$\delta\sigma = -\frac{DVR\rho C_P}{\alpha T e} \quad (2.1)$$

where  $D$  is responsivity of the SPATE detector ( $KV^{-1}$ ),  $V$  is the RMS amplitude of the thermoelastic response voltage at the operating frequency (V),  $R$  is a correction factor which compensates for temperature-dependant changes in radiation intensity and wave length [10], it is based on Stefan-Boltzmann law modified to take into account the photon flux of a specified spectrum bandwidth. ' $e$ ' is the surface emissivity.

A time the calibration is made, the setup is ready for acquisition and stress analysis.

By summarising, the advantages [2],[5],[12] of SPATE-based approach are:

- A rapidly assessment of qualitative full-field stress pattern,
- Minimal surface preparation required,
- Possibility to investigate complex geometries or features IR emission is fairly independent of viewing angles of up to  $60^\circ$  from normal, and the instrument has a wide depth of focus,
- Possibility to reduce significantly the spatial resolution,
- Better stress sensitivity of the instrument of 1 MPa than other techniques,

The disadvantages [13],[17] of using such the technique can be resumed as:

- High costs of equipment,
- Dynamic loading,
- Principal stress vectors are not measured, since the output is represented by the sum of principal stress.
- Displacements normal to the viewing angle may produce edge errors and smear the stress estimates. Metallised mirrors may be used to minimise this effect.

### **2.1.2 First Order Thermoelastic Temperature Variations**

In this paragraph, the temperature variations induced by the deformation must be considered as a response. For a homogeneous stress and strain fields the temperature field will be also homogeneous provided, as will be shown, that the boundary conditions are adiabatic.

The following equations do not account for heat exchanged with the environment or heat conduction determining a space and time dependent temperature field.

The adopted approach is thermodynamic [18-22]. The physical state of a small, but still macroscopic, volume of a solid is defined by local values of macroscopic variables, such as the stress tensor and the temperature and by its microstructure. In this case, the term ‘microstructure’ indicates a whole spectrum of features. In the case of crystalline materials the microstructural state is determined by the distributions of point defects (vacancies, or interstitials), dislocation network or mesoscopic defects like grain boundaries or precipitates. However, the elastic case is the simplest one, in which the microstructure is not altered at all. The state of the system is completely specified by the macroscopic variables. In the elastic regime reversible paths are easily identified between any possible state.

By applying a stress state to a body, it experiences volume changes, which produce temperature variations. As previously said, these variations are called: thermoelastic effect. If the body behaviour is linear elastic, it is possible to use the concept of ‘reversibility’ for describing the transformations which occurs [5], [12], [23].

A reversible transformation is defined between two fixed states, in this case, moreover, the reversible transformation in an elastic body can be assumed as a series of small quasi-static status characterised by infinitesimal changes of the system properties, by starting from initial status to ending status. By just taking into account this initial/ending state the behaviour of the body is completely assessed, no matter if a real thermodynamics equilibrium condition is present [24].

From thermodynamics point of view the state of an elastic body can be described by using the strain tensor and the temperature as state variables. Since the description of the behaviour of an elastic body involves the linear relations between stress-strain-temperature, even the stress can be understood as state variable.

The simplest mechanical behaviour of a linear elastic and isotropic material is described by Hooke's law [25], which represents the constitutive relationships (equations 2.2):

$$\begin{aligned}
 \sigma_{11} &= (2\mu + \lambda)\epsilon_{11} + \lambda\epsilon_{22} + \lambda\epsilon_{33} + \beta\Delta T \\
 \sigma_{22} &= \lambda\epsilon_{11} + (2\mu + \lambda)\epsilon_{22} + \lambda\epsilon_{33} + \beta\Delta T \\
 \sigma_{33} &= \lambda\epsilon_{11} + \lambda\epsilon_{22} + (2\mu + \lambda)\epsilon_{33} + \beta\Delta T \\
 \sigma_{12} &= 2\mu\epsilon_{12} \\
 \sigma_{23} &= 2\mu\epsilon_{23} \\
 \sigma_{31} &= 2\mu\epsilon_{31}
 \end{aligned} \tag{2.2}$$

In these equation the  $\sigma$  represents respectively the axial stress and the axial strain, the subscripts 1,2,3 refer to the principal directions. In general, stress and strain fields are homogeneous.  $\Delta T$  are the temperature changes as consequence of stress and strains variations while  $\mu$  and  $\lambda$  are the Lamé constants and  $\alpha$  is the linear thermal expansion coefficient for isotropic materials. The coefficient  $\beta$  can be evaluated as :

$$\beta = (3\lambda + 2\mu)\alpha \tag{2.3}$$

A state function which describes the thermodynamics status of the system can be the internal energy  $u$ :

$$u = u(\epsilon_{ij}, T) \tag{2.4}$$

By differentiating the equation 2.4 with respect status variables, it is possible to obtain the total derivative of internal energy,  $du$ , that is:

$$du = \left( \frac{\partial u}{\partial \varepsilon_{ij}} \right)_T d\varepsilon_{ij} + \left( \frac{\partial u}{\partial T} \right)_{\varepsilon_{ij}} dT \quad (2.5)$$

The equation 2.5 has the characteristic of state function: infinitesimal increments are exact differential. By full understanding internal energy  $u$ , the First Principle of Thermodynamics can be written:

$$du = \delta w + \delta q \quad (2.6)$$

Where  $w$  and  $q$  are respectively work and heat exchanged between the system and its environment.

The Second Principle of Thermodynamics, for a reversible process states:

$$ds = \frac{\delta q}{T} \geq \frac{(\delta q)_{\text{irreversible}}}{T} \quad (2.7)$$

Where the quantity introduced represents the entropy,  $s$ , of the system, another state function. In elastic regime, the entropy variation is the sum of vibrational and configurational entropy variations. These contributes are function of the temperature and volume variation as will be showed in the following sections. In case the system was isolated  $ds \geq 0$ .

As previously said, by supposing the system composed by an infinitesimal element in terms of volume and mass, under the following hypothesis [20-22]:

- The element is in equilibrium
- The deformations are quasi-static
- The deformations are small with respect the dimension of the element

It is possible to write the Virtual Work principle, which affirms that “If a system in equilibrium under the action of a set of forces is given a virtual displacement, the virtual work done by the forces will be zero”, mathematically:

$$\delta w = \frac{\sigma_{ij} d\varepsilon_{ij}}{\rho} \quad (2.8)$$

Another state variable is the Helmholtz free energy (per unit of mass), defined as:

$$H = u - Ts \quad (2.9)$$

By deriving equation 2.9 with respect the time:

$$dH = du - Tds - sdT \quad (2.10)$$

By substituting in the differential form of Helmholtz free energy, the Second Thermodynamics laws and Virtual Work principle, it follows a relation of H in function of temperature and deformation:

$$dH = \frac{\sigma_{ij} d\varepsilon_{ij}}{\rho} - sdT \quad (2.11)$$

Where H is an exact differential with respect temperature and deformation, and then it can be expressed also in the following form:

$$dH = \frac{\partial H}{\partial \varepsilon_{ij}} d\varepsilon_{ij} + \frac{\partial H}{\partial T} dT \quad (2.12)$$

Since  $T$  and  $\varepsilon$  are arbitrary, by comparing equations 2.11 and 2.12, it is possible to write separately differential terms:

$$\sigma_{ij} = \rho \frac{\partial H}{\partial \varepsilon_{ij}} \quad (2.13)$$

$$s = - \frac{\partial H}{\partial T} \quad (2.14)$$

Since entropy is function of free energy H, entropy per mass-unit is a state function of adopted state variables, this characteristic relating entropy to strain and temperature can be mathematically written as:

$$ds = \frac{\partial s}{\partial \varepsilon_{ij}} d\varepsilon_{ij} + \frac{\partial s}{\partial T} dT \quad (2.15)$$

By using the definition of entropy, together with equations 2.14 and 2.15, it is possible to define the specific heat per unit-mass and zero-deformation  $C_\varepsilon$  as directly function of temperature and second-order partial derivative of free energy of Helmholtz, all the mathematical steps are:

$$c_\varepsilon = \left( \frac{\delta q}{dT} \right)_{\varepsilon_{ij}} = \left( \frac{Tds}{dT} \right)_{\varepsilon_{ij}} = T \left( \frac{d}{dT} \left( \frac{\partial H}{\partial T} \right) \right)_{\varepsilon_{ij}} = T \left( \frac{\partial^2 H}{\partial T^2} \right)_{\varepsilon_{ij}} \quad (2.16)$$

Hence, entropy can be re-written as:

$$ds = \frac{\partial^2 H}{\partial \varepsilon_{ij} \partial T} d\varepsilon_{ij} + \frac{\partial^2 H}{\partial T^2} dT \quad (2.17)$$

By considering equations 2.13 and 1.16, the final expression for the derivative of entropy is:

$$ds = \frac{1}{\rho} \frac{\partial \sigma_{ij}}{\partial T} d\varepsilon_{ij} + c_\varepsilon \frac{dT}{T} \quad (2.18)$$

Substituting in the equation 2.18 the expression of Second Law of Thermodynamics:

$$\frac{\delta q}{T} = \frac{1}{\rho} \frac{\partial \sigma_{ij}}{\partial T} d\varepsilon_{ij} + c_\varepsilon \frac{dT}{T} \quad (2.19)$$

Which leads to obtain a relation representing temperature variation, stress and heating:

$$dT = \frac{T}{\rho c_\varepsilon} \frac{\partial \sigma_{ij}}{\partial T} d\varepsilon_{ij} + \frac{\delta q}{c_\varepsilon} \quad (2.20)$$

The terms  $(\frac{\partial \sigma_{ij}}{\partial T})$  represents the partial derivative of the stress tensor with respect to the temperature. By using the stress-strain-temperature relation (equation 2.2) which is valid per homogeneous and isotropic materials, and by assuming that Lamé constants are temperature independent, it is possible to obtain:

$$\frac{\partial \sigma_{ij}}{\partial T} = \beta \delta_{ij} \quad (2.21)$$

Where  $\delta_{ij}=1$  if  $i=j$ , or  $\delta_{ij}=0$  if  $i \neq j$ .

By combining these results, with expression 2.17, it is possible to obtain:

$$ds = c_\varepsilon \frac{dT}{T} - \frac{1}{\rho} \frac{\partial \sigma_{ij}}{\partial T} d\varepsilon_{ij} = c_\varepsilon \frac{dT}{T} + \frac{\beta}{\rho} \delta_{ij} d\varepsilon_{ij} \quad (2.22)$$

The product  $\delta_{ij} d\varepsilon_{ij}$  equals to  $d\varepsilon_{kk}$ , the first strain invariant, hence is possible to write:

$$ds = c_\varepsilon \frac{dT}{T} + \frac{\beta}{\rho} d\varepsilon_{kk} \quad (2.23)$$

By integrating and by setting  $s=0$  as initial condition, when  $\varepsilon_{ij}=(\varepsilon_{ij})_0$  and  $T=T_0$ , equation 2.23 provides:

$$s = c_\varepsilon \log \left( 1 + \frac{\Delta T}{T_0} \right) + \frac{\beta}{\rho} \Delta \varepsilon_{kk} \quad (2.24)$$

By considering that  $\Delta T \ll T_0$ , by expanding the logarithm in power series whose the first term only is stored, by considering adiabatic process ( $s=0$ ) equation 2.24 becomes:

$$\Delta \varepsilon_{kk} = - \frac{\Delta T}{\beta T_0} \rho c_\varepsilon \quad (2.25)$$

By exploiting the relation between stress-strain-temperature and Lamé constants, equation 2.25, transforms in:



$$\Delta \varepsilon_{kk} = \frac{\alpha}{\beta} (\Delta \sigma_{kk} + \beta \Delta T) \quad (2.26)$$

By combining equations 2.25 and 2.26, the stress-temperature relations is assessed:

$$\Delta \sigma_{kk} = \Delta T \frac{\rho c_\varepsilon}{\alpha T_0} + \beta \quad (2.27)$$

By taking into account the equation 2.3, and the relation  $(3\lambda + 2\mu) = E/(1-2\nu)$ , equation 2.27 becomes:

$$\Delta \sigma_{kk} = \Delta T \frac{\rho}{\alpha T_0} \left[ C_\varepsilon + \frac{E \alpha^2 T_0}{(1-2\nu)\rho} \right] \quad (2.28)$$

It is note Worthing to note that the material constants have been supposed constants with the temperature. This approach is consistent with the Kelvin's [18] approach which supposes the temperature variations strictly related to stress variations. Furtherly, since the term in square parenthesis corresponds to the definition of specific heat at constant pressure  $C_p$ , it follows that:

$$\Delta T = T_0 K_0 \Delta \sigma_{kk} \quad (2.29)$$

Where,  $K_0$  is called the thermoelastic constant [26-27]:

$$K_0 = \frac{\alpha}{\rho C_p} \quad (2.30)$$

This equation is the classical equation describing thermoelastic effect [12-23], it is valid for isotropic bodies undergoing elastic loading under adiabatic conditions by assuming that thermal and elastic properties do not change in function of the temperature, and also by assuming no internal heat sources.

Whenever the stress and strain fields are non-homogeneous, the temperature field is also non homogeneous and heat conduction occurs within the solid.

A more general discussion provides the different heat contribution of a body together with the thermoelastic contribute [28-31].

It has been considered that an entropy variation occurs when the sample undergone cyclic loading and then it allows the development of thermoelastic effect theory.

In order to highlight better the temperature variation due to volume (strain field) changes in the body it is possible to consider the Energy Balance equation:

$$Q = \rho C_{\varepsilon} \Delta T + \frac{T_0 E \alpha}{1-2\nu} \Delta \varepsilon_{kk} \quad (2.31)$$

Where the quantities are well-known (E Young modulus,  $\nu$  Poisson's ratio). By using the Heat Conduction equation without any external heat supply:

$$\frac{dQ}{dt} = k \nabla^2 T \quad (2.32)$$

Where  $k$  is thermal conductivity, by differentiating equation 2.31 with respect of the time, and by combining it with equation 2.32, the Diffusion Heat Equation in absence of external heat sources is obtained:

$$k \nabla^2 T = \rho C_{\varepsilon} \frac{\partial T}{\partial t} + \frac{T_0 E \alpha}{1-2\nu} \frac{\partial \varepsilon_I}{\partial t} \quad (2.33)$$

This equation contains a term, which represents an internal heat source due to the coupled thermos-mechanical heat source.

By rewriting the equation 2.33, in function of specific heat at constant pressure  $C_p$ , and the first stress invariant:

$$\frac{\partial T}{\partial t} = - \frac{1}{\rho C_p} \left[ T_0 \alpha \frac{\partial \sigma_I}{\partial t} - k \nabla^2 T \right] \quad (2.34)$$

By examining all the terms of equation 2.34, it is possible to observe that the heat exchange depends on [28], [31]:

- $k \nabla^2 T$  Laplacian operator, representing the thermal gradient in the body,
- Thermal conductivity of materials  $k$ ,
- Loading frequency  $\left(\frac{\partial \sigma_I}{\partial t}\right)$

Since the heat generated is a function of the temperature variation  $\partial T / \partial t$  due to strain variations, the thermal gradient will be a function of the stress. In case the term  $T=0$  no heat

conduction is present and body is in adiabatic conditions, if conductivity  $k$  is low, adiabatic condition are also provided. If the just said quantities are finite in value, the body will be in pseudo-adiabatic conditions.

Under adiabatic condition, the equation 2.34 describes also thermoelastic effect.

Equation 2.34 is linear and the thermoelastic effective source is a linear function of the local strain. The relationship between the temperature and elastic strain is linear, as well as the relation between temperature and stress. It represents the basis for TSA theory. Clearly, the relation between temperature and stress, in case plastic strains occur, is non-linear. The case of cracked samples is also different, since in proximity of the crack tip the behaviour involves non-linear deformation and damage processes active while far away the material behaves as elastic undamaged body. In fact, the presence of a crack introduces small localised non – linearity in a globally elastic behaviour.

In case of damage, it is of critical importance considering that the damage processes modify continuously the state of the material and the measured signals are not stationary, this as will be explained furtherly, leads to set different approach to study the behaviour of the material under plastic conditions [9], [31], .

However, in general, the macroscopic (both thermal and mechanical) behaviour is then essentially linear, with small deviants from linearity. In order to observe the non-linear effects, the main objective of a measurement is the discrimination of a small non-linear component from a predominant linear response.

However, for the purpose of performing TSA approach, if the damage process is slow enough, the signal characteristic evolves slowly, and the spectral analysis techniques remain applicable. In practice, the Fourier Transform remains meaningful if, during the time window required to perform a reliable transform, the modifications of the spectrum of a signal remain of the order of uncertainty in the determination of the spectrum itself [1],[7],[16].

When the spectral analysis is applicable, uniform sinusoidal loading is best suited to discriminate the linear and non-linear components of the responses, because the linear components falls at the excitation frequency, while the non-linear components give contributions at other frequencies. The separation, is however, not complete because a non-linear periodic response can also contain a component at the excitation frequency [2], [9], [12], [17].

### 2.1.3 Cyclic Testing and High Order Temperature Variations

In this paragraph, it will be showed the mathematical steps to apply the cyclic loading to TSA theory [32-36].

By considering the constitutive law (equation 2.2) in the form that the material properties depend on temperature:

$$\frac{\partial \sigma_{ij}}{\partial T} = 2 \frac{\partial \mu}{\partial T} \varepsilon_{ij} + \left( \frac{\partial \lambda}{\partial T} \varepsilon_{kk} - \frac{\partial \beta}{\partial T} \delta T - \beta \right) \delta_{ij} \quad (2.35)$$

The substitution of equation 2.35 in equation 2.19, yields:

$$\delta q = T \left[ 2 \frac{\partial \mu}{\partial T} \varepsilon_{ij} + \left( \frac{\partial \lambda}{\partial T} \varepsilon_{kk} - \frac{\partial \beta}{\partial T} \delta T - \beta \right) \delta_{ij} \right] \dot{\varepsilon}_{ij} - \rho C_\varepsilon \dot{T} \quad (2.36)$$

Where  $\delta q$  is a small heat exchanged between the body surface and the environment. In case of a stress-induced temperature field  $\delta T$  is small, an order to magnitude analysis shows that whilst  $\frac{\partial \beta}{\partial T} \delta T$  may be neglected compared to  $\beta$ , the terms  $\frac{\partial \mu}{\partial T} \varepsilon_{ij}$  and  $\frac{\partial \lambda}{\partial T} \varepsilon_{kk}$ , can be of significant order. By assuming adiabatic conditions, it is possible to obtain [2], [29-30]:

$$\rho C_\varepsilon \frac{\dot{T}}{T} = 2 \frac{\partial \mu}{\partial T} \varepsilon_{ij} \dot{\varepsilon}_{ij} + \left( \frac{\partial \lambda}{\partial T} \varepsilon_{kk} - \beta \right) \dot{\varepsilon}_{kk} \quad (2.37)$$

In terms of the stress, equation 2.37 becomes:

$$\rho C_\varepsilon \frac{\dot{T}}{T} = - \left[ \alpha + \left( \frac{\nu}{E^2} \frac{\partial E}{\partial T} - \frac{1}{E} \frac{\partial \nu}{\partial T} \right) \sigma_{kk} \right] \dot{\sigma}_{kk} + \left( \frac{1+\nu}{E^2} \frac{\partial E}{\partial T} - \frac{1}{E} \frac{\partial \nu}{\partial T} \right) \sigma_{ij} \dot{\sigma}_{ij} \quad (2.38)$$

Where  $\sigma_{kk}$  is the first stress invariant.

As is possible to observe from equation 2.38, the temperature is then function of stress and its rate of variation.

In a more practical approach, let's consider the effective case of uniaxial cyclic loading in the form:

$$\sigma_{11} = \sigma_{kk} = \sigma_m + \delta \sigma \sin \omega t \quad (2.39)$$

$$\sigma_{22} = \sigma_{33} = \sigma_{12} = \sigma_{13} = \sigma_{23} = 0 \quad (2.40)$$

By substituting equation 2.40 into equation 2.38, it is possible to obtain:

$$\rho C_\varepsilon \frac{\dot{T}}{T} = \left[ \alpha - \left( \frac{1}{E^2} \frac{\partial E}{\partial T} \sigma_m + \delta \sigma \sin \omega t \right) \right] \omega \delta \sigma \cos \omega t = - \left( \alpha - \frac{1}{E^2} \frac{\partial E}{\partial T} \sigma_m \right) \delta \sigma \cos \omega t + \frac{1}{2E^2} \frac{\partial E}{\partial T} \omega (\delta \sigma)^2 \sin 2\omega t \quad (2.41)$$

By integrating equation 2.41 and assuming that  $\delta T = T - T_0 \ll T_0$  and nothing that energy transfer to the surroundings would ensure a vanishing static component in  $\delta T$ , equation n2.41 becomes:

$$\rho C_\varepsilon \frac{\delta T}{T_0} = - \left( \alpha - \frac{1}{E^2} \frac{\partial E}{\partial T} \sigma_m \right) \delta \sigma \sin \omega t - \frac{1}{4E^2} \frac{\partial E}{\partial T} \omega (\delta \sigma)^2 \cos 2\omega t \quad (2.42)$$

The difference between this response and that which is predicted by Kelvin theory, may be seen by neglecting the temperature-dependent terms in equation 2.42, namely [9]:

$$\rho C_\varepsilon \frac{\delta T}{T_0} = -(\alpha) \delta \sigma \sin \omega t \quad (2.43)$$

The equation 2.42 represents the temperature response to an applied sinusoidal load. One immediate observation is that it is composed of two harmonic components. The first component occurs at the mechanical frequency  $\omega$ , and its amplitude is a function of both  $\sigma_m$  and  $\delta \sigma$ , while the second at frequency  $2\omega$ , is dependent only on the square of the stress amplitude  $(\delta \sigma)^2$ . This component is also characterised by the term  $\frac{1}{4E^2} \frac{\partial E}{\partial T}$  which is relatively small, even in case it becomes significant when the applied stress amplitudes are sufficiently large.

In general, the double frequency component exists only in case Young's modulus depends on the temperature at higher stress values while the component at the mechanical frequency exists every time, and depends from mean stress in case Young's modulus depends on the temperature.

In a purely thermoelastic approach the double frequency component is not taken into account, and the amplitude of the temperature variations is:

$$\frac{\delta T}{T_0} = \frac{1}{\rho C_\varepsilon} \left( \alpha - \frac{1}{E^2} \frac{\partial E}{\partial T} \sigma_m \right) \delta \sigma \quad (2.43)$$

By comparing this equation with the Kelvin's Law:

$$\frac{\delta T}{T_0} = -K_0 \delta \sigma \quad (2.44)$$

Where  $K_0 (\alpha/\rho C_p)$  is the material constant independent from applied stress, it possible to

see that the revised formulation yields an effective thermoelastic parameter which, is mean-stress dependent, namely:

$$K_e = \frac{1}{\rho C_p} \left( \alpha - \frac{1}{E^2} \frac{\partial E}{\partial T} \sigma_m \right) \quad (2.45)$$

It is interesting to see that the stress dependence of the thermoelastic parameter arises as a result of the temperature dependence of the material's stiffness [26].

Given that the IR detector of SPATE has a linear response to changes in irradiation flux  $\delta\Phi$ , where [34-35]:

$$\delta\Phi = 4eBT_0^3\delta T \quad (2.46)$$

in which  $e$  is the surface emittance, and  $B$  is the Stefan-Boltzman constant, the detector response should be linearly proportional to the right-hand side of equation 2.42. By focusing the attention on just the first harmonic component, the signal recorded can be written as [2]:

$$S = -4RBT_0^4 \left( \alpha - \frac{1}{E^2} \frac{\partial E}{\partial T} \sigma_m \right) \frac{\delta\sigma}{\rho C_\epsilon} \quad (2.47)$$

In the following paragraph starting from the signal  $S$  arrived to thermal sensor, it will be discussed another parameter which can lead to consider the TSA theory even if adiabatic conditions are lose.

### 2.1.4 Thermoelastic Phase Analysis

In general, the output from a lock-in amplifier often has two output channels, the amplitude of the signal  $R$  and the  $\varphi$  phase shift between acquired temperature signal and reference signal. These parameters are more commonly that the components whose they are related: X real part (associated to stress sign information (tension or compression)) and Y imaginary part of such the input signal [15], [37].

In order to understand the impact of these parameters on TSA equations it is necessary to understand in depth the lock-in filtering signal procedure, integrated for example in the infrared detector working in the way represented by Figure 2.2.

Lock-in amplifiers are used to detect and measure very small AC- signals all the way down to a few nanovolts, the TSA signal can be roughly of 0.02 V peak-to-peak. Accurate measurements may be made even when the small signal is obscured by noise sources many

thousands of times larger. Lock-in amplifiers use a technique known as phase-sensitive detection to single out the component of the signal at a specific reference frequency and phase. Noise signals, at frequencies other than the reference frequency, are rejected and do not affect the measurement.

The amplifier combines the reference loading sinusoidal wave and the detector output waveform (square waveform).

Usually the system is connected to a low-pass filter. The amplifier combines the detector and reference signal by forming the product of the two signals, both waveforms run at the same frequency ( $\omega$ ).

In this way, the resultant signal contains the sum and difference of the input frequencies. The difference component of the mixer output is represented as a DC level proportional to the amplitude of both detector and reference signals. The circuit normalises the reference signal so that the DC level is proportional to only the amplitude of the detector signal (at the frequency of the reference signal). Any noise present in the detector signal that is not at the reference signal frequency is also multiplied by the reference and presented at the output of the mixer. The residual component of noise is reduced by passing through a low pass filter. The term 'phase sensitive' refers to that the measurements require a frequency reference (reference signal).

If the reference signal is a square wave at frequency  $\omega_r$ . This might be the synchronous output from a function generator. If the sine output from the function generator is used to excite the experiment, the response might be the signal waveform shown in Figure 2.3.

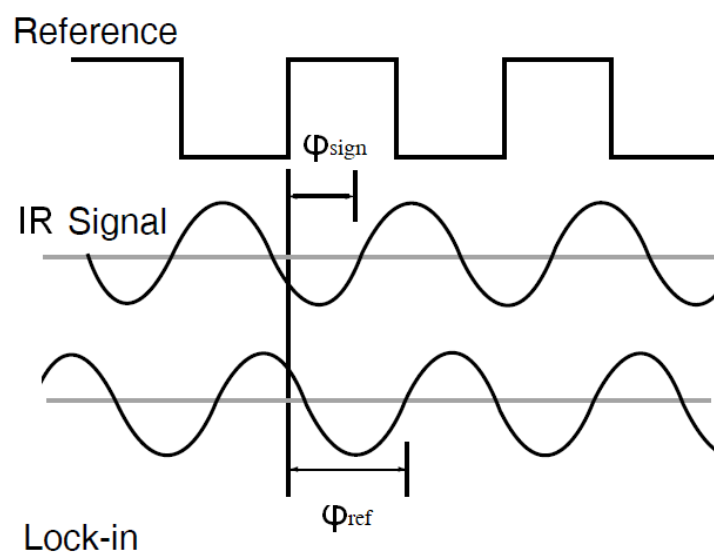


Figure 2.3. Waveform of Reference, IR detector and Lock-in amplified signals.

The signal can be described by the function:

$$S_s \sin(\omega_s t + \varphi_{sign}) \quad (2.48)$$

Where  $S$  is the amplitude of the signal,  $\omega_s$  is the pulsating signal ( $2\pi f$ ) and  $\varphi_{sign}$  is the signal's phase.

Lock-in amplifier generates their own internal reference signal usually by a phase-locked-loop locked to the external reference. The internal reference is described by:

$$S_r \sin(\omega_r t + \varphi_{ref}) \quad (2.49)$$

Where  $R$  is the amplitude of the signal,  $\omega_r$  is the pulsating signal ( $2\pi f$ ) and  $\varphi_{ref}$  is the reference signal's phase.

The lock-in amplifies the signal and then multiplies it by the lock-in reference using a phase-sensitive detector or multiplier. The output  $O$  is simply the product of two sine waves:

$$S_o = S_s S_r \sin(\omega_r t + \varphi_{ref}) \sin(\omega_s t + \varphi_{sign}) = \frac{1}{2} S_s S_r \cos[(\omega_r - \omega_s)t - \varphi_{ref} + \varphi_{sign}] - \frac{1}{2} S_s S_r \cos[(\omega_r + \omega_s)t + \varphi_{ref} + \varphi_{sign}] \quad (2.50)$$

The phase sensitive detector lock-in output is two AC signals, one at the difference frequency ( $\omega_r - \omega_s$ ) and the other at the sum frequency ( $\omega_r + \omega_s$ ).

When the signal passes through a low pass filter, the AC signals are removed, moreover, if  $\omega_r = \omega_s$  the difference frequency component will be a DC signal, and the output  $O$  becomes:

$$S_o = \frac{1}{2} S_s S_r \cos[\varphi_{sing} - \varphi_{ref}] \quad (2.51)$$

That is the DC signal proportional to the signal amplitude. It's important to consider the physical nature of this multiplication and filtering process in different types of lock-ins. In traditional analog lock-ins, the signal and reference are analog voltage signals. The signal and reference are multiplied in an analog multiplier, and the result is filtered with one or more stages of RC filters [37-38].

By considering that the output is a signal  $S_o$  proportional to  $S_s \cos[\varphi]$  where  $\varphi = [\varphi_{sing} - \varphi_{ref}]$ , it is possible to observe that two other outputs are provided:



$$X = S_s \cos \varphi \quad (2.52)$$

$$Y = S_s \sin \varphi$$

These two quantities represent the signal as a vector relative to the lock-in reference oscillator.  $X$  is the in-phase component, while  $Y$  is the 'quadrature' component. This is because when  $\varphi=0$ ,  $X$  measures the signal while  $Y$  is zero.

By computing the magnitude ( $R$ ) of the signal vector, the phase dependency is removed:

$$R = (X^2 + Y^2)^{1/2} = S_s \quad (2.53)$$

$R$  measures the signal amplitude and does not depend upon the phase between the signal and lock-in reference.

A dual-phase lock-in has two phase-sensitive detectors with reference oscillators  $90^\circ$  apart, and can measure  $X$ ,  $Y$ , and  $R$ , directly. In addition, the phase  $\varphi$  between the signal and lock-in is defined as:

$$\varphi = \tan^{-1} (Y/X) \quad (2.54)$$

The present discussion allows a consideration: since the apparatus for performing TSA tests allows obtain the amplitude as well as the phase shift parameter, one can consider also this latter as parameter to study the behaviour of the body.

How and Why?

The use of the simple connection between the amplitude of the temperature fluctuation and that of the stress fluctuation is dependent upon the presumption of adiabaticity that is, that all the heat generated in an element goes towards producing a temperature rise in that element, and does not leak away into surrounding material or environment [2].

It was observed by Beghi [14], Belgen [6],[29-30], that adiabaticity can fall down for three mechanisms:

- heat loss from the element to the environment by conduction, convection and radiation from the surface being observed,
- conductive heat loss from the element to surrounding material whose temperature is less than that of the element under consideration,
- for the purposes of improving the level of the uniformity of radiation a coating is applied that has a significantly different thermoelastic constant from test-piece, then the temperature amplitude on the external surface will in general be different from that at the surface of the test material, and in presence of these mechanisms, a signal

attenuation between the actual temperature and the temperature of adiabatic conditions were observed.

These phenomena, leading the lost of adiabatic condition allow also  $\varphi$  variations, the just said angle representing the phase shift between the loading machine signal and temperature signals.

Therefore a somewhat relation between two phase lag has to exist, hence an estimation of such the phase lag can be assessed by assessing  $\varphi$ : this has been the basis of the Thermoleastic Phase Analysis approach.

In the case of uniaxial stress with sinusoidal loading, and by introducing the predicted phase shift, equation 2.43 transforms in:

$$\frac{\delta T}{T_0} = -K\delta\sigma \sin(\omega t + \varphi) = K\delta\sigma \sin(\omega t + \varphi + \pi) \quad (2.55)$$

In presence of linear elastic behaviour of material and steady state conditions, phase can slightly change through the area analysed due to a non-perfect homogeneity of the surface conditions, it is basically insensitive to change of loading amplitude, but it depends on a number of parameters such as, for example, thickness of the painting or the grips of the loading machine.

Significantly, phase can change [39-40]:

- in presence of viscoelastic or plastic behaviour of material [39-41],
- in presence of high stress gradient leading to heat conduction in material and to the loss of adiabatic conditions [2][28][42-45], in this regard, the more the material is conductive for example, the more it is affected by the phase attenuations and then phase variations.

As just stated, other authors [46],[47] used the amplitude of thermoelastic signal as a parameter to evaluate the fatigue damage and the fatigue limit of material.

In other works [39-40][42] phase variations have been measured during fatigue tests in correspondence with plastic and viscoelastic behaviours of material and in the case of high stress gradient. In particular, during a fatigue test, the phase signal remains constant up to plastic phenomenon occurrence in the material and with increase of damage, phase variations can be observed due to the phenomena described previously [41].

The following chapters will be focused on presenting an in-depth study of phase variations in order to correlate better such the parameter to fatigue and damage behaviours of materials. The following two paragraphs of this Chapter will be focused on presenting two main

application of thermoelastic phase shift as well as thermoelastic signal amplitudes, involving in the fracture mechanics study of the plastic behaviour around the crack tip and the thermoelastic response study by orthotropic materials.

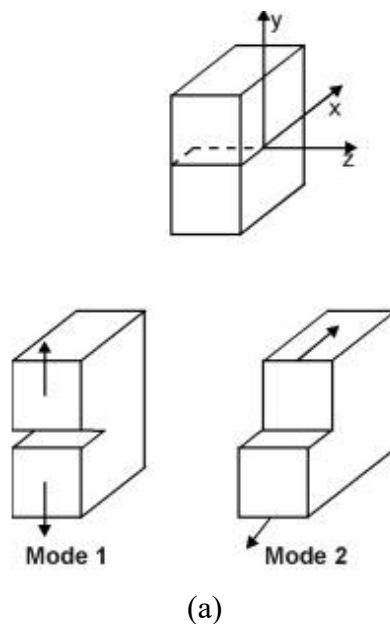
### 2.1.5 Application of TSA on cracked specimens

The analysis and characterisation of crack-tip stress fields, and the determination of stress intensity factors and the relevant material parameters are topics making importance in fracture mechanics [48-57].

Since the development of SPATE system, it was understood the capability of TSA to detect the crack tip stress field [41]. In recent years, TSA approach has been furtherly attractive referring to the crack growth and damage accumulation monitoring [58-71] due to the advent of systems based on infrared detector arrays, making possible the reduce the time for image capture.

Stanley and Chan [8],[12], developed a method that related the thermoelastic signal to the first two terms of Westergaard's equation for the elastic stresses in the vicinity of a crack tip under mode I and mode II loading, figure 2.4(a).

According to this approach a crack in a flat plate is considered, under conditions of plane stress figure 2.4(b), subjected to mode I (opening) and mode II (sliding) loading.



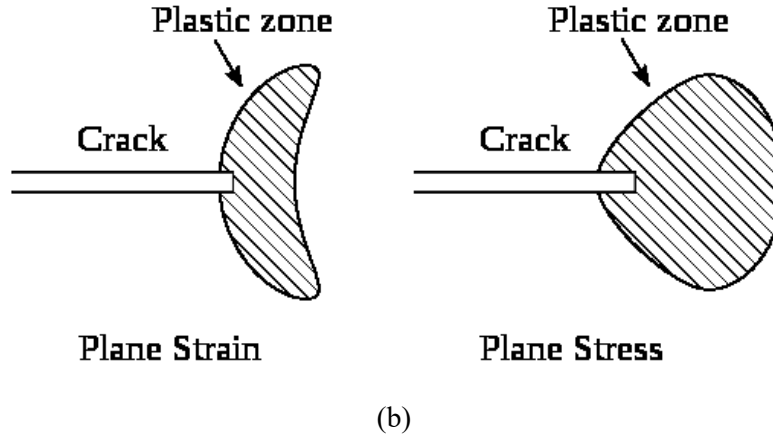


Figure 2.4 (a) fracture modes [72], (b) representation of the plastic zone under plane strain and plane stress conditions,

Figure 2.4(b) represents the differences between the morphology under plane strain and plane stress. However, in the present discussion, only the second condition will be taken into account. In order to determine the stress intensity factors for both the modes loadings let consider the Westergaard's equations [73] which give a solution for the elastic stresses  $\sigma_x, \sigma_y, \tau_{xy}$  in the region of the crack tip in the form of:

$$\begin{bmatrix} \sigma_x \\ \sigma_y \\ \tau_{xy} \end{bmatrix} = \frac{K_I}{\sqrt{2\pi r}} \cos(\theta/2) \begin{bmatrix} 1 - \sin(\theta/2) \sin(3\theta/2) \\ 1 + \sin(\theta/2) \sin(3\theta/2) \\ \sin(\theta/2) \sin(3\theta/2) \end{bmatrix} + \frac{K_{II}}{\sqrt{2\pi r}} \begin{bmatrix} [-\sin(\theta/2)] [(2 + \cos(\theta/2)\cos(3\theta/2))] \\ [\sin(\theta/2)] [\cos(\theta/2)\cos(3\theta/2)] \\ [\cos(\theta/2)] [1 - \sin(\theta/2) \sin(3\theta/2)] \end{bmatrix} \quad (2.56)$$

Where  $K_I$  and  $K_{II}$  are the mode I and II stress factors and  $r, \theta$  are polar coordinates measured from the crack tip and the continuation of the line of the crack respectively, as represented in figure 2.5.

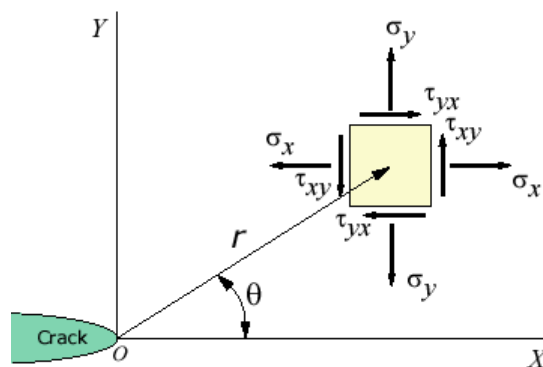


Figure 2.5. Crack tip stresses [74]

Equation 2.56 is the widely used form of a more general equation containing an infinite

succession of higher-order terms, it is strictly valid only for an infinitely extensive specimen. In the immediate vicinity of the crack tip, the effects of local yielding invalidate the equation, and as the coordinate point approaches the specimen edges it becomes necessary to retain increasingly more terms from the general equation.

Under adiabatic loading, the signal  $S$  from a linear elastic solid is proportional to the change in the sum of the principal surface stresses ( $\sigma_1 + \sigma_2$ ) at the point under consideration:

$$\sigma_1 + \sigma_2 = AS \quad (2.57)$$

Where  $A$  is the calibration constant [2] and  $(\sigma_1 + \sigma_2)$  is the the first invariant of a two-dimensional stress system and is therefore equal to the sum of the coordinate normal stresses  $\sigma_x, \sigma_y$ , it follows that:

$$\sigma_x + \sigma_y = AS \quad (2.58)$$

Substituting from equation 2.56 for the stress terms in equation 2.58, for the generic point  $(r, \theta)$ , in a crack-tip stress field an important relation from any combination of mode I and mode II loading, is obtained:

$$AS = \frac{2K_I}{\sqrt{2\pi r}} \cos(\theta/2) - \frac{K_{II}}{\sqrt{2\pi r}} \sin(\theta/2) \quad (2.59)$$

Equation 2.59 allows the assessment of stress intensity factors of mode I and II by using TSA signal.

In case the pure mode I loading prevails ( $K_{II}=0$ ), and replacing the term  $r$  by  $y/\sin \theta$  (figure 2.5) to give:

$$AS = \frac{2K_I}{\sqrt{2\pi y}} \sqrt{\sin(\theta/2)} \cos(\theta/2) \quad (2.60)$$

It is readily shown from equation 2.60 that the partial derivative of  $S$  with respect to  $\theta$  is zero when  $\theta = 60^\circ$ , hence, the maximum signal in a line plot taken parallel to the crack occurs at  $\theta = 60^\circ$ . In order to analyse the mode I loading the study can interest signal plots along lines parallel to the line of crack, equation 2.59 becomes:

$$AS_{max} = \frac{2K_I}{\sqrt{2\pi y}} \sqrt{\frac{\sqrt{3}}{2} \frac{\sqrt{3}}{2}} \quad (2.61)$$

or

$$y = \frac{2K_I^2}{(\pi A)^2 S_{max}^2} \quad (2.62)$$

It is clear from equation 2.62 that  $1/S_{max}^2$  and  $y$  are linearly related and that, provided the constant  $A$  is known,  $K_I$  can be obtained directly from the gradient of a graph of  $y$  versus  $1/S_{max}^2$ .

For the mode II [2], [66] loading the equation 2.59 becomes:

$$AS = -\frac{2K_{II}}{\sqrt{2\pi y}} \sqrt{\sin(\theta)} \sin(\theta/2) \quad (2.63)$$

The partial derivative of the signal  $S$  with respect to  $\theta$  is determined and equated to zero to give the  $\theta$  – value of the maximum (or minimum) signal along a line plot parallel to the crack length (i.e.  $y=\text{constant}$ ). The derived  $\theta$  –values are  $\pm 120^\circ$  for positive and negative  $y$ -values respectively. Taking the positive  $\theta$ -value, the following relationship between the maximum (negative) signal  $S_{max}$  along a line of constant positive  $y$  and the  $y$ -coordinate of the line is:

$$y = \frac{3\sqrt{3}2K_{II}^2}{(4\pi A)^2 S_{max}^2} \quad (2.64)$$

For  $\theta=120^\circ$  (i.e along a line of constant negative  $y$ ) the peak signal is positive and a similar equation is obtained with a minus sign on the right hand side. Equation 2.64 is similar to equation 2.62, and the procedure described after the latter equation for the determination of  $K_I$  applies equally for the determination of  $K_{II}$  from the  $S_{max}$  observed in a series of line scans parallel to a crack under mode II loading.

Except for the initial and final stages of growth characterised by high growth rates, the increase in length  $a$  of a propagating fatigue crack per cycle  $N$  of applied load is related to the stress intensity range over the load cycle  $\Delta K_I$  by the well-know Paris's Law:

$$\frac{da}{dN} = C(\Delta K_I)^m \quad (2.65)$$

In demonstrating the validity of this expression , and eriving values for  $C$  and  $M$ , it is necessary to obtain simultaneous values of  $\Delta K_I$  and  $\frac{da}{dN}$ .

By using the TSA these quantities can be assessed by plotting lines in the crack tip regions ( $y=0$ ).  $\Delta K_I$  can be calculated by using perpendicular to crack tip regions plot and  $\frac{da}{dN}$  is obtained as the gradient of a plot of the crack length versus the number of cycles.

Referring to the thermoelastic signal amplitude, another important result was presented by [58], [60].

Dulieu-Smith [75] presented an approach based on the fact that the isopachic contour at the crack tip region generally takes the form of a cardioid curve centred on the crack tip figures 2.6. This approach is very interesting since it allows firstly discriminating the plastic zone from other zones, localising the crack tip and finally measuring crack length.

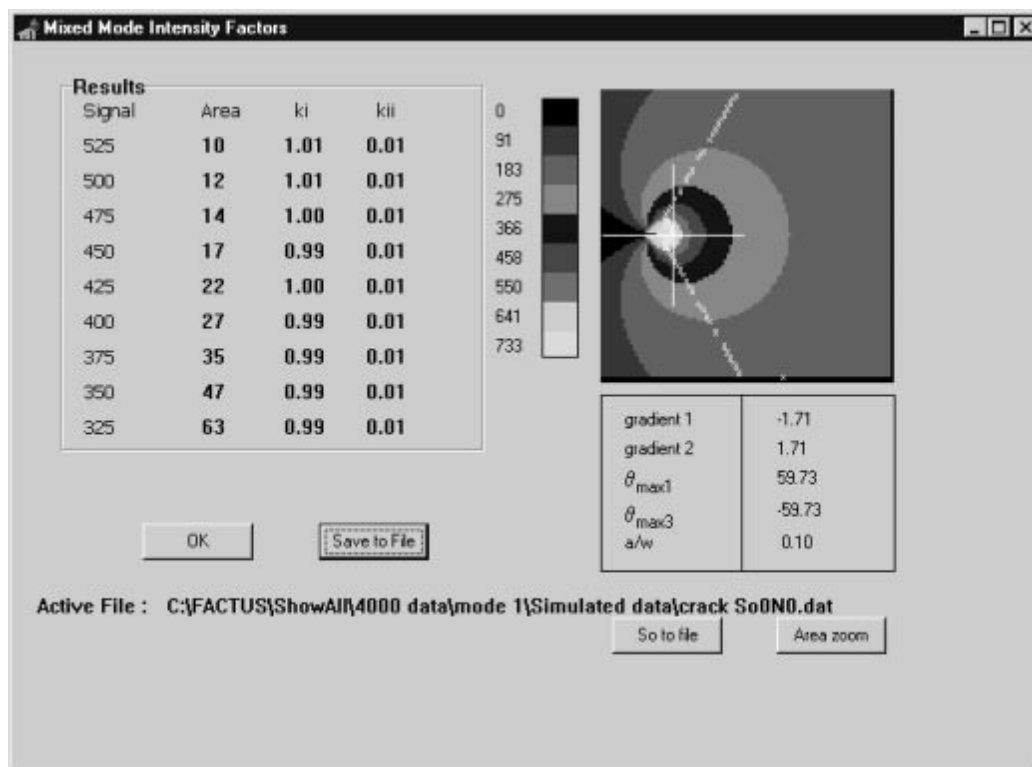


Figure 2.6 Cardioid morphology of the plastic zone [75].

As previously presented, thermoelastic signal is normally presented as a vector where the modulus is proportional to the change in temperature experienced by the specimen due to the thermoelastic effect and the phase denotes the angular shift between the thermoelastic and the reference signals. The magnitude of the phase is normally constant unless adiabatic conditions are not achieved, in these conditions occur heat generation due to plastic work and high stress gradients.

Both of phenomena occur near the crack tip region. Consequently, in these circumstances heat conduction starts taking place blurring the data at those regions, making direct observation of the crack tip from a thermoelastic image difficult. Nevertheless, the

thermoelastic data are rich in information and works has been conducted [41-42] to develop a methodology based on the phase map to estimate the crack tip location.

In the work of [76], by analysing the phase maps, they should be zero in all those points where adiabatic conditions are achieved and differ from zero near the crack tip where, as previously explained, plasticity and high stress gradients lead to a loss of adiabatic conditions. In figure 2.7(a) the dissipating zone is clearly evident.

The authors provide an explanation for specific regions assessed by analysing a phase profile along the crack, figure 2.7(b). In particular, in region A the adiabatic condition are achieved, region B, according to the author, indicates a loss of adiabaticity due to monotonic plasticity and presence of high stress gradients. The region C where phase takes negative values is attributed to the presence of reverse plasticity, while from the point O onwards the phase starts changing continuously from positive to negative. Such behaviour is attributed in part to contact between the crack faces and also the background reflection coming from inside of the crack mouth as it is opening. In this case, the point O is adopted as an initial estimate of the crack tip and then also adopted for calculating the SIF from thermoelastic data.

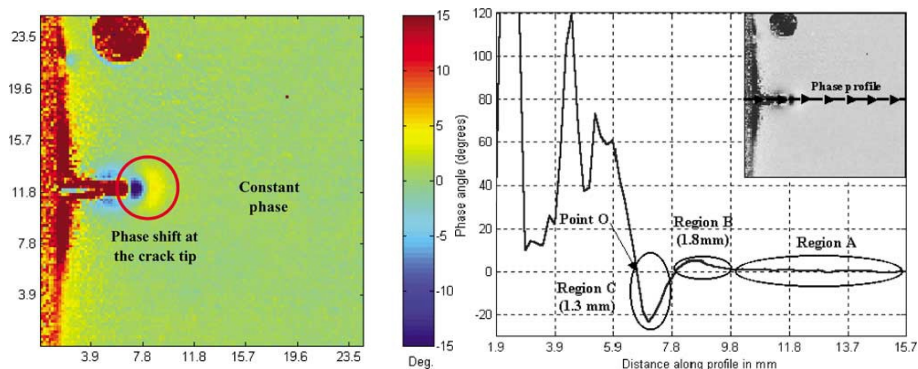


Figure 2.7 (a) Phase map: plastic zone, (b) phase profile along the crack [76].

However, the limit of this methodology is such that it does not provide an exact location for the crack tip or does not provide to detect and to separate the phenomena of crack closure and plasticization, even if it helps in finding an approximate location required for calculating the SIF.

The developed thermal approach, on the contrary, will provide the assessment of more information in the plastic zone as well as a better understanding of the physics of such phenomena.



### 2.1.6 Application of TSA on orthotropic materials

In this paragraph, another application of TSA will be discussed referring to a special type of anisotropic material: orthotropic materials whose property variations are symmetric about axes at right angles. As an example of orthotropic material, the Composites have to be mentioned. In general, it will demonstrate the validity of the equations for orthotropic laminates to also, with some modification, to more generally case of anisotropic materials in which mechanical properties vary with direction [2], [77-81].

Thermoelastic analysis is based on the measurement of temperature fluctuations in the surface ply, whose in-plane orthotropic axes, 1 and 2, will not necessarily be coincident with those of the laminate (x,y). A third set of axes (j,k) are those of the principal stresses in the surface ply and these will not generally be coincident either with the laminate orthotropic axes (x,y) or with those of the surface ply (1,2).

The equations and the processes are supposed to be wholly adiabatic and the stresses and strains in subsurface layers must be derived from those of the surface ply by laminate analysis.

The failure mechanisms in highly anisotropic materials tend to be dominated by material anisotropy rather than by the orientation of the principal stresses or strains. For example, fibre composites generally fail due to the fracture or instability of the fibres or by the propagation of cracks running parallel to the fibres. In the design and evaluation of fibre-composite structures, the stress analyst is not therefore primarily interested in principal stresses and strains but in the stress and strains related to the material coordinate system. The thermoelastic equations for these materials will therefore be expressed in terms of material axes rather than principal stress or strain axes. It should also be noted that it is generally more convenient to work in terms of strain rather than stress in the analysis of laminated composite materials. The in plane stresses within a particular ply depend upon ply orientation but are related to the laminate stress resultants by conditions of strain compatibility.

The more general form applicable to anisotropic materials derived by Potter et al. [82]:

$$\rho C_\varepsilon \frac{dT}{T} = \frac{\partial C_{ijkl}}{\partial T} \left( \varepsilon_{kl} - \alpha_{kl}(T - T_0) - C_{ijkl} \left( \alpha_{kl} + \frac{\partial \alpha_{kl}}{\partial T} (T - T_0) \right) \right) d\varepsilon_{ij} \quad (2.65)$$

In this equation, the summation convention implies that, where a suffix is repeated in a product, the summation is made with the suffix increasing from 1 to 3.

A part from the well-known symbols of presented equations,  $C_{ijkl}$  is the elasticity tensor for composites. In case of a sinusoidal waveform imposed to sample, equation 2.65 can be

integrated to give:

$$\rho C_\varepsilon \ln \frac{T}{T_0} = \left[ \frac{\partial C_{ijkl}}{\partial T} \bar{\varepsilon}_{kl} - \alpha_{kl} C_{ijkl} \right] \Delta \varepsilon_{ijkl} \sin(\omega t) - \frac{1}{4} \frac{\partial C_{ijkl}}{\partial T} \Delta \varepsilon_{kl} \Delta \varepsilon_{ij} \cos(2\omega t) \quad (2.66)$$

Even if equation 2.66 shows the presence of a second order component at  $2\omega$ , in general what is interesting is the first order component due to the second order effect are usually negligible, so that equation 2.66 changes in:

$$\rho C_\varepsilon \frac{\Delta T}{T_0} = \left[ \frac{\partial C_{ijkl}}{\partial T} \bar{\varepsilon}_{kl} - \alpha_{kl} C_{ijkl} \right] \Delta \varepsilon_{ij} \quad (2.67)$$

A further simplification can be also to ignore the term  $\frac{\partial C}{\partial T}$ , which allows a very small error, hence equation 2.67 becomes:

$$\rho C_\varepsilon \frac{\Delta T}{T_0} = -\alpha_{kl} C_{ijkl} \Delta \varepsilon_{ij} \quad (2.68)$$

This equation represents the linear form of the thermoelastic equation commonly assumed. Except for totally anisotropic materials, the material symmetry will normally allow further simplification of this equation. In the case of isotropic materials, the diagonal terms of the thermal expansion tensor are equal and the other terms are zero. In addition, the strain-stiffness products add up to the sum of the hydrostatic stress components. This is clearly also equal to the sum of the principal stresses.

However, for orthotropic materials for which the diagonal terms in the thermal expansion tensor are not equal, and then they are not zero. In addition, there are no stiffness terms coupling dilatational stresses to shear strains ( $C_{iikl} = C_{klji} = 0$  if  $k \neq i$ ). The thermoelastic equation therefore becomes:

$$\rho C_\varepsilon \frac{\Delta T}{T_0} = -\alpha_{kk} C_{iikk} \Delta \varepsilon_{ii} \quad (2.69)$$

When observing the surface of orthotropic sample a free surface is being observed so plane stress conditions prevail. This means that  $\varepsilon_{23} = \varepsilon_{13} = 0$  and  $\Delta \varepsilon_{33}$  is a function of  $\Delta \varepsilon_{11}$  and  $\Delta \varepsilon_{22}$ .

By expressing in form of stresses equation 2.68, because of free surface  $\sigma_{33}=0$  and the appropriate equation is:

$$\rho C_\varepsilon \frac{\Delta T}{T_0} = -(\alpha_{11} \Delta \sigma_{11} + \alpha_{22} \Delta \sigma_{22}) \quad (2.70)$$

By observing equation 2.70 it can be pointed out that in case the expansion coefficients were equal, it reduces to a form similar to that which is commonly used for isotropic materials. If the term  $\frac{\partial C}{\partial T}$  may not be neglected, equation 2.68 becomes:

$$\rho C_\varepsilon \frac{\Delta T}{T_0} = \left[ \frac{\partial C_{iikk}}{\partial T} \bar{\varepsilon}_{kk} - \alpha_{kk} C_{iikk} \right] \Delta \varepsilon_{ii} + \frac{\partial C_{1212}}{\partial T} \bar{\varepsilon}_{12} \Delta \varepsilon_{12} \quad (2.71)$$

Equation 2.71 represents the general form of the thermoelastic equation for orthotropic materials. The term  $\frac{\partial C}{\partial T}$  can be however neglected since its effect is secondary and it is not specific to anisotropic materials. In any case, this term vanishes in case the mean strain is zero.

Despite the theoretical complexities and practical difficulties, thermoelastic methods have been used successfully on highly anisotropic materials, giving information which would be difficult, if not impossible, to obtain by other current techniques.

The potential of TSA for analyzing composite materials has been reported in the works of Emery et al. [79] and Fruehmann et al. [83].

In particular, the first investigates various polymer-matrix composites with different laminate types, while the second highlights the possibility of using the phase signal for evaluation of fatigue damage, even at low stress.

Also, Pitarresi [80], in its work performed a quantitative thermoelastic stress analysis on Carbon Fibers-Reinforced Plastic laminates by implementing bulk method theory, using homogenised bulk properties of the material (BM) at lamina level (the thermoelastic effect law extended to orthotropic material behaviour), and the strain witness (SW) theory assuming that the surface resin-rich layer behaves as a strain witness of the laminate.

Some effects are discussed in particular such as the influence of the laminate lay-up and the strong mismatch between the thermal expansion coefficients of the polymer matrix and the fibres. One of the meaningful results of the analysis is such that the thermoelastic signals is strongly affected by the fabric pattern of the outer surface lamina which, can produce regular variations in surface resin density.

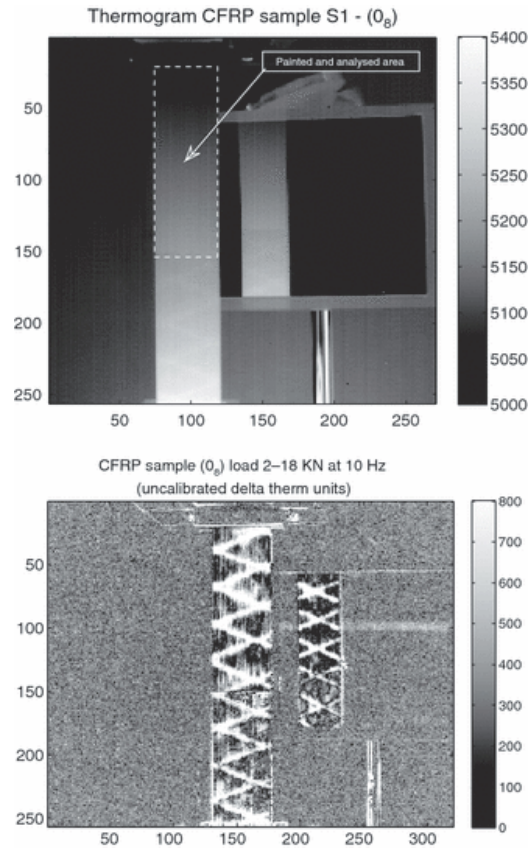


Figure 2.8. Maps of: absolute temperature on the top and at the bottom side, thermoelastic signal in uncalibrated units.

These work, highlight the necessity of an adequate experience of both the thermoelastic method and the behaviour of anisotropic materials in order to detect anomalies in the stress or strain patterns of complex structural components.

In the following chapters of the present thesis will be discussed the advances of the proposed approach for studying the behaviour of orthotropic materials. In particular, the adopted thermal approach provides more parameters which allows the assessment of more information about the incoming damage in the materials.

## 2.2 Thermal Methods

Temperature measurements have ever caught the scientific interest, even if, only in recent years since the development of more accurate infrared devices, the success of Thermography increased.

In this chapter, it will be provided an overview of thermal methods by discussing both the strong and weak points of each method.

Mostly these latter represented the scientific reason for developing the adopted approach.

In order to summarise the relevant features of each approach, Figure 2.9 is made by the intention to present the current state of the art of thermography based approaches [84-93].

The first distinction which can be made, refers to the type of the test, static or cyclic loading since it influences the results that can be obtained.

Another factor determining the results is the Thermography-based approach adopted, as reported in figure 2.9:

- measurement and monitoring of the superficial temperature [84], [89],
- evaluation of the thermal heat sources (dissipative sources evaluation) [31],
- thermal signal analysis [9], [47],
- thermoelastic sources and phase thermoelastic signal (TPA method) [39-40][42].

Each of them has been used in different contexts such as material critical energy assessment [87], fatigue limit evaluation [84][89] or dissipative heat sources evaluation [92], or plastic volume determination [22].

The major part of the approaches is based on measuring the temperature from a body under cyclic loading, but Risitano [91] for example presented a novel procedure for determining the fatigue limit of a material by performing a static test.

In the presented approach, the fatigue limit was assumed to be the point at which plastic phenomena predominate on elastic reversible ones. However, this approach requires to be calibrated for each material (ductile, brittle, biphasic.....) and does not take into account the specific microstructure behaviour.

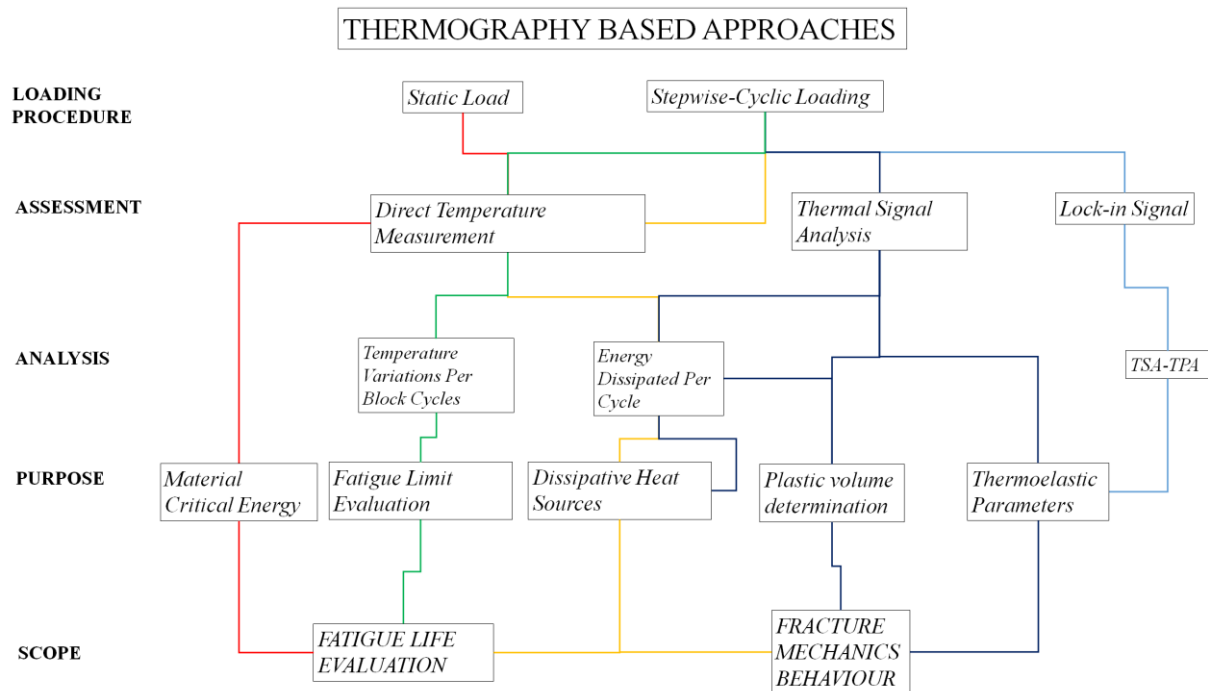


Figure 2.9. Overview of Thermography based approaches.

During the cyclic test, the temperature measurements are useful to study the thermal heat sources related to the fatigue damage of materials [85-86], and then to evaluate the fatigue limit of the material [89-90] or fracture mechanics behaviour since thermal methods can provide additional information about the position and dimension of cracks of material [58-63].

The approach involving the direct temperature measurement to evaluate the fatigue limit of materials has been developed to overcome the extremely long lasting duration of Conventional experimental campaigns. In effect, traditional methods generally used to obtain the fatigue limit in respect to thermographic techniques are dramatically time-consuming (i.e. the “Stair case method” [94] requires more than 15 specimens and 2/3 months of a hydraulic loading machine to characterize a material, compared to maximum one week needed by thermographic techniques).

The approach is based on the evaluation of the application of specific loading procedure and on the evaluation of a temperature which could be the maximum temperature achieved during the loading procedure or the temperature plateau, the related fatigue limit was calculated in graphical way.

Luong firstly [84] adopted an approach based on temperature measurements, to describe the heat production mechanism correlated to intrinsic dissipation in material. He found that by monitoring temperature variations during the test, it is possible to evaluate the dissipations and to find the fatigue limit of material by means of a graphic method.

A similar approach has been proposed by Morabito et al. [86] and Risitano and Risitano [87].

It is based on a suitable procedure in which the specimen is subjected to stress amplitudes which are gradually increased until failure. When the stress amplitude is higher than fatigue limit, surface temperature of the specimen increases and then reaches a plateau value. The fatigue limit of material can be assessed either considering the heating rate ( $DT/DN$ ) or the steady-state temperature. Both procedures involve in linear regression straight lines in order to approximate thermal data and to find the fatigue limit.

A critical issue of using temperature data is represented by the procedure to evaluate the fatigue limit, in fact, different authors [90-92] attempted to find an automatic and iterative methods. In particular, the method proposed by Curà et al., [90] tried to give more objectivity for the breakdown point assessment by choosing a trial stress value that divides data in two different series: above and below fatigue limit, respectively. The intersection of straight lines interpolating data, gives the value of beginning damage. The iteration steps are repeated until the iteration error between the two stress values mentioned (one chosen and one obtained by intersection) is minimized.

However the common denominator is such that these methods require to bring the specimen to failure. Moreover, the quality of the results of all these methods strongly depends on the number of available data with load higher than fatigue limit. This means that the result is not univocally determined.

In this field, goals of the present Thesis are represented by on the assessment of procedures:

- to smooth temperature data from any noise factors,
- to determine in an automatic and objective way the fatigue limit of the materials by using a residual static analysis.

A part from the novelty of filtering the temperature signal and determining in a more accurate way the fatigue limit, the adopted test procedure will involve NDT fatigue tests, since it is not necessary to bring the sample to failure, as will be detailed explained in further chapters. Another limit of referring to a plateau temperature [89], [95-97] as index for studying the fatigue behaviour of materials, is such that it could be not accurate since the temperature trend does not always present a plateau value [98], [99] and in this case, the described approach cannot be used anymore. This is the case, for instance, of brittle and high thermal diffusivity materials such as aluminium alloys and martensitic steels [100]. Moreover, the intrinsic heterogeneity can determine a different thermal behaviour [101-106] of the material due to the presence of internal microstructural processes associated with fatigue damage [107], as in the case of biphasic microstructure. Following these considerations, the validity of the method based on the plateau temperature measurements should be verified. One of the

goals of the present Thesis is to demonstrate that some materials do not achieve the plateau condition due to the influence of microstructure properties, in particular algorithms for assessing thermal parameters differently from plateau temperature will be proposed in further chapters.

Another approach considers a local energy determination. Different works are based on the evaluation of thermal sources to describe damage phenomena due to fatigue. These works [31][86] consider the heat diffusion equation in order to quantify and separate dissipative and thermoelastic sources. This approach requires a great deal of informatics resources and thus time-consuming analyses, this approach is physical and requires to be validated and calibrated with a wide experimental campaign providing full-field measurements. Sometimes these approaches adopt a very simplified model, as in the case of [31], that refer to 0D model too much simplified for studying the problem.

Meneghetti [99] by measuring the temperature, developed an energetic approach for quantifying the “specific thermal energy loss” during fatigue tests of AISI 304L notched and smooth specimens. “Specific thermal energy loss” is due to thermal energy dissipated per unit volume and per cycle (Q parameter). The energy released by material as heat during a dynamic test is related to temperature, and then to fatigue behaviour.

However, despite these procedures representing a valid and effective method for obtaining fatigue limit, it is important to underline that generally the measurement of thermal signal is sensitive to external thermal noise sources that could compromise the results of tests [42].

Examples of noise sources are environmental temperature and the elevated temperature of the grips of the hydraulic loading machine. The importance of these noise sources could become significant in the case of low heat sources produced by fatigue damage phenomena. This is the case of stainless steels (martensitic and precipitation hardening steels) characterized by brittle behaviour associated with low deformations, or biphasic stainless steels.

When such conditions occur, the methods used in literature to evaluate the fatigue limit could lead to ambiguous results. As in the case of determining the breakdown point of the series, in fact, some other methods propose a procedure based on linear regression of thermal data at the beginning of the test and for the last steps for which energy dissipation is clear and evident [92].

Infrared thermography was also proposed for the study of the fracture behaviour of materials subjected to fatigue loading [59][62] [107-110]. In particular, a temperature rise due to the heat dissipations can be observed around the crack tip where the plastic zone is located. In this regard, Carrascal *et al.*, [108] used IRT for evaluating the Paris Law constants of a polymer (polyamide) with an experimental methodology. A good agreement was found with



respect to traditional calculation methods. However, this procedure may find limitation in those cases in which temperature changes on material related to the plastic zone are very low (short cracks) and, moreover, high performance equipment and a difficult set-up are required. This is the case, for instance, with brittle materials (such as martensitic steels), welded joints and aluminium alloys [42].

Another approach to study the fatigue behaviour of material is represented by analysis of thermal signal [47].

In this regard, TSA represents the basis for the development of novel approaches and methods based on the assessment of surface temperature variation related to strain variation, for studying the behaviour of material.

Important are the findings in the field of fracture mechanics by using the Thermoelastic Phase Analysis [41], [76], [111-112].

In particular, by knowing the sum of the principal stresses, it is possible to determine the stress intensity factor and, at the same time, it is possible to determine the crack growth rate by analyzing the phase data [111-112]. In particular, Tomlinson et al. [59], [62], demonstrated the potential of TSA by using the amplitude of the thermoelastic signal for the crack tip and the SIF evaluation. In the previous exposed works of Diaz et al., [111] the phase signal was proposed for detecting the crack tip position. In fact, phase changes of the signal are due to high stress gradients which may be ascribed to the non-adiabatic conditions and to the plastic behaviour of the crack tip. The characteristic performance of the phase signal at the crack tip contains a double reversal of sign, notably caused by the two cited effects which have the opposite sign influence [113-114].

In the present Thesis, it will be showed a procedure for assessing in accurate way the crack tip position and then to evaluate Paris's Law in automatic way. The procedure is based on thermoelastic phase analysis determination. These results is very important for in-situ operating conditions of real components.

Not only for cracked samples but also, for smooth samples, the phase signal is also considered as an effective parameter for the identification of local damage and for the evaluation of fatigue damage in materials since it represents a parameter describing in a very local way the behaviour of material which is dissipating energy as heat [115-119].

However, by the development of TSA, other techniques and methods where studied for assessing otherwise the temperature variations in view of distinguish both reversible and irreversible heat sources.

Enke [9] attempted to separate the elastic and plastic component of thermal signal by using a Fourier Sine Series, he proposed also a model describing the temperature variations associated to dissipation in the material which run at twice the mechanical frequency, in this

case, they are not reversible heat sources and are made a different phenomenon from second order thermoelastic temperature variations previously presented. The present Thesis will be also focused on highlight the different physical meaning of temperature component at twice the mechanical frequency.

Krapez [47] firstly operated a temperature signal analysis in frequency domain so that the first and the second order signal frequency are used to describe the nonlinear signal contents in the temperature evolution, due to thermomechanical coupling phenomena and dissipative phenomena.

By using a suitable algorithm, the approach of Palumbo and Galietti [39-40] involves extracting the phase shift of thermoelastic signal in order to study the fatigue of complex shaped metals.

The limit of these approaches is such that it does not explain the physical meaning of the components of thermal signal, so that it becomes of difficult interpretation and application. However, the approaches based on the thermal signal analysis allow to extract both thermoelastic and dissipative parameters, hence, they are very useful for studying the fatigue behaviour of materials.

In the present thesis, thermal signal analysis will be used to develop an enhanced approach:

- for evaluating fatigue life of materials,
- for an in-depth explanation of the physics of the parameters
- for better processing the data,
- for studying material damage,
- for assessing the energy involved in fatigue processes.

By starting from the limit of the aforementioned techniques, the purpose of the present Thesis is firstly to unify all the theories by providing univocal physical explanation of temperature variations related to energy variation in the materials. To do this the adopted approach will involve in the thermal signal analysis, specifically focused on the assessment of phase and second order temperature variations in order to evaluate energy effectively dissipated in the material as heat, correlated to the portion of volume material which is dissipating.

The presented approach is applicable both to smooth and cracked samples, respectively for determining fatigue life or fracture mechanics propagation law or crack tip position and separating crack closure and plastic volume regions.

## Conclusions

In the present chapter the Thermoelastic Stress Analysis providing the reversible relation between the temperature and the first invariant of stress, under adiabatic conditions, is presented as very powerful technique to determine the surface behaviour of materials.

It was also presented as the signal from a lock-in amplifier contains not only the information of thermoelastic signal but also a phase information, that leads to the development of a wider theory of thermoelastic phase variations, valid somehow in case adiabatic conditions are lost to study the damage of materials. The use of phase allows more localised analysis of damage processes even if it requires a special smoothing algorithm.

After presenting the technique, have been presented the most important applications referring to cracked samples for studying the fracture mechanics behaviour and orthotropic materials such as composites.

The aim of the first part of the chapter is to show how powerful the TSA is.

In the field of experimental mechanics based on Thermography, other methods have been developed based on direct temperature measurement and analysis. Nevertheless these techniques (TSA and temperature measurements) very interesting for studying the reversible and irreversible heat sources in the materials present some limits due to the achievement of adiabatic conditions (TSA) and material-properties-dependence of temperature parameter.

These limitations represent the basis for setting up novel methods to overcome also some critical issues related:

- to better explain and relate temperature variations of different orders to physical processes,
- to filter temperature data,
- to determine the fatigue limit in accurate, objective and rapid way,
- to determine the fracture mechanics behaviour (Paris's Law, crack length..) in accurate way,
- to assess the energy dissipated as heat in the material for more accurate estimations of plastic volume dissipating during damage processes.

This last skill is very important to extend the discussion to real and complex shaped materials under operating condition loading.

The following chapter will be devoted to explain the adopted approach, by starting from the physics of the phenomena producing temperature variations running at the mechanical frequency or a multiplies of it.

The focus is to present a theory, an algorithm which includes all the thermal contributions, in order to unify the different approaches.

After it will presented the algorithms developed as well as the procedure and all the equipment and layout of machines for performing experimental campaigns.

Finally results will prove the strengthen of such an Approach.

## References

- [62] D. S. Mountain, J. M. B. Webber. Stress Pattern Analysis By Thermal Emission (SPATE). In: Proc. SPIE 0164, 4th European Electro-Optics Conf, (25 July 1979); doi: 10.1117/12.965516;
- [63] N. Harwood, W.M. Cummings. Thermoelastic Stress Analysis. Adam Hilger, Bristol, 1991.
- [64] J.C. Thompson, H. Abou el Atta. On the application of complex potentials and photoelastic data to the solution of plane problems. Journal of British Society of Strain Measurement, 11, 1975.
- [65] R. Rocca, M.B. Bever. The Thermoelastic Effect in Iron and Nickel as a Function of Temperature. Trans. Am. Inst. Mech. Eng., 188, 327-333, 1950.
- [66] M.A. Biot. Thermoelasticity and Irreversible Thermodynamics. Journal of Applied Physics, 27, 240-253, 1956.
- [67] M.E. Belgen. Infrared Radiometric Stress Instrumentation Application Study. NASA CR-1067, 1968.
- [68] S.T. Lin, J.P. Miles, R.E. Rowlands. Image enhancement and stress separation of thermoelastically measured data under random loading. Experimental Mechanics, 37, 3, 1997.
- [69] P. Stanley, W.K. Chan. Quantitative Stress Analysis by Means of the Thermoelastic Effect. Journal of Strain Analysis, 20(3), 129-137, 1985.
- [70] N.E. Enke. An Enhanced Theory for Thermographic Stress Analysis of Isotropic Metals. In: Proceedings Society of Photo-Optical Instrument. Engineers, 1084, 84-95, 1989.
- [71] G.F.C. Rogers, Y.R. Mayhew. Engineering Thermodynamics, Work and Heat Transfer, 3<sup>rd</sup> edition, Longman, London, 1980.
- [72] J.M.B. Webber. Principles of Infrared Measurements and Review of Instrumentation Techniques for Thermoelastic Stress Analysis. In: Proc. SPIE 0731, Stress Analysis by Thermoelastic Techniques, 1987; doi: [10.1117/12.937882](https://doi.org/10.1117/12.937882).
- [73] P. Stanley, W. K. Chan. Assessment And Development Of The Thermoelastic Technique For Engineering Applications : Four Years Of Progress. In: Proc. SPIE 0731, Stress Analysis by Thermoelastic Techniques, 1987, doi: 10.1117/12.937883.
- [74] J. McKelvie. Consideration Of The Surface Temperature Response To Cyclic Thermoelastic Heat Generation. In: Proc. SPIE 0731, Stress Analysis by Thermoelastic Techniques, 1987, doi: 10.1117/12.937886.

- [75] M. G. Beghi, C. E. Bottani, G. Caglioti, A. Fazzi. A Spectral Analyzer for the Thermoelastic and Thermoplastic Response of Solids to Low Frequency Dynamic Loads . In: Proc. SPIE 0731, Stress Analysis by Thermoelastic Techniques, 1987, doi: 10.1117/12.937887.
- [76] O. Breitenstein, W. Warta, M. Langenkamp. Lock-in Thermography. Second Edition. Springer, Verlag Berlin Heidelberg 2003, 2010.
- [77] R. G. Bream, B. C. Gasper, B. E. Lloyd, S. W. J. Page. The SPATE 8000 Thermo-Elastic Camera For Dynamic Stress Measurement On Nuclear Plant Components. Proc. SPIE 0731, Stress Analysis by Thermoelastic Techniques, 1987, doi: [10.1117/12.937894](https://doi.org/10.1117/12.937894).
- [78] W. N. Reynolds. T.S.A. and Thermography. In: Proc. SPIE 0731, Stress Analysis by Thermoelastic Techniques, 1987, doi: [10.1117/12.937898](https://doi.org/10.1117/12.937898).
- [79] W. Thomson, (Lord Kelvin). On the thermoelastic, thermomagnetic and pyro-electric properties of matters. *Philosophical Magazine* 5, 4–27, 1878.
- [80] A.K. Wong. Thermoelastic Stress Analysis. Reference Module in Materials Science and Materials Engineering, <https://doi.org/10.1016/B978-0-12-803581-8.03343-9>.
- [81] A.K. Wong. Stress Distribution: Analysis Using Thermoelastic Effect, Encyclopedia of Materials: Science and Technology (Second Edition), 8897-8901, 2001.
- [82] A.K. Wong, J.G. Sparrow, S.A. Dunn. On the revised theory of the thermoelastic effect. *Journal of Physics and Chemistry of Solids*, 49, 4, 394-400, 1988.
- [83] G. Pitarresi, E.A. Patterson. A review of the general theory of thermoelastic stress analysis. *Journal of Strain Analysis*, 35:35–39, 1999.
- [84] J. M. Dulieu-Smith. Alternative calibration techniques for quantitative thermoelastic stress analysis. *Strain* 31, 9–16, 1995.
- [85] J. H. Vansant. Conduction Heat Transfer Solutions. Lawrence Livermore National Laboratory, 1980.
- [86] S. Timoshenko and J. Goodier. Theory of Elasticity. McGraw-Hill, 1951.
- [87] A.K. Wong, R. Jones, and J.G. Sparrow. Thermoelastic constant or thermoelastic parameter? *Journal of Physics and Chemistry of Solids*, 48, 8, 749–753, 1987.
- [88] A. S. Machin; J. G. Sparrow; M. G. Stimson. The Thermoelastic Constant. Proc. SPIE 0731, Stress Analysis by Thermoelastic Techniques, 1987, doi: 10.1117/12.937884.
- [89] W.J. Wang , J.M. Dulieu-Barton, Q. Li. Assessment of Non-Adiabatic Behaviour in Thermoelastic Stress Analysis of Small Scale Components. *Experimental Mechanics*, 50, 449-461, 2010. DOI 10.1007/s11340-009-9249-2
- [90] M.H. Belgen. Structural stress measurements with an infrared radiometer. *ISA, Trans.*, 6, 1967.
- [91] M.H. Belgen. Infrared radiometric stress instrumentation application range study. NASA CR-1087, 1968.
- [92] T. Boulanger, A. Chrysochoos, C. Mabru, and A. Galtier. Calorimetric analysis of dissipative and thermoelastic effects associated with the fatigue behaviour of steels. *International Journal of Fatigue*, 26:221–229, 2004.

- [93] A.S. Machin, J.G. Sparrow, and Stimson M.G. Mean stress dependence of the thermoelastic constant. *Strain*, 23:27–30, 1997.
- [94] T.G. Ryall, A.K. Wong. Infrared staring arrays and digital signal processing. In *Proc. SEM Spring Conference*, 1993.
- [95] T.G. Ryall, A.K. Wong. Design of a focal-plane array thermographic system for stress analysis. *Experimental Mechanics*, pages 144–147, 1995a.
- [96] T.G. Ryall, A.K. Wong. Performance of the fast system for stress analysis. *Experimental Mechanics*, pages 148–152, 1995b.
- [97] F. Carofiglio, J.M. Dulieu-Barton, and U. Galietti. Dispositivo per la determinazione sperimentale degli stress principali attraverso la sola analisi termoelastica. In *XXXV Convegno Nazionale AIAS*, 2006.
- [98] About Lock-In Amplifiers. Technical Guide of SRS Research Systems. Website: <http://www.thinksrs.com/>. Assessed in August 25, 2017.
- [99] J. Scofield. A frequency-domain description of a lock-in amplifier. *American Journal of Physics*, 62, 2, 129–133, 1994.
- [100] Galietti, U., Palumbo, D. Application of thermal methods for characterization of steel welded joints. *EPJ Web of Conferences*, 6, 38012, 2010.
- [101] D. Palumbo, U. Galietti. Thermoelastic Phase Analysis (TPA): a new method for fatigue behaviour analysis of steels. *Fatigue and Fracture of Engineering Materials & Structures*, 00, 1-12 2016. doi: 10.1111/ffe.12511.
- [102] F.A. Diaz, E.A. Patterson, R. Tomlinson, J.R. Yates. Measuring stress intensity factor during fatigue crack growth using thermoelasticity. *Fatigue Fracture of Engineering Material and Structures* 27, 571–583, 2004.
- [103] D. Palumbo, U. Galietti. Characterization of steel welded joints by infrared thermographic methods. *Quantitative Infrared Thermography. Journal*, 11, 29–42, 2014.
- [104] J.M. Dulieu-Barton. Introduction to thermoelastic stress analysis. *Strain*, 35, 35–40, 1999.
- [105] S.A. Dunn. On the effects of through-thickness thermal conduction on stress measurement by thermoelastic techniques. *Exp. Mech.*, 33, 32–36, 1993.
- [106] S. Offerman, J.L. Beaudoin, C. Bissieux, H. Frick. Thermoelastic stress analysis under nonadiabatic conditions. *Exp. Mech.*, 37, 409–413, 1997.
- [107] T. Ummenhofer, J. Medgenberg. On the use of infrared thermography for the analysis of fatigue damage processes in welded joints. *International Journal of Fatigue*, 31, 130–137, 2009.
- [108] J.K. Krapez, D. Pacou, G. Gardette. Lock-in thermography and fatigue limit of metals. *Quantitative Infrared Thermography Journal*, 6, 277–282, 2000.
- [109] R.O. Ritchie. Mechanisms of fatigue-crack propagation in ductile and brittle solids. *International Journal of Fracture* 100, 55–83, 1999. (doi:10.1023/A:1018655917051)
- [110] J.C. Newman. A crack-closure model for predicting crack growth under aircraft spectrum loading. In *Methods and models for predicting fatigue crack growth under random loading* (eds JB Chang, CM Hudson) , 53–84. STP748. West Conshohocken, PA: ASTM, 1981.

- [111] S.Y. Lee SY, P.K. Liaw, H. Choo, R.B. Rogge. A study on fatigue crack growth behaviour subjected to a single tensile overload. Part I. An overload-induced transient crack growth micromechanism. *Acta Materialia*, 59, 485–494, 2011, doi:10.1016/j.actamat.2010.09.049.
- [112] S.Y. Lee, H. Choo, P.K. Liaw, K. An, C.R. Hubbard. A study on fatigue crack growth behavior subjected to a single tensile overload. Part II. Transfer of stress concentration and its role in overload-induced transient crack growth. *Acta Mater.* 59, 495–502, 2011, doi:10.1016/j.actamat.2010.09.048.
- [113] G.R. Irwin. Plastic zone near a crack and fracture toughness. In *Proc. 7th Sagamore Ordinance Materials Conf.*, Raquette Lake, NY, 16–19 August 1960, 63–78. New York: Syracuse University.
- [114] W. Elber. Fatigue crack closure under cyclic tension. *Engineering Fracture Mechanics*. 2, 37–45, 1970. (doi:10.1016/0013-7944(70)90028-7).
- [115] N.A. Fleck. Finite-element analysis of plasticity-induced crack closure under plane-strain conditions. *Eng. Fract. Mech.* 25, 441–449, 1986, doi:10.1016/0013-7944(86)90258-4.
- [116] Y.G. Xu, P.J. Gregson, I Sinclair. Systematic assessment and validation of compliancebased crack closure measurements in fatigue. *Mater. Sci. Eng. A* 284, 114–125, 2000, doi:10.1016/s0921-5093(00)00758-9.
- [117] P. Lopez-Crespo, P.J. Withers, F. Yusof, H. Dai, A Steuwer, J.F. Kelleher, T. Buslaps. Overload effects on fatigue crack-tip fields under plane stress conditions: surface and bulk analysis. *Fatigue Fract. Eng. Mater. Struct* 36, 75–84, 2013, doi:10.1111/j.1460-2695.2012.01670.x.
- [118] P. Lopez-Crespo, P.J. Withers, A. Kyrieleis, Y-C. Hung. Evolution of crack-bridging and crack-tip driving force during the growth of a fatigue crack in a Ti/SiC composite. *Proc. R. Soc. A* 468, 2722–2743, 2012.doi:10.1098/rspa.2012.0070.
- [119] P. Stanley, J. M. Dulieu-Smith. The determination of crack-tip parameters from thermoelastic data. *Experimental Technology* 31, 21-23, 1996.
- [120] R. A. Tomlinson, E. J. Olden. Thermoelasticity for the analysis of crack-tip stress fields—a review. *Strain* 35, 49–55, 1999.
- [121] P. Stanley, J. M. Dulieu-Smith. Progress in the thermoelastic evaluation of mixed-mode stress intensity factors. In: *Proceedings SEM Spring. Conference on Exp. Mech.*, Dearborn, 617–626, 1993.
- [122] P. Stanley, W.K. Chan. The determination of stress intensity factors and crack-tip velocities from thermoelastic infrared emissions. In: *Proceedings International Conference on Fatigue of Engineering Materials and Structures (I.Mech.E.)*, Sheffield, UK, 105–114, 1986.
- [123] R. A. Tomlinson, A. D. Nurse, E. A. Patterson. On determining stress intensity factors for mixed-mode cracks from thermoelastic data. *Fatigue Fract. Engng Mater. Struct.* 20, 217–226, 1997.
- [124] S. A. Dunn. On the effects of through-thickness thermal conduction on stress measurements by thermoelastic techniques. *Exp. Mech.* 33, 32–36, 1993.

- [125] J.R. Lesniak, D.J. Bazile, B. R. Boyce, M.J. Zickel, K.E. Cramer, C.S. Welch. Stress intensity measurement via infrared focal plane array. *Non-Traditional Methods of Sensing Stress, Strain, and Damage in Materials and Structures*. ASTM STP 1318, Philadelphia, 1997.
- [126] S.T. Lin, Z. Feng, R.E. Rowlands. Thermoelastic determination of stress intensity factors in orthotropic composites using the J-integral. *Engng Fract. Mech.* 56, 579–592, 1997.
- [127] A.D. Nurse, E.A. Patterson. Determination of predominantly mode II stress intensity factors from isochromatic data. *Fatigue Fract. Engng Mater. Struct.* 16, 1339–1353, 1993.
- [128] R. Sanford, J.W. Dally. A general method for determining mixed-mode stress intensity factors from isochromatic fringe pattern. *Engng Fract. Mech.* 11, 621–633, 1979.
- [129] W. Elber. Fatigue crack closure under cyclic tension. *Engng Fract. Mech.* 2, 37–45, 1970.
- [130] W. Elber. The significance of fatigue crack closure. *Damage Tolerance in Fatigue Aircraft Structures*. ASTM STP No.486, 230–242, 1971.
- [131] M.C. Fulton, J.M. Dulieu-Barton, P. Stanley. Improved evaluation of stress intensity factors from SPATE data. In: *Proceedings of the 11th International Conference in Experimental Mechanics*, Oxford, UK, pp. 1211–1216, 1998.
- [132] H. Batchelor, E.A. Patterson, J.R. Yates. Detection of fatigue crack closure using thermoelastic stress analysis. In: *Proceedings of the 17th International Conference on Offshore Mechanics and Arctic Engineering*, Lisbon, 1998.
- [133] DTD Handbook Handbook for Damage Tolerant Design, Section 2.2.0. Fracture Mechanics Fundamentals, website: [http://www.afgrow.net/applications/DTDHandbook/sections/page2\\_2\\_0.aspx](http://www.afgrow.net/applications/DTDHandbook/sections/page2_2_0.aspx), assessed: September 2017.
- [134] T.L. Anderson. *Fracture Mechanics Fundamentals and Applications*. Fourth Edition. CRC Press (Taylor and Francis Group), Boca-Raton, FL, 2017.
- [135] Website: [http://www.efunda.com/formulae/solid\\_mechanics/fracture\\_mechanics/fm\\_lefm\\_K.cfm](http://www.efunda.com/formulae/solid_mechanics/fracture_mechanics/fm_lefm_K.cfm). Assessed : September, 2017.
- [136] J. M. Dulieu-Smith, P. Stanley.  $\sigma_{0x}$  and its role in the determination of crack-tip isopachics. In: *Proceedings BSSM Annual Conference*, Sheffield, UK, 28–30, 1995.
- [137] F.A. Diaz, E.A. Patterson, R.A. Yates. Some improvements in the analysis of fatigue cracks using thermoelasticity. *International Journal of Fatigue* 26, 4, 365–12, 2004.
- [138] R. H. Owens. Application of the Thermoelastic Effect to Typical Aerospace Composite Materials. *Proc. SPIE 0731, Stress Analysis by Thermoelastic Techniques*, 1987, doi: 10.1117/12.937889.
- [139] R. T. Potter. Stress Analysis In Laminated Fibre Composites By Thermoelastic Emission. In: *Proc. SPIE 0731, Stress Analysis by Thermoelastic Techniques*, 1987, doi: 10.1117/12.937892.
- [140] T.R. Emery, J.K. Dulieu-Barton. Thermoelastic stress analysis of the damage mechanisms in composite materials. *Compos Part A*, 41, 1729e42, 2010



- [141] G. Pitarresi, U. Galietti. A quantitative analysis of the thermoelastic effect in CFRP composite materials. *Strain*, 46:446e59, 2010.
- [142] A.K. Wong. A non-adiabatic thermoelastic theory for composite laminates. *Journal of physics and chemistry of solids*, 52, 3, 483–494, 1987.
- [143] R.T. Potter, L.J. Greaves. The application of thermoelastic stress analysis technique to fibre composites. In *Proceedings of the Conference on Optical and Opto-electronic Applied Science and Engineering*, volume 817, pages 134–146, 1988.
- [144] R.K. Fruehmann, J.M. Dulieu-Barton, S. Quinn. Assessment of the fatigue damage evolution in woven composite materials using infra-red techniques. *Composite Science Technology* , 70, 937e46, 2010..
- [145] Luong MP. Infrared thermographic scanning of fatigue in metals. *Nucl Eng Des* 1995;158:363–73.
- [146] Meneghetti G. Analysis of the fatigue strength of a stainless steel based on the energy dissipation. *Int J Fatigue* 2007;29:81–94.
- [147] Morabito AE, Dattoma V, Galietti U. Energy-analysis of fatigue damage by thermographic technique. *Thermosense XXIV Conference*; 2002; 4710:460–467.
- [148] Risitano A, Risitano G. L'importanza del Parametro Energetico Temperatura per la Caratterizzazione Dinamica dei Materiali. *Frattura ed Integrità Strutturale* 2009;9:113–24.
- [149] Kordatos EZ, Dassios KG, Aggelis DG, Matikas TE. Rapid evaluation of the fatigue limit in composites using infrared lock in thermography and acoustic emission. *Mech Res Commun* 2013;54:14–20.
- [150] La Rosa G, Risitano A. Thermographic methodology for rapid determination of the fatigue limit of materials and mechanical components. *Int J Fatigue* 2000;22:65–73.
- [151] Curà F, Curti G, Sesana R. A new iteration method for the thermographic determination of fatigue limit in steels. *Int J Fatigue* 2005;27:453–9.
- [152] Risitano A, Risitano G. *Analisi Termica per la Valutazione del Danno negli Acciai*. Forni di Sopra: Workshop IGF; 2010.
- [153] Morabito AE, Chrysocos A, Dattoma V, Galietti U. Analysis of heat sources accompanying the fatigue of 2024 T3 aluminium alloys. *Int J Fatigue* 2007;29:977–84.
- [154] Chrysochoos A, Huon V, Jourdsan F, Muracciole JM, Peyroux R, Wattrisse B. Use of full-field digital image correlation and infrared thermography measurement for the thermomechanical analysis of material behaviour. *Strain* 2009;46:117–30.
- [155] R. Giovannozzi. *Costruzione di Macchine*. Patron Editore. 3a edizione, 2012.
- [156] G. Fargione, A. Geraci, G. La Rosa, A. Risitano. Rapid determination of the fatigue curve by the thermographic Method. *Int J Fatigue* 24, 11-19, 2002.
- [157] M.P. Luong. Infrared observation of thermomechanical couplings in solids. *Thermosense XXIV, SPIE's Aerosense 2002* 1-5 April 2002, Gaylord Palms Resort and Convention Center, Orlando, Florida USA, 2002.

- [158] A. Lipsky. Rapid Determination of the S - N Curve for Steel by means of the Thermographic Method. *Advanced Material Science Eng* 4, 1-8, 2016.
- [159] B. Yang, P.K. Liaw, M. Morrison, C.T. Liu, R.A. Buchannan, J.Y. Huang, J.Y. Huang, R.C. Kuo, J.G. Huang, D.E. Fielden. Temperature evolution during fatigue damage. *Intermetallics* 13, 419-28, 2005.
- [160] G. Meneghetti. Analysis of the fatigue strength of a stainless steel based on the energy dissipation. *Int J Fatigue* 29, 81–94, 2007.
- [161] S.S.M. Tavares, J.M. Pardal, L. Menezes, C.A.B. Menezes, C. D'Ávila. Failure analysis of PSV springs of 17-4PH stainless steel. *Engineering Failure Analysis* 16, 1757–1764, 2009.
- [162] S. Li, Y. Wang, X. Wang. Effect of ferrite content on the mechanical properties of thermal aged duplex stainless steels. *Material Science Engineering A* 625, 186-193, 2015.
- [163] N. Jia, R. Lin Peng, Y.D. Wang, S. Johansson, P.K. Liaw. Micromechanical behavior and texture evolution of duplex stainless steel studied by neutron diffraction and self-consistent modeling. *Acta Materialia* 56, 782-793, 2008.
- [164] U. Krupp, I. Alvarez-Armas. Short fatigue crack propagation during low-cycle, high cycle and very-high-cycle fatigue of duplex steel – An unified approach. *International Journal of Fatigue* 65, 78-85, 2014.
- [165] H. Knobbe, P. Starke, S. Hereñú, H.J. Christ, D. Eifler. Cyclic deformation behaviour, microstructural evolution and fatigue life of duplex steel AISI 329 LN. *International Journal of Fatigue* 80, 81-9, 2015.
- [166] U. Krupp, A. Giertler, M. Söker, H. Fu, B. Dönges, H.J. Christ, A. Husecken, U. Pietsch, C.P. Fritzen, W. Ludwig. The behaviour of short fatigue cracks during Very High Cycle Fatigue (VHCF) of duplex stainless steel. *Engineering Fracture Mechanics* 145, 197-209, 2015.
- [167] R. Dakhloui, C. Braham, A. Baczmański. Mechanical properties of phases in austeno-ferritic duplex stainless steel-Surface stresses studied by X-ray diffraction . *Material Science Engineering A* 444, 6-17, 2007.
- [168] D. Dyja, Z. Stradomski, A. Pirek. Microstructural and fracture analysis of aged cast duplex steel. *Strength Mater.* 40, 122-5, 2008.
- [169] I. Carrascal, J.A. Casado, S. Diego, R. Lacalle, S. Cicero, J.A. Álvarez. Determination of the Paris'law constants by means of infrared thermographic techniques. *Polymer Testing*, 40, 39-47, 2014.
- [170] P.R. Guduru, A.T. Zehnder, A.J. Rosakis, G. Ravichandran. Dynamic full field measurements of crack tip temperatures. *Engineering Fracture Mechanics*, 68:1535-22, 2001.
- [171] A.Y.U. Fedorova, M.V. Bannikov, O.A. Plekhov, E.V. Plekhova. Infrared thermography study of the fatigue crack propagation. *Frattura ed Integrità Strutturale*, 21, 46-58, 2012.
- [172] F.A. Diaz, E.A. Patterson, R.A. Yates. Application of thermoelastic stress analysis for the experimental evaluation of the effective stress intensity factor. *Frattura ed Integrità Strutturale*, 25. 109-8, 2013.

- [173] F.A. Diaz, E.A. Patterson, R.A. Yates. Differential Thermography Reveals Crack Tip Behaviour? In: Proc 2005 SEM Annual Conf on Exp App Mech, Society for Experimental Mechanics, 1413–6, 2005.
- [174] J. Weertman. Theory of fatigue crack growth based on a BCS crack theory with work hardening. International Journal of Fatigue, 9, 125–31, 1973.
- [175] N.W. Klingbeil. A total dissipated energy theory of fatigue crack growth in ductile solids. International Journal of Fatigue 117-12, 2003.
- [176] M. Mazari, B. Bouchouicha, M. Zemri, M. Benguediab, N. Ranganathan. Computer Material Science, 41:344–6, 2008.
- [177] P. Kucharski, G. Lesiuk, M. Szata. Description of fatigue crack growth in steel structural components using energy approach – influence of the microstructure on the FCGR. In: Fatigue failure and fracture mechanics XXVI: proceedings of the XXVI Polish National Conference on Fatigue Failure and Fracture Mechanics, (Dariusz Skibicki, ed.), AIP Publishing, 2016.
- [178] N. Ranganathan, F. Chalon, S. Meo. Some aspects of the energy based approach to fatigue crack propagation. International Journal of Fatigue 30, 1921–8, 2008.
- [179] S. Ikeda, Y. Izumi, M.E. Fine. Plastic work during fatigue crack propagation in a high strength low alloy steel and in 7050 Al alloy. Engineering Fracture Mechanics, 9, 123–6, 1977.
- [180] T.S. Gross, J. Weertman. Calorimetric measurement of the plastic work of fatigue crack propagation in 4140 steel. Metall Trans A, 13A, 2165–72, 1982.

---

## ***Chapter 3: Toward a Unified Approach: Thermographic Signal Analysis***

---

**I**n previous chapter the thermography based approaches have been presented capable to provide several indexes to study the behaviour of material under cyclic loading.

In particular the Thermoelastic Stress Analysis allows assessing the thermoelastic signal amplitude or phase shift between stress and temperature that are useful to study the fracture mechanics behaviour of the dissipative phenomena causing the loss of adiabatic conditions in the plastic zone. In this sense, the Thermoelastic Phase Analysis, based on the study of phase parameter variations is important to study in a more localised way the dissipative processes. It has been shown also that, depending on the dependence of material properties (i.e. Young modulus) to the temperature, a mean stress dependence of temperature variation arises together with a high order temperature component reversible, running at twice the mechanical frequency.

Otherwise, thermal approaches which involves the analysis of thermal signal are made to assess, not only reversible thermoelastic temperature variations but also the dissipative components. As will be shown in the present chapter, temperature can be modelled as composed by several contributions, those that are correlated to dissipative phenomena, runs at twice the mechanical frequency. Dissipative temperature variations are produced by internal heat sources related to damage and they are clearly irreversible temperature variation (different from thermoelastic high order temperature variations).

The necessity of using a novel approach is based on overcoming the issues of traditional approaches:

- High computational costs and relatively simplified adopted models (sometimes 0 dimension diffusion models),
- The one based on to assessing thermal heat sources, filters the temperature signal out of thermoelastic components,
- No relation between temperature variation and microstructures (influence of grain boundary in polycrystal or biphasic materials),
- No physics explanations of temperature variations, mostly referring to dissipative processes,

- No energetic explanation provided, for better studying and separating the typical phenomena in the crack tip region.

Moreover, by using only the temperature as parameter for studying the behaviour of material some problems arise due to high diffusivity materials in which the temperatures detected are so lower compared to the effective temperature, due to brittle materials behaving with low dissipations, and then little temperature variations. In these cases, an accurate Infrared setup is required to detect the temperature variations.

In those cases in which the frequency of loading is higher, the temperature of the body could increase dramatically, hence a system to reduce it have to be arranged.

A final consideration on temperature as parameter to study the behaviour of material is such that it is a global parameter, and as will be showed in further paragraphs, it becomes difficult to study much localised plastic processes, as in the case of fatigue damage processes.

Therefore, by starting from the weak points of previous approaches, in the present thesis, it has been developed a new approach which includes in a unique theory both thermoelastic and dissipative temperature variations under a single model has been pursued.

The model unifies also, both the components at the mechanical frequency and of higher order ( twice the mechanical frequency) and provides to relate these on energy produced in the material.

Energetic considerations are the basis of the discussion about temperature variations, in order to well explain the proposed model, the study of the energy involved in the dissipative processes comes firstly of all. This approach allows determining the dissipative heat sources which the cause of the fatigue damage phenomena.

Moreover, in the whole discussion on the physical basis of temperature variations, the influence of microstructure will be also discussed and possibly correlated to the specific temperature variation.

Each component represents a signal and will be identified as ‘parameter’ for studying a specific phenomenon.

### 3.1 Evaluation of dissipated energy $E_d$ in form of heat

The energy of a hysteresis loop provided by a cyclic excitation [1-3] is essential in order to relate the energetic contribution of the material to the residual fatigue life.

Such energy can be directly derived from the First Principle of Thermodynamics in the well-known form [4]:

$$W_p = \Delta U + Q \quad (1)$$

where  $W_p$  represents the mechanical energy per cycle and  $\Delta U$  is the internal energy due to the formation of persistent slip bands and to irreversible dislocation movements. A portion of this energy does not remain under the mechanical form but switches into heating, in particular, it contributes to the development of irreversible heat sources in the material and subsequently affects the temperature growth [5-6].  $Q$  represents the heat which flowing out from the material by convection, conduction and radiation. All quantities are expressed in unit of volume of material.

To take into account the various processes affecting the material under fatigue regime, Equation 1 can be split into several terms:

$$W_p = \oint \sigma_{ij} d\varepsilon_{ij} = \Delta U + Q = E_p + E_d + Q \quad (2)$$

The term  $E_p$  is the remaining strain energy while the last term,  $E_d$ , represents the energy per cycle dissipated as heat and related to plastic or viscous phenomena [7-8], it is strongly affected by material mechanical properties. These the portions ( $E_p + E_d$ ) of internal energy ( $\Delta U$ ) contribute to produce plastic deformations in the material.

Equation 2 shows how different phenomena could affect the energy dissipated in the hysteresis loop, and then the thermal response of specimen can be various depending on its microstructure.

For instance, let us consider a simplified bilinear model of a generic hysteresis loop, Figure 1a. In presence of a linear elastic behaviour of material (tract  $h-k$ ), all the elastic energy is recovered in one cycle by the material and no-irreversible dissipative sources are generated (the viscoelastic effects are neglected). Since plastic phenomena occur twice per loading cycle, part of the total mechanical energy is dissipated as heat, twice in a cycle during both the tensile loading ( $a-b$ ) and the compression loading ( $c-d$ ) [9-10].

Under the assumption of adiabatic conditions ( $Q=0$ ), and supposing a linear increase of the dissipated energy takes place from points  $a$  to  $b$ , and  $c$  to  $d$  of the diagram [9], the thermal contribution  $E_d$  can be assumed as increasing linearly during a loading cycle according to the curve represented in Figure 1b.

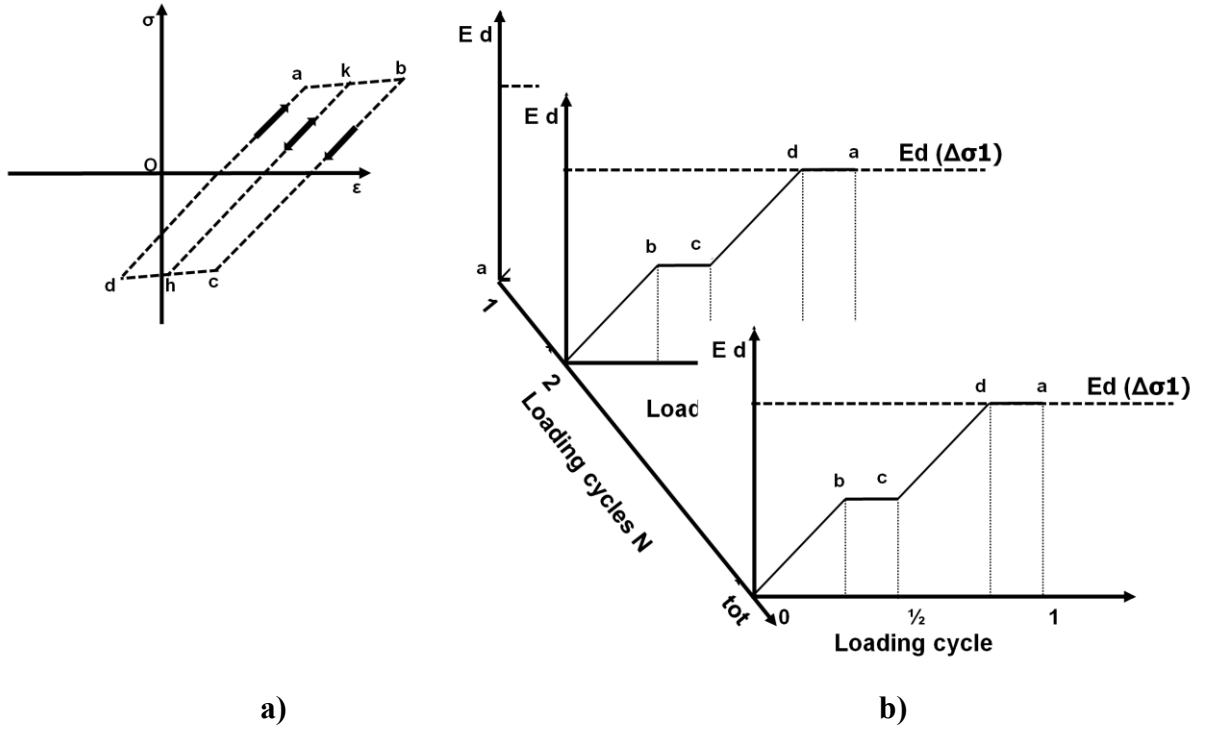


Figure 1. Energy accumulation during fatigue test: (a) correlated hysteresis loop (b) trend of  $E_d$  for the first stress level ( $\Delta\sigma_1$ ) during the loading cycle and during loading cycles of the loading block.

In particular, in figure 1b,  $E_d$  increases two times ( $a$ - $b$ ,  $c$ - $d$  trends) but it tends to achieve a fixed value, which remains constant for a generic stress level ( $\Delta\sigma_i$ , the subscript 'i' indicates the generic stress level). In fact, since the energy produced and dissipated in the material is a characteristic of each material, for a generic material it is possible to state that the energy produced in each cycle is the same for all the cycles at stress level  $\Delta\sigma_1$  (the first stress level for example):

$$E_d(\Delta\sigma_1): E_d(N_1)=E_d(N_2)=\dots\dots E_d(N_{tot}) \quad (3)$$

Where  $N_1$ ,  $N_2$ ,  $\dots\dots$ ,  $N_{tot}$ , is the Series of cycles number and generic subscript indicates the specific cycle of the series. Moreover, since  $E_d$  exists at each time of the test during the stepwise loading procedure there is an energy accumulation (both for the specific loading level and the total loading levels) which can be indicated as the correlated accumulated energy  $E_{d\_acc}$  [J],:

$$E_{d\_acc} = \int E_d(N) dN \quad (4)$$

$E_{d\_acc}$  indicates the cumulated energy, cycle after cycle for a fixed loading level.

The Figure 2 gives graphically the idea of the single energy contributions  $E_d$ ,  $E_p$  and  $Q$  in the plastic volume referring to cracked specimen (plastic volume at the crack tip-figure 2a) and smooth specimen (plastic volume in the gauge length-figure 2b).

The next level of the analysis involves the evaluation of energy dissipated which produces temperature variations of second order related to fatigue and damage processes.

Both the cases will be discussed in further chapters, but it is worth noting that the strong point of the approach is such that, as will be explained, a single mathematical algorithm allows assessing the same parameters for studying both fracture mechanics and fatigue behaviour.

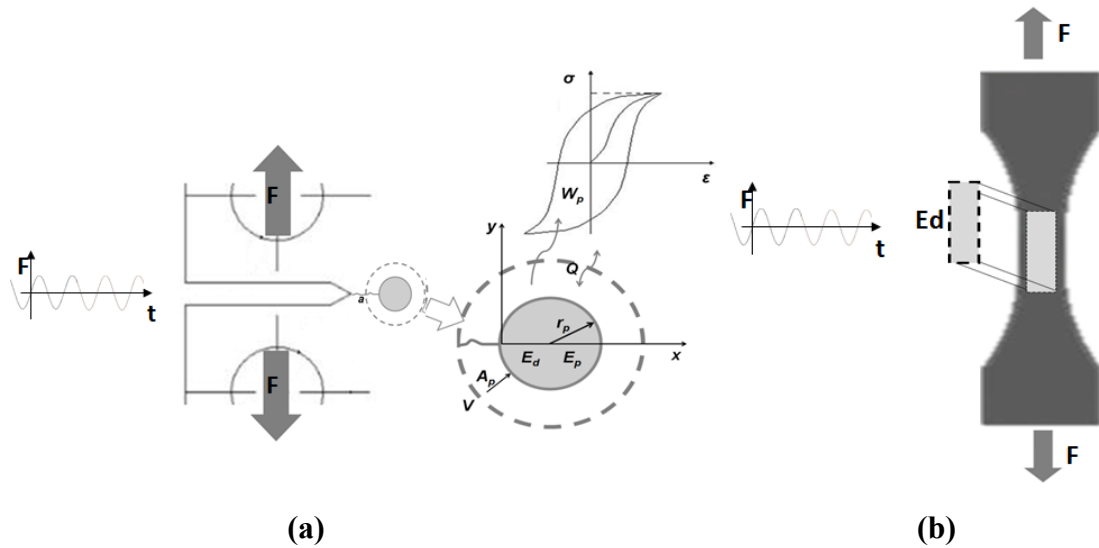


Figure 2. Energy contribution in the plastic volume (a) crack-tip of fracture mechanics samples (b) gage length of smooth samples.

In order to summarise the dissipative phenomena producing energy dissipation in the material, figure 3 provides an overview of the different processes related to the presence of hysteretic behaviour.

In particular, in case of elastic regime (no hysteresis behaviour) the heat sources present in the material are those provided by the relation between elastic properties of material and thermoelastic behaviour, the correlated temperature variation are low, and no accumulation effect is present, so that in a cycle they disappear. The heat sources present under elastic regime are those provided by the viscoelastic behaviour: the internal friction determines an



energy loss per cycle and then, until the stress is below the fatigue limit, also in this case minor thermal effect are detected depending on the specific material microstructural too [4][6].

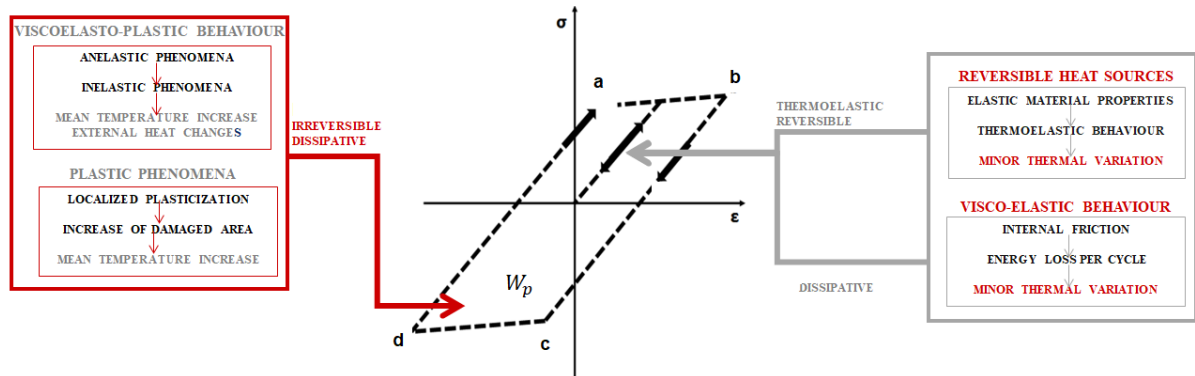


Figure 3. Overview of reversible and irreversible phenomena induced by hysteresis loop, and relative temperature variation.

When hysteresis loop is completely developed, viscoelastoplastic phenomena together with local plasticizations produce the temperature growth. The former processes determine an increase of the energy loss by the materials, while the latter involve an increase of damaged areas [8-9].

In the next paragraph, the temperature variations related to the energy production in the material will be discussed.

In particular the, as will be showed, the thermoelastic phase shift and second order temperature variations are related somewhat to these phenomena. In the following chapter the results will provide an evidence of these assumptions.

### 3.2 Temperature Changes Provided By Energy Variations

Temperature variations produced by such the energy variations are represented in figure 4. The temperature variations follow  $E_d$  behaviour, this means that the temperature, in the assumption of adiabatic conditions, will always increase and it will do so twice a cycle as already stated.

Given that energy dissipated during damage is always present during the loading cycles,  $E_d$  will always provide heat in the material. What will change during the loading step is the fact that there will be a difference of temperature that will determine heat exchange between the volume that is generating this heat and the surroundings (conduction toward part of the specimen which is not damaging, and secondly convection and radiation). It indicates that during the loading step the hypothesis of adiabatic conditions is no longer valid and so, at a certain stage, a steady state regime, Figure 4, between heat generated and heat exchanged with environment will be set and temperature will remain constant.

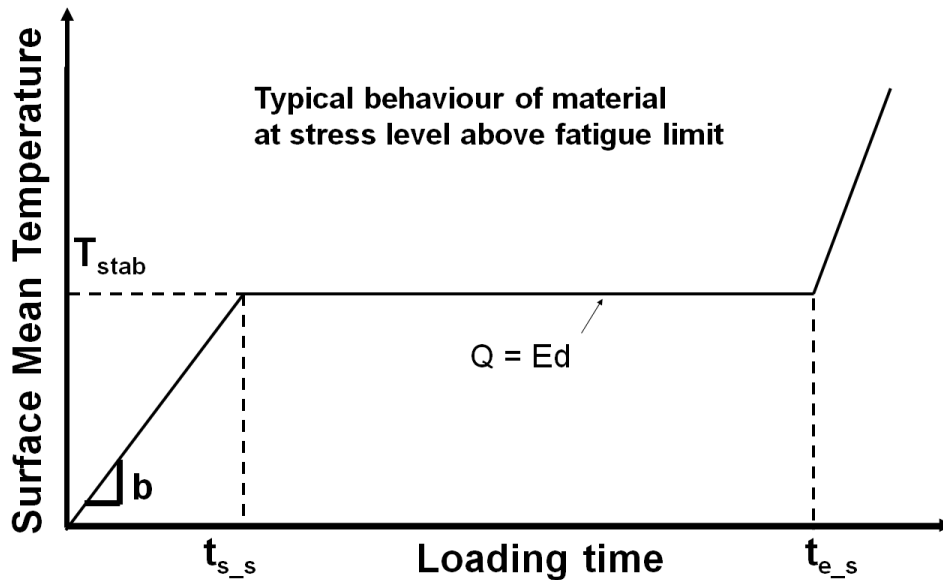


Figure 4. Typical temperature trend toward loading cycles. Rough schematic of temperature behaviour. First part in adiabatic conditions and thereafter with heat flowing out from the material.

In other words, the material acts like a tank, which accumulates energy each cycle due to intrinsic processes of the specific material and the presence of the hysteresis loop is strictly connected to the occurrence and accumulation of plastic processes which generate irreversible heat sources in the material [11-14].

The surface temperature can be used as an index correlated to the heat dissipated in the material [15-22]. In Figure 4, the typical surface temperature trend of a specimen subjected to a stress level above its fatigue limit is represented.

The first phase, from 0 to  $t_{s\_s}$ , includes the time instants after imposition of the stress. In this phase in the material dislocations are activated because of the imposed load, so that the first principle of thermodynamics is:

$$W_p = E_p + E_d = \Delta U \quad (5)$$

The duration of this phase is short [18], in fact its influence is of 5% of the total duration of the stepwise test, due to its rapidity the total amount of the heat exchanged with environment ( $Q$ ) is not significant considering the energy produced in the material by inelastic effects, since there is no time for heat exchanges. In this phase, inelastic phenomena predominate [21] and the supplied energy ( $W_p$ ) is totally converted in energy producing plastic deformations ( $E_p$ ) and energy which dissipates as heat ( $E_d$ ), hence  $Q \ll E_d + E_p$ . The increment of temperature in this phase is due to the application of the higher stress level that produces energy of plastic deformation  $E_p$  (new dislocations created and motion of existing dislocation) and heating  $E_d$ . Generally, during this stage, the plastic phenomena (inelastic [21][23-24]) dominate over other phenomena such as heat exchange, in fact even if  $Q$  exists, it is negligible, and does not appear in equation 5.

Slope  $b$  relating to the first temperature rise is assumed to be roughly constant during the test.

After some loading cycles, a temperature plateau is achieved due to the equal contribution of inelastic phenomena and thermal exchanges.

The equilibrium phase involves the most part of the test from  $t_{s\_s}$  to  $t_{e\_s}$ . At this stage, the heat flowing out from the material becomes significant compared to internal energy variations, moreover, there is time for heat exchanges with environment and possibly a steady state condition can be achieved (figure 4,  $E_d = Q$ ). When heat exchanges balance dissipative phenomena, the heat  $Q$  is equal to energy  $E_d$ , and the temperature is constant. Even the dislocation production achieves a saturation condition and the term  $E_p$  in this phase refers only to plastic deformation energy related to dislocation motion. This is mathematically described by equation 2.  $E_d$  will be produced until  $W_p$  is supplied. In all these cases,  $E_d$  is constant while  $E_{d\_acc}$  tends to increase.

The intrinsic dissipations can be estimated, generally, by detecting the surface temperature of the specimen during the test.

The temperature variations of the material associated to the  $E_d$  will be hereafter indicated as  $T_d$  while the total temperature variation in one cycle as  $\Delta T_d$ .

The direct correlation between energy dissipated per cycle and in a unit volume of material  $E_d$  and  $T_d$  is:

$$E_d = \rho c_p \Delta T_d \quad (6)$$

where  $\rho$  is the density and  $c_p$  is the specific heat at constant pressure of the material.

As previously explained, since the linear increasing of energy is found to be twice per cycle, in the material, the temperature variation due to irreversible processes of fatigue damage will occur at twice the mechanical loading frequency [25].

As explained in previous chapter,  $T_{stab}$  reported in figure 3, is the thermal index to which different authors [16][21][26] refer as parameter to study the behaviour of material, in particular fatigue behaviour and fatigue life assessment.

The relation between  $T_{stab}$  and  $T_d$  will be furtherly reported and opportunely modelled.

However, in some cases, a steady state value of temperature is not always observable or evaluable, this indicates that  $T_{stab}$  is not a robust thermal parameter for fatigue limit evaluations. The aspect of not achieving the temperature plateau will be in depth discussed in further chapters where the application of thermographic analysis will be discussed on duplex stainless steels.

Moreover, in Equation 2, thermoelastic source is not present because of its reversible nature, which provides a null contribution in one cycle. In the case of uniaxial stress with sinusoidal loading, the relative temperature variations can be expressed in frequency domain as follows:

$$T = T_{the} \sin(2\pi ft + \pi + \varphi) \quad (7)$$

where  $T_{the}$  are the temperature variations running at the mechanical exciting frequency  $f$  and  $\varphi$  is the phase angle between temperature and loading signal. The  $\pi$  sign has been included in order to preserve the ‘thermoelastic’ phase shift between temperature and stress invariant. The assessed  $\varphi$  depends on several factors, for instance in linear elastic and adiabatic conditions, the phase shift represents the lag between the temperature and the first stress invariant, which is fixed, (0 or  $\pi$ ) depending on the sign of the first stress invariant. However, the measured phase shift  $\varphi$  can change in presence of viscous phenomena that lead to the loss of adiabatic conditions. Dissipation always present in the lattice, involves heating in the form of two distinct contributions:

- heat produced under the hysteresis conditions (viscoelastic regime) [21][27],
- heat produced under the static hysteresis conditions (plastic deformations regime) [28],

In order to understand the causes of variation of phase signal,  $\varphi$ , let us consider the curves of strain/stress/and thermoelastic temperature as sinusoidal waveforms (Figures 5) for the sake of simplicity.

The analysis involves three physical cases:

- 1- perfect linear elastic behaviour Figure 5a,
- 2- theoretical viscous behaviour Figure 5b,
- 3- viscos-plastic behaviour with material damage Figure 5c.

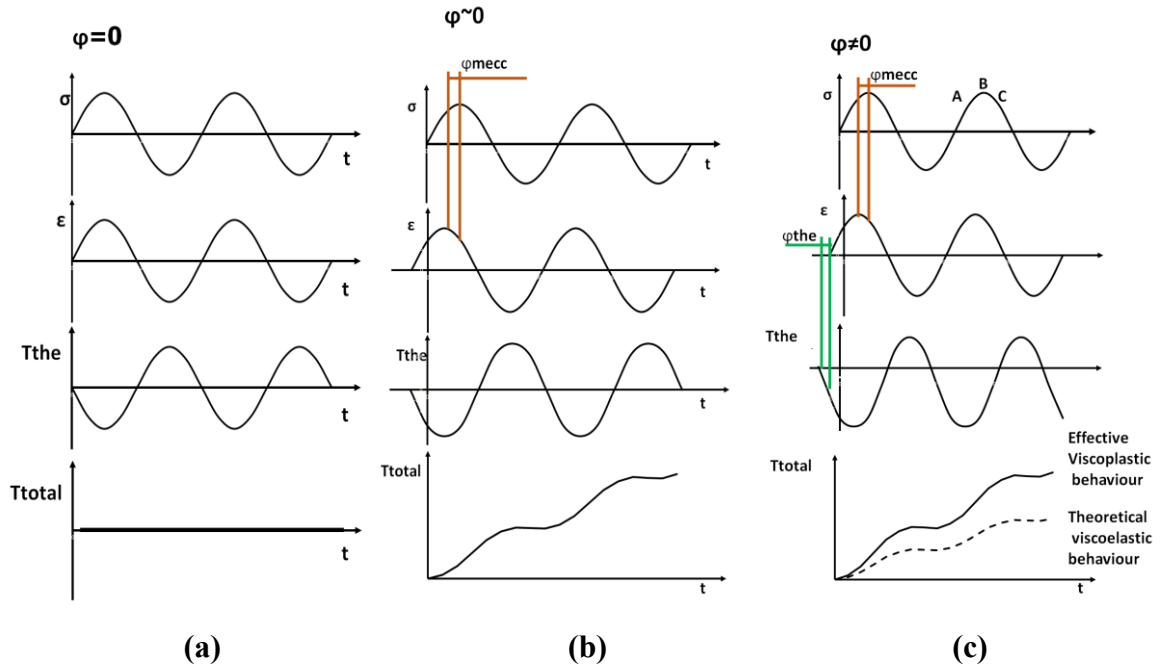


Figure 5. Graphical representation of phase shift: (a) elastic conditions, (b) theoretical viscos-elastic conditions (c) viscos-plastic behaviour.

Generally, what is directly measureable is the strain  $\epsilon$ , while the stress  $\sigma$  is a derived quantity. Under the assumption of perfect elastic behaviour (absence of dumping and plastic phenomena),  $\epsilon$  and  $\sigma$  can be supposed as in-phase signals, and the only phase shift present, is  $\pi$  (positive sign of the first stress invariant of Eq. 7), Figure 5a. In Figure 5a, the behaviour of the total temperature  $T_{total}$  is also reported, which is zero since the thermoelastic component of the temperature  $T_{the}$  provides a total zero temperature increase (integral to the cycle equal to zero). Under theoretical viscous-elastic conditions, Figure 5b, the dumping behaviour must be considered in the analysis. In fact, the phase shift  $\varphi_{mecc}$  is caused by hysteresis loop.

However, in theoretical viscous regime, if the frequency and the heating produced do not affect adiabatic conditions (this hypothesis is true especially of high diffusivity materials [29]) in fact, temperature  $T_{the}$  follows the strain behaviour, Figure 5b, and the heating produced in viscous conditions also involves the increment of total temperature  $T_{total}$ .

If visco-plastic behaviour occurs, Figure 5c, there is a joint effect on intrinsic material heating due to both dynamic dumping and plastic phenomena. These phenomena give rise to significant conduction heat exchanges through the sample.

Such heating involves the loss of adiabatic conditions and it contributes to the phase lag  $\varphi_{the}$ , between assessed temperature and thermoelastic temperature. In this case, the  $T_{total}$  tends to increase with a more severe slope change than the increase in viscos-elastic regime, due to the quantity of heat dissipated in the material.

Viscos-plastic behaviour can be described differently: when the stress approaches a point near the maximum B (point A Figure 5c), the dissipative phenomena rise ( $\epsilon$  and  $T_{the}$  are rising) and persist until the stress reaches point 'C' where the material is supposed to achieve an internal equilibrium (microstructure rearrangement processes are arrested and all the energy remains stored) [26]. Even if the stress is lower than previous values (points A and B), phase shifts are present ( $\varphi_{mecc}$  and  $\varphi_{the}$ ), and the material acts like a tank which accumulates the energy.

The assessed phase shift depends on internal phenomena but also on external factors such as:

- non perfect homogeneity of surface coating
- geometric surface imperfections
- electronic noise of hardware.

### **3.3 The Components Of Thermal Signal: The Temperature Model**

In paragraph 3.1, it has been shown how the heat dissipation increases twice per cycle with a typical trend in the case of adiabatic conditions ( $Q=0$ ). In order to estimate the heat dissipated, it is necessary to detect the surface temperature of the specimen during the test. The temperature variations of the material associated with the  $E_d$  will be hereafter indicated as  $T_d$  while the total temperature variation in one cycle as  $\Delta T_d$  (Figure 6). In fact, since the linear increasing of energy is found as twice per cycle, in the material, the temperature variation due to irreversible processes of fatigue damage will occur at twice the mechanical loading frequency [9].

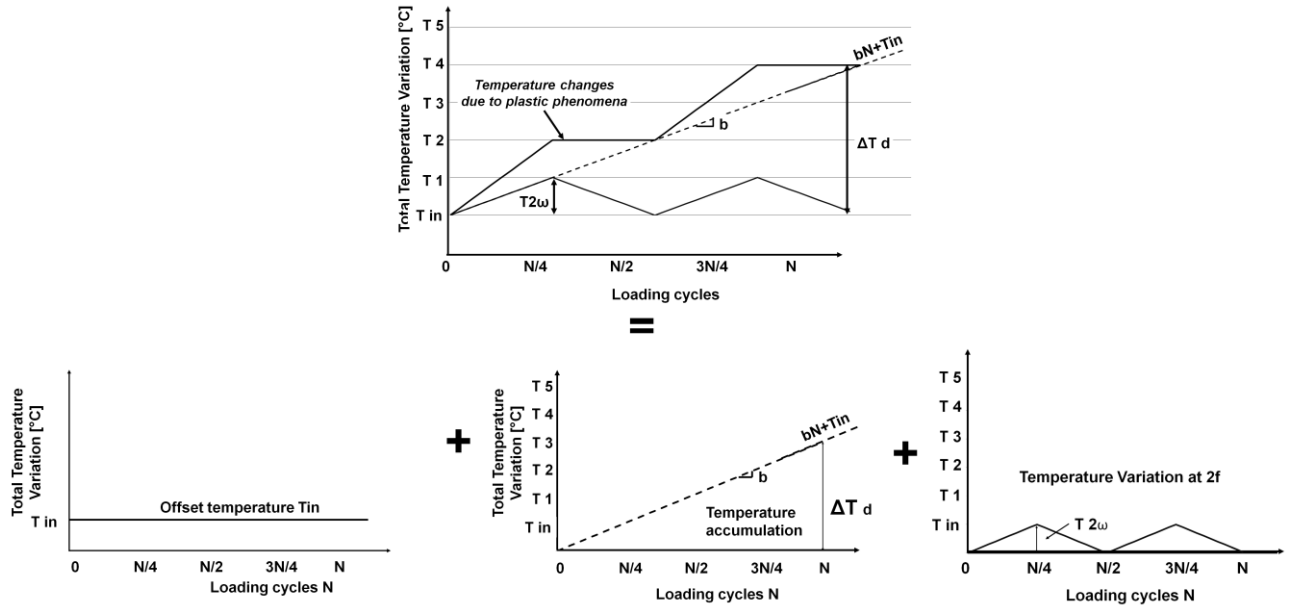


Figure 6. Temperature variations due to heat dissipated during a loading cycle in the case of adiabatic conditions.

Figure 6 shows the temperature variations due to the heat dissipated during a loading cycle in the event that heat exchange by conduction, convection and radiation are null ( $Q=0$ ). It is easy to prove that the  $T_d$  trend can be decomposed as:

- an offset temperature ( $T_{in}$ ), supposed to be constant in a loading cycle and in general, this assumption is valid for the duration of the test at fixed loading level.  $T_{in}$  represents the temperature of the body when the cycle starts,
- a linear temperature increasing, with slope  $b$  over the number of cycles [11],
- a periodic temperature variation with amplitude  $T_{2\omega}$  and period equal to  $(1/2)N$ .

Moreover, the total temperature variation  $\Delta T_d$  and the temperature amplitude  $T_{2\omega}$  are related as depicted in Figure 7.

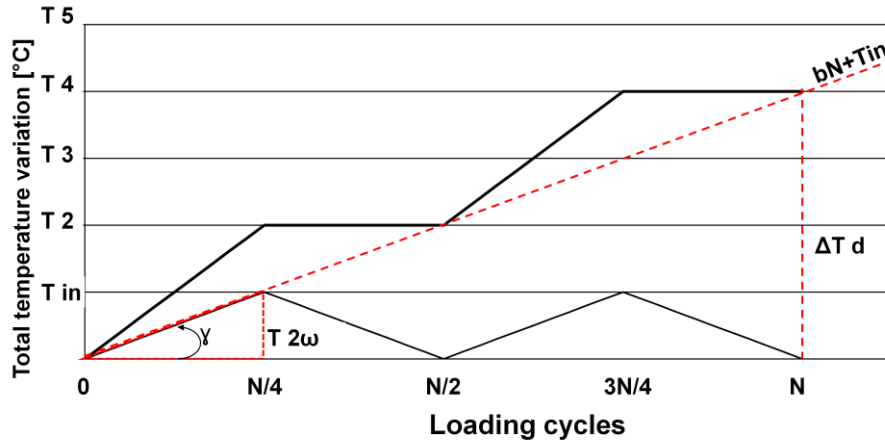


Figure 7. Geometrical relation between the total temperature variation ( $\Delta T_d$ ) and the temperature amplitude at twice the loading frequency ( $T_{2\omega}$ ).

The relation is described by Equation 8:

$$\gamma = \arctg(T_{2\omega}/(N/4)) = \arctg(\Delta T_d / N) \quad (8)$$

and then:

$$4T_{2\omega} = \Delta T_d \quad (9)$$

$T_{2\omega}$  can be obtained by assuming that the relative thermal signal component is a triangular function pulsating at  $\omega_0=2\omega=2(2\pi f)$  and it can be expanded as the sum of cosine function terms:

$$T(t) = T_{2\omega}/2 - A \sum_1^{\infty} ([1/(2n+1)^2] \cos(2n-1)\omega_0 t) \quad (10)$$

with

$$A = 4T_{2\omega}/9\pi^2 \quad (11)$$

Excluding high order components, for  $n=1$ :

$$T(t) = [T_{2\omega}/2] - A \cos(2\omega t) \quad (12)$$

Equation 12, shows how the amplitude of the cosine term is directly related to  $\Delta T_d$ . In other



words, it is possible to obtain  $\Delta T_d$ , by measuring the thermal signal component that occurs at twice the mechanical frequency,  $T_{2\omega}$ .

$$\Delta T_d = 4T_{2\omega} = 4(9\pi^2 / 4)A = 9\pi^2 A \quad (13)$$

Generally, by simply assessing slope  $b$  or the amplitude  $T_{2\omega}$  the term  $E_d$  is fully determined. Moreover, the term  $T_{2\omega}/2$  in equation 12, will be included in the linear part of temperature variation.

It follows that the assessment of temperature signal plays a determining role in the study of fatigue behaviour of material.

In the frequency domain the adopted model which in part refers to [10], is represented by Equation 14:

$$T(t) = T_0 + bt + T_{the} \sin(\omega t + \pi + \varphi) + A \cos(2\omega t + \psi) \quad (14)$$

Where ‘ $T_0 + bt$ ’ represent the linear part of temperature increase, this offset temperature include also the offset of second order temperature variations ( $T_{2\omega}/2$ ), and ‘ $\psi$ ’ is the phase signal of the temperature component at the twice the loading frequency.

However, it possible also to refer to the thermal uncalibrated signal, not to the temperature directly measured, in case the purpose is to assess the variation of the indexes, that are significant when damage conditions occur. In this case, a signal calibration is not influent on results.

Consequently, Equation 14 can be rewritten as:

$$S(t) = S_0 + bt + S_{the} \sin(\omega t + \varphi) + S_d \cos(2\omega t + \psi) \quad (15)$$

where ‘ $S$ ’ is the uncalibrated thermal signal and ‘ $S_0$ ’, ‘ $S_{the}$ ’, ‘ $S_d$ ’ and ‘ $\varphi$ ’ are the four indexes considered in this work to study the fatigue behaviour of material. These indexes are related respectively to: the linear part of temperature increase, the amplitude of thermoelastic signal, dissipative sources and the phase of signal ‘ $S$ ’ at the frequency ‘ $f$ ’.

The model presented, clearly describes the temperature signal of a single pixel of the scientific scenario as represented by figure 8.

In particular in figure 8, the portion of the gauge length investigated by means of an InfraRed detector, can be though as a pixels matrix, for each pixels the temperature evolution can be describe using the 14 or 15. Hence, for the gauge length behaviour can be described by a

parameter pixel matrix.

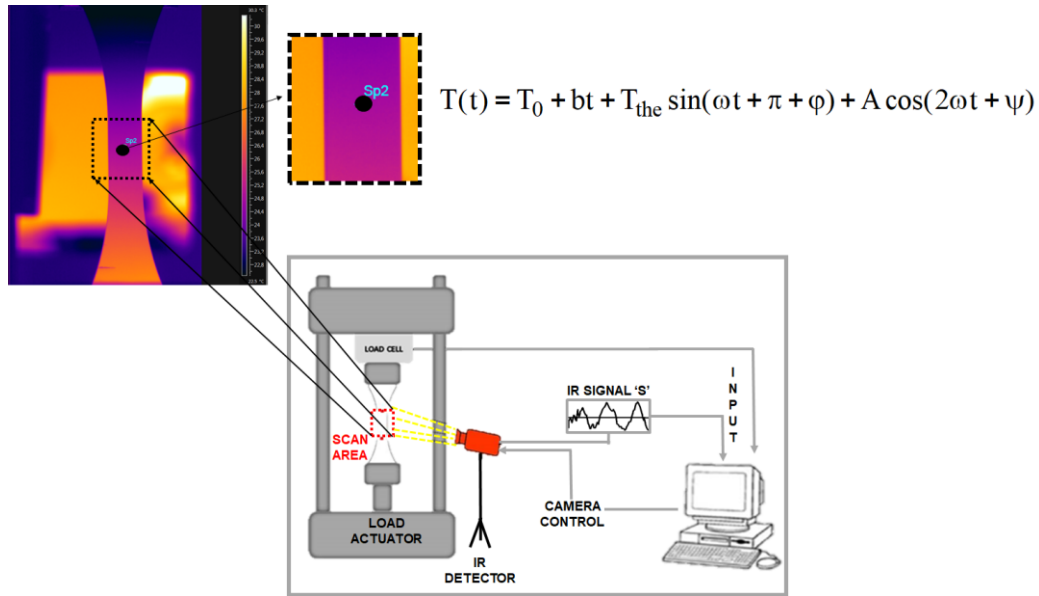


Figure. 8 Graphical understanding of the scanned area and pixel by pixel temperature variations.

Where clearly the term  $A$  in figure 8 is proportional to  $T_{2\omega}$  or  $T_d$ .

In the following paragraph 3.5, it will be presented the method for assessing the components of thermal signal.

It is worth noting that from a single data acquisition, single data analysis all the component of temperature can be assessed, and then the generic fatigue process can be entirely described.

Before discussing the adopted algorithms and procedure for quantitatively studying the thermal variations, it is necessary to show the experimental campaign from preliminary tests to the procedure adopted and machine setups.

### 3.4 Experimental Campaign

In this paragraph, it will be shown firstly the preliminary considerations for performing the fatigue experimental campaign such as the emissivity tests, after all the tested material and geometries will be presented together with the specific test procedure (self-heating) which involves imposing stress in different regimes (from elastic to plastic). For each material a specific loading table, has been then designed.

Finally, the geometries, the machines and layout of the laboratory is presented.

### 3.4.1 Emissivity

Emissivity is one of the most important concerns related to the application of InfraRed Thermography, as discussed in Chapter 1, this is because, before the testing had been necessary to set up a preliminary characterisation of the coating before choosing the best coating for the surface of samples in order to maximise the radiation detected.

The matt black spray have been evaluated under two point of views :

- by using a stimulated NDT technique,
- by using the thermoelastic signal and phase shift.

In order to realise the stimulated technique it has been adopted a 500 Watt lamp while. The purpose of the analysis was to investigate the emissive behaviour in order to assess the spray providing the maximum emissive efficiency. TSA tests were adopted for studying elastic properties in order to eliminate or reduce the risk of coating failure. TSA tests involve a cyclic loading test at different frequencies.

Figure 9, presents the overall experiments addressed to study the emission behaviour of coating.

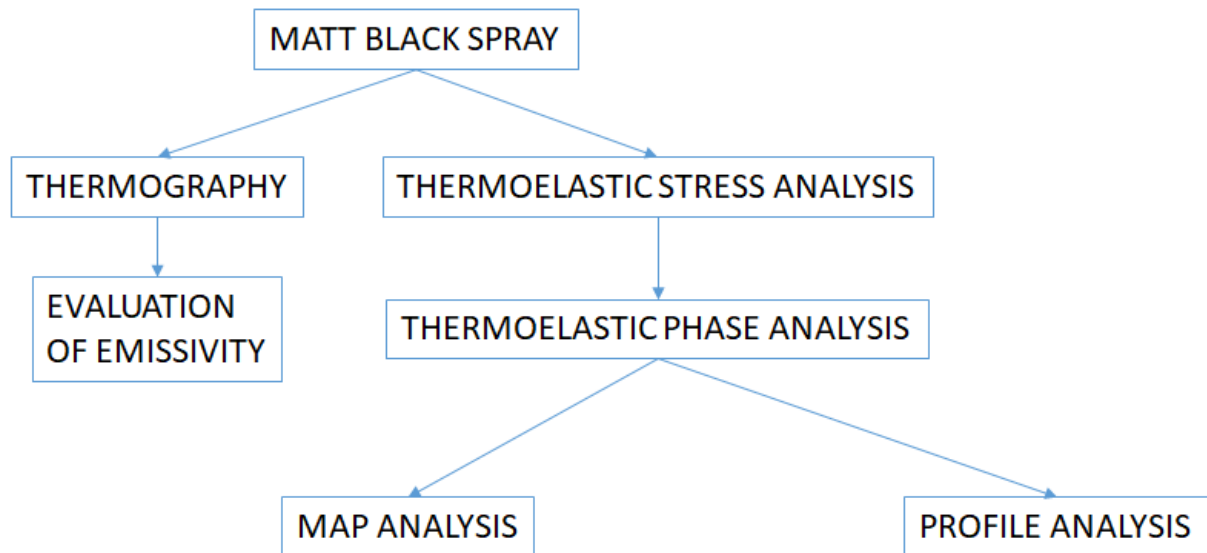


Figure. 9. Scheme of the coating behaviour investigations.

The tested coatings were:

1. LUXENS DECO
2. DUPI COLOR ECOPLUS
3. THERMO 800°C SPECIAL

#### 4. SOLCOLOR

All the coating were sprayed on stainless steel sample, with known thermal properties.

Referring to the first test procedure for evaluating the emissivity from coated surface, the four different coating have been sprayed on surface in different zones, as depicted in figure 10.

In figure 10, the first area of sample is coated with the first coating, in the second area are present the second coating together with electrical tape, and the remaining areas, have been coated respectively coating 3 and 4.

The following measurements have to be performed:

- Room temperature
- Relative Umidity
- Distances from detector
- Reflected Temperature

All these quantities are reported in table 2.

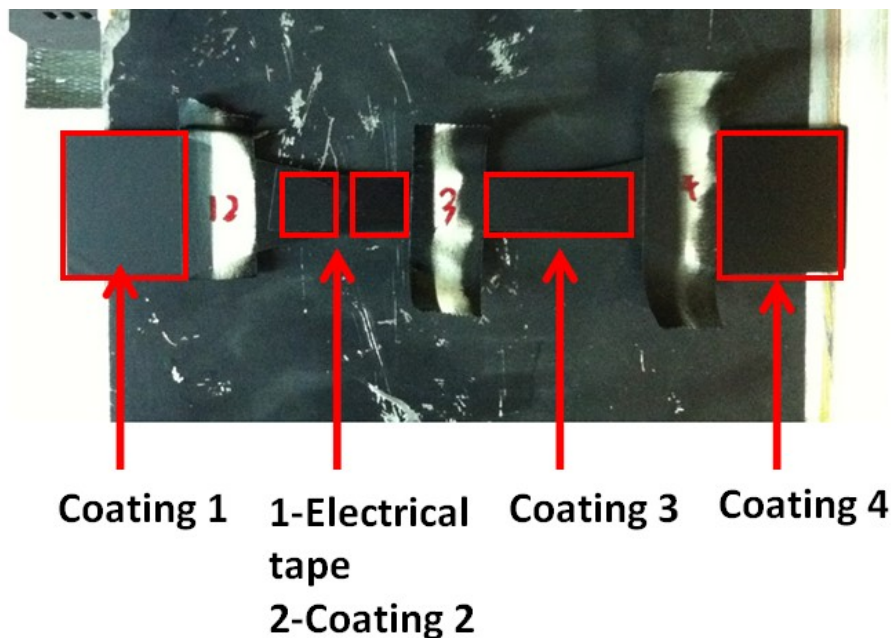


Figure 10. Layout of coating on metallic sample.

Room Temperature	Relative Umidity	Reflected Temperature	Distances
20,6 °C	50%	21,2 °C	660 mm

Table 2. Measured parameters for emission evaluations.

The evaluation of the reflected temperature requires a specific Standard procedure ASTM 1862-97 [30], it can be performed by overlapping an extremely reflective body on the material, such as a thin aluminium lamina. By setting the emissivity on maximum value, on Software providing thermal measurements, and by measuring the temperature in an area of the sample, after heating it, it can be read directly on the Software Flir the value of temperature of the area. This is the value of reflected temperature.

In particular, the sample has been heated by using a 500 W lamp, after the thermal stabilisation has been achieved in each zone, the temperature has been evaluated by using the function «Emissivity Calculation» of Thermacam, the emissivity of each zone has been assessed.

The third coating (Thermo 800°C Special) is the most emissive at 80°C. The emissivities for each zone are repoted in table III.

Coating	emissivity (80°C)
1	0,869
2	0,871
<b>3</b>	<b>0,934</b>
4	0,865

Table III. Coating Emissivities.

From the TSA point of view two samples of stainless steels have been coated with four coatings, figure 11. Each side of the sample have been coated. Moreove the influence of the operators (R and F) has been investigated.

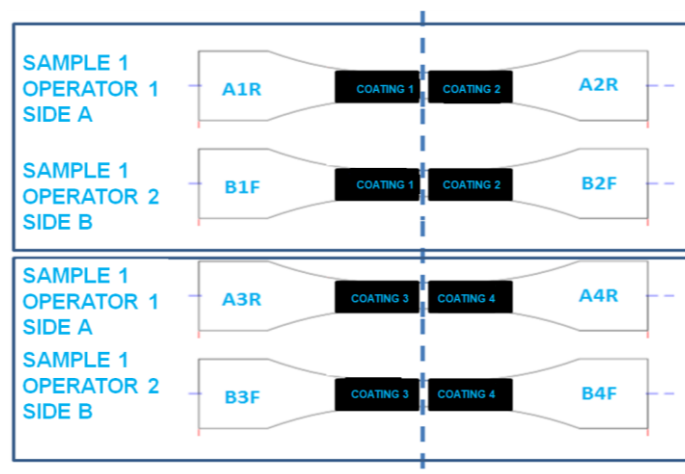


Figure 11. Layout of coating on metallic samples for TSA measurements.

Both the sides of the samples have been investigated by using two microbolometric thermal cameras whose the laboratory is equipped. Referring to the specification of the detectors in the last paragraph 3.4.5 of the present chapter will be provided all the specifications.

The tests have been performed with two input parameters:

1. Constant amplitude and variable frequency (7, 13 e 17 Hz)
2. Variable amplitude and constant frequency (17 Hz)

Loading table is reported in figure 12. The adopted loading ratio is 0.5, each load is progressively applied.

LOADING STEP	$\Delta\sigma/2$ [MPa]	$\Delta\sigma$ [MPa]	$R = \frac{\sigma_{min}}{\sigma_{max}}$	$\sigma_{min}$ [MPa]	$\sigma_{max}$ [MPa]
1	45	90	0,5	90	180
2	75	150	0,5	150	300
3	100	200	0,5	200	400
4	125	250	0,5	250	500
5	150	300	0,5	300	600
6	175	350	0,5	350	700
7	200	400	0,5	400	800
8	225	450	0,5	450	900

Figure 12. Loading table for thermoelastic coating evaluations.

The loading levels are eight, for each load configuration Sono stati realizzati 8 step di carico per realizzare le prove a carico variabile. The thermographic acquisitions have been performed just for loading levels 1, 3 and 7 at different loading frequencies. The thermographic sequence acquired lasts two minutes and it is acquired roughly 30 second after the variation of stress or frequency.

Figure 13 shows, for sample 1, a vertical profile (red) which refers to longitudinal direction in the two zone of a side of the sample coated by operator 1 and 2, at a fixed stress level 1 and frequency of 7 Hz, the maximum load imposed is 8 N.

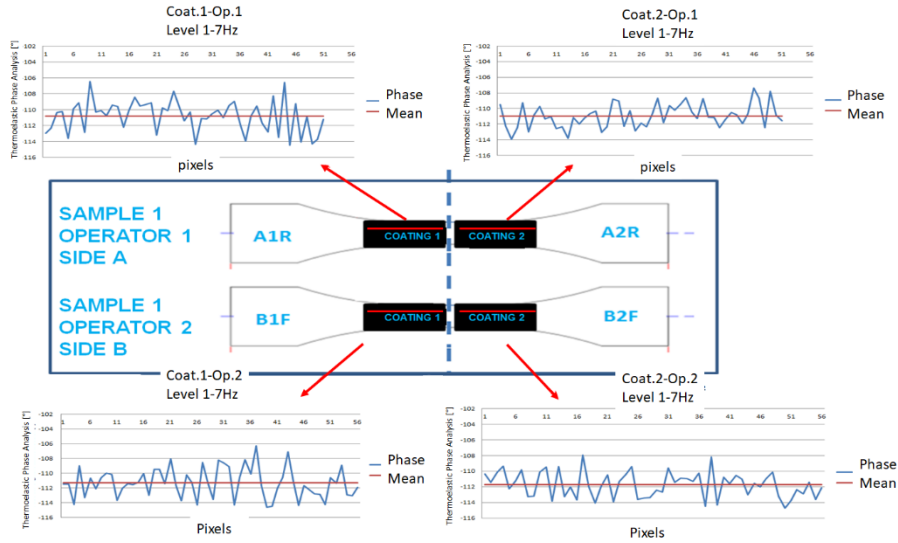


Figure 13. Results of phase signal for sample 1, coating 1 and 2.

Figure 14 shows, for sample 2, a vertical profile (red) which refers to longitudinal direction in the two zone of a side of the sample coated by operator 1 and 2, at a fixed stress level 1 and frequency of 7 Hz, the maximum load imposed is 8 N.

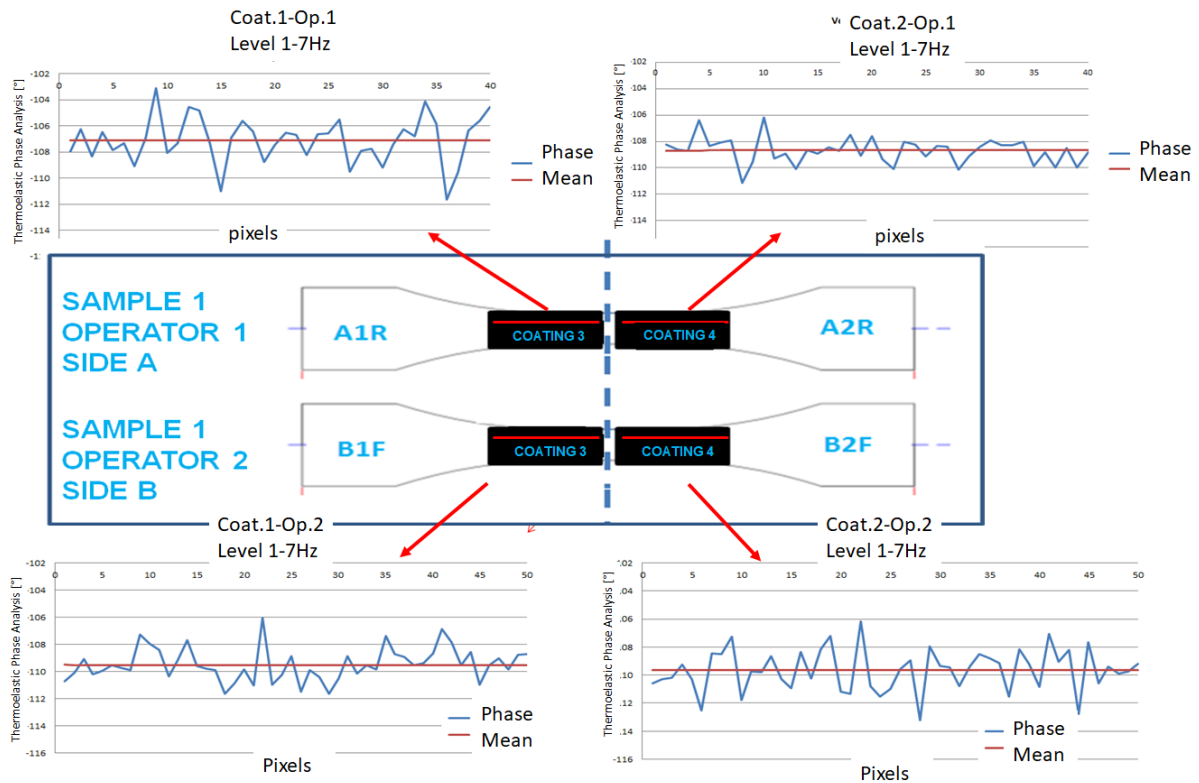


Figure 14. Results of phase signal for sample 2, coating 3 and 4.

In figures 13 and 14 are reported for each profile the relative phase signal and mean value. As it is possible to see the dispersion of the data with respect to the mean value is roughly the same for each operators and coatings.

So that, the phase signal appears to be not influenced by the operator 'expertise'.

The figure 15 shows the results in terms of standard deviation for all loading configurations

(loading levels), two operators at 17 Hz. As it is possible to see, the data scattering is generally higher at low stress level and it tends to reduce at relatively high stress values, all the coatings behaves roughly in a similar way for all the loading conditions.

It is interestingly to observe the results for different loading frequencies, figure 16. In particular, for operator 1 it seems that the data scattering between the different coatings of phase data reduced with the increasing of the loading frequency while for operator 2 the data scatter is higher mostly at lower and higher loading frequency.

However, the standard deviation of the data is roughly of  $1^\circ$  referring to the worst conditions, it is possible to conclude that from thermoealstic point of view, the coatings behave in the same way, and then all the coatings are efficient. The matt black chosen is the number 3 (**THERMO 800°C SPECIAL**), since it exhibits higher value of emissivity in comparison with the others.

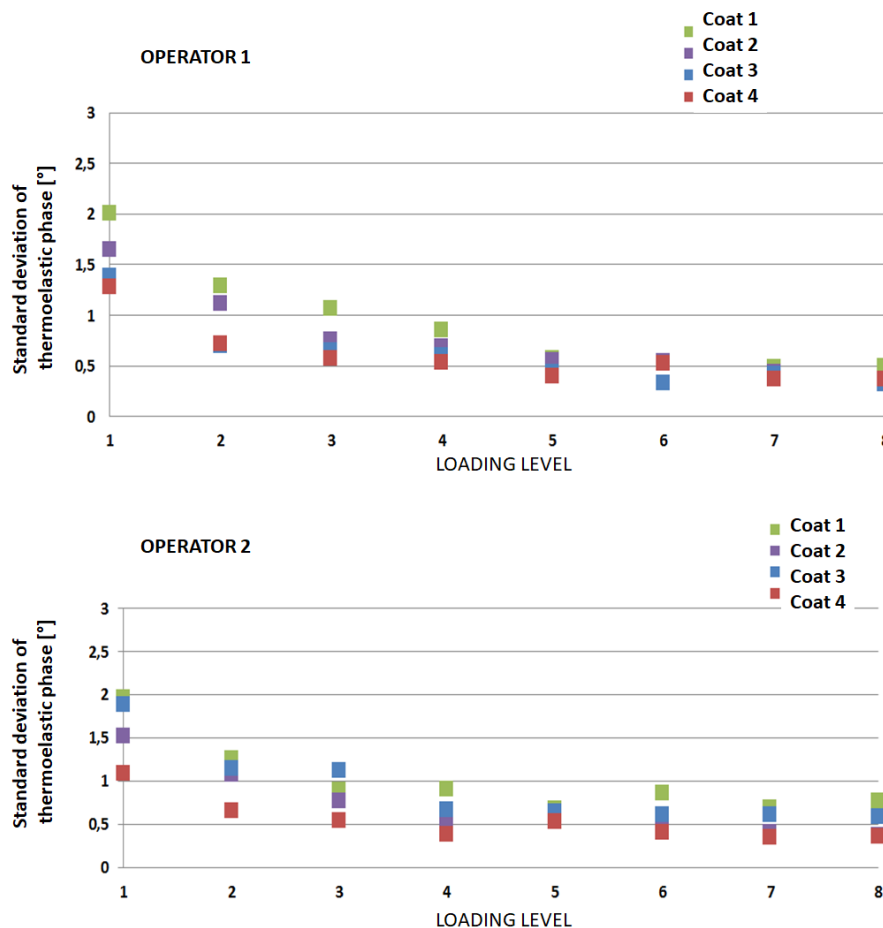


Figure 15. thermoelastic phase shift standard deviations for two operator at 17 Hz and different loading levels.



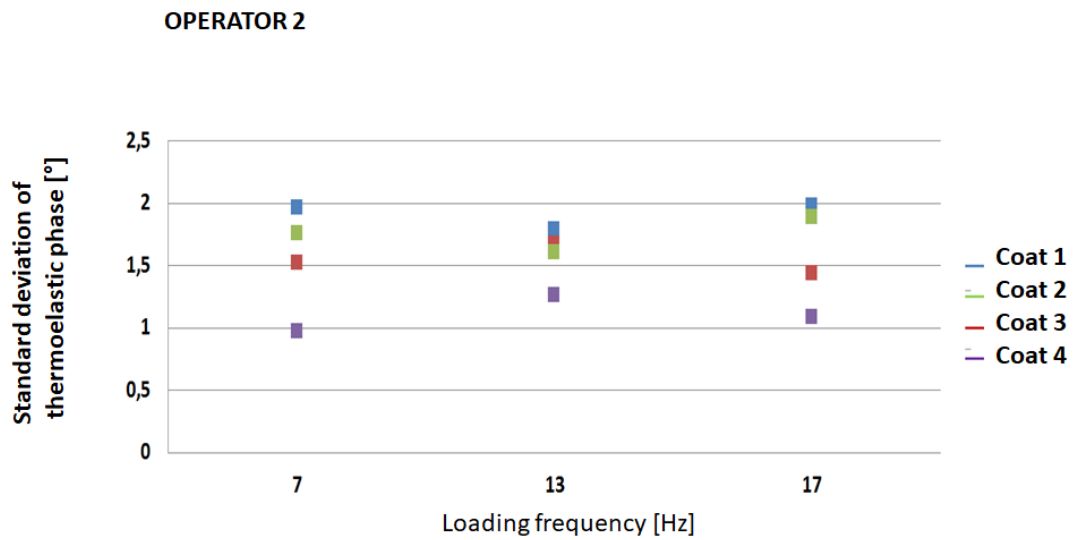
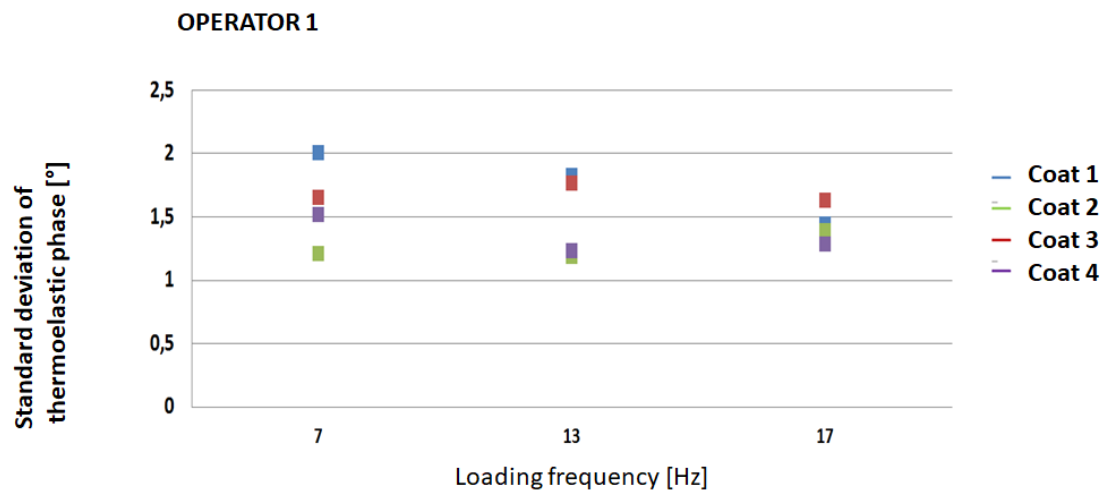


Figure 16. Thermoelastic phase shift standard deviations for two operator at stress level 1 and different frequencies.

### 3.4.2 Materials

In this section, all the metallic materials tested adopted for fatigue tests will be presented, in particular in this section the attention will be focused on metallic ferrous alloys.

The martensitic stainless steels are:

- X4 Cr Ni Mo 16–5–1,
- AISI 422
- ASTM A 182 grade F6NM
- 17-4PH

The latter is a precipitation hardening type martensitic stainless steels with a higher mechanical strength obtained by a quenching heat treatment but limited corrosion resistance. In X4 Cr Ni Mo 16–5–1 ( $\sigma_{UTS} = 850$  MPa [31]) and ASTM A 182 grade F6NM the addition of Chromium (11–16% in weight) allows for improvement of corrosion resistance through the formation of oxides, and it also allows for avoidance of the depleting of Chrome from lattice [31-33].

In particular, ASTM A182 grade F6NM is a low carbon Chromium Nickel steel, exploited mostly in the Gas & Oil field due to its higher mechanical strength properties and corrosion resistance. The metallurgy of this material is complex: low carbon content associated with the addition of nominally 4% nickel, allows for the formation of martensitic lath after tempering results in an improvement of mechanical properties [34-35]. The composition, as well as the mechanical properties, are listed in TableS IV-V.

In AISI 422 (Table IV-V) the percentage of chromium is 10–13% in weight, and moreover, the presence of W, V and Mo alloys in the lattice, favourites the complex carbide precipitation. So, this steel can be tempered at a relatively high temperature (650 °C) without having chromium depletion of the lattice. It is a standard type of martensitic stainless steel [32].

17–4 PH is a typical martensitic precipitation hardening stainless steel. By applying suitable heat treatments, a wide range of mechanical properties can be obtained [33], mechanical properties and compositions are reported in table IV and V. 17-4 PH adopted in a centrifugal compressor for rotor and stator parts, exhibits specific reference to stress corrosion cracking resistance but is susceptible to chloride [34].

Another alloy adopted is the X4CrNiMo16-5-1( $\sigma_{UTS} = 850$  MPa) [36] that is forged martensitic steel are employed in the industrial fields operating within a corrosive

environment.

The tested stainless steels have also an austenitic lattice: AISI 316 (CF8M) and AISI 316L (CF3M). The peculiarity of austenitic steels is such that the corrosion resistance is higher to the higher percentage of chromium. In Tables V and VI, the chemical composition and the mechanical properties of the stainless steel tested are presented [31-37].

elements %wt / alloy	C	P	Si	Ni	V	Mn	Cr	S	Mo	W	Cu
AISI 422	0.2-0.25	0.025	0.40	0.5-1.0	0.15-0.30	1.0	10-13	0.025	0.75-1.25	0.75-1.25	-
CF3M	0.03	0.015	1.0	10-14	-	2.0	10-18	0.03	2.0-3.0	-	-
CF8M	0.08	0.015	1.0	10-14	-	2.0	14-18	0.03	2.0-3.0	-	-
ASTM A 182	0.05	0.03	0.6	3.5-5.5	-	0.5-1.0	11-14	0.03	0.5-1.0	-	-
17-4PH	<= 0.080	-	<1.0	3.0-5.0	-	<1.0	15.5-17.5	<0.04	2.0-2.5		3.0-5.0

Table IV. Components of alloys.

Material	Young Modulus (MPa)	$\sigma_{\text{yield}}$ [MPa]	$\sigma_{\text{UTS}}$ [MPa]
AISI 422	200	760	966
CF3M	200	275	586
CF8M	200	275	551
ASTM A 182	200	517	655
17-4PH	206	884	975

Table V. mechanical properties of materials.

All the presented stainless steels are monophasic steels.

These materials exhibit good mechanical properties and corrosion resistance and are used for the manufacturing of components for extreme conditions such as high-temperature/high-pressure atmospheres.

In present Thesis will be also presented the results of a biphasic steel ASTM A890 grade 4a denominated as duplex.

Biphasic stainless steel is the duplex ASTM A890 grade 4a, supplied in casting alloy type with equal volume fractions of ferrite and austenite, typically of 45:55. Duplex samples were prepared for chemical etching, in order to investigate the microstructure layout with metallographic analysis. The adopted chemical solution was the number 87 provided by ASTM E-407 [38]. Quantitative metallography was carried out with the VEGA3 Tescan SEM and the Optical Microscope of Materiais e Processos de Fabricação of Instituto Tecnológico de Aeronáutica (ITA).

The composition in weight of a portion of material is listed for single phase in TableVI, as representative of the whole microstructure composition. The results have been obtained by Energy Dispersive X-ray Spectrometry technique integrated in a Vega3 SEM. The chemical

composition is in agreement with the overall composition of the material, found in literature [39].

To investigate the microstructure of duplex steel, a cylindrical sample was prepared for metallography, Figure 17. The cylindrical sample was in the same condition of the ‘dog-bone’ duplex specimen used for fatigue tests. In Figure 17, the SEM micrographs of two extracted sections, are useful for an understanding of the layout and the morphology of phases present in duplex stainless steels. In particular, in Figure 17, two regions are represented: A and B in which a series of 10 repetitions of each measurement have been performed.

The morphology of the phases shown at a magnification of 200, involves austenitic grains organized in pseudo-equiaxed or elongated clusters and a darker ferritic phase embedding austenitic clusters. The global heterogeneity of the duplex microstructure, visible from the micrographs, clearly affects the behaviour of material.

Chemical Composition of ASTM A890	AUSTENITE Wt% ( $\sigma$ )	FERRITE Wt% ( $\sigma$ )
Fe	63.9 (0.1)	50.4 (0.2)
Cr	23.3 (0.1)	17.3 (0.2)
Ni	5.3 (0.1)	/
Mo	3.3 (0.1)	2.0 (0.1)
Si	0.9 (0.0)	0.6 (0.0)

Table VI. Chemical composition of each phase of ASTM A 890 grade 4a ( $\sigma$  represents standard deviation).

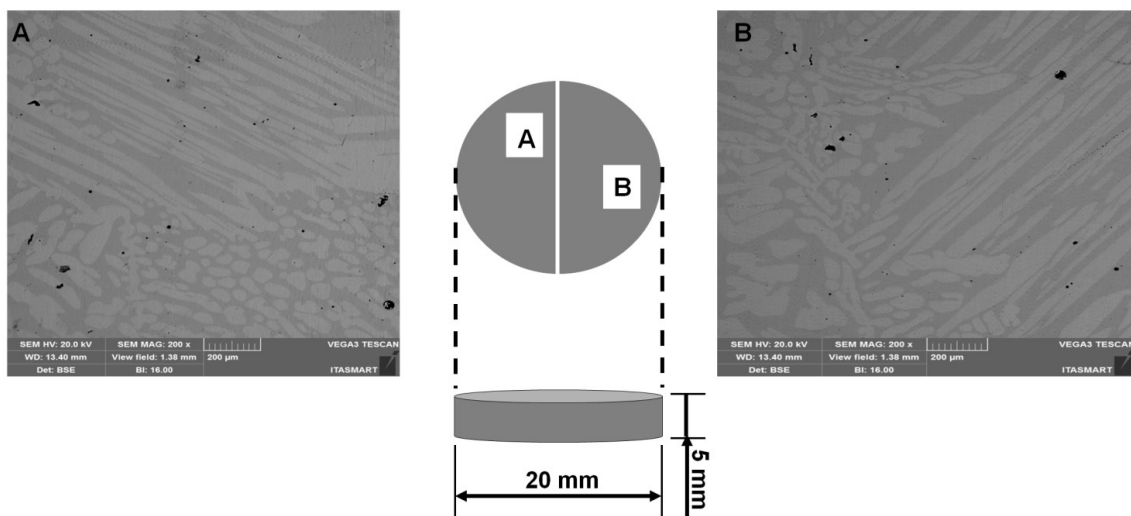


Figure 17. SEM micrographs of sample: elongated/equiaxed/pseudo-equiaxed texture.

### 3.4.3 Self-Heating Test And Specific Loading Tables

The fatigue test on smooth samples consists of a stepwise loading procedure sequentially applied to the specimen (Appendix A-Loading Tables) up to the point of failure of material. The procedure is also called Self-Heating test [18].

The load was imposed to cover a wide range of stress levels: from elastic to plastic.

The procedure involves applying for a small number of cycles (100,000), a stress sequence below the yield strength of material. The following loading levels are performed at stress levels above yield strength, up to the material failure (total loading cycles roughly 300,000). Specifically it requires at least five load steps below the fatigue limit ( $\sigma_L$ ) of material. The authors recommend starting with a stress amplitude value ( $\Delta\sigma/2$ ) of no more than 10% of ultimate tensile strength and completing the remaining steps increasing the stress amplitude by less than 20 MPa.

At the end of each step, mean and amplitude of the applied load was increased. The procedure requires halting the loading machine between consecutive loading blocks, in this way temperature can return to environmental value and the influence of interval time between each loading block is negligibly small.

Each loading level is characterized by a constant frequency of 17 Hz, constant duration (approximately 20,000 cycles of loading machine) and a fixed stress ratio ( the results showed in this thesis refer to stress ratio: 0.5, -0.1, figure 18). In Figure 18 the black edges of the area under the loading configurations, represent the imposed maximum and minimum stresses with respect to the applied stress semi-amplitudes. The 0.2% proof stress line reported refers to the a martensitic stainless steel tested ASTM A 182, such the line divides the elastic and plastic regions of loading. At  $R=0.5$  the loading table includes more load levels in the plastic regime than the one at  $R=-0.1$ . This will affect the specific behaviour of material as will be shown in the following chapter.

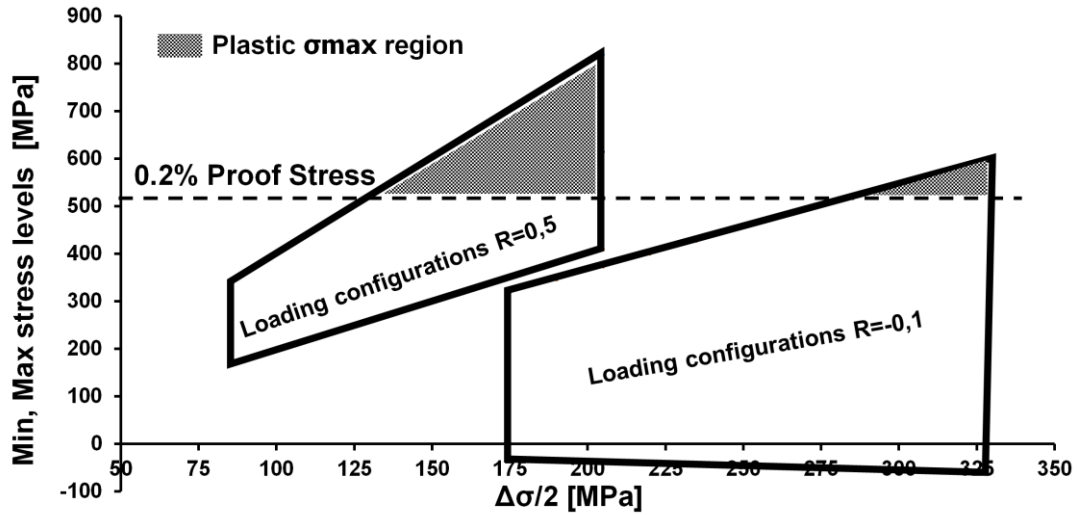


Figure 18. Loading configurations at R=0.5 and R=-0.1.

However, the choice of initial loading level depends on the mechanical properties of material. Usually, the first step is a fixed percentage of UTS value. As an example for Duplex stainless steels, the ultimate tensile strength of the material, obtained by performing a tensile test at 20 MPa/s, was 799 MPa while the assessed yield strength ( $\sigma_Y$ ) was 450 MPa. The initial loading stress semi-amplitude was 65 MPa, approximately 10% of  $\sigma_{UTS}$  value as well as the value of initial stress level for austenitic and martensitic stainless steels.

### 3.4.4 Fracture Mechanics Tests

Referring to Fracture Mechanics Tests the constant-force-amplitude procedure was used with a constant force range  $\Delta P$ , fixed stress ratio  $R=0.1$  and loading frequency  $f$  of 13Hz. The loading ranges used during the tests for each material are 12.4 kN (X4CrNiMo16-5-1 and 9.90 kN for AISI 316L.

All samples were pre-cracked up to a crack length of 2.5 mm according to ASTM E-647 [40].

### 3.4.5 Sample Geometries

Referring to the fatigue test on metals the specimens (three in number) were used with dimensions according to ASTM E 466-96 geometry [41]. In figure 19, the most important dimensions of specimen are reported: nominal gauge length, nominal thickness and nominal width.

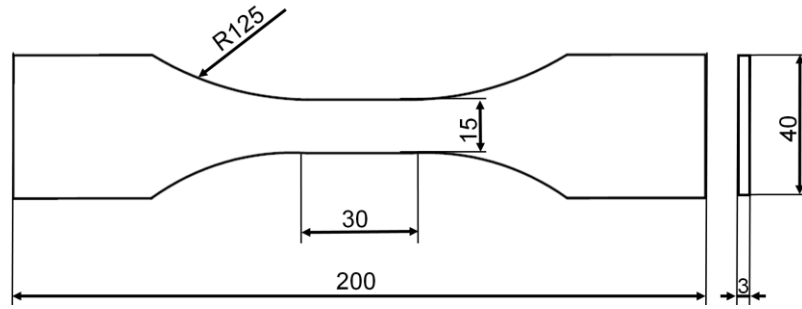


Figure 19. Dimensions (mm) and geometry of specimens.

Cracked samples where Compact Tension (CT) samples, three sample tested for each material, sized according to ASTM E 647 [40], figure 20, measures in mm.

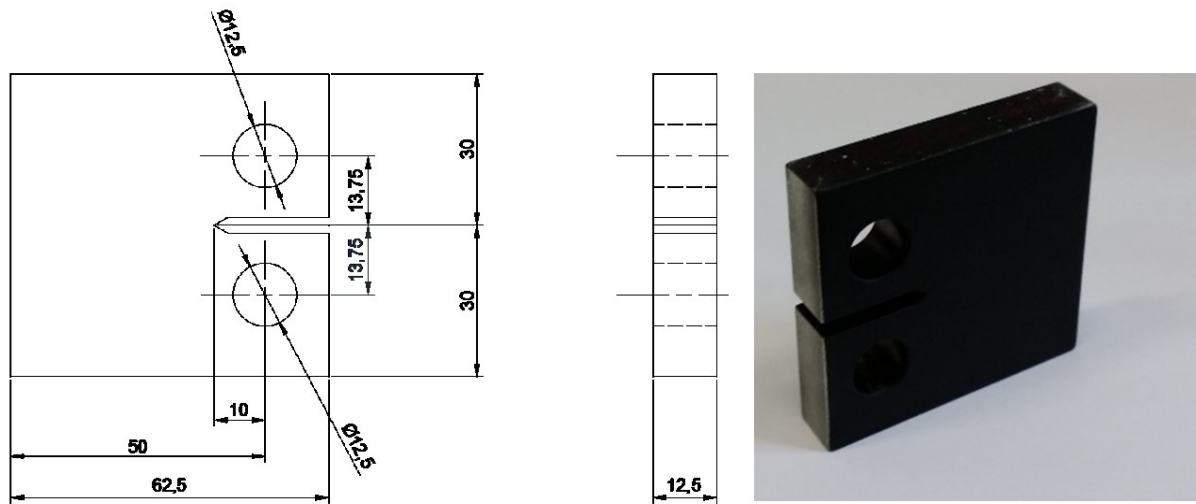


Figure 20. Dimensions (mm) and geometry of CT specimens.

All the samples were coated with the specified matt black in order to increase the emissivity to 0.95.

### 3.4.6 Machines and Layout

The tests were carried out with the MTS model 370 servo hydraulic fatigue machine with a 100 kN capacity. The IR camera FLIR SC 640 was used to obtain thermal data. It is based on a microbolometric detector (640 x 480 pixels) with a thermal sensitivity NETD < 30 mK. Specimens were also enclosed in an insulating chamber to avoid heat reflections due to eventual external heat sources. A painted unloaded aluminum plate acting as a black body was used to monitor the environmental temperature inside the insulating chamber, figure 21(a) and (b).

Thermographic data were acquired during the entire test with a frequency of 0.1 frames per

second. This thermal camera allows assessing the temperature parameter  $T_0$ .

For performing thermographic signal analysis during the fatigue test also a cooled FLIR IR X6540 SC infrared camera with an InSb detector (640x512 pixels) and acquisition rate of 123 Hz, has been used, figure 21 (c). Figure 21(c) shows the setup for the testing on ASTM A182.

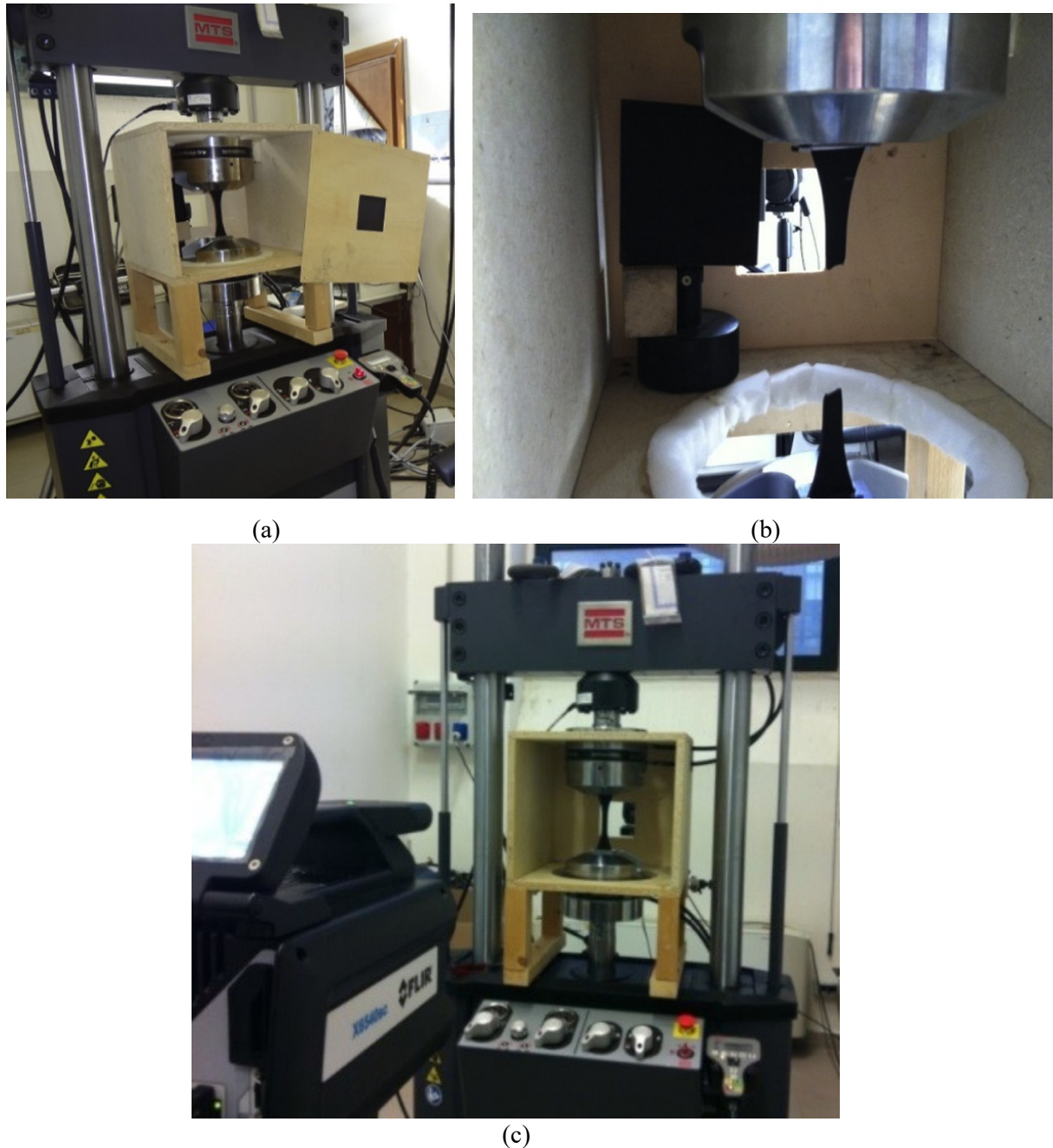


Figure 21. Loading machine, insulated chamber, specimen and (b) inside of insulated chamber: specimen, black body and IR camera, (c) IR cooled detector for fatigue testing.

Thermographic sequences were acquired with constant intervals of 2000 cycles by using a cooled FLIR IR X6540 SC infrared camera, Figure 22.



The software adopted for acquiring the sequences is Flir software RIR Max.

A geometrical resolution of 0.067 mm/pixel was obtained by placing the thermocamera at 170 mm from the specimen and by using a 50 mm lens with a 12 mm extension ring.

All specimens were pre-cracked to a crack length of 2.5 mm according to ASTM E-647.

A second infrared camera, Deltatherm 1560 by Stress Photonics, with an InSb photonic detector

(320x256 pixels) on the opposite side of the specimen was used only to monitor the crack size

according to Standard [41].



(a)



(b)

Figure 22. Machines and setup for CT samples: (a) cooled IR detector FLIRX6540SC and (b) detail of CT sample .

### 3.5 Processing Procedures

The model presented in section 3.3 has been implemented in the software IRTA, which performs the processing in frequency-domain of the thermographic signal in order to extract the different signal components in terms of images (data matrix) as shown in Figure 23. In particular, in figure 23 is presented the procedure for assessing the single component, and as an example it was reported four data matrix of parameters  $S0$ ,  $S_{the}$ ,  $Sd$ ,  $\varphi$ .

Such the parameters can be used for studying the fatigue in all its aspects, that is on smooth samples and notched ones. So that the procedure which are going to be presented allows the quantitative study of both cases. However, the case of notched samples is quite different from smooth samples, since the just presented parameters are adopted for assessing and determining different other quantities such as plastic volume, crack length or the crack tip position. In fact, Chapter 5 will provide a detailed description about how  $S0$ ,  $S_{the}$ ,  $Sd$ ,  $\varphi$  indexes lead the evaluation of typical of Fracture Mechanics parameters.

In figure 23, are reported the signal maps for two stress levels (initial and ultimate), the effect of the stress is easily detectable since the two matrixes are very different in terms of Signal Units (SU) values. However, according to the algorithm the measured thermographic signal ( $S_{measured}$ ) and the modelled thermographic signals ( $S_{modelled}$ ) are time instant by instants ( $i$ ) compared by using the least square method, from the first instant of the test to the last ( $n$ ). Once the function  $J$  is assessed, the function is derived with respect each parameter and the relative partial derivative is set equal to zero. In this way, by solving the system of  $n$  equations and  $n$  variables (where  $n$  is the parameters of the adopted algorithm) the matrix of each parameter is assessed referring to a fixed time instant and stress level, as depicted in figure 23.

In a few steps, a number of indexes have been assessed from a single data analysis related to temperature signal and expressed in signal units, Figure 23.

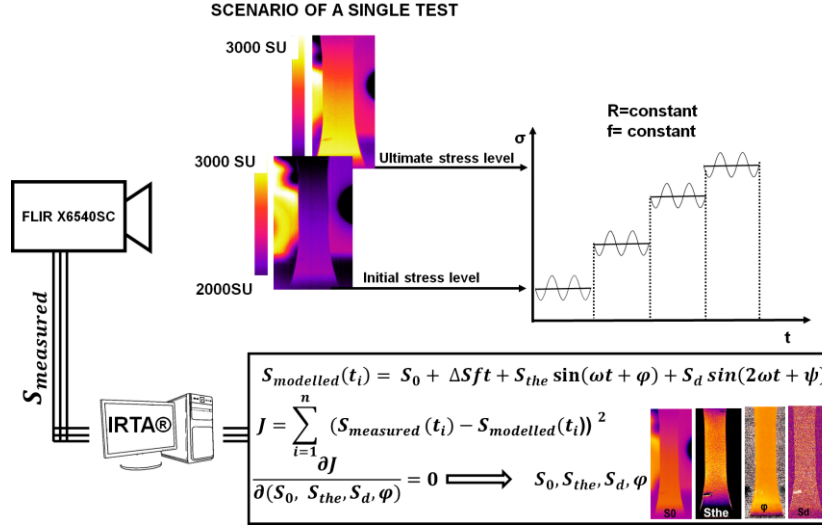


Figure 23. From thermographic signal to thermal and phase parameters: how IRTA runs.

After assessing the thermal parameters maps, specific algorithms have been developed for processing and analysing the data since each parameter represents a specific thermal signal variation. All the algorithms for processing data matrix have been implemented in Matlab ® and are reported in Appendix B-Matlab Routines.

Each procedure starts by sizing the scientific scenario in the area of interest.

### 3.5.1 Linear temperature variation ( $T_0$ parameter)

The  $S_0$  ( $T_0$ ) parameter refers to the portion of linear temperature increase which represents the offset of temperature. Generally, it when it achieves the stabilisation,  $S_0$  ( $T_0$ ) can be understood as  $T_{stab}$  as shown in section 3.2, figure 4 and figure 24 that is the temperature of the second phase (phase 2). However, in order to understand the influence of the different loads (in terms of stress amplitudes:  $\sigma_{a1}$ ,  $\sigma_{a2}$ ,  $\sigma_{a3}$ ) on temperature behaviour in figure 24 different trends are shown [17].

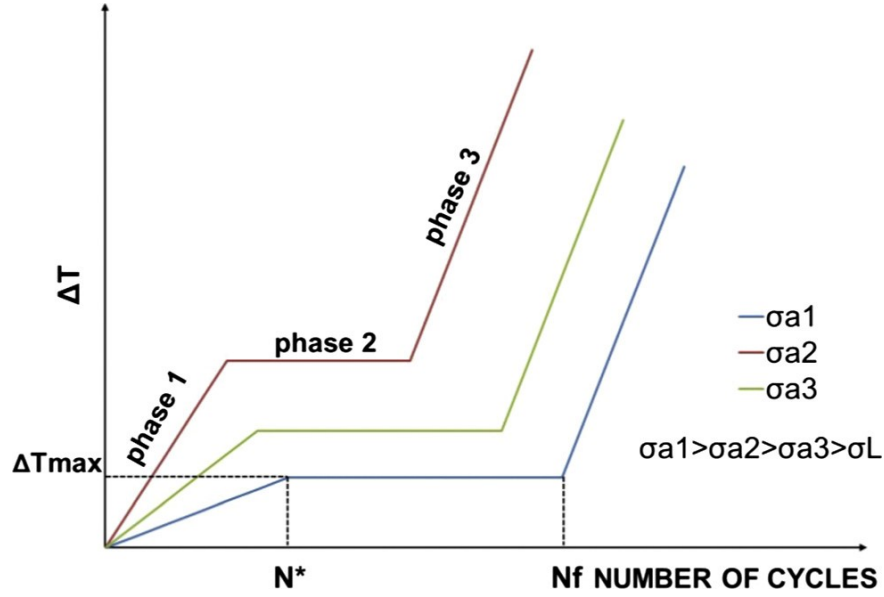


Figure 24. Expected temperature trend during a fatigue test at different load stress values above fatigue limit.

As just explained in the previous paragraphs, temperature changes during a fatigue test are due to dissipative sources resulting from damage phenomena. However, other external heat sources can cause variations of superficial temperature of specimen. In fact, the environmental temperature and the heating produced by the loading machine contribute to a superficial temperature increase of specimen. Hence, in the gauge area of specimen, the temperature  $T$  for a generic pixel with coordinates  $(x, y)$ , can be expressed by the following equation:

$$T(x, y, t) = f[T_d(x, y, t), T_{amb}(t), T_{lm}(x, y, t)] \quad (16)$$

where  $t$  is a fixed time instant,  $T_d$  indicates the temperature increment due to dissipation phenomena,  $T_{lm}$  is the temperature increment effect due to continuous heat flow transferred from loading machine to specimen and  $T_{amb}$  is the environmental temperature.

The only temperature change correlated to damage phenomena  $T_d$  for brittle or high conductive materials can have the same order of magnitude as the other effects becoming difficult to assess.

The proposed procedure is capable of filtering most of the external heat sources that can compromise the correct measurement of dissipative sources.

Figure 25 shows a thermographic image acquired at a given time during the loading step 13/15 (corresponding to  $\Delta\sigma/2 = 180$  MPa) and related to specimen 1 of a martensitic steel ASTM A 182 grade F6NM. Areas  $A_1$  and  $A_2$  refer-respectively-to the specimen gauge area, and black body area used for evaluation of the environmental temperature.  $T_{amb}$  represents

the temperature mean value measured on the black body in the  $A_2$  area. To take into account the influence of environmental conditions,  $T_{amb}$  has been subtracted from temperature  $T$  into  $A_1$  matrix, pixel by pixel.

In light of this, for the evaluation of environmental temperature, the black body corresponds to a dummy specimen that is arranged in the test chamber. The necessity of using the same material as the sample as a reference is due to need for the same thermal properties ( $\alpha$  thermal diffusivity) to provide an in-phase thermal signal with tested material.

Temperature trend along a generic profile  $p$  (figure 25), shows the effect of hot oil in the cylinder of the loading machine. This heat is transferred by the loading machine to the specimen through the grips and it is not constant but increases during the test.

Typically, when dissipative phenomena occur, a non-symmetrical thermal profile appears, figure 25(b) and (c).

If a profile along the specimen  $p$  is plotted when there is only external heat and no inner heat source due to damage (figure 25b), the temperature along the specimen varies linearly from the hottest (bottom) to the coolest (upper) part. As first approximation, even with significant heat dissipation from the specimen (figure 25c), the contribution of the loading machine  $T_{lm}$  was then considered linear.

Another effect, even if not so high in amplitude, related to the time delay in the heating of specimen (directly connected with the ‘heat source’) and blackbody (that will heat up due to environmental change of temperature in the insulating chamber) due to the fact that blackbody is not in contact with the loading machine heat source. In fact, even with evident absence of dissipation heat source (figure 25b) there is a  $\Delta T_p$  slightly different from the expected zero value. This effect will be filtered in the next step.

A straight line was used to assess  $T_{lm}$  that connects two values on the boundary of the  $p$  profile obtained substituting the central value of the first and last set of five pixels, respectively with their mean values.

The effect of  $T_{lm}$  was filtered out for each profile along the specimen in the analysis area  $A_1$ . Compared with other kinds of filters-as physical filters, for instance-this has the advantage of being straightforward and very simple to implement, giving equally good results.

Referring to figure 25 (b) and (c), the trends of unfiltered thermal profiles tend to overestimate the value of  $\Delta T_p$  compared to filtered data.

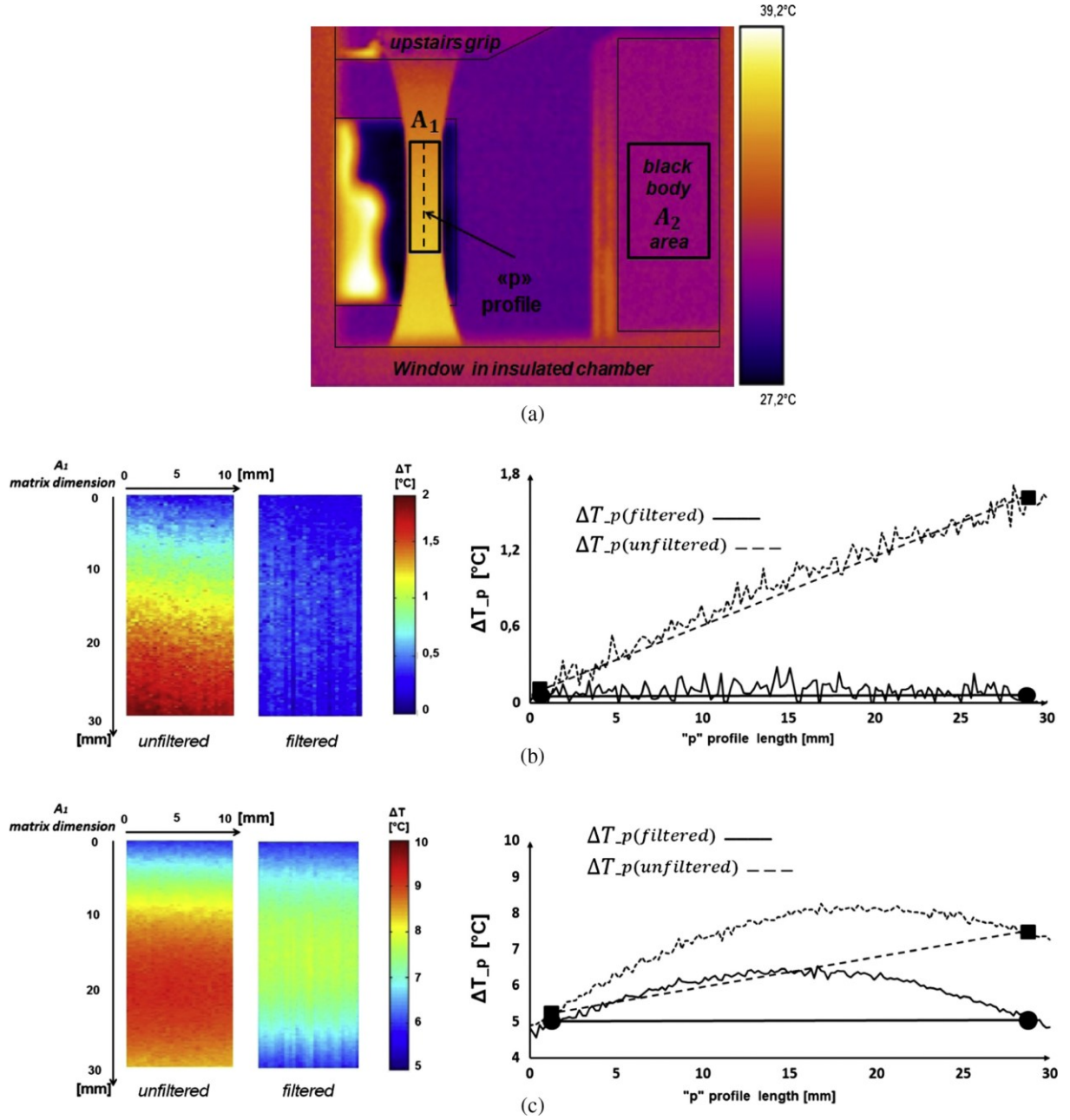


Figure 25. (a) Areas and thermal profile “p” considered for analysis (ASTM A182, specimen 1):  
 (b) temperature trend along “p” profile at load step 8 (140 MPa), (c) temperature trend along “p” profile at load step 13 (180 MPa).

The  $\Delta T_{max}$  (figure 26) considered in this work is obtained as the maximum of the  $\Delta T_p$  of the analyzed  $A_1$  area. As an example, the thermal data for two martensitic stainless steels ASTM A 182 and X4 Cr Ni Mo 16–5–1 (figure 26(a) and (b)), are presented as function of stress semi-amplitude ( $\Delta\sigma/2$ ) imposed during fatigue test and by comparing unfiltered and filtered data.

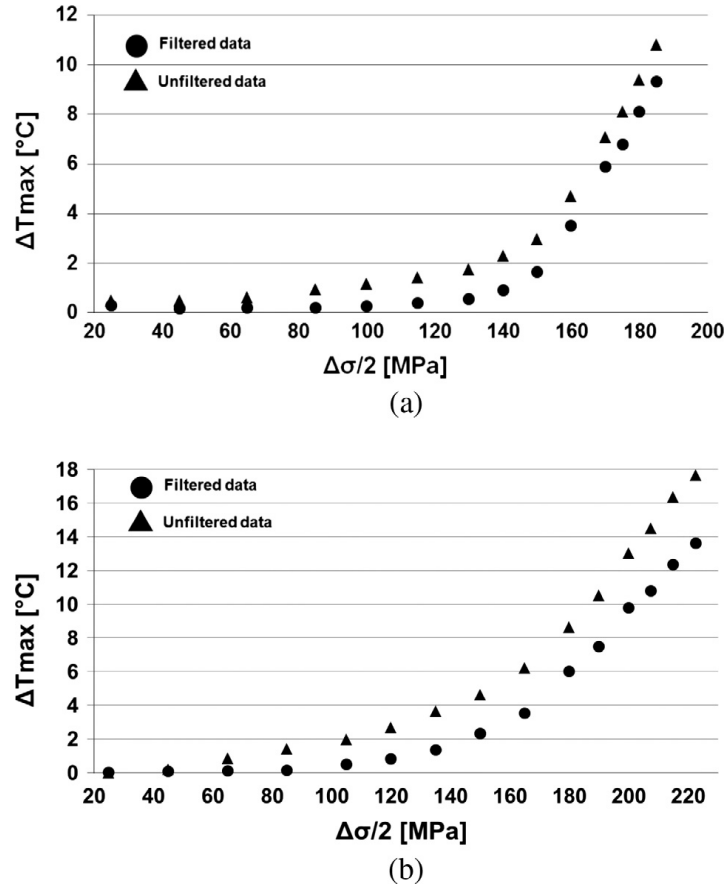


Figure 26. (a) Filtered and unfiltered temperature data, specimen 1, ASTM A 182 grade F6NM, (b) filtered and unfiltered temperature data, specimen 1 X4 Cr Ni Mo 16–5–1.

Referring to [17], unfiltered data trend were obtained by subtracting the environmental temperature from the steady state temperature  $\Delta T_{max}$  achieved during each step.

In general, in order to avoid outliers in the analysis, due to the presence of bad pixels in the matrix, the analysis could be also referred not to  $\Delta T_{max}$  but to 98<sup>th</sup> percentile extracted from the data matrix  $\Delta T_{0\_98}$  ( $\Delta S_{0\_98}$ ).

Since for the presented materials, the temperature variations are high, using  $\Delta T_{max}$  or  $\Delta T_{0\_98}$  does not influence the accuracy of the results.

As presented in figure 26, all data are characterized by two different trends related to two different behaviours of material. The first steps of fatigue test are placed below the fatigue limit so no damage occurs to materials and the temperature variations detected are negligible. When damage phenomena occur, a significant temperature increase variation is observed. This behaviour can be approximately represented with a linear function that relates the temperature variations to the level of stress of material. As shown in this paragraph, an inaccurate evaluation of all heat sources involved in the measurement of temperature could compromise the correct evaluation of the dissipative heat sources linked to fatigue damage phenomena. Moreover, some problems might occur in the evaluation of fatigue limit of material.

The flow chart in figure 27 summarizes the procedure above described even if the last three blocks of the algorithm will be discussed in depth in further Chapter 4, since they refer to the evaluation of the fatigue limit of materials by using the statistical threshold method. However, let's consider the case in which temperature plateau is not achieved.

As stated, the temperature trend during loading cycles can be affected by external heat 'disturbance' sources [42]. As already discussed in [15], two external effects can induce significant thermal variations of the specimen: the environmental temperature and the hot grip of the hydraulic loading machine [14].

After filtering out all the 'disturbing heat sources' by using the procedure just described, temperature trend is assessed in order to study the thermal behaviour of each material.

Figures 28a-b-c, present the mean temperature curves (mean temperature refers to the gauge length area as depicted in Figure 25) of the last stress level of Sample 1 of biphasic and martensitic, austenitic steels. At first sight, it appears that for austenitic and duplex steels the plateau phase is not achieved by the temperature over time, even at higher stress levels.

Duplex stainless steel (Figures 28a) behaves with a remarkable decrease (after the initial increase) during the test and an abrupt increase in the last cycles of the test. 17-4 PH martensitic lattice (Figure 28b), presents the same initial increase, but afterwards it reaches an equilibrium phase and finally a minor increase before failure. The specimen fails some moments after the beginning of another stress level, which has not been reported. The same slight decrease in temperature signal, before failure, was observed by [42] on martensitic SA533B112 steel tested at  $R=0.2$  and 1000 Hz.

The austenitic microstructure (Figure 28c) exhibits approximately the same behaviour of the duplex stainless steel (Figure 28a); in fact, it is characterized by a less sloped decrease and a shift upward in the final phase.

Such atypical behaviour does not allow the determination of the commonly adopted parameter for evaluating fatigue limit: steady state temperature value. In this case, the temperature pattern for loading cycles is different from the one expected and reported in literature for most steels [19-20] and the fatigue limit estimation can be inaccurate. Hence, a new procedure of data has been setup.



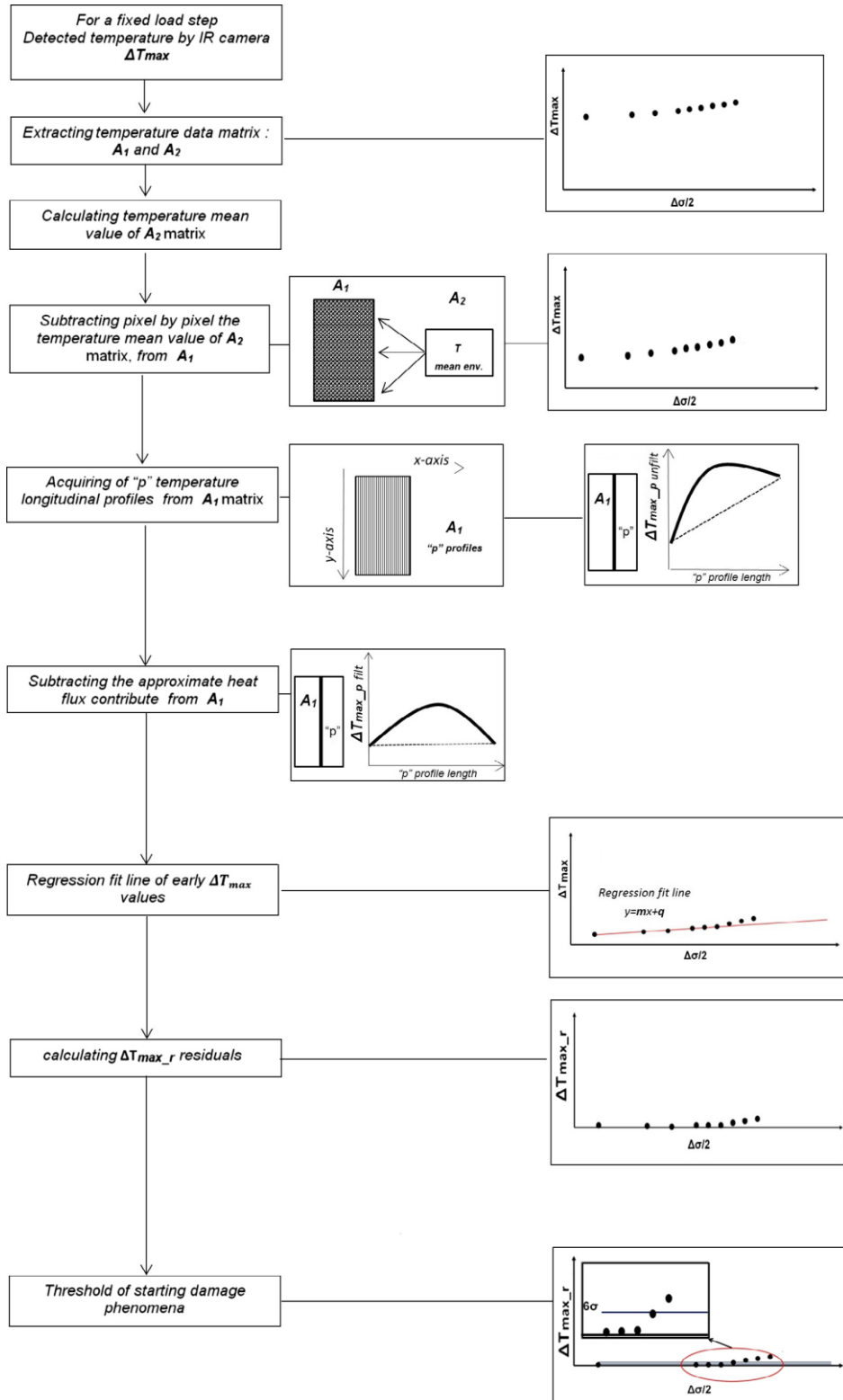


Figure 27. scheme of the proposed procedure.

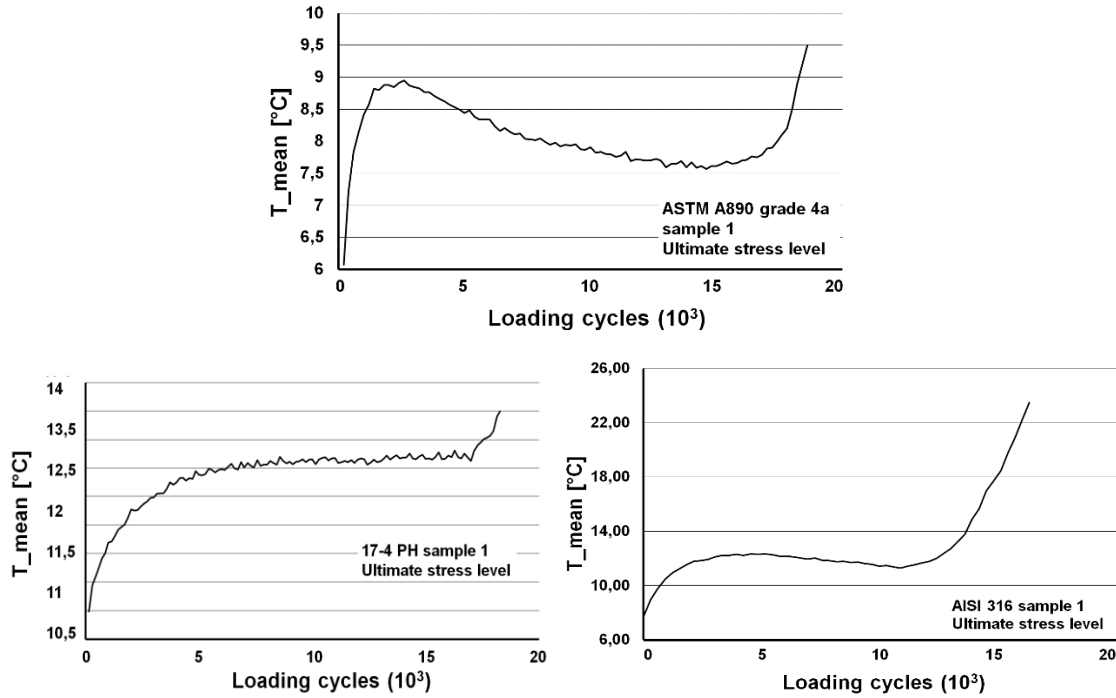


Figure 28. Mean temperature pattern at stress level very close to the failure (ultimate stress level):  
(a) Duplex stainless steel, (b) 17-4 PH, (c) AISI 316.

In Figure 29, for example referring to the  $T_{mean}$  of duplex (mean value of temperature in the area shown in Figure 25), the parameters adopted for assessing fatigue limit are:

- the maximum temperature variation ( $T_{max}$ ) which replaces stabilization temperature,
- the slope of the linear section representing the initial temperature increase after applying the load,  $S_{slope}$ ,
- the mean value ( $T_{mean\_in}$ ) of the same data series adopted for estimating  $S_{slope}$ . Such series of temperature values represents the first linear increase of the temperature after imposing load.

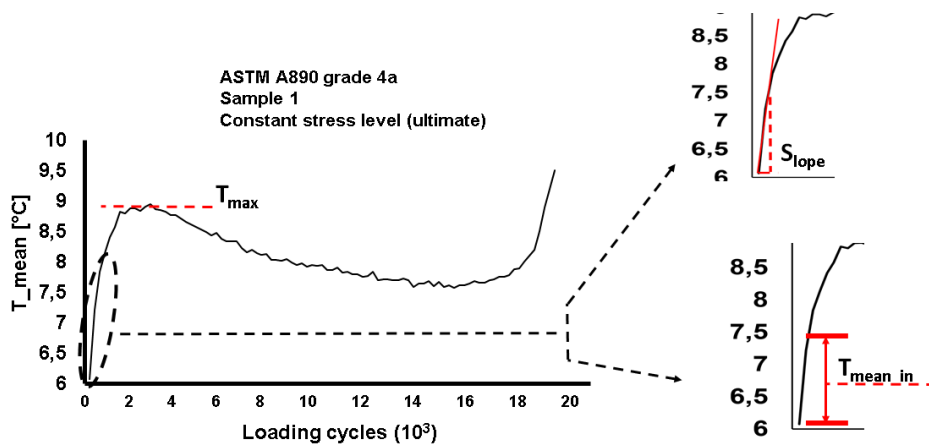


Figure 29. Indexes for evaluation of the fatigue limit:  $T_{max}$ , Slope and  $T_{mean\_in}$  of initial data.

To assess each parameter, three algorithms have been set up in Matlab® and integrated in a

more complex algorithm providing fatigue limits. Figure 30 shows the overall procedure for determining fatigue limit by starting from the mean temperature data series  $T_{mean}$ , obtained for each loading level.

The algorithm starts by initializing the values and vectors:

- $N$  is the number of loading cycles of the generic loading level (usually 20,000 cycles);
- $V_{cycles}$  is a vector which contains loading cycles, from the first to the total number of a generic loading level ( $N$ );
- $V_{T_{mean}}$  includes the temperature values ( $T_{mean}$ , the mean temperature trend of an area in the gauge length versus loading cycles, Figure 29) correlated with the values of  $V_{cycles}$ , of a generic loading level. By plotting the couples  $(V_{cycles}, T_{mean})$ , it is possible to obtain the graph similar to the one shown in Figure 29, for a fixed stress level.

After the initialisation of the quantities, evaluation of the indexes starts.

The block of inputs represented at the left branch of Figure 30, represents all the operations to assess the slope ( $S_{lope}$ ) and mean value ( $T_{mean\_in}$ ) of the linear section of the data series. 'Linear section' includes all the data couples  $(V_{cycles}, V_{T_{mean}})$  of the first linear increase of temperature trend (i.e. Figure 29, Figure 30 in the middle of the diagram).

The indexes  $S_{lope}$  and  $T_{mean\_in}$  were not evaluated as overall linear temperature trend (from 0 to  $T_{max}$ ) but a partition of the data (from 0 to  $T_{max}$ ) were considered in order to evaluate the best fit of the curve. In doing so, the  $R^2$  parameter has been used to assess the linearity of the considered linear temperature trend.

Hence, the procedure requires setting the number of subset data ( $J$ ), which are used to interrogate the temperature vector along the number of cycles and to extract the finally reduced set of data providing the maximum value of  $R^2$ .  $J$  in the present analysis was equal to 1000 cycles (roughly 100 data couples), and represented the minimum number of data, each time considered, to evaluate the slope and the mean temperature of the first linear trend. After setting the  $J$  value, the subset of data is represented by the vectors  $(V_{cycles\_red}, V_{T_{mean\_red}})$ . Since the value of  $R^2$  is calculated for each  $i$ -th data couple  $(V_{cycles\_red}, V_{T_{mean\_red}})$ , the  $(R_i^2)$  values filled the vector  $V_{R^2}(i)$  which memorizes the  $i$ -th values of calculated  $R^2$ . Finally, the maximum value of the vector  $V_{R^2}$ , is calculated, which is the maximum value of the  $i$ -th series of  $R^2$ ,  $(R_{max}^2)$ , and the index ' $i$ ' to which the maximum  $R^2$  refers to,  $[(i_{R^2})_{max}]$ . After finding the data couples which present the maximum correlation  $R^2$ ,  $(V_{cycles\_R^2}, V_{T_{mean\_R^2}})$ , it is possible to evaluate the slope of the couples and mean value, which are, respectively:  $S_{lope}$  and  $T_{mean\_in}$ .

The algorithm also provides the third index, which is the maximum value of the temperature pattern  $T_{max}$ , calculated in the series represented by vector  $V_{T_{mean}}$ .

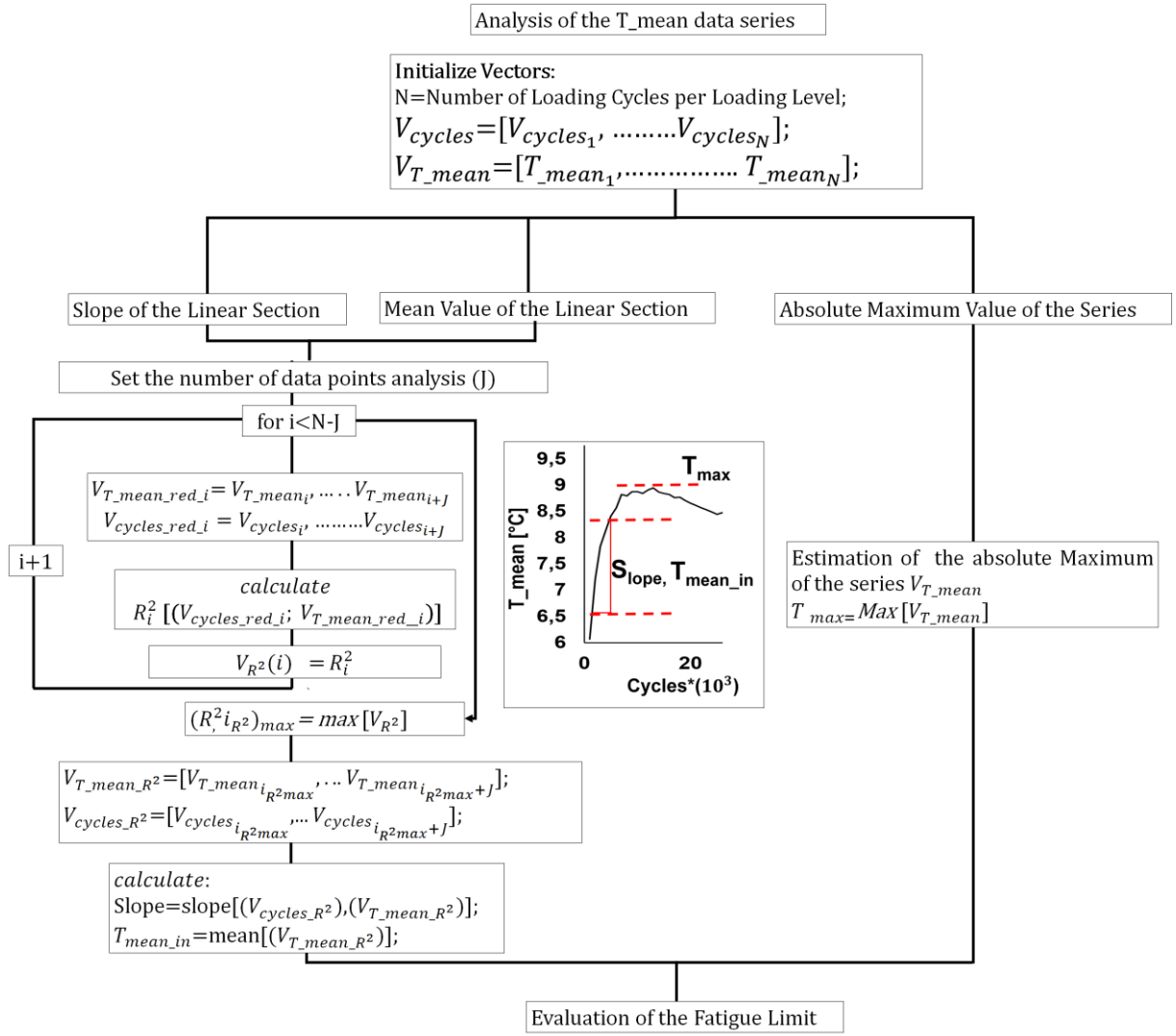


Figure 30. Implemented algorithm for optimizing parameters and assessing fatigue limit.

Of course, the evaluation of such indexes can also be performed even in those cases where the temperature plateau is achieved.

The results of processing in terms of the couples  $(\Delta\sigma/2, T_{max})$ ,  $(\Delta\sigma/2, S_{slope})$ ,  $(\Delta\sigma/2, T_{mean\_in})$ , are graphically illustrated in Figures 31-33 respectively for Duplex, 17-4PH and AISI 316.

By analysing the graphs represented in Figures 31a-c, a tiny scattering arises which characterizes the first loading levels (60-100 MPa) mostly for  $S_{slope}$  and  $T_{max}$  data series.  $T_{mean\_in}$  appears to be more regular in the initial data points of the series except for the stress level of around 120 MPa, Figure 31b.

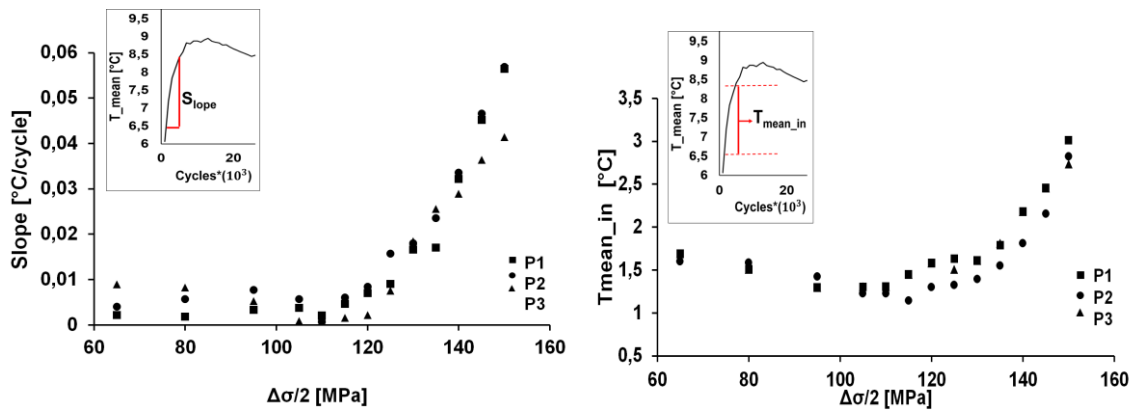
However, all the parameters exhibit a good reproducibility of the curves. Furthermore, a reduction in value is evident in the first loading levels, which stop roughly around 120 MPa. This phenomenon can be explained by observing that at lower stress amplitudes, the signal-to-noise ratio is low, since the thermal signal is low. The low level of noise that is characteristic of the signal could prove misleading in the evaluation of the indexes, as will

be shown in depth in the following sections.

It is worth mentioning that the overall temperature variation ( $T_{max}$ ) is slightly higher than 1.5°C. The last point of the series was not considered since it affects the evaluation of the curves by flattening the scales of the graphs. Moreover, in Figures 31b, the values are shifted at a temperature different from zero. This effect could be attributed to the heating from the loading machine grip, which was not completely eliminated from the filtering procedure.

The martensitic stainless steel 17-4 PH exhibits very reproducible curves except for  $S_{lope}$  curves (Figure 32a) in which slight noise is observed. In Figure 32b-c, a change in slope is recorded in the temperature variation curves. This effect may be related to viscoelastic behaviour of the material [26]. The total thermal variation reported in Figure 32b is 5°C, clearly higher than the temperature variation of duplex steels. Even for martensitic steel, the last testing point has not been included in the graphs of Figures 32 in order to avoid an excessive compression of the initial values.

Austenitic microstructure behaves with temperatures considerably higher than other steels (higher heat dissipations and deformations), as represented in Figures 33a,b,c. In Figure 33c, the total variation is of approximately 10°C (the ratio between maximum temperatures of duplex and AISI 316 is roughly 1/10). The results for AISI 316 in terms of  $S_{lope}$  and  $T_{mean\_in}$  parameters (Figures 33a-b) are very reproducible even for  $T_{max}$  (except for the initial loading levels, Figure 33c).



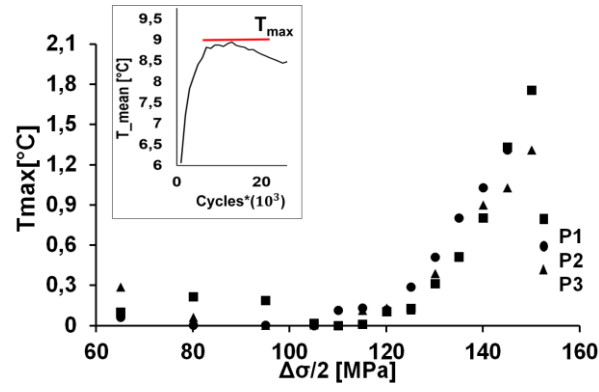


Figure 31. Results for Duplex: (a)  $S_{lope}$ , (b)  $T_{mean\_in}$ , (c)  $T_{max}$  parameters.

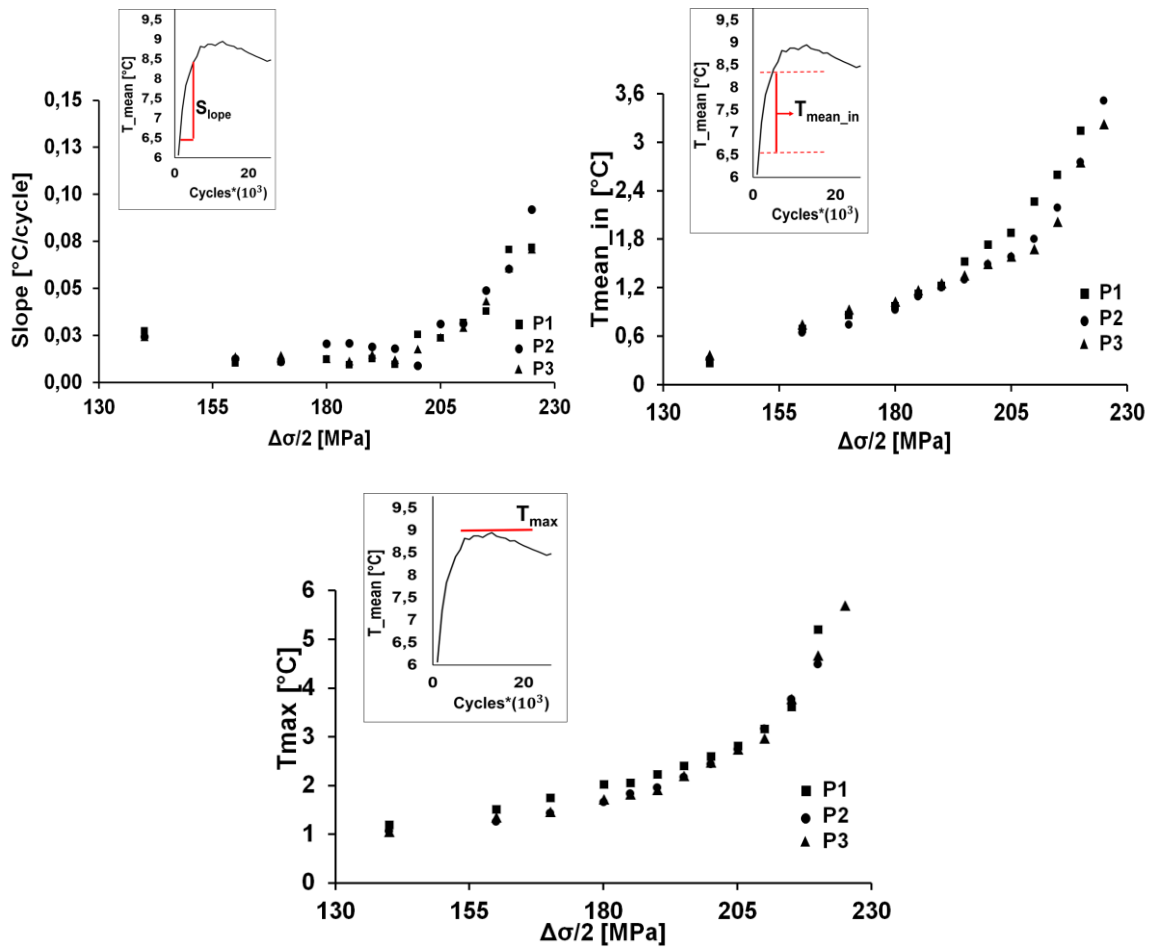


Figure 32. Result for 17-4PH: (a)  $S_{lope}$ , (b)  $T_{mean\_in}$ , (c)  $T_{max}$  parameters

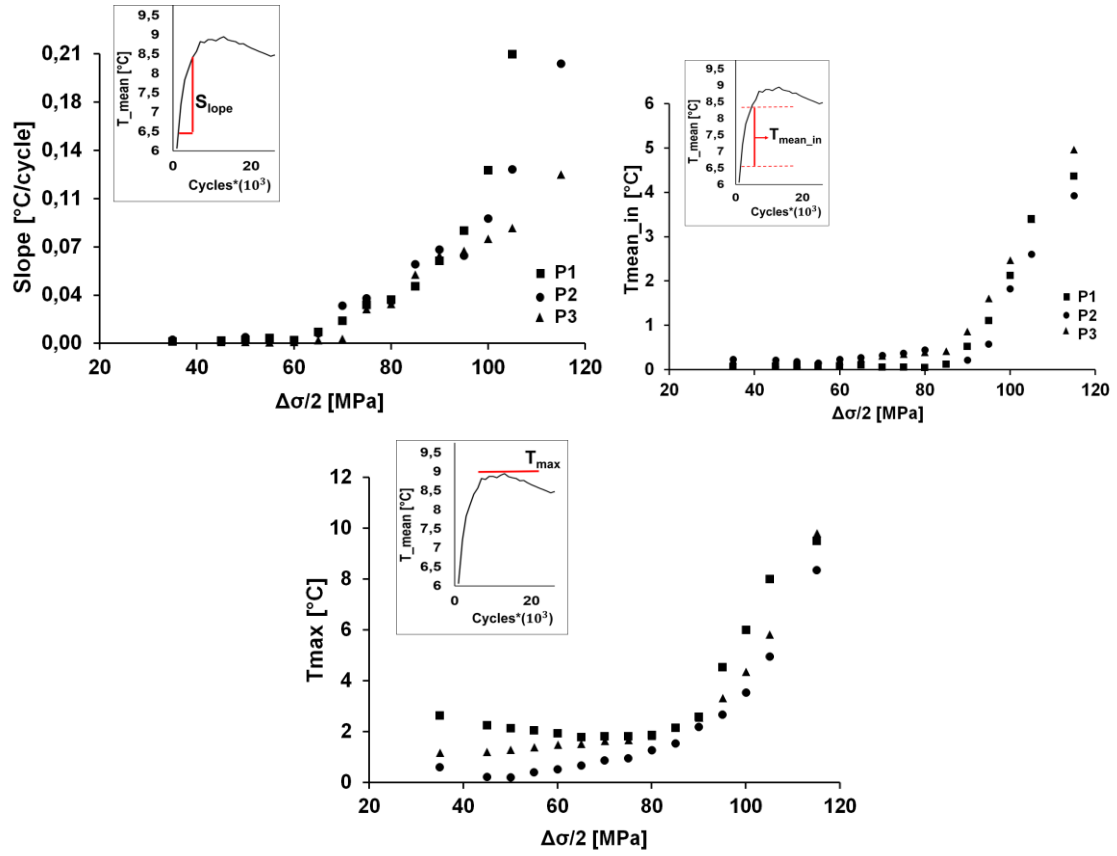


Figure 33. Result for AISI 316: (a)  $S_{lope}$ , (b)  $T_{mean\_in}$ , (c)  $T_{max}$  parameters.

### 3.5.2 Thermoelastic temperature variation ( $T_{the}$ parameter)

The operation for processing the Thermoelastic temperature variation running at the mechanical frequency is simple, in particular it involves firstly the application of a double dimension Gaussian kernel which served to filter out the noise.

After the  $T_{the}$  ( $S_{the}$ ) matrixes (of generic loading block) were also divided pixel by pixel to relative stress amplitude ( $\Delta\sigma$ ), and subsequently the 98<sup>th</sup> percentile values were extracted from the  $T_{the}$  matrixes,  $T_{the\_98}$ .

### 3.5.3 Thermoelastic phase variation ( $\phi$ parameter)

The algorithm developed in Matlab® framework, figure 23, processes the phase data ' $\phi$ ' obtained as represented in figure 34.

As depicted in figure 34, the phase matrixes are primarily smoothed by using a double-dimension Gaussian kernel and subsequently the analysis required a matrix windowing of the scenario, from  $[\phi]_{M \times N}$  to  $[\phi]_{m \times n}$ , to focalise the investigation to only the gauge length of the specimen. Physically, the  $\phi$  values in the matrix represent the lag between points in adiabatic conditions and points under non-adiabatic conditions.

After filtering, since the phase data of the first loading steps [27] are scattered due to the low value of signal to noise ratio, a further processing is required to reduce such an effect. By supposing that the first three loading levels are definitely in elastic regime, where phase variations are zero,  $\Delta\phi=0^\circ$ , a single mean phase matrix  $[\phi_m]_{m \times n}$  has been considered in place of the first three steps.

Each value of the matrix is considered as a non-damaged phase value, then all subsequent matrixes can be referred to this 'undamaged condition' by the calculation reported in equation 17.

$$[\Delta\phi_j] = [\phi_j] - [\phi_m] \quad j=4, \dots, N \quad (17)$$

where N is the last loading level.

From  $[\Delta\phi_j]$  matrixes, the percentile values 98<sup>th</sup> and 2<sup>nd</sup> were extracted and the difference between percentiles is calculated in order to take into account the phase variations. In this way, for a single loading block, the phase parameter used for fatigue limit estimations, has a fixed value ( $\Delta\phi_{98-2\_j}$ ).

The choice of 98<sup>th</sup> and 2<sup>nd</sup> percentiles is designed to avoid possible outliers of data in the



analysis and at the same time to refer to values very close to the maximum values of the specific index.

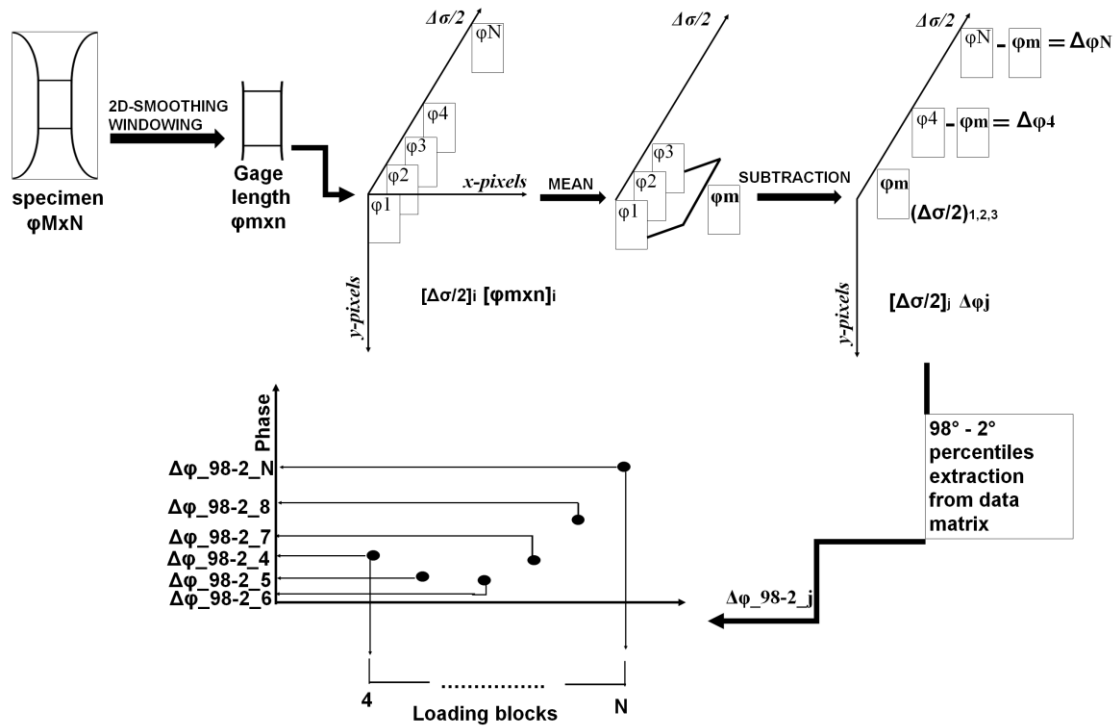


Figure 34. Phase data processing procedure: from 2D map to phase index.

After this processing procedure, the data are furtherly processed for fatigue limit estimations or graphical damage analysis. Just said procedure together with the results will be showed in the following Chapter 4.

### 3.5.4 Temperature variation of second order (Td parameter)

The temperature changes related to dissipations  $T_d$  ( $S_d$ ) were processed simply by considering smoothing and sizing of the matrix, in order to determine the 98 percentile of data by the matrix,  $S_{d\_98}$ , which is the thermal parameter related to the damage. Figure 35 provide a graphical understanding of the processing procedure.

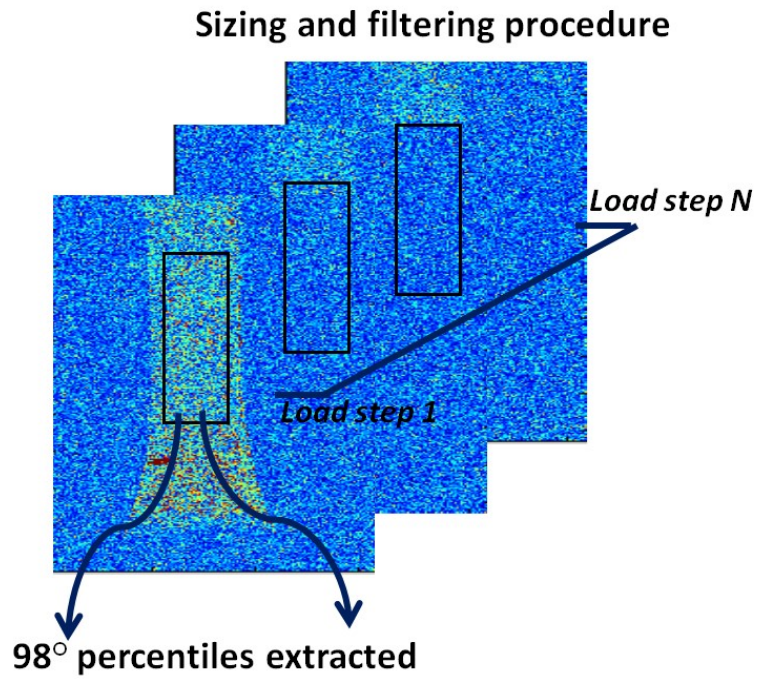


Figure 35. Processing of  $T_d$  ( $S_d$ ) data.

## Conclusions

In this Chapter, the theoretical approach based on thermographic signal analysis has been presented.

At first sight, the most important achievement of the presented model, and algorithms is such that all the theories and procedures for assessing reversible and irreversible temperature components have been unified under just one equation representing the temperature evolution. Moreover, the approach can be understood as an energetic approach since it begins by considering the energetic behaviour of the material undergoing a cyclic test. In this sense, all the assumption made on energy dissipated, involve the physical correlation between energy variations/temperature variations/physical processes which determine damage mechanisms.

Beyond the theory discussion on temperature variations, and the model presented, the equipment for performing the tests has been presented, together with the processing procedures for analysing the thermographic signal.

The innovative contents of the present Chapter, allows for a better study of the fatigue processes in metals and composites, under the point of view of localising the damage and study its propagation in the microstructure.

Finally, it is possible to state that the innovation presented in the field of experimental mechanics involves several levels from the theory to the data processing and finally to the assessment of parameters to determine quantitatively the fatigue life.

In the following chapter the most important results of the application of such the approach on metals and composites will be presented, and finally the same approach will be discussed as capable of studying the fatigue behaviour at the crack tip in the plastic region.

## References

- [181] T. Akazawa, M. Nakashima, O Sakaguchi. Simple model for simulating hysteretic behaviour involving significant strain hardening. Paper n 264. *Eleventh World Conference on Earthquake Engineering, 1996*. ISBN 0 08042822 3
- [182] X.G. Wang, V. Crupi, C. Jiang, E. Guglielmino. Quantitative Thermographic Methodology for fatigue life assessment in a multiscale energy dissipation framework. *International Journal Fatigue* 81, 249–256, 2015.
- [183] J. Kaleta, R. Blotny, H. Harig. The accumulated internal energy in the fatigue strength region. *Proceedings of the 7th International Conference On Fracture (ICF7)*, Houston, Texas, 20–24 March 1989 2, 1195-1202, 1989.

- [184] G. Meneghetti. Analysis of the fatigue strength of a stainless steel based on the energy dissipation. *International Journal of Fatigue*, 29:81–94, 2007.
- [185] R. Strubbia, S. Hereñú, I. Alvarez-Armas, U. Krupp. Short fatigue cracks nucleation and growth in lean Duplex Stainless Steel LDX 2101. *Material Science Engineering A* 615, 169-74, 2014.
- [186] C. Wang, A. Blanche, D. Wagner, A. Chrysochoos, C. Bathias. Dissipative and microstructural effects associated with fatigue crack initiation on an Armco iron. *International Journal Fatigue* 58, 152–157, 2014.
- [187] D. Shiozawa, T. Inagawa, T. Washio, T. Sakagami. Fatigue limit estimation of stainless steels with new dissipated energy data analysis. *Procedia Struct. Integrity* 2, 2091–2096, 2016.
- [188] A. Akai, D. Shiozawa, T. Sakagami, S. Otake, K. Inaba, K. Relationship between dissipated energy and fatigue limit for austenitic stainless steel. 15 *International Conference on Experimental Mechanics (ICEM 15)*, Porto 22-27 July 2012. Paper Ref. 2600.
- [189] N.F. Enke, B.I. Sandor. Cyclic plasticity analysis by differential infrared thermography. *Proceeding of the VI International Congress on Experimental Mechanics* June 7 1988, 830-835, 1988.
- [190] J.K. Krapez, D. Pacou, G. Gardette. Lock-in thermography and fatigue limit of metals. *Quantitative Infrared Thermography Journal* 6, 277-82, 2000.
- [191] A. Chrysochoos, B. Wattrisse, J.M. Muracciole, Y. El Kaïm. Fields of stored energy associated with localized necking of steel. *Journal of Mechanics of Materials and Structures* 4, 245-62, 2009.
- [192] C. Doudard, S. Calloch, F. Hild, S. Roux. Identification of heat source fields from infra-red thermography: Determination of ‘self-heating’ in a dual-phase steel by using a dog bone sample. *Mech Mater.* 42, 55–62, 2010.
- [193] T. Boulanger, A. Chrysochoos, C. Mabrub, A. Galtier. Calorimetric analysis of dissipative and thermoelastic effects associated with the fatigue behavior of steels. *International Journal Fatigue* 26, 221–9, 2004.
- [194] A. Chrysochoos, O. Maisonneuve, G. Martin, H. Caumon, J. Chezeaux. Plastic and dissipated work and stored energy. *Nucl Eng Des* 114, 323–333, 1989.
- [195] M.P. Luong. Infrared thermographic scanning of fatigue in metals. *Nuclear Engineering* 158, 363-76, 1995.
- [196] R. De Finis, D. Palumbo, F. Ancona, U. Galietti. Fatigue Behaviour of Stainless Steels: A Multi-parametric Approach. *Residual Stress, Thermomechanics & Infrared Imaging, Hybrid Techniques and Inverse Problems, Proceedings of the 2016 Annual Conference on Experimental and Applied Mechanics*, 9, 1-8, ISBN: 978-3-319-42254-1, DOI: 10.1007/978-3-319-42255-8\_1, 2016.
- [197] R. De Finis, D. Palumbo, F. Ancona, U. Galietti. Fatigue limit evaluation of various martensitic stainless steels with new robust thermographic data analysis. *Int J Fatigue* 74, 88-96, 2015.

- [198] G. La Rosa, A. Risitano. Thermographic methodology for rapid determination of the fatigue limit of materials and mechanical components. *Int J Fatigue* 22, 65–73, 2000.
- [199] J. Fan, X. Guo, C. Wu. A new application of the infrared thermography for fatigue evaluation and damage assessment. *Int J Fatigue* 44, 1–7, 2012.
- [200] V. Crupi, E. Guglielmino, M. Maestro, M. Marinò. Fatigue analysis of butt welded AH36 steel joints: Thermographic Method and design S–N curve. *Mar Struct* 22, 373–386, 2009.
- [201] B. Yang, P.K. Liaw, M. Morrison, C.T. Liu, R.A. Buchanan, J.Y. Huang, K.C. Kuo, J.G. Huang, D.E. Fielden. Temperature evolution during fatigue damage. *Intermetallics* 13, 419-28, 2005.
- [202] A. Lipsky. Rapid Determination of the S - N Curve for Steel by means of the Thermographic Method. *Adv Mater Sci Eng* 4, 1-8, 2016.
- [203] C. Mareau, V. Favier, B. Weberc, A. Galtierd, M. Berveillera. Micromechanical modeling of the interactions between the microstructure and the dissipative deformation mechanisms in steels under cyclic loading. *Int J Plast* 32–33, 106–120, 2012.
- [204] N. Connesson, F. Maquin, F. Pierron. Dissipated energy measurements as a marker of microstructural evolution: 316L and DP600. *Acta Mater* 59, 4100–15, 2011.
- [205] T. Sakagami, S. Kubo, E. Tamura, T. Nishimura. Identification of plastic-zone based on double frequency lock-in thermographic temperature measurement. International Conference of Fracture ICF11, Catania (Italy), 2015.
- [206] F. Maquin, F. Pierron. Heat dissipation measurements in low stress cyclic loading of metallic materials: From internal friction to micro-plasticity. *Mech Mater* 41, 928–942, 2009.
- [207] D. Palumbo, U. Galietti. Thermoelastic Phase Analysis (TPA): a new method for fatigue behaviour analysis of steels: TPA: A New Method for Fatigue Behaviour Analysis of Steels. *Fatigue Fract Eng Mater Struct* DOI: 10.1111/ffe.12511, 2016.
- [208] G. Frunză, E.N. Diaconescu. Hysteresis and mechanical fatigue. The annals of university “dunărea de jos “ of galați fascicle VIII, Tribology 61-66, issn 1221-4590, 2006.
- [209] A.E. Morabito, A. Chrysochoos, V. Dattoma, U. Galietti. Analysis of heat sources accompanying the fatigue of 2024 T3 aluminium alloys. *Int. J Fatigue* 29:977-984, 2007.
- [210] ASTM 1862-97- Measuring and Compensating for Reflected Temperature Using Infrared Imaging Radiometers.
- [211] M.F. McGuire. Martensitic Stainless Steels. In: McGuire MF, editor. *Stainless Steels for Design Engineers*. Asm International; 2008. p. 123–35.
- [212] R. Tomei. Criteri di scelta degli acciai inossidabili in funzione degli impieghi. In: Tomei R, editor. *La meccanica italiana*; 1981. p. 55.
- [213] J.H. Wu . High-temperature Mechanical Properties, Fatigue and Fracture Behaviour of 17–4PH stainless steel. Ph.D. Thesis. Department of Mechanical Engineering, National Central University, Taiwan R.O.C.; 2003.
- [214] M. Giannozzi, L. Baldassarre, M. Cecconi, M. Camatti , D. Becherucci , X. Coudray. About design, materials selection and manufacturing technologies of centrifugal compressors for

extreme sour and acid service. ADIPEC Technical Conference 10-13 November, Abu Dhabi(UAE), 2013..

- [215] Technical guide HOWCO group: [www.howcogroup.com](http://www.howcogroup.com)
- [216] [www.industeel.info/products/stainless-steels/ferritic-martensitic/virgo-39/](http://www.industeel.info/products/stainless-steels/ferritic-martensitic/virgo-39/). accessed on 4 November 2016.
- [217] Industeel Belgium, ArcelorMittal. Technical Data Sheet VIRGO 39—Ed 28.07. 2003. Available online: <http://industeel.arcelormittal.com/products/stainless-steels/ferritic-martensitic/virgo-17-4-ph/>
- [218] ASTM E-407 (2007). Standard Practice for Microetching Metals and Alloys. ASM International, USA.
- [219] M. Boniardi, V. Boneschi. Generalità sugli acciai inossidabili bifasici ed aspetti metallurgici della loro saldatura. Convegno Nazionale “La saldatura degli acciai inossidabili”. Bologna, Italy, November 18, 1999.
- [220] ASTM E 647–00. Standard Test Method for Measurement of Fatigue Crack Growth Rates, 2000. Available online: <http://www.astm.org/Standards/E647> (accessed on 4 November 2016).
- [221] ASTM E E466-96. Standard Practice for Conducting Force Controlled Constant Amplitude Axial Fatigue Tests of Metallic Materials. 1996. Available online: <http://www.astm.org/DATABASE.CART/HISTORICAL/E466-96.htm> (accessed on 4 November 2016).
- [222] B. Yang, P.K. Liaw, H. Wang, L. Jang, J.Y. Huang, R.C. Kuo, J.G. Huang. Thermographic investigation of the fatigue behaviour of reactor pressure vessel steels. *Mater Sci Eng A* 314, 131–9, 2001.

---

## ***Chapter 4: On The Application Of Thermographic Signal Analysis To Fatigue Of Smoothed Samples***

---

**I**n this chapter the most important achievements are presented referring to the application of thermography to study the fatigue behaviour of smoothed samples. The developed procedures are aimed to both reduce the economic and temporal costs of the experimental campaign and to furtherly provide more information about the incoming damage in the material.

In light of the presented processing procedures to assess and analyse thermal parameters, it will be discussed the Threshold and the Slope methods for assessing the fatigue limit of different stainless steels and correlated results will be presented compared with those provided by the Standards.

The presented results will involve the stress ratio effect influence on thermal parameters, in particular on thermoelastic phase shift which is related to the internal dumping of the materials, secondly it will be discussed the influence of microstructure on thermal signals, since the presence of different phase materials requires suitable procedures and data analysis for estimating the fatigue properties.

The example discussed is represented by biphasic stainless steels which involve in double phase microstructure with ferritic and austenitic grains. In this case, the presence of a interphase-grain boundary activity influences both the formation and nucleation of crack depending on the fatigue regime of loading.

Moreover, it will be shown also the graphical analysis for assessing the intrinsic dissipations in the material connected to the formation of crack processes. In this sense, the damage mechanisms determination and monitoring will be presented by highlighting that all the parameters allow assessing complementary information on fatigue behaviour of materials.

The importance the approach is such that it leads to the monitoring of the heat dissipative processes in real and operating components.

## 4.1 Multi-signal analysis for fatigue life estimations

In the present section, two methods implemented for fatigue limit estimation will be presented: the threshold method which can be applied on the thermal signal parameters, and the method based on the evaluation of the slope of phase data series. In effect, the reason for performing a different method for processing phase data is because of the nature of these latter. These latter are very noisy, especially at relative lower stress amplitudes, moreover, due to low signal-to-noise ratio in the first loading levels of the dispersion of the data is high and the trend of post-processed phase data presents a typical ‘spoon’ behaviour.

### 4.1.1 The Threshold Method

The proposed method allows for assessment of the stress amplitude value for which damage phenomena in material become statistically significant in terms of temperature change. This stress value will be characterized by a  $\Delta T_{max}$  statistically different from those obtained in the first five steps and it represents an estimate of the fatigue limit [1].

The method is applied on  $\Delta T_{max}$  data evaluated for each value of  $\Delta\sigma/2$  and consists of the following stages:

1. linear regression analysis of the first five couples of data ( $\Delta\sigma/2, \Delta T_{max}$ ) and evaluation of the best fit line ( $y = mx + q$ ),
2. evaluation of residuals of  $\Delta T_{max}$  ( $\Delta T_{max\_r}$ ) for each step by means of the following equation:

$$(\Delta T_{max\_r})_i = [(\Delta T_{max})_i - m \left( \frac{\Delta\sigma}{2} \right)_i + q] \quad \text{for } i=1,2,\dots,N \quad (16)$$

where N is the number of the loading steps,

3. evaluation of standard deviation  $\sigma_{\Delta T_{max\_r}}$  of residuals ( $\Delta T_{max\_r}$ ) of the first five data of all tests (in this case three specimens and then a total of fifteen data),
4. evaluation of the threshold value  $\Delta T_{h\_6\sigma} = 6 * \sigma_{\Delta T_{max\_r}}$ ,
5. evaluation of the first loading step (or  $\Delta T_{max\_r}$  data) for which the condition  $(\Delta T_{max\_r})_N > \Delta T_{h\_6\sigma}$  is verified. From this loading step, the fatigue damage is considered to be statistically significant.

The value of  $\Delta\sigma/2$  in correspondence with this loading step provides an estimate of fatigue



limit ( $\sigma_L$ ).

In figures 1 is represented a comparison between the well-known in literature graphical method (Luong's method, presented in previous Chapter 2-Thermal Methods), and the applied just explained procedure.

Once the threshold value is assessed, it is possible to stop the test procedure without bring the sample to the failure. This could be the onset of a new type of fatigue tests: the 'non-destructive' fatigue tests.

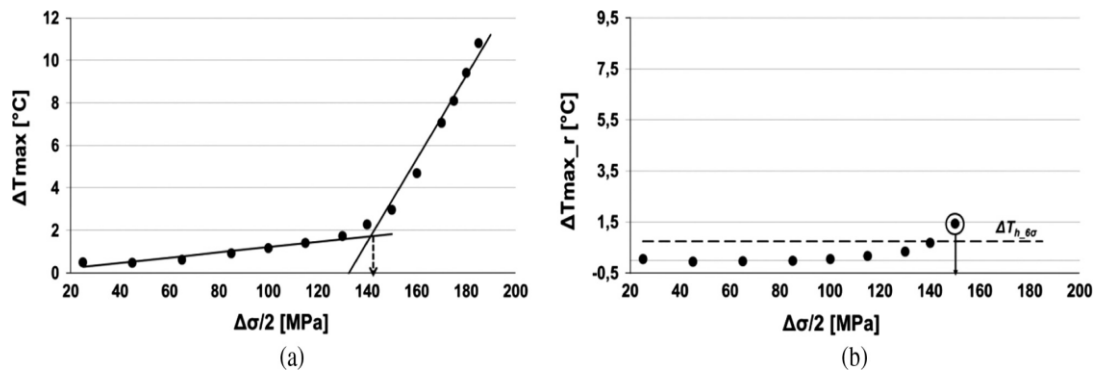


Figure 1. Fatigue limit evaluation: (a) comparison between Luong's method and (b) proposed method, ASTM A 182 grade F6NM, specimen 1.

For instance, in Table 1 thermal data relative to ASTM A 182 grade F6NM are present, obtained by the filtering procedure. For each specimen, the constants  $m$  and  $q$  were evaluated. In Table 1 the residuals used to calculate the values  $\sigma_{\Delta T_{max\_r}}$  and  $\Delta T_{h\_6\sigma}$  are shown. In this way-for example-the value of  $\Delta T_{h\_6\sigma}$  statistically significant for the specimen 1 is 1.44 and the fatigue limit is 150 MPa.

		specimen 1		specimen 2		specimen 3		$\sigma_{\Delta T_{max\_r}}$ [°C]	$\Delta T_{h\_6\sigma}$ [°C]
N	$\Delta\sigma/2$ [MPa]	$\Delta T_{max}$ [°C]	$\Delta T_{max\_r}$ [°C]	$\Delta T_{max}$ [°C]	$\Delta T_{max\_r}$ [°C]	$\Delta T_{max}$ [°C]	$\Delta T_{max\_r}$ [°C]		
1	25	0,29	0,06	0,94	0,25	0,7	0,07	0,12	0,72
2	45	0,17	-0,05	0,4	-0,21	0,6	-0,04		
3	65	0,19	-0,03	0,36	-0,17	0,54	-0,1		
4	85	0,2	-0,02	0,38	-0,07	0,64	-0,01		
5	100	0,27	0,05	0,6	0,21	0,72	0,07		
6	115	0,38	0,17	0,78	0,45	0,83	0,18		
7	<b>130</b>	0,55	0,34	1,23	<b>0,96</b>	1,1	0,44		
8	<b>140</b>	0,9	0,69	1,39	1,16	1,46	<b>0,8</b>		
9	<b>150</b>	1,65	<b>1,44</b>	2,16	1,97	2,13	1,47		
10	160	3,52	3,32	3,81	3,66	3,97	3,31		
11	170	5,89	5,68	5,96	5,85	6,39	5,72		
12	175	6,79	6,59	7,34	7,25	7,43	6,76		
13	180	8,12	7,92	9,07	9	8,43	7,76		
14	185	9,34	9,13	9,98	9,93	10,03	9,36		
<i>m</i>		- <b>1,7*10<sup>-4</sup></b>		<b>-4*10<sup>-3</sup></b>		<b>2,6*10<sup>-4</sup></b>			
<i>q</i>		<b>0,23</b>		<b>0,79</b>		<b>0,62</b>			

Table I. Thermal data of ASTM A 182 grade F6NM, specimen 1 after processing: graphic parameters: *m*, *q*; temperature residuals  $\Delta T_{max\_r}$ ; standard deviation of residuals,  $\sigma_{\Delta T_{max\_r}}$ ; threshold value  $\Delta T_{h\_6\sigma}$  for evaluating fatigue limit (the results of procedure for each specimen are shown in bold).

#### 4.1.1.1 Application on Martensitic Stainless Steels

In this paragraph a comparison between “traditional graphic method” [2] and the proposed procedure for thermal data analysis and subsequent evaluation of fatigue limit was performed. For 17-4 PH material and ASTM A182 a “stair case” test has been carried out with a run-out limit of  $10^7$  cycles in order to obtain a comparison with the classic procedure. All the results are summarized in tables II-VI for each material. Comparable results were obtained between the two thermographic methods used. However, the proposed method allows for an early-stage automatic and univocal determination of the fatigue limit.

Differences were obtained between thermal data and the Stair Case method. In particular, the fatigue limit obtained with thermal data is lower than with the Stair Case method for all tested materials. Such difference can be attributed to run-out cycles imposed to choose the fatigue limit. In fact, for steels including martensitic lattice types (such as 17-4PH) [3] there is a difference between the fatigue limit evaluated at  $10^7$  and  $10^9$  cycles (around 100-200 MPa). Therefore, thermal dissipations seem linked to damage fatigue phenomena that can occur for load levels lower than endurance evaluated at  $10^7$ .

Specimen	Traditional Graphic Method ( $\sigma_L$ ) [MPa]	Proposed Method ( $\sigma_L$ ) [MPa]	Stair Case Method ( $\sigma_L$ ) [MPa]
1	141,4	150,0	
2	146,0	130,0	
3	129,3	140,0	
Average	<b>138,9</b>	<b>140,0</b>	<b>169,3</b>
Standard Deviation	<b>8,6</b>	<b>10,0</b>	<b>4,4</b>

Table II. ASTM A 182 F6NM fatigue results: comparison between graphic and proposed methods.

Specimen	Traditional Graphic Method ( $\sigma_L$ ) [MPa]	Proposed Method ( $\sigma_L$ ) [MPa]	Stair Case Method ( $\sigma_L$ ) [MPa]
1	207,7	200,0	
2	200,2	200,0	
3	207,0	205,0	
Average	<b>205,0</b>	<b>201,7</b>	<b>212,1</b>
Standard Deviation	<b>4,1</b>	<b>2,9</b>	<b>3,8</b>

Table III. 17-4 PH fatigue results: comparison between graphic and proposed methods.

Specimen	Traditional Graphic Method ( $\sigma_L$ ) [MPa]	Proposed Method ( $\sigma_L$ ) [MPa]
1	129,2	142,5
2	127,8	145,0
3	139,2	140,0
Average	<b>132,1</b>	<b>142,5</b>
Standard Deviation	<b>6,2</b>	<b>2,5</b>

Table IV. AISI 422 fatigue results: comparison between graphic and proposed methods.

Specimen	Traditional Graphic Method ( $\sigma_L$ ) [MPa]	Proposed Method ( $\sigma_L$ ) [MPa]
1	157,8	150,0
2	154,4	150,0
3	142,8	165,0
Average	<b>151,7</b>	<b>155,0</b>
Standard Deviation	<b>6,4</b>	<b>8,7</b>

Table V. X4 CR NI MO 16-5-1 fatigue results: comparison between graphic and proposed methods.

The proposed method leads to a new way of performing fatigue tests with thermal analysis. As said, in many works (e.g. [1], [4],[5]) the procedure used to perform fatigue tests consists in incremental cyclic loads imposed on the specimen up to failure and the evaluation of fatigue limit takes into account, in particular, the temperature variations of the last loading steps.

By applying the proposed procedure it is possible to obtain fatigue limit avoiding specimen failure: in fact, the test can be stopped when the threshold value  $\Delta T_{h\_6\sigma}$  is reached (figure 1). Moreover, a more accurate assessment of fatigue limit is possible. When the threshold  $\Delta T_{h\_6\sigma}$  is reached, it is possible to refine the test decreasing the load back to the previous step and imposing smaller load increments.

As shown in tables II-V, the proposed method provides discrete value of fatigue limit. By imposing smaller load increments - as just said - the standard deviation (which corresponds to load increment for ASTM A 182 in table of Appendix A) could decrease. This approach can improve the evaluation of fatigue limit.

The results are in good agreement with traditional graphic thermographic method used in literature. However, thermographic technique seems to underestimate fatigue limit in respect to the Stair-Case method. This is probably due to the fact that fatigue limit is conventional at  $10^7$  cycles (see very high cycle fatigue phenomena [3]). Further works will focus on studying and comparing of the fatigue limit at  $10^7$  and  $10^9$  cycles with both thermal and Stair Case for very high cycle fatigue.

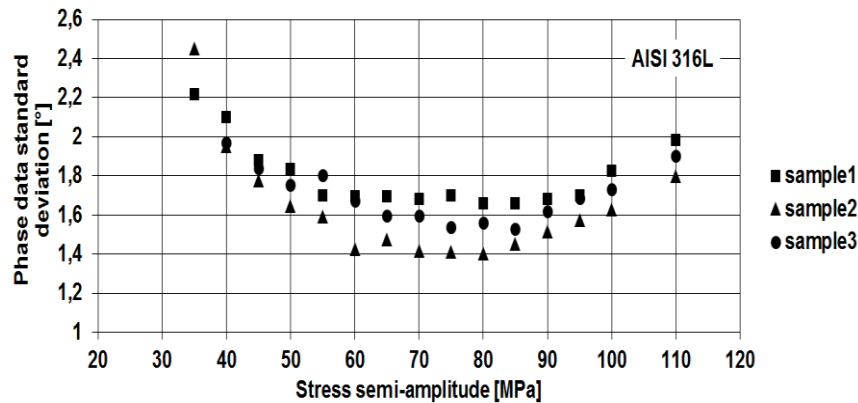
#### 4.1.1.1.2 Comparison between Austenitic and Martensitic Stainless Steels

The potential of the technique are related not only to the possibility of in-situ and online detection of the damage but also, the determination of the fatigue limit of materials.

The data considered for analysis described in section 3, are the standard deviation values extracted for each loading levels of the test. In particular, the raw data for austenitic stainless steel are represented in Figure 2, [6].

Phase standard deviation (figure 2(a)) show a typical trend represented by initial reduction followed by an increase. This behaviour could be explain by the fact that in the prime loading level (elastic regime) the signal-to-noise ratio is so low due to the absence of dissipative phenomena in the matrix, and thus data scattering is high. Conversely, by increasing the stress semi-amplitude, signal becomes higher with respect to noise that remains constant, and data scattering is reducing in the last part of the test occurring in plastic regime.

Figure 2b show the raw data for  $S_d$  parameter, in particular 98<sup>th</sup> percentiles have been extracted from the matrix,  $S_{d\_98}$ . In this case, two trend can be pointed out: the data remains roughly constant for loading level occurring in elastic regime, firstly, as the load increases the series became more sloped.



(a)

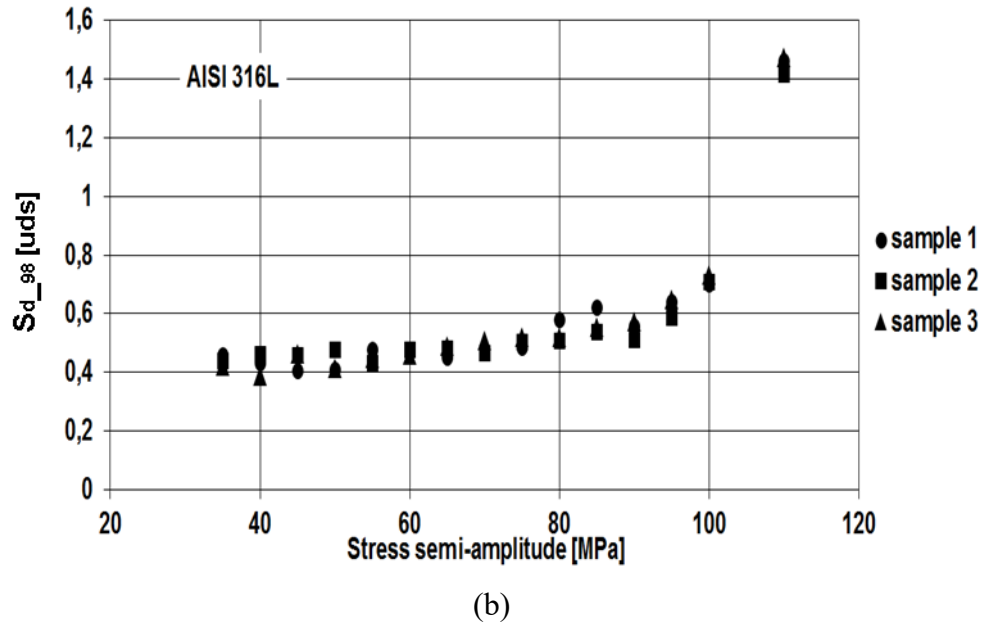
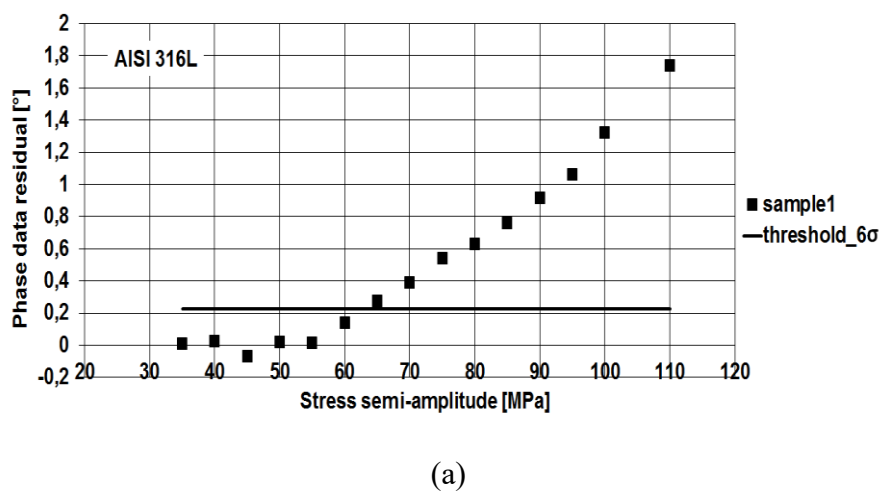


Figure 2. AISI 316L, (a) standard deviation of phase data and (b) standard deviation of  $Sd_{98}$  data versus loading level (stress semi amplitude of applied load) for overall tests.

In figure 3, residual analysis allows for obtaining a threshold value ( $\mu+6\sigma$ ) referring to the first five data couples ( $\Delta\sigma/2$ ;  $\varphi$ ) or ( $\Delta\sigma/2$ ;  $Sd_{98}$ ) of the series showed in figure 2a-b. By adopting the threshold method, all the criticalities related to the application of graphic method [1][7], such as the choice of the breakdown point of data series, are avoided. In this way, an objective method to evaluate fatigue limit is performed to avoid misinterpretation of data series.



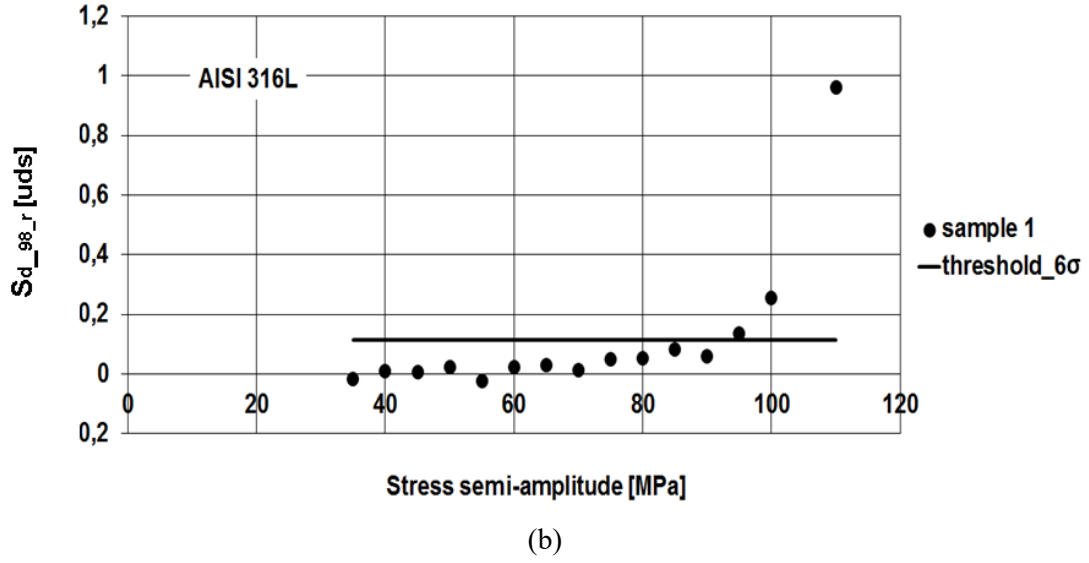


Figure 3. AISI 316L, (a) phase data residual and (b) S2 data residual, and thresholds versus loading level (stress semi amplitude of applied load) for sample 1.

The method has been applied to both austenitic and martensitic microstructures. The results are shown in Table VI. AISI 316L shows large scattering between mean values of fatigue limit found by using phase data and Sd<sub>98</sub> data. As it is shown in figure 3, the variation of signal Sd<sub>98</sub> are very low in value, then it results difficult to fix appropriate threshold. For X4 Cr Ni Mo 16-5-1, both the phase and Sd<sub>98</sub> parameters show very close fatigue limits.

In literature, little data is available referring to the fatigue limit of these stainless steels at R=0.5. In fact, in order to make a comparison with Thermal data results, the fatigue limit of AISI 316L has been extrapolated by using the Goodman model [8]. In order to provide a reference for X4 CR NI MO 16-5-1 of the fatigue limit at R=0.5, the same procedure as adopted for austenitic steel, has been applied to achieve an estimation of the fatigue limit.

The reference value of the fatigue limit for X4 Cr Ni Mo 16-5-1 is 187 MPa. Both  $\phi$  and Sd<sub>98</sub> show good agreement with reference values and, moreover, they may be used for describing the fatigue behaviour of X4 Cr Ni Mo 16-5-1 stainless steel.

A standard value of fatigue limit at the adopted loading ratio, was estimated by applying the Goodman model [8]:

$$\frac{\sigma_a}{\sigma_0} + \frac{\sigma_m}{\sigma_{UTS}} = 1 \quad (1)$$

In which  $\sigma_a$  represents the stress amplitude of unknown fatigue limit at R=0.5,  $\sigma_m$  is the mean stress value,  $\sigma_0$  is the amplitude of fatigue limit at R=-1, while  $\sigma_{UTS}$  is the ultimate tensile stress of material. By rewriting the amplitude (equation 2) and the mean stress (equation 3) in function of maximum stress:

$$\sigma_a = \frac{(1-R)\sigma_{\max}}{2} \quad (2)$$

$$\sigma_m = \frac{(1+R)\sigma_{\max}}{2} \quad (3)$$

By substituting the values of amplitude and means stress, as shown in Eq.2 and Eq.3, Eq.1 provides the value of fatigue limit. For austenitic stainless steel, the values of  $\sigma_0 = 120 \text{ MPa}$  and  $\sigma_{UTS} = 515 \text{ MPa}$  have been provided by [9] respectively the amplitude of fatigue limit at  $R=-1$  and ultimate tensile strength. The value of fatigue limit found was 70.63 MPa. The result of the application of threshold method on austenitic stainless steel shows an overestimation of the fatigue limit with respect to the reference found. Referring to the phase shift, results fit very well with those provided by the reference of 70.63 MPa, while for the  $S_{d\_98}$  results, it seems that the method overestimates the fatigue limit.

The amplitude of the thermal signal at double the mechanical frequency is very low, and moreover, the signal-to-noise ratio is low. The influence of noise on the  $S_{d\_98}$  parameter affects the evaluation of the fatigue limit by determining an overestimation of the fatigue limit. This difference between the parameters  $\phi$  and  $S_{d\_98}$ , will enhance the development of new processing procedures.

By applying the same procedure as used for austenitic AISI 316L, the reference value of the fatigue limit for X4 Cr Ni Mo 16-5-1 is 187 MPa. All the assessed parameters ( $\phi$ ,  $S_{d\_98}$ ) show good agreement with the value of reference and moreover, may be used for describing the fatigue behaviour of X4 Cr Ni Mo 16-5-1 stainless steel, except for a slightly higher value of the standard deviation for phase data. As expected, different behaviour of phase and  $S_{d\_98}$  parameters were obtained for different materials and in this regard, further works will be focused on the optimization of the proposed procedure for each material.

SAMPLE	AISI 316L <sup>1</sup>		X4 Cr Ni Mo 16-5-1 <sup>1</sup>	
	$\phi$	$S_{d\_98}$	$\phi$	$S_{d\_98}$
1	65,00	95,00	180,00	180,00
2	75,00	95,00	165,00	190,00
3	90,00	100,00	190,00	185,00
MEAN	76,67	96,67	178,33	185,00



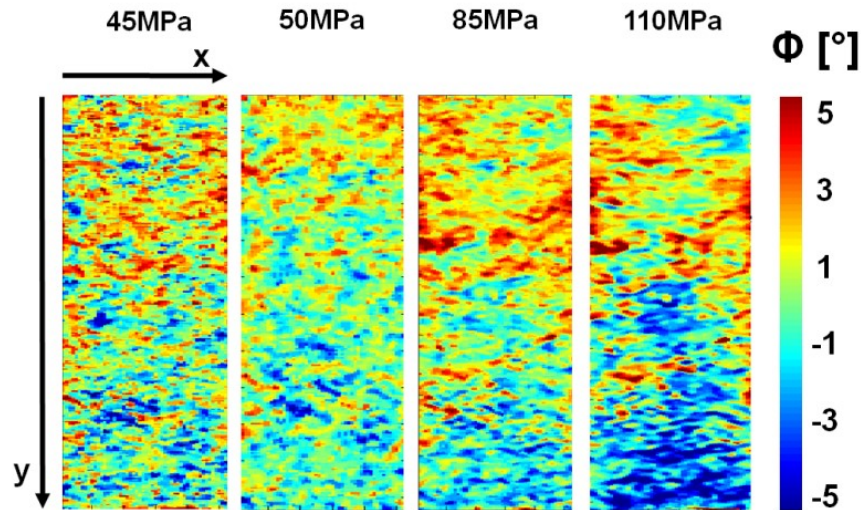
STD.DEV.	12,58	2,89	12,58	5,00
----------	-------	------	-------	------

Table VI. Fatigue limit evaluation results by using both parameters for AISI 316L and X4 Cr Ni Mo 16-5-1. <sup>1</sup>results expressed in mm.

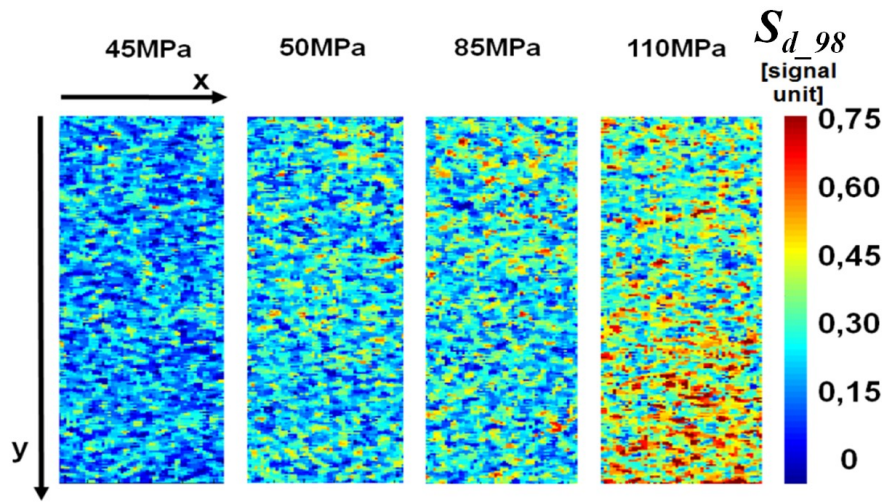
In this section the different behaviour of material (austenitic lattice and martensitic lattice), will be discussed in terms of phase shift  $\varphi$  and second order parameter  $S_{d\_98}$ .

Figure 4 represents respectively  $\varphi$ ,  $S_{d\_98}$  maps for AISI 316L austenitic steel, the maps have been provided by MatLab® software after several processing steps as described in previous chapter 3.

Figure 4(a), shows phase shift data, referred to the gage length of specimen. In particular high stress gradients affect the underlying part of gage length (85-110 MPa), and plasticization seems occur at stress level above 50 MPa in localized zones. Figure 4(b) shows  $S_{d\_98}$  values. Slight increase in  $S_{d\_98}$  thermal signal appears starting from 50 MPa in localized areas, but the most significant variation occurs at 110 MPa in the underlying part of matrix. This area is coincident with the one found in Figure 4(a) referring to phase data. In this case, the large variation of  $S_{d\_98}$  at 110 MPa can be explained as the large energy involved in damage, thus  $S_{d\_98}$  parameter confirms phase data results, referring to the damaged zone.



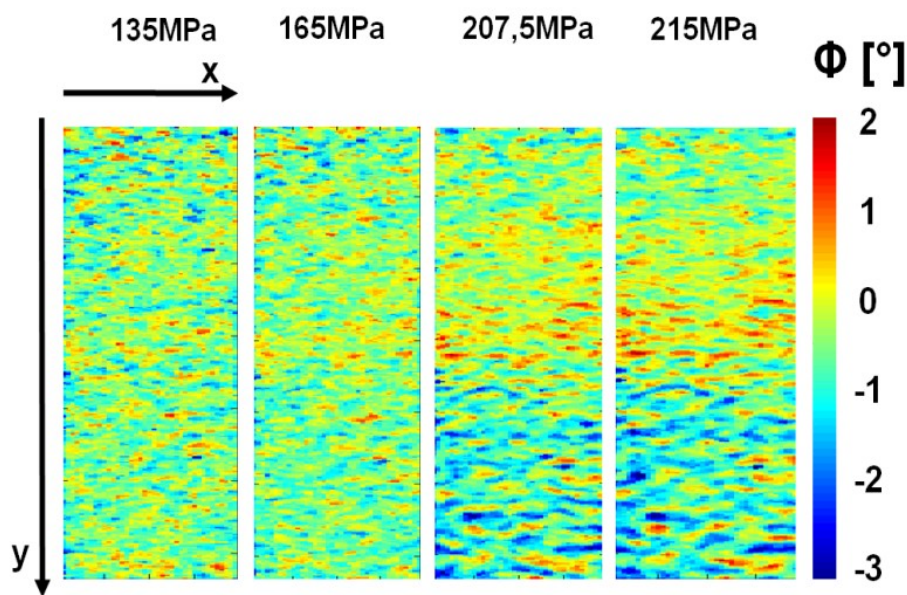
(a)



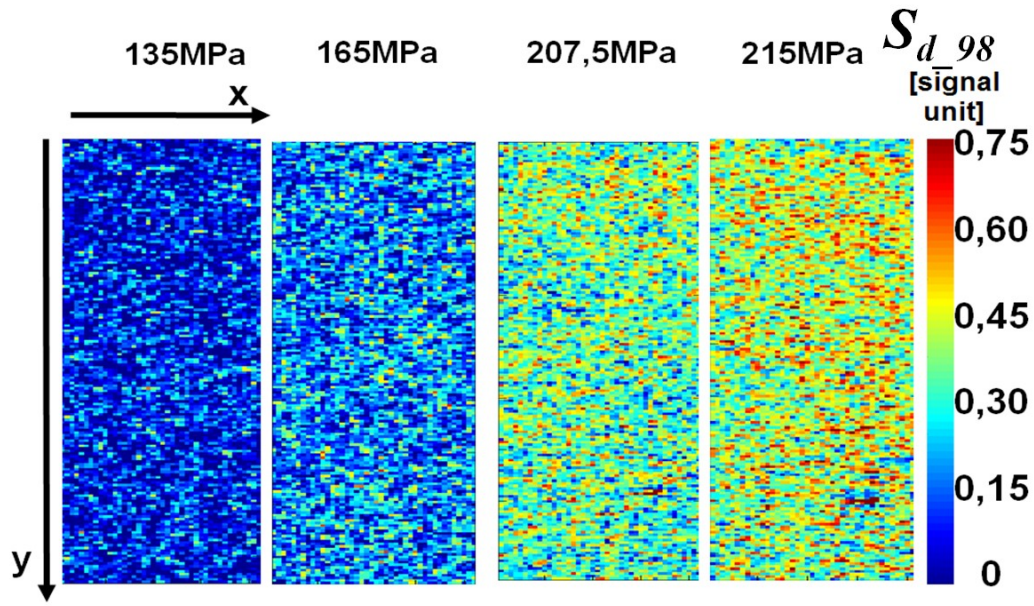
(b)

Figure 4. AISI 316L, specimen 1, maps of (a) phase data, (b) second order parameter.

In Figure 5 are represented phase maps and  $S_{d\_98}$  maps for martensitic microstructure of X4 CR NI MO 16-5-1. The most important effects appear starting from 207.5 MPa as depicted in Figure 5a and b for both parameters. In Figure 5a, phase data shows the most stressed area in underlying part of gage length, in particular in this area some cluster of nearby positive/negative values appear localized, with evidence starting from 165 MPa. Even for this microstructure, the localization of dissipative phenomena seem to be confirmed by  $S_{d\_98}$  parameter map (Figure 5b) which allows for detecting the same area in the phase data.



(a)



(b)

Figure 5. X4 Cr Ni Mo 16-5-1, specimen 1, maps of (a) phase data, (b) second order parameter.

By comparing Figures 4 and 5 it is possible to point out the difference between different microstructure affecting phase data: in fact the phase shift ranges between  $-5/5$  degree for austenitic lattice while for martensitic structure it ranges between  $-2/3$  degree. The interval of variation of  $S_{d\_98}$  is roughly similar for both materials. Therefore, phase data could be used as indicator of the microstructure behaviour in chapter 5, it will also seen that the phase shift, assumed different values for both the materials, in the crack tip region. Results demonstrate that the two parameters related to dissipative phenomena, could be adopted in synergetic way to characterise the damage processing in the lattice during fatigue tests.

#### 4.1.1.1.3 Application on Duplex Stainless Steels

In this section the application of threshold method of a biphasic steel ASTM A890 grade 4a will be presented, compared with the behaviour The of AISI 316 and 17-4 PH. The values of fatigue limit obtained by applying the Threshold Method are represented in Table VII a, b, c, for each estimated parameter ( $T_{max}$ ,  $S_{slope}$ ,  $T_{mean\_in}$ ) assessed according the procedure presented in paragraph 3.5.1.

Moreover, for each material a reference value has been determined by performing standard fatigue tests. The Dixon method, applied on seven samples of AISI 316, provided a fatigue limit of 64.58 MPa (standard deviation 9.27 MPa). Staircase set up for 17-4PH using fifteen specimens, provided a fatigue limit of 212 MPa (standard deviation 4.38 MPa). These results

and all the information referring to Standard Test methods are reported in Table VIII(a) (AISI 316) and Table IX(b) (17-4PH).

For Duplex stainless steel, the reference value has been determined by considering Goodman's diagram and knowing the value of the fatigue limit at  $R=-1^{10}$  and Ultimate Tensile Strength (determined by performing a tensile test <sup>11</sup>, as described in the previous section).

Table VII summarizes the results obtained for all tested materials and the comparison with standard methods.

For Duplex stainless steel (Table VIIa), the value of fatigue limit calculated by using  $S_{lope}$  and  $T_{mean\_in}$  parameters is in agreement with the reference value of 122 MPa, while  $T_{max}$  parameter seems to overestimate the fatigue limit with respect to the reference.

An overestimation of the fatigue limit value is obtained considering  $T_{mean\_in}$  and  $T_{max}$  for the austenitic steel (Table VIIb), while  $S_{lope}$  provides a value very close to the Dixon method.

In Table VIIc, the estimated fatigue limit is reported by using the three indexes on 17-4PH steel. The  $S_{lope}$  allows a suitable fatigue limit estimation, very close to the value provided by the Staircase method, while  $T_{mean\_in}$  and  $T_{max}$ , seem to slightly underestimate the fatigue limit. The reason for a slight underestimation of the fatigue limit could be explained by examining Figures 6a-b-c, in which the thermal trends,  $T_{mean}$ , have been represented for each material at three loading levels: elastic-elastoplastic-plastic regimes.

For both duplex and austenitic stainless steels, the signal in the elastic regime is very noisy, even at stress levels near the fatigue limit. Moreover, some difficulties arise for determining the  $T_{max}$  univocally. Moreover, the noisiness of the thermal signal explains the scattering in graphs of  $S_{lope}$  and  $T_{mean\_in}$  in Figures 6a-c at stress levels before the fatigue limit.

In this case, even Figure 6c demonstrates a noisy  $T_{mean}$  pattern for loading cycles, which affects the estimation of fatigue limit. However, the noise reduces in the final loading levels (Figure 6a-b-c).

Martensitic lattice, a more brittle material, presents a well-defined signal trend (Figure 6b) for each loading level. At loading levels near the fatigue limit, the temperature ( $T_{mean}$ ) exhibits a well-defined pattern in which it is possible to assess univocally all the quantities:  $T_{max}$ ,  $S_{lope}$  and  $T_{mean\_in}$ .

In summary,  $T_{max}$  is the index more affected by the 'quality' of the temperature signal while  $S_{lope}$  seems more robust and very promising as regards a reduction of the experimental campaign since it can be evaluated in the first stage of the temperature trend.

DUPLEX A890 GRADE 4A STEEL (values in MPa)			
Sample/Parameter	$T_{max}$	$S_{slope}$	$T_{mean\_in}$
P1	130.00	135.00	120.00
P2	130.00	125.00	120.00
P3	135.00	125.00	135.00
Average	<b>131.67</b>	<b>128.33</b>	<b>125.00</b>
Standard Deviation	<b>2.89</b>	<b>5.77</b>	<b>8.66</b>
Reference Value: Goodman Modified Diagram			<b>122.00</b>

(a)

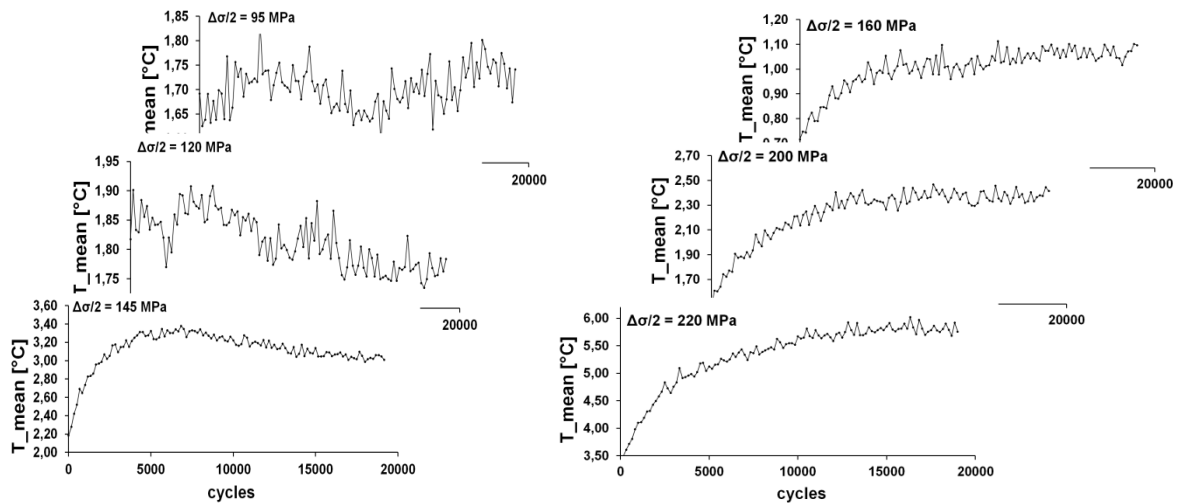
AISI 316 AUSTENITIC STEEL (values in MPa)			
Sample/Parameter	$T_{max}$	$S_{slope}$	$T_{mean\_in}$
P1	70.00	65.00	65.00
P2	85.00	70.00	80.00
P3	85.00	65.00	75.00
Average	<b>83.33</b>	<b>66.67</b>	<b>73.33</b>
Standard Deviation	<b>2.89</b>	<b>2.89</b>	<b>7.64</b>
Reference Value: Dixon Method		<b>64.58</b> (average) <b>9.27</b> (std.dev.)	

(b)

PRECIPITATION HARDENING 17-4 MARTENSITIC STEEL (values in MPa)			
Parameter Sample	$T_{max}$	$S_{lope}$	$T_{mean\_in}$
P1	205.00	220.00	195.00
P2	200.00	205.00	210.00
P3	205.00	210.00	215.00
Average	<b>203.33</b>	<b>211.67</b>	<b>206.67</b>
Standard Deviation	<b>2.89</b>	<b>7.64</b>	<b>10.41</b>
Reference Value: Staircase Method		<b>212.00</b> (average) <b>4.38</b> (std.dev.)	

(c)

Table VII. Fatigue Limit evaluation for (a) Duplex, (b) 17-4PH and (c) AISI 316





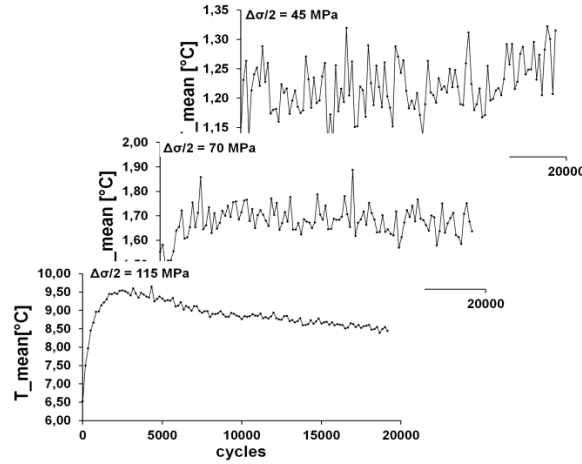


Figure 6. Mean temperature pattern toward cycles for three stress levels of the first sample of: (a) Duplex stainless steels, (b) 17-4 PH (c) AISI 316.

### 4.1.2 The Slope Method

The assessment of the fatigue limit by analysing the phase data involves a specific data analysis algorithm. The calculations assume that the fatigue limit is “the point of the series, from which the signal prevails over the noise”. Following this, a slope analysis was performed to determine the point of the slope change, which is the first positive value of the series ( $\Delta\phi$  threshold is 0 degrees).

The method has been already successfully adopted on the phase data of composite materials in the work of [12] as will be presented in paragraph 4.4.

By considering the typical high scattering trend of phase data in the first loading cycles, a new procedure has been developed to estimate the fatigue limit of material. For each specimen and for each sub-step, the adopted procedure consists of:

1. For  $i=2:N-1$  with step 1, linear regression analysis of three data couples  $(\frac{\Delta\sigma}{2}_{i-1}; \phi_{i-1})$ ,  $(\frac{\Delta\sigma}{2}_i; \phi_i)$ ,  $(\frac{\Delta\sigma}{2}_{i+1}; \phi_{i+1})$ , and evaluation of the slope  $m_i$  of the best fit line ( $y=mx+q$ ). where  $N$  represents the number of loading steps and  $\phi$  is the thermoelastic phase shift parameter.
2. the previous point provides the vector of the slope data of dimension  $(N-2)$ ,
3. the evaluation of the first loading step for which the condition :  $m_i > 0$  is verified. The first loading step exceeding the condition is considered the estimation of fatigue limit. In this case,  $m_i$  are considered rounded to the nearest hundredth.

In this way, the adopted threshold for slope method is understood as the loading step that reaches the minimum value of data, and then the minimum in the dispersion of data, is considered to be the fatigue limit of material.

In paragraph 4.2 an interesting application of the slope method on a martensitic stainless steel will be presented. The slope methods is substituting the methods for determining fatigue life by using thermoelastic phase data. In Chapter 5 the application of thermographic signal analysis on composites involve the use of slope method on phase data.

## **4.2 Fatigue Damage and Fatigue regimes on Metals: Stress Ratio Influence and Graphic Analysis of Intrinsic Dissipations**

The presence of viscous behaviour of the material is very influent on temperature variations since it produces a second order temperature effect or thermoelastic phase shift [13]. Viscous behaviour is also promoted by stress ratio [14] since it determines the morphology of hysteresis loop and besides the quantity of heat produced is correlated to damage. In fact, R-ratio is of great importance in fatigue testing [15-24], referring to the crack formation/propagation at different fatigue regimes (LCF, VHCF etc.) and referring to fracture toughness [25-27] since it is a common opinion that the fatigue strength reduces as R-ratio increases [16][20-21].

However, even if the stress ratio is an imposed input parameter affecting macroscopic behaviour of material, several studies [28-32] demonstrate how, in presence of dissipative mechanisms (crack nucleation/initiation/propagation), locally the stress amplitude conditions could differ from the imposed ones, due to the incoming plasticization effects.

In the work of [41] it has been observed that, at the notch root, the accumulation of deformation involves signal inversion of R ( $R < 0$ ). The phenomenon is completely governed by plastic phenomena, which, also blur any other effect such as, for example, the presence of residual stresses [31].

The aim is to give an overall view of the capability of the presented four indexes provided by the analysis of the same thermal sequence data to describe the fatigue behaviour of a martensitic stainless steel at different loading ratios.

The attention is focused on:

- The phase shift of thermoelastic signal (Thermoelastic Phase Analysis – TPA approach [13]) related to the internal dumping of material and plastic phenomena, the value is null in the event that damage is absent.
- The amplitude of second order temperature signal [33-35], related to heat dissipated in the material in presence of damage.
- The total temperature signal variations strictly related to the mean temperature increase [36-38], a well-known thermal index for fatigue life evaluations.

- The thermoelastic signal variations correlated with the first stress invariant [39].

During an hysteretic process, as previously explained the:

- Unloading of viscous behaviour of the lattice, which is present with a low effect at relatively low stress amplitudes. This effect becomes important at higher stress values [14][38].
- Internal stress gradients produced by the onset of damage processes which produce phase shift [4].

these phenomena involve in losing the adiabatic conditions determining a the phase variation from 0° (or 180°) condition.

The results will be presented for martensitic stainless steel ASTM A182 F6NM tested at two stress ratio (0.5, -0.1) by highlighting the influence of the stress ratio and the possibility to achieve complementary information for studying the damage behaviour.

A critical discussion on the influence of loading ratio on the specific thermal index will be presented, after the application of presented processing algorithms.

The results of the application of processing procedure, previously explained (Chapter 3, paragraph 3.5.3) for phase data are represented in Figure 7(a) for R=-0.1 and Figure 7 (b) for R=0.5 for three samples.

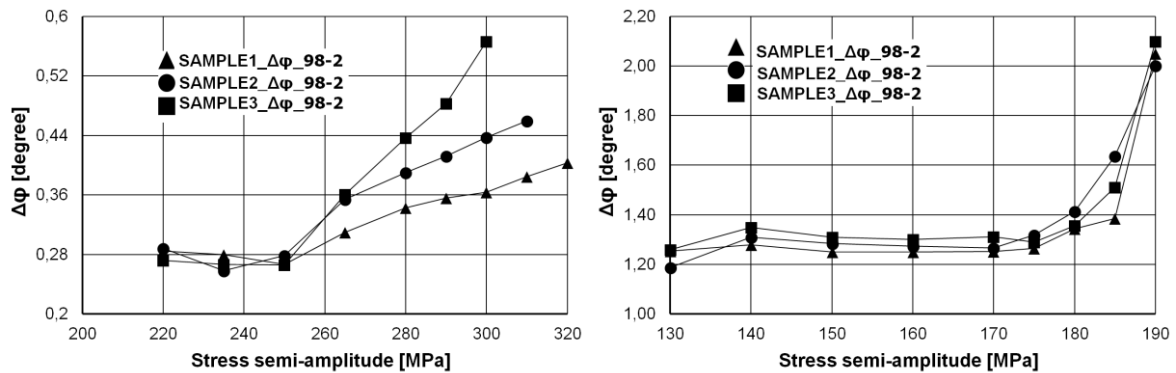


Figure 7. Results: phase data ( $\Delta\phi_{98-2}$ ) at R=-0.1 (a) and R=0.5 (b).

In Figures 7 (a) and (b) the test seems to be very reproducible, since the data scatter is low, even the conditions of each test can vary from test to another.

It has been observed also, that the higher the stress ratio is, the higher the phase values are: at R=0.5 the phase interval ranges between 1.2-2 degrees, while at R=-0.1 the phase variation is roughly 0.3-0.6 degrees.



A possible explanation can be due to the stress amplitude effect. At smaller stress amplitudes (higher 'R'), the hysteresis loop is flattened, the plastic phenomena related imposed plastic stress regime prevails on viscous phenomena [8]. On the contrary, when the stress amplitude is wider, the viscous phenomena are predominant. The phase signal seems more sensitive to dissipative phenomena related to plastic stress regime. Generally, brittle materials, such as martensitic steels, behave with lower internal damping [40], which can justify the different ranges of variation of ' $\Delta\phi_{98-2perc}$ ' at different loading ratios.

However, locally, mostly in correspondence with plastic zones [32], the loading ratio can switch into negative values ( $R < 0$ ), even if the macroscopic imposed R is positive, making any considerations difficult.

Referring to the thermoelastic signal, in Figures 2, the output is represented in terms of  $S_{the\_98}$  curves at  $R = -0.1$  (Figure 8a) and  $R = 0.5$  (Figure 9b). It is evident that the range of variation of  $S_{the}$  is the same, even if the fatigue mechanisms are different.

Even if all tests at two different loading ratios provide stress blocks in both elastic and plastic regimes, a significant signal increase is obtained before the yield strength for  $R = -0.1$ , Figure 8a, and after the yield value for  $R = 0.5$ , Figure 8b. In fact, as already explained, the thermoelastic signal depends on the stress semi-amplitude and then in the case of  $R = -0.1$  the relative higher semi-amplitude stresses induce non-linearity of the signal before the yield stress.

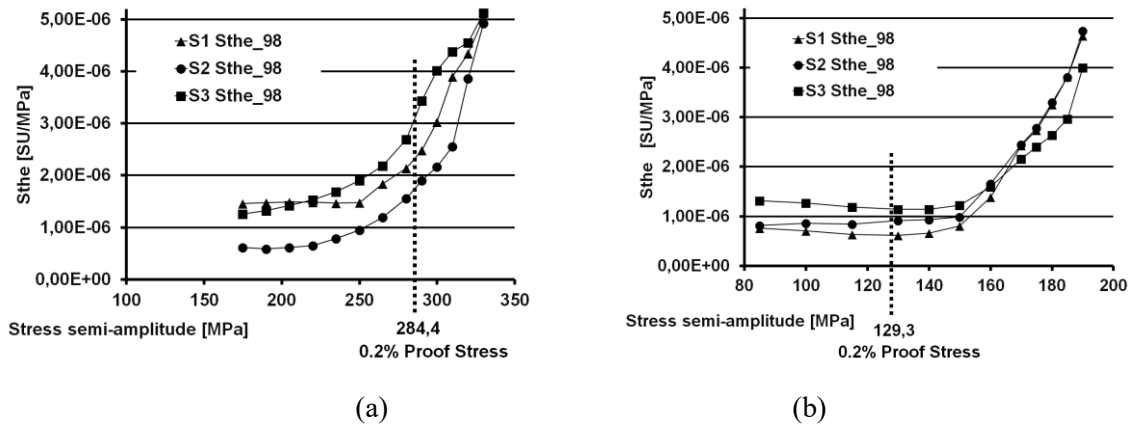


Figure 8.  $S_{the\_98}$  results at (a)  $R = -0.1$  (b)  $R = 0.5$ .

In Figures 9, the results of  $S_{d\_98}$  data are presented and a different range of variation is detected at two loading ratios even if the behaviour of whole curves is similar, meaning that the tests are perfectly reproducible.

The temperature signal of intrinsic heat dissipated depends on both plastic and viscous phenomena. When  $R < 0$ , the higher stress amplitude determines a wide hysteresis loop area, so that viscous phenomena could justify the values of  $S_d$  higher than  $R > 0$ .

At  $R=0.5$ , the energy of plastic phenomena is relatively small, as is the hysteresis loop with respect to  $R=-0.1$ , and  $S_d$  has small values.

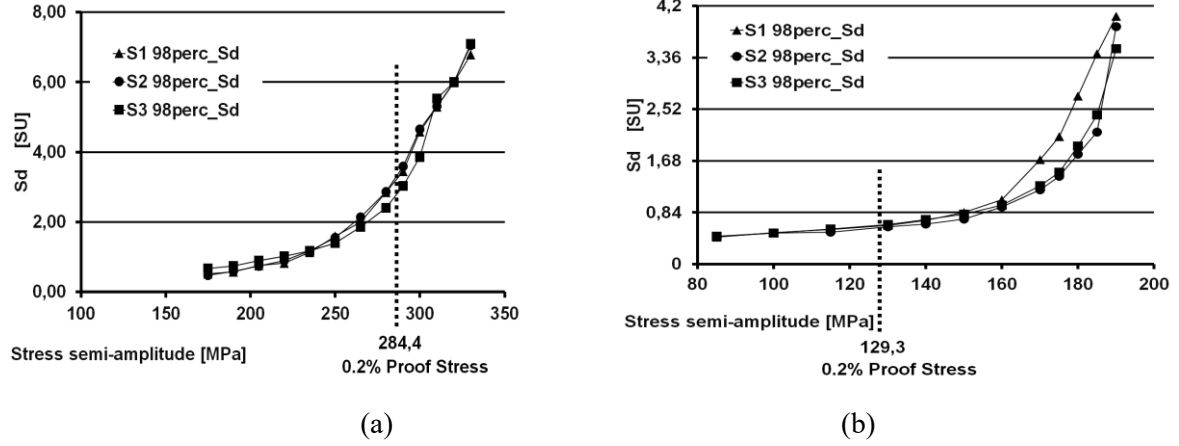


Figure 9.  $S_{d\_98}$  results at (a)  $R=-0.1$  (b)  $R=0.5$ .

Generally, the temperature is a global parameter, affected by several disturbing heat sources [2], [5], [7]. By observing the graphs in Figures 10, it is possible to note that the range of data variation at two loading ratios is the same. Even if the smoothing procedures are the same for both loading ratios, the noisy characteristic of the curves is more evident at  $R=-0.1$  (Figure 4a) than  $R=0.5$  (Figure 4b). Moreover, even for  $\Delta S_{0\_98}$  data, there is not a clear separation in the behaviour specifically at  $R=-0.1$ .

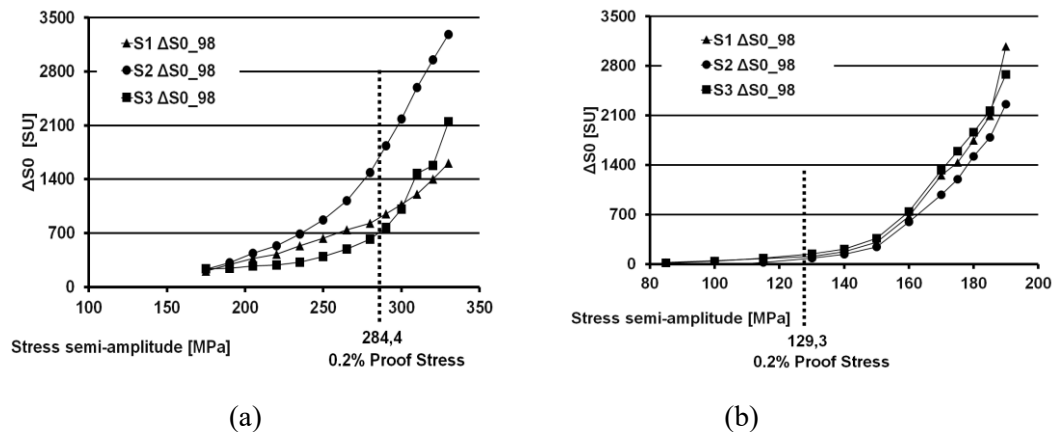


Figure 10.  $\Delta S_{0\_98}$  results at (a)  $R=-0.1$  (b)  $R=0.5$ .

However, for all the curves of Figures 7-10, the initial sloped trend is more accentuated for temperature signal data at lower stress ratio ( $R<0$ ). This characteristic could be due to the viscous effect produced by the wider stress amplitudes and hysteresis area.

A consideration arises from the previous analysis:  $\Delta S_{0\_98}$  and  $S_{the\_98}$  do not show any remarkable difference within the tests at two loading ratios, while results of  $S_{d\_98}$  and  $\Delta\phi_{98-2}$  exhibit difference depending on the loading ratio adopted.

The effect of stress ratio has also been studied in Fracture Mechanics [41], [42-43]. In the work of [41] the influence of stress ratio on the crack closure effect has been demonstrated, crack growth rate ' $da/dN$ ', for a DISPAL aluminium alloy. Other studies [42] have highlighted some differences in the 'actual loading ratio' at the crack tip and at a distance from it. However, higher  $R$  means lower stress amplitude, and lower fracture toughness [43]. The ' $R$ ' influence on fatigue testing was studied on Ti-Al-V alloys for engine turbine blade applications [21], in VHCF regime, by discussing the relation between ' $R$ ' and the failure modes. The result was that a high stress ratio plays an important role in promoting subsurface micro-cracks.

In an energetic approach, the author [44] deals with the energy stored in the material, which depends on dislocation arrangement, as well as energy reduction due to clustering and cell formations. The main focus of the work was that the quantity of energy stored in the material increased as the loading ratio ' $R$ ' decreased.

This phenomenon opens a wide discussion on the relation between stress ratio and energy involved in the fatigue process, which is represented by the energy of hysteresis loop. It is likely that the stress ratio can influence the energy contribution within the material, since the stress amplitude promotes the type of hysteresis in the material. By considering the Goodman diagram [8], the higher the stress ratio (lower stress amplitudes), the tighter the hysteresis loop.

It follows that the energy associated with damage processes occurring in the material is lower than in the case of a material undergoing fatigue testing at lower stress ratios (higher stress amplitudes); moreover, it depends on the specific dissipative process activated in the material [45].

Under the hysteresis regime, where both components exist, one can predominate on other depending on the stress ratio. In particular, at stress ratio close to 1, the test runs very close to the mechanical static properties of materials, such as the yield strength, and the plastic phenomena may be more probable than other viscous phenomena [23]. These latter occur at lower stress ratios, where the hysteresis loop is wider as well as the intrinsic frictions at grain scale.

The  $\Delta\varphi_{98.2}$  data are higher at  $R=0.5$  than  $R=-0.1$ , possibly due to the dominating plastic effects on hysteresis loop. It seems that the phase data is more influenced by the plasticity than the dumping properties.

At lower stress ratios, the viscous phenomena are enhanced [16], due to the wider characteristic of the hysteresis loop. The  $S_{d_{98}}$  results, on the contrary, exhibit higher values at  $R=-0.1$  than at  $R=0.5$ . A possible explanation for such a phenomenon can be attributed to the size of hysteresis loop, which determines major energy dissipated during fatigue

processes in the material.

Phase data have been analysed by using the previously presented Slope method. For sake of simplicity, the results are shown quantitatively in Table VIII and graphically in Figures 11.

In Table VIII, for example, the data series  $\Delta\phi_{98-2}$  at  $R=0.5$  and  $R=-0.1$  are reported for each sub-step, as well as the mean value and the slope calculations for Sample 1.

The criterion adopted was to consider as fatigue limit the first value above the 0 degree threshold, so that for Samples 1 at  $R=0.5$  it is 160 MPa while for the test running at  $R=-0.1$ , it is 250 MPa.

Figure 11a-b reports the comparison of Slope  $\Delta\phi_{98-2}$  at respectively,  $R=0.5$  and  $R=-0.1$ . At  $R>0$  there is low scatter and good reproducibility between the curves while the results at  $R=-0.1$ , appear affected by noise, especially at higher stress semi-amplitudes. However, the points of the data series significant for the purpose of evaluating the fatigue limit are those occurring at lower stress amplitudes.

Above the fatigue limit point, specific behaviour is recorded for each specimen, due to specific plastic mechanisms activated in the sample.

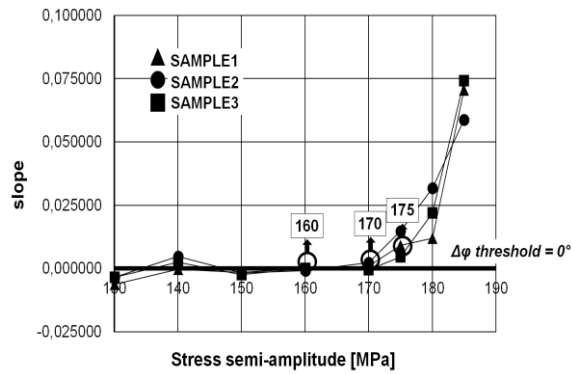
In order to evaluate the fatigue life, the threshold method has been adopted on the series  $\Delta S_{0\_98}$ ,  $S_{the\_98}$ ,  $S_{d\_98}$ .

The global results, are shown in Table IX along with the results of Staircase [11] tests carried out on fifteen specimens (loading frequency 39 Hz), to provide a reference at both loading ratios. The assessed fatigue limit at  $R=0.5$  generally underestimates the value obtained by the reference test method (particularly for  $\Delta S_0$ ). However, a more accurate evaluation can be achieved by reducing the 'distance' between each loading block.  $\Delta\phi$  seems to be the only value providing a fatigue limit very close to the Staircase reference.

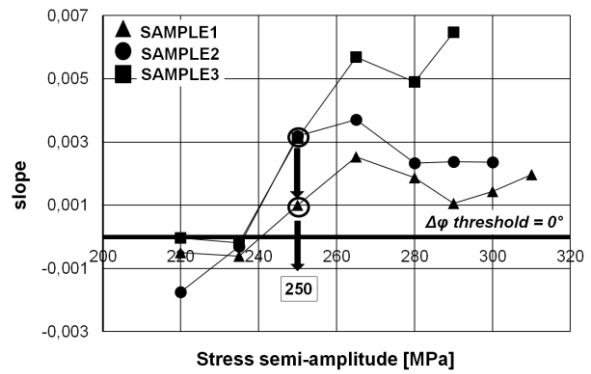
$\Delta\sigma/2$ [MPa]	R=0.5				
	$\Delta\varphi_{98-2}$ [degree]				Slope $\Delta\varphi_{98-2}$
	Sub-step1	Sub-step2	Sub-step3	Mean	
85	2,58	2,63	2,55	2,59	
100	1,70	1,67	1,62	1,66	-0,03881
115	1,41	1,41	1,46	1,43	-0,01362
130	1,27	1,26	1,23	1,25	-0,00629
140	1,27	1,27	1,29	1,28	-0,00022
150	1,24	1,26	1,25	1,25	-0,00146
160	1,22	1,27	1,26	1,25	0,00012
170	1,24	1,25	1,27	1,25	0,00089
175	1,27	1,26	1,26	1,26	0,00914
180	1,33	1,37	1,33	1,34	0,01195
185	1,34	1,42	1,39	1,38	0,07056
190	1,99	2,07	2,09	2,05	

$\Delta\sigma/2$ [MPa]	R=-0.1				
	$\Delta\varphi_{98-2}$ [degree]				Slope $\Delta\varphi_{98-2}$
	Sub-step1	Sub-step2	Sub-step3	Mean	
175	0,31	0,32	0,33	0,32	
190	0,29	0,29	0,32	0,30	-
205	0,28	0,29	0,31	0,29	0,00086
220	0,27	0,28	0,30	0,28	-
235	0,27	0,27	0,29	0,28	0,00050
250	0,26	0,26	0,28	0,27	-
265	0,29	0,31	0,33	0,31	0,00100
280	0,35	0,33	0,35	0,34	0,00254
290	0,36	0,34	0,37	0,36	0,00188
300	0,36	0,35	0,38	0,36	0,00106
310	0,38	0,38	0,40	0,38	0,00144
320	0,40	0,39	0,43	0,40	0,00197

Table VIII. Data series of  $\Delta\varphi_{98-2}$ , for fatigue limit estimation of Sample 1: (a) loading ratio 0.5 (b) -0.1.



(a)



(b)

Figure 11. Phase data, slope results for each specimen at (a) R= 0.5 (b) R= -0.1

Loading Ratio R=-0,1						Loading Ratio R=0,5					
Values in MPa						Values in MPa					
Sample	1	2	3	average	std. dev.	Sample	1	2	3	average	std. dev.
$\Delta\phi$	250.00	250.00	250.00	<b>250.00</b>	<b>0.00</b>	$\Delta\phi$	160.00	170.00	175.00	<b>168.33</b>	<b>7.64</b>
$\Delta S_0$	265.00	250.00	250.00	<b>255.00</b>	<b>8.66</b>	$\Delta S_0$	140.00	150.00	150.00	<b>146.67</b>	<b>5.77</b>
$S_{the}$	265.00	235.00	250.00	<b>250.00</b>	<b>15.00</b>	$S_{the}$	150.00	160.00	150.00	<b>153.33</b>	<b>5.77</b>
$S_d$	235.00	235.00	250.00	<b>240.00</b>	<b>8.66</b>	$S_d$	150.00	160.00	140.00	<b>150.00</b>	<b>10.00</b>
Staircase Fatigue Limit Reference				<b>250,00</b>	<b>4,77</b>	Staircase Fatigue Limit Reference				<b>169,40</b>	<b>4,38</b>

Table IX. Fatigue Limit estimations by using Phase data and Thermal parameter data at (a) R=0,5 and (b) R=-0.1

Results for the tests running at  $R < 0$ , are closer to the fatigue limit Staircase reference. In this case,  $\Delta S_0$  slightly overestimates the reference value, while  $S_d$  provides an underestimation of the fatigue limit with the same data scatter (standard deviation 8.66 MPa). Even in this case,  $\Delta\phi$  is capable of accurately determining a fatigue limit very close to the reference in the same way as  $S_{the}$ , apart from data scattering.

Belong to the quantitative analysis also the Graphical analysis can prove a useful tool to localise and determine the region of occurring dissipative phenomena, and failures.

For the first sample of each loading ratio,  $\phi$ ,  $S_{the}$ ,  $S_d$  maps will be presented to observe the onset of damage in the material, and to provide a possible explanation referring to the specific damage mechanism associated with loading ratio regime. Figures 12-13 depict the maps for three stress semi-amplitude levels: before, after and at the estimated fatigue limit: 140/165/180 MPa (test at R=0.5), 220/250/300 MPa (tests at R=-0.1).

In Figures 12(a)-(b)-(c) respectively,  $\phi$ ,  $S_d$ ,  $S_{the}$  maps exhibit the onset of the damage process in correspondence with the stress level of the estimated fatigue limit (approximately at 165 MPa). The region interested as well as the dimension seems to be similar. To better observe these processes, a profile contouring operation (two levels) was performed with Matlab® software. This analysis shed light on the effective dimension of the damaged regions. In particular, the areas detected in phase maps and  $S_{the}$  coincides with less than the sign which is specular, while  $S_d$  seems to describe a moving front of dissipations of the regions localised in  $\phi$  and  $S_{the}$  maps. However, the results slightly depend on the number of the contouring level chosen.

In Figure 12(d), for the specific loading level above the fatigue limit (180 MPa), whole profiles have been superimposed in a single map (called ALL), demonstrating that the areas belong to the same region, and all the parameters provide a single information on the damage. The potential of the technique clearly involves the joint use of the maps to detect the onset

of dissipative mechanism.

Nevertheless, by comparing three images it is possible, even qualitatively, to detect the region of damage, at the early stages. The specimen failed in the zone in the black squared region.

At  $R < 0$ , in Figure 13(a), no predominant effect of damage is present but widespread positive/negative clusters are detectable in the matrix. A global phase signal increase is recorded from below to above-fatigue-limit stress blocks.

In Figure 13(b),  $S_d$ , exhibits a global increasing signal from 220 MPa to 300 MPa. In effect, high maximum values of the signal are evident at the stress level above the fatigue limit (300 MPa). This effect concerns the downward direction of the  $S_d$  map and it is characterised by large clusters. In the phase and  $S_d$  maps, the attention can be focused on the zone enclosed by a black line, which is the region of failure where the dissipative phenomena seem to be concentrated.

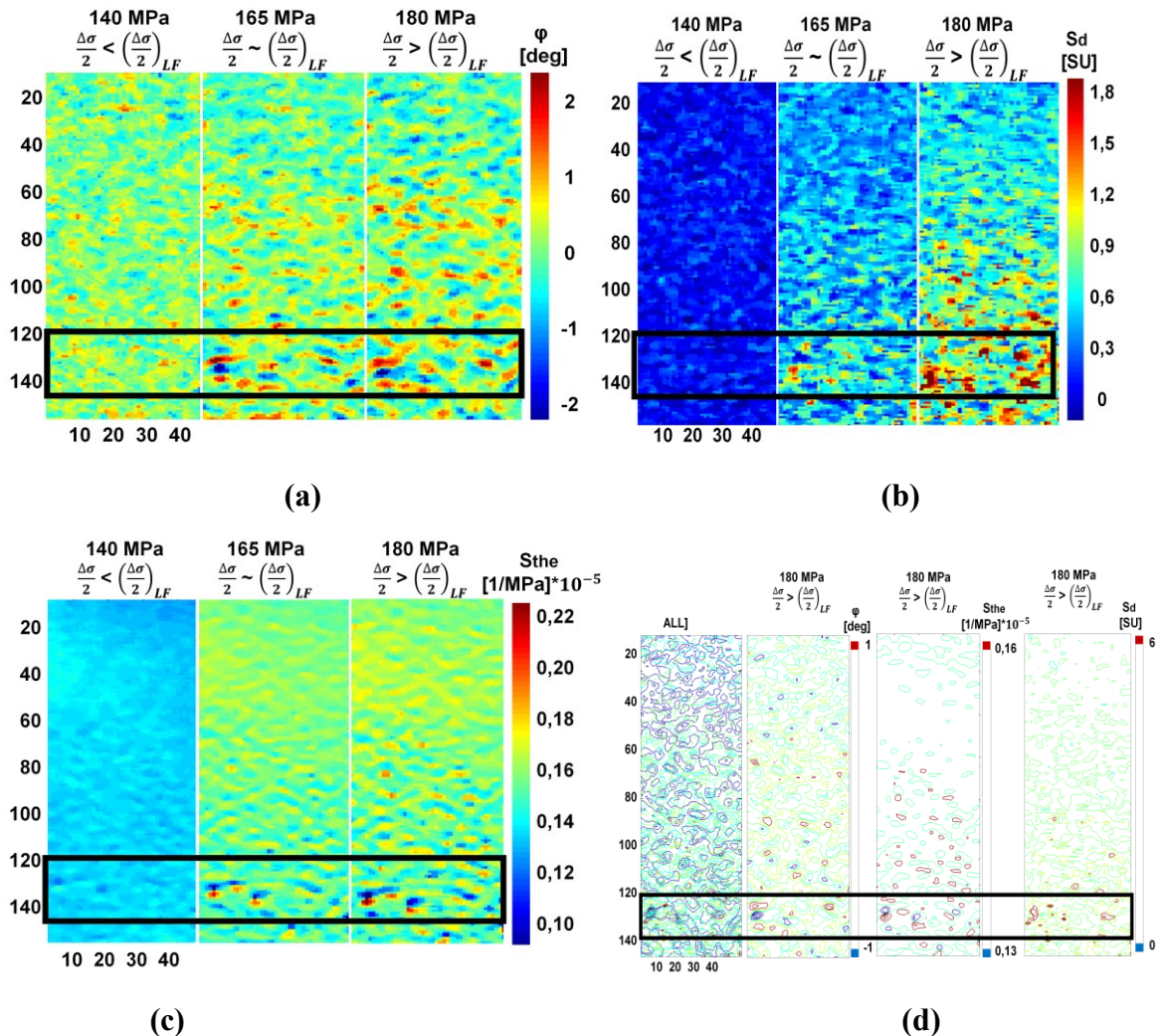


Figure 12. Damage analysis of Sample 1, tested at  $R=0.5$  (a) phase (b)  $S_d$  (c)  $S_{the}$  (d) contouring of all parameter maps.



The  $S_{the}$  signal at  $R=-0.1$ , Figure 13(c), presents a signal increase in the central part of the gauge length and a localised process is detected at the bottom right side of the matrix, starting at 250 MPa. Even for three parameters evaluated at  $R=-0.1$ , it is possible to correlate the zone of the dissipative phenomena with the proximity of a crack process.

As represented by the maps in Figures 12-13, the dissipative phenomena are different depending on the loading ratio. At  $R=0.5$  the contrast between damaged/undamaged zones, is higher than  $R=-0.1$ . In particular, at  $R=0.5$  the onset of a crack is easily detectable, Figure 12(a-d) and the plastic component is predominant.

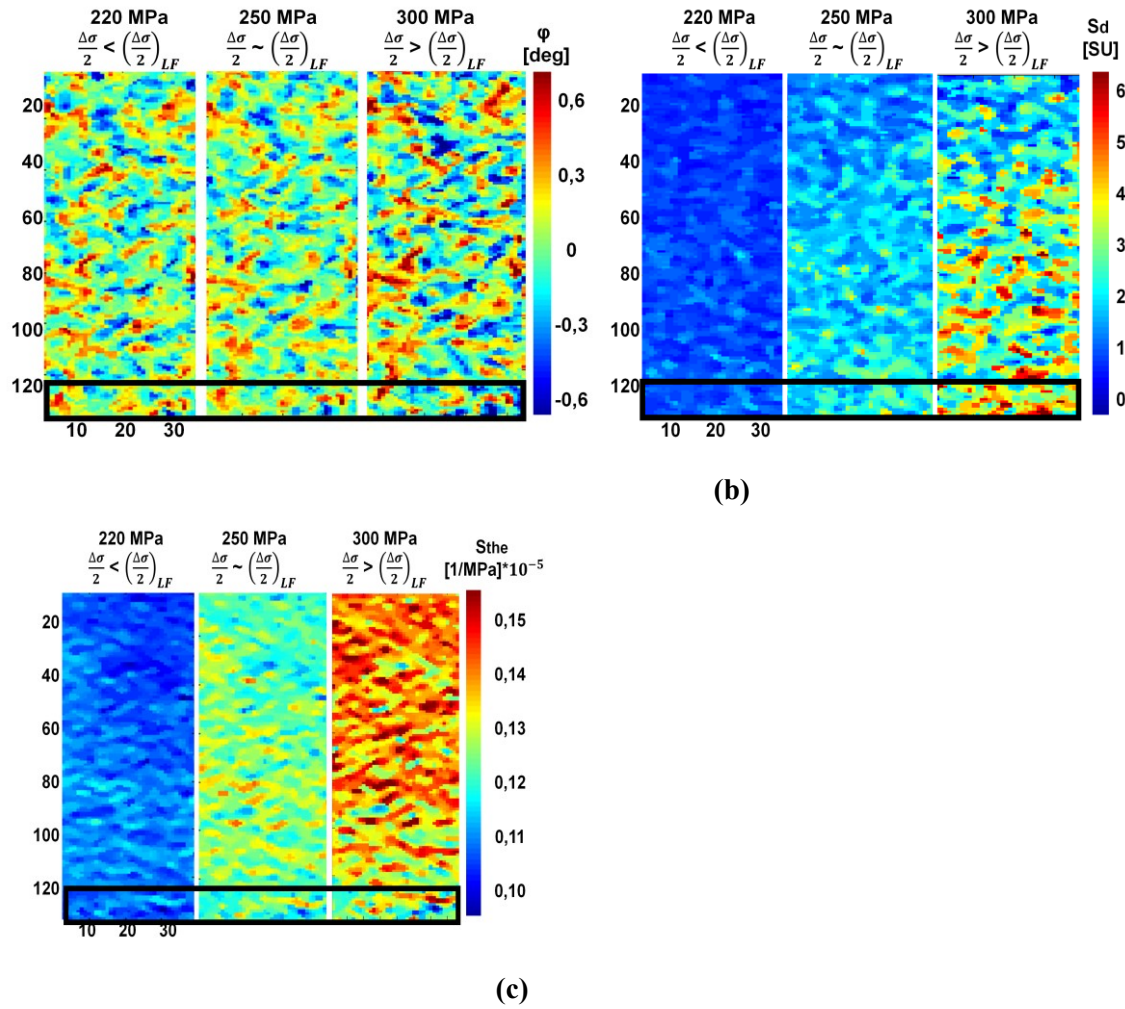


Figure 13. Damage analysis of Sample 1, tested at  $R=-0.1$ , (a) phase (b)  $S_d$  (c)  $S_{the}$

On the contrary, at  $R=-0.1$ , where the viscous component prevails, Figure 13, the dissipative phenomena are widespread in the gauge length. The  $S_{the}$  seems to be more accurate in detecting the onset of crack, with respect to the phase maps.  $S_d$  maps at  $R=-0.1$ , present a visco-plastic zone, mostly in the area represented by the black box. The fact that there is no localised damage could be due to the viscous behaviour, which prevails over the plastic one.



### **4.3 Influence of Microstructure of Metals on Thermal Signal**

Stainless steels play an important role for the Industry, due to their high mechanical performances in presence of high temperature and corrosive environments [46-49]. In this regard, a wide variety of steel alloys is easily available and depending on the type of test and the severity of the operating environment, the choice may involve either monophasic or biphasic stainless steels.

The fatigue life characterisation acquires a fundamental role for investigating their mechanical performance, even if, literature refers prevalently to Very High Cycle Fatigue or Low Cycle Fatigue regimes [50-53] with the principal purpose of studying damage behaviour [3]. In fact, several authors [54-57], enhance the understanding of damage mechanisms correlated to the presence of two different phases in the lattice rather than the fatigue limit evaluation.

In effect, in biphasic steels, austenitic grains, in ‘as cast conditions’, can exhibit lamellar and/or spheroidal [47] morphology of the clusters. The presence of such the clusters with different shapes, implies intrinsic heterogeneities and lattice mismatches [45], hence the duplex stainless steels are so complex materials characterised by complex mechanisms occurring at phase boundary scale which makes difficult the investigation of damage behaviour.

Therefore, it results that the global resistance of material is a combination of behaviour of both phases [52].

The most important phenomena occurring at microscale affecting the material response, are related to the ‘load transfer’ mechanism, which influences the propagation of damage and then the crack nucleation sites. Secondly, the role of interfaces is important since the phase boundaries can act like either as a crack sites or as a barrier for short crack propagation [55]. Large discussions concern the development of glide and piling-up of dislocations, their kinetics [51] up to the study of well-known phenomenon of ‘crack branches’ in duplex [53]. The common denominator of these phenomena is that they affect the energy available in the material [54], hence this energy must be detected somehow.

In fact, fatigue performance represents a key point in choosing the most useful among these steel alloys since a large part of mechanical components during their life are subjected to dynamic loadings. The fatigue characterisation of steels is generally carried out by performing conventional test methods (i.e. Wohler curve, Staircase...).

By using thermographic data for determining fatigue performances, the presence of the plateau condition is not certain a priori, so that determined procedures have to be set up, as

previously presented.

The issue however, is not only represented by the existence of the plateau which influence the fatigue limit evaluation, as it is the case of biphasic steels, but also their intrinsic heterogeneity can determine a different thermal behaviour [50-55] of the material due to the presence of , just explained, internal microstructural processes associated with fatigue damage [55-57].

The texture of the ASTM 890 grade 4a, specifically is composed by a lattice mismatch 50, lattice discontinuities (grain interfaces, distribution of grain orientation, interstitial/substitutional atoms in the matrix 51), different grain shapes ('equiassie' or 'columnar/elongated'). All these factors can affect the temperature evolution of the material since the overall behaviour of material depends on the differences in strength and ductility for both phases which are, in turn, influenced by grain size/geometry/orientation [53-57].

Beyond the better accuracy of fatigue limit estimation provided by the proposed three indexes, paragraph 3.5.1 and 4.1.1.3, as previously presented, also interesting considerations can be drawn by correlating the temperature changes with the different microstructure of investigated steels.

In fact, a remarkable aspect of the analysis is that, generally, the measured temperature variation of duplex is less than that of other investigated materials. In fact, referring to Figure 6 at loading level in the plastic regime (145 MPa) near the failure, the maximum temperature variation of duplex steel is approximately of 1 °C while, 3.5 °C at 115 MPa and 2 °C at 220 MPa were obtained for AISI 316 and 17-4 PH respectively. It is worth noting that the temperature variations of austenitic and martensitic stainless steels are in agreement with the temperature changes reported in literature [58-60]

The temperature variation of duplex is lower than in austenitic and martensitic material, even if the material experiences large deformations, as represented by Figure 14. In this figure, in effect, the ductile behaviour of duplex is confirmed: the deformation (170 mm) is nearly equivalent to that of AISI 316 which is 200mm.

Such low temperature changes are not justified by the large deformation undergone. The question remains regarding what has happened to the energy dissipated in the material.

In a biphasic material, the matrix discontinuities could represent stress concentration zones influencing the strength of the material 27, in fact for ASTM A 890, the overall behaviour of material depends on the differences in strength and ductility of both phases which are, in turn, influenced by grain size/geometry/orientation [52-55]. This effect is more predominant in a biphasic steel than in a monophasic one.

In literature, the influence of the grain boundaries on total energy dissipation in the material is well-known [54-55], [57], [61-62]. Moreover, in this paper the experimental analysis on

temperature variations confirms that an amount of the supplied total mechanical energy is not completely transformed into heat, but remains stored in the material. The material acts like a tank, which accumulates the energy for overpassing the grain boundaries. Considering that the duplex steel presents the austenitic clusters embedded in the ferritic bulk, the phase-to-phase grain boundary represents a barrier for dislocation movements [63]. To support this assumption, optical micrographs (Figure 15a) and SEM micrographs (Figure 15b) are shown, capable of demonstrating the role of grain boundary activity on microstructural phenomena involved in fatigue.

In Figure 15a, two types of fatigue crack are shown: an inter-granular crack between two austenitic grains and a trans-granular crack passing through austenitic clusters and ferritic bulk. The presence of an inter-granular crack, arrested at austenitic interfaces, validates the hypothesis of considering the grain boundary as an obstacle to the movement of dislocations. Such an influence is relevant, particularly between grains of different microstructures rather than grains of the same material [60-64]. The trans-granular crack, on the other hand, demonstrates that the formation of hardening/softening regions (due to accumulation of slip bands) at grain boundary [61], is involved in the development of fatigue crack. In the event that a critical value for sheer stress is achieved [65], the deformation moves toward the other phase. In Figure 15b, SEM micrographs report the presence of a mismatch at the austeno-ferritic interfaces and demonstrate the grain boundary activity during cyclic dynamic load. These processes could justify a significant amount of mechanical energy being spent for the microstructure rearrangement, while a lower dissipated energy (lower temperature) is measured, despite the large amount of deformation.

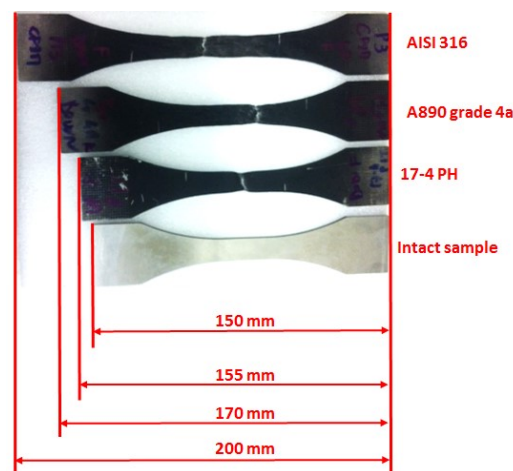


Figure 14. Dog-bone samples: comparison between tested and intact specimens.

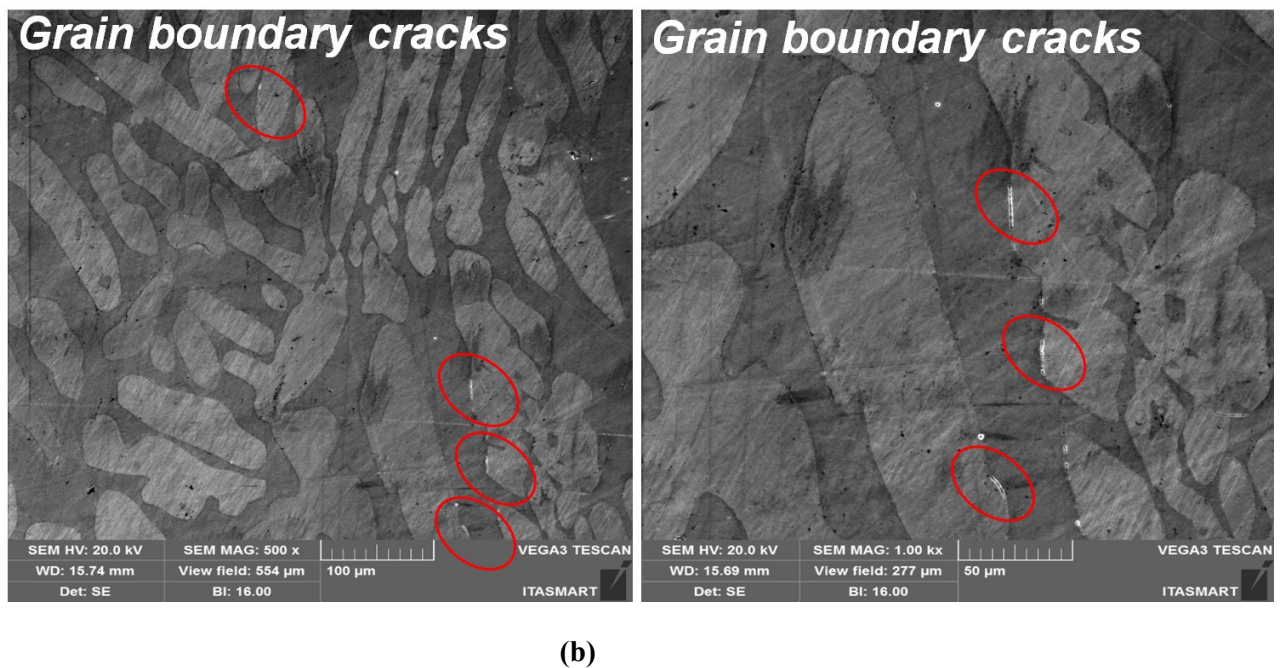
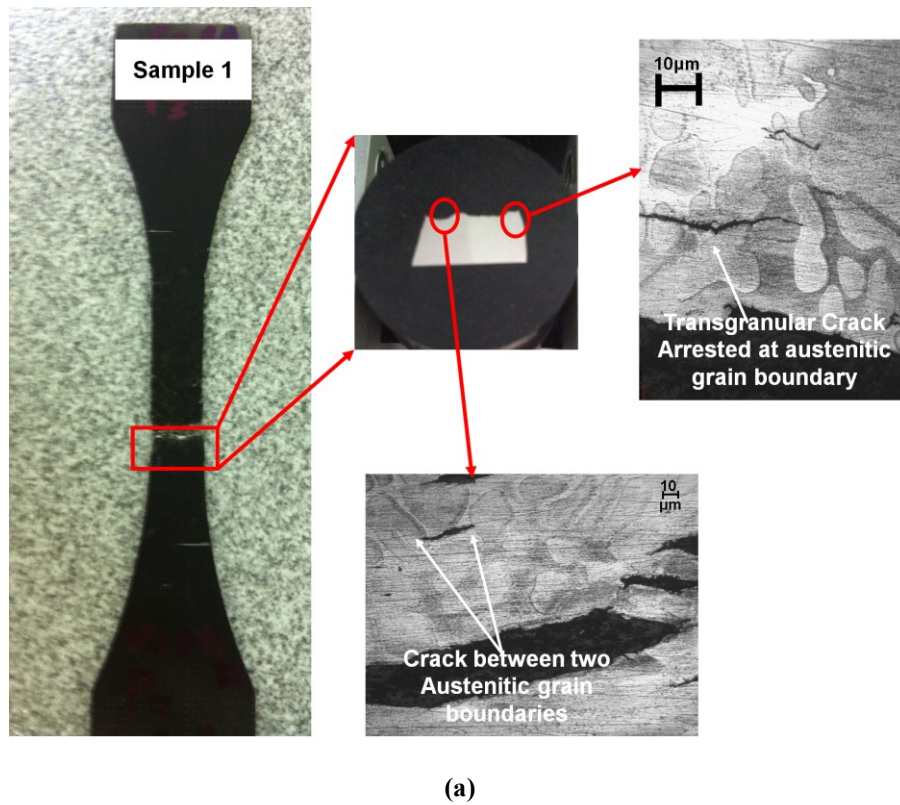


Figure 15. Duplex dog-bone tested sample 1. (a) Optical Microscope: inter-granular and trans-granular fatigue crack, (b) SEM micrograph: grain boundary activity (red marked).

## Conclusions

In the present chapter, different results have been presented, in particular referring to the application of Threshold and Slope methods on different metals (stainless steels alloys).

The Threshold method involves an accurate measurement of temperature relative to dissipative phenomena and an automatable procedure has been proposed to determine the fatigue limit while the slope methods improves the evaluation of fatigue limit by using phase data.

The proposed procedure also represents a possible non-destructive technique that can be used for monitoring, studying and predicting the fatigue behaviour of materials since once the thresholds have been achieved it is not necessary to carry on the test. Besides, it can be exploited for the monitoring of large scale operating components.

Fatigue tests were carried out on martensitic and precipitation hardening steels, austenitic and biphasic steels. The martensitic steels are characterised by a brittle behaviour and the temperature variations related to damage phenomena are one order less than austenitic steel ones. So a more accurate set up was needed in order to evaluate the superficial temperature of specimen.

Referring to  $S_0$  parameter, the results are globally in good agreement with traditional graphic thermographic methods used in literature, even if the use of temperature  $S_0$  seems to slightly underestimate fatigue limit in respect to the Stair-Case method. Maybe  $S_0$  indicates the high cycle fatigue limit, and then further works will focus on studying and comparing of the fatigue limit at  $10^7$  and  $10^9$  cycles.

Austenitic steels ductile steels together with biphasic steels, may not present a plateau in the  $S_0 + at$ , so that, different from the well-known parameters have been used for studying the fatigue behaviour:

the slope of the first temperature data series, the mean value of the same series, and the maximum temperature reached in the loading step were identified as indexes for fatigue estimations.

The obtained empirical results fit very well with those provided by reference values of fatigue limits and it was also demonstrated how just three samples allow for a statistically significant estimation of the fatigue limit, hence, the experimental campaign substantially benefits from a material cost reduction. Moreover, since  $S_{slope}$  or  $T_{mean\_in}$  refer to initial data, it follows that, it is not necessary to perform the test until the plateau is reached.

Referring to the parameters ( $\Delta\phi$ ,  $S_{the}$ ,  $S_d$ ) representing both the thermoelastic and dissipative effects the quantitative analysis allows for determination of the fatigue limit of the material while the qualitative analysis of parameter maps provide the assessment of the onset and the

dimension of the damaged areas, and differences have been detected in the behaviour of the material between the two loading ratios.

The goals of the activity are resumed by the following points:

- A more in depth understanding of proposed indexes:  $\Delta\phi$  seems to be more influenced by plastic than visco-plastic behaviour, while  $S_d$  is related to the energy of intrinsic dissipations in the material.
- The possibility to reduce the time of an experimental campaign: When the threshold is assessed, theoretically, it is not mandatory to run the test until failure of sample.
- Fatigue limit estimation in good agreement with Stair-case method at two different loading ratios,
- Capability of a multi-parameter approach for estimation of the fatigue behaviour of material.
- A more complete analysis of fatigue behaviour, described quantitatively by  $\Delta\phi$  and  $S_d$ , in order to determine the fatigue limit and graphically by  $S_{the}$ , in order to detect crack initiation.

Some improvement will be focused on the evaluation of the fatigue limit, in fact, the loading table can be refined to reduce the data scatter. The contouring analysis can be investigated as a tool to provide a more accurate evaluation of the damaged zones. Finally, further study will focus on the assessment of entire fatigue life curve by analysing the  $S_d$  index.

Finally, an explanation has been given regarding the temperature variations measured for the ASTM A890 grade 4a. In fact, the temperature changes from the beginning to the failure were much lower compared with the other two materials. This phenomenon can be correlated to grain boundary activity due to the lattice mismatch. In fact, as confirmed by microscopy, in presence of two phases, a share of supplied mechanical energy does not convert into heating but remains stored in the microstructure and is used for passing through to the grain boundary.

Further development of the technique will involve a more detailed analysis of thermal signal in order to achieve more information from thermoelastic and dissipative heat sources.

The following chapter will be devoted to present the application of the same approach to Composites. It will be shown the feasibility of the thermal and phase parameters to assess quantitatively and qualitatively the fatigue behaviour of the materials in order to highlight the behaviour of fibers and bulk, and detect the presence of damage mechanisms.

## References

- [1] R. De Finis, D. Palumbo, F. Ancona, U. Galietti. Fatigue Limit Evaluation of Various Martensitic Stainless Steels with New Robust Thermographic Data Analysis. *International Journal of Fatigue*, 74, 88-96, 2014.
- [2] M.P. Luong. Infrared thermographic scanning of fatigue in metals. *Nucl Eng Des*, 158:363–73, 1995.
- [3] I. Marines, X. Bin, C. Bathias. An understanding of very high cycle fatigue of metals. *Int J Fatigue*, 25, 1101–7, 2003.
- [4] D. Palumbo, U. Galietti. Characterization of steel welded joints by infrared thermographic methods. *Quant Infrared Thermogry*, 11, 29–42, 2014.
- [5] A. Risitano, G. Risitano. Analisi Termica per la Valutazione del Danno negli Acciai. Forni di Sopra: Workshop IGF; 2010.
- [6] R. De Finis, D. Palumbo, U. Galietti. Mechanical behaviour of Stainless Steels under Dynamic Loading: An Investigation with Thermal Methods. *J Imaging*, 2(4), 32, 2016.
- [7] G. La Rosa, A. Risitano. Thermographic methodology for the rapid determination of the fatigue limit of materials and mechanical components. *Int. J. Fatigue* 22, 65-73, 2000.
- [8] R. Juvinall, K. Marshek. *Fundamental of Machine Component Design*. Edited by ETS, 1994.
- [9] Matweb. Available online: <http://www.matweb.com/>.
- [10] C. Camerini, R. Sacramento, M.C. Areiza, A. Rocha, R. Santos, J.M. Rebello, G. Pereira. Eddy current techniques for super duplex steel characterisation. *J. Magn. Mater.* 388, 96-100, 2015.
- [11] ASM Handbook (1996). *Fatigue end Fracture*. ASM International Handbook Committee, USA. ISBN 0-87170-385-8
- [12] D. Palumbo, R. De Finis, P.G. Demelio, U. Galietti. A new rapid thermographic method to assess the fatigue limit in GFRP composites. *Compos Part B*, 103, 60-67, 2016.
- [13] D. Palumbo, U. Galietti. Thermoelastic Phase Analysis (TPA): a new method for fatigue behaviour analysis of steels: TPA: A New Method for Fatigue Behaviour Analysis of Steels. *Fatigue Fract Eng Mater Struct*, 2016. DOI: 10.1111/ffe.12511.
- [14] A.L. Audenino, V. Crupi, E.M. Zanetti. Correlation between thermography and internal damping in metals. *Int J Fatigue* 25, 343-351, 2003.
- [15] H. Mayer, R. Schuller, U. Karr, M. Fitzka, D. Irrasch, M. Hahn, M. Bacher-Höchst. Mean stress sensitivity and crack initiation mechanisms of spring steel for torsional and axial VHCF loading. *Int J Fatigue* 93, 309-317, 2016.
- [16] P. Surajit Kumar. Numerical models of plastic zones and associated deformations for elliptical inclusions in remote elastic loading–unloading with different R-ratios. *Eng Fract Mech* 152:72-80, 2016.

- [17] T. Sakai ,Y. Sato, Y. Nagano, M. Takeda ,N. Oguma . Effect of stress ratio on long life fatigue behavior of high carbon chromium bearing steel under axial loading. *Int J Fatigue* 28:1547-1554, 2006.
- [18] H. Mayer, R. Schuller, U. Karr, D. Irrasch, M. Fitzka, M. Hahn, M. Bacher-Höchst. Cyclic torsion very high cycle fatigue of VDSiCr spring steel at different load ratios. *Int J Fatigue* 70:322–327, 2015.
- [19] S. Ishihara, A.J. McEvily , M. Sato, K. Taniguchi, T. Goshima. The effect of load ratio on fatigue life and crack propagation behavior of an extruded magnesium alloy. *Int J Fatigue* 31:1788–1794, 2009.
- [20] S.V. Kamat, M. Srinivas. Effect of load ratio on the fatigue crack growth behaviour of DISPAL 2 alloy. *Int J Fatigue* 21:169-172, 1999.
- [21] K. Yang, C. He, Q. Huang,Z. Yong Huang,C. Wang,Q. Wang, Y.J. Liu, B. Zhong. Very high cycle fatigue behaviors of a turbine engine blade alloy at various stress ratios. *Int J Fatigue* 99:35-43, 2017.
- [22] M. Karadag, R.I. Stephens. The influence of high R ratio on unnotched fatigue behavior of 1045 steel with three different heat treatments. *Int J Fatigue* 25:191–200, 2003.
- [23] T. Müller , M. Sander. Investigation of variable amplitude loading and stress ratio in the very high cycle fatigue regime using micro-notched specimens. *Proc Eng* 101:322 – 329, 2015.
- [24] S. Kovacs, T. Beck, L. Singheiser. Influence of mean stresses on fatigue life and damage of a turbine blade steel in the VHCF-regime. *Int J Fatigue* 49:90-99, 2013.
- [25] A. Pannemaecker, S. Fouvry, M. Brochu, J.Y. Buffiere. Identification of the fatigue stress intensity factor threshold for different load ratios R: From fretting fatigue to C(T) fatigue experiments. *Int J Fatigue* 82: 211–225, 2016.
- [26] M.L. Zhu, F.Z. Xuan, S.T. Tu. Effect of load ratio on fatigue crack growth in the near-threshold regime: A literature review, and a combined crack closure and driving force approach. *Eng Fract Mech* 141:57–77, 2015.
- [27] J. Toribio , J.C. Matos, B. González. Micro- and macro-approach to the fatigue crack growth in progressively drawn pearlitic steels at different R-ratios. *Int J Fatigue* 31:2014–2021, 2009.
- [28] AT. Htoo, Y. Miyashita, Y. Otsuka , Y. Mutoh , S. Sakurai. Variation of local stress ratio and its effect on notch fatigue behaviour of 2024-T4 aluminum alloy. *Int J Fatigue* 88: 19–28, 2016.



- [29] M. Knop, R. Jones, L. Molent, C. Wang. On the Glinka and Neuber methods for calculating notch tip strains under cyclic load spectra. *Int J Fatigue* 22:743–755, 2000.
- [30] S. Kumar Paul, N. Stanford, A. Taylor, T. Hilditch. The effect of low cycle fatigue, ratcheting and mean stress relaxation on stress–strain response and microstructural development in a dual phase steel. *Int J Fatigue* 80: 341–348, 2015.
- [31] V. Gaur, V. Doquet, E. Persent, C. Mareau, E. Roguet, J. Kittel. Surface versus internal fatigue crack initiation in steel: Influence of mean stress. *Int J Fatigue* 82, 437–448, 2016.
- [32] V. Kazymyrovych, J. Bergström, F. Thuvander. Local stresses and material damping in very high cycle fatigue *Int J Fatigue* 32: 1669–1674, 2016.
- [33] N.F. Enke, B.I. Sandor. Cyclic plasticity analysis by differential infrared thermography. *Proceeding of the VII International Congress on Experimental Mechanics* 830-835, 1988.
- [34] T. Sakagami, S. Kubo, E. Tamura, T. Nishimura. Identification of plastic-zone based on double frequency lock-in thermographic temperature measurement. *International Conference of Fracture ICF11, Catania (Italy)*, 2015.
- [35] J.K. Krapez, D. Pacou, G. Gardette. Lock-In Thermography and Fatigue Limit of Metals. *Quantitative Infrared Thermography, QIRT*, 18-21 July, Reims (France), 2000.
- [36] M.P. Luong. Infrared Thermographic scanning of fatigue in metals. *Nucl Eng Des* 158:363-373, 1995.
- [37] M.P. Luong. Infrared observation of thermomechanical couplings in solids. *Thermosense XXIV Conference, part of SPIE's Aerosense*, 1-5 April, Orlando (Florida), 2002.
- [38] B. Yang, P.K. Liaw, M. Morrison, C.T. Liu, R.A. Buchanan, J.K. Huang, R.C. Kuo, J.G. Huang, D.E. Fielden. Temperature evolution during fatigue damage. *Intermetallics* 13:419-428, 2005.
- [39] W. J. Wang, J.M. Dulieu-Barton, Q. Li. Assessment of Non-Adiabatic Behaviour in Thermoelastic Stress Analysis of Small Scale Components. *Exp Mech* 50:449-461, 2010.
- [40] D. Palumbo, U. Galietti. Data Correction for Thermoelastic Stress Analysis on Titanium Components. *Exp. Mech.* 2016; DOI 10.1007/s11340-015-0115-0.
- [41] S.V. Kamat, M. Srinivas. Effect of load ratio on the fatigue crack growth behaviour of DISPAL 2 alloy. *Int J Fatigue* 21:169-172, 1999.
- [42] D. Kujawski. Enhanced model of partial crack closure for correlation of R-ratio effects in aluminum alloys. *Int J Fatigue* 23: 95-102, 2001.
- [43] J. Zhang, X.D. He, S.Y. Du. A simple engineering approach in the prediction of the effect of stress ratio on fatigue threshold. *Int J Fatigue* 25: 935–938, 2003.
- [44] J. Warren, D.Y. Wei. A microscopic stored energy approach to generalize fatigue life stress ratios. *Int J Fatigue* 32:1853–1861, 2010.
- [45] F. Maquin, F. Pierron. Heat dissipation measurements in low stress cyclic loading of metallic materials: From internal friction to micro-plasticity. *Mech Mater* 41:928–942, 2009.
- [46] McGuire, MF (2008). *Stainless steel for Design Engineers*. ASM International, USA.

- [47] M. Boniardi, V. Boneschi. Generalità sugli acciai inossidabili bifasici ed aspetti metallurgici della loro saldatura. Convegno Nazionale “La saldatura degli acciai inossidabili”. Bologna, Italy, November 18, 1999.
- [48] F. Iacoviello, V. Di Cocco, M. Cavallini, S. Natali, E. Franzese. Acciai inossidabili duplex: resistenza alla propagazione della cricca di fatica in aria. Convegno Nazionale IGF XX, Torino 24-26 giugno 2009, 88-99 .
- [49] M.P. Weiss, E. Lavi, E (2016). Fatigue of metals – What the designer needs? *Int J Fatigue* 84, 80–90.
- [50] S. Li, Y. Wang, X. Wang. Effect of ferrite content on the mechanical properties of thermal aged duplex stainless steels. *Mater Sci Eng A* 625, 186-193, 2015.
- [51] N. Jia, R. Lin Peng, Y.D. Wang, S. Johansson, P.K. Liaw. Micromechanical behavior and texture evolution of duplex stainless steel studied by neutron diffraction and self-consistent modeling. *Acta Mater* 56, 782-793, 2008
- [52] U. Krupp, I. Alvarez-Armas. Short fatigue crack propagation during low-cycle, high cycle and very-high-cycle fatigue of duplex steel – An unified approach. *Int J Fatigue* 65, 78-85, 2014.
- [53] H. Knobbe, P. Starke, S. Hereñú, H.J. Christ, D. Eifler. Cyclic deformation behaviour, microstructural evolution and fatigue life of duplex steel AISI 329 LN. *Ing J Fatigue* 80, 81-9, 2015.
- [54] U. Krupp, A. Gierler, M. Söker, H. Fu, B. Dönges, H.J. Christ, A. Husecken, U. Pietsch, C.P. Fritzen, W. Ludwig. The behaviour of short fatigue cracks during Very High Cycle Fatigue (VHCF) of duplex stainless steel. *Eng Fract Mech* 145, 197-209, 2015.
- [55] R. Dakhlaoui, C. Braham, A. Baczmański. Mechanical properties of phases in austeno-ferritic duplex stainless steel-Surface stresses studied by X-ray diffraction . *Mater Sci Eng A* 444, 6-17, 2007.
- [56] E.I. Mehtedi, S. Spigarelli, P. Ricci, C. Paternoster, E. Quadrini. Caratterizzazione meccanica delle fasi dell'acciaio Duplex 2205 mediante nanoindentazione. *La metallurgia Italiana* 9, 11-6, 2010.
- [57] D. Dyja, Z. Stradomski, A. Pirek. Microstructural and fracture analysis of aged cast duplex steel. *Strength Mater.* 40, 122-5, 2008.
- [58] A.E. Morabito , A. Chrysochoos, V. Dattoma, U. Galietti. Analysis of heat sources accompanying the fatigue of 2024 T3 aluminium alloys. *Int. J. Fatigue* 29, 977-984, 2007.
- [59] M. Giannozzi, L. Baldassarre, M. Cecconi, M. Camatti, D. Becherucci, X. Coudray, C. Puaut, C . About design, materials selection and manufacturing technologies of centrifugal compressors for extreme sour and acid service. *ADIPEC 2013 Technical Conference*, 2013.
- [60] C. Bathias, L. Drouillac, P. Le Francois. How and why the fatigue S–N curve does not approach a horizontal asymptote. *Int J Fatigue* 23, 143–151, 2001.
- [61] S. Bugat, J. Besson, A.F. Gourgues, F. N’Guyen, A. Pineau. Microstructure and damage initiation in duplex stainless steels. *Mater Sci Eng A* 317, 32–6, 2001.
- [62] A. Das. Grain boundary engineering: fatigue fracture. *Philos. Mag. A* <http://dx.doi.org/10.1080/14786435.2017.1285072>, 2017.

- [63] I. Alvarez-Armas, U. Krupp, M. Balbi, S. Hereñú, M.C. Marinelli, H. Knobbe. Growth of short cracks during low and high cycle fatigue in a duplex stainless steel. *Int J Fatigue* 41, 95–100, 2012.
- [64] A. Akai, D. Shiozawa, T. Sakagami, T. S. Otobe, K. Inaba. Relationship between dissipated energy and fatigue limit for austenitic stainless steel. 15 International Conference on Experimental Mechanics (ICEM 15), Porto 22-27 July 2012. Paper Ref. 2600, 2012.
- [65] C. Mareau, V. Favier, B. Weberc, A. Galtier, M. Berveillera. Micromechanical modeling of the interactions between the microstructure and the dissipative deformation mechanisms in steels under cyclic loading. *Int J Plast* 32–33, 106–120, 2012.

---

## ***Chapter 5: Thermographic Signal Analysis for Composites***

---

**I**n this chapter it will be presented an interestingly application of the adopted approach based on thermographic signal analysis on composite materials.

In the first part, the attention will be focused on presenting the most important achievement resulting from the adopted algorithms for data processing and analysis for assessing the fatigue life of composites.

In fact, conventional procedures and methods used for obtaining the fatigue performance of materials represent a critical aspect of mechanical characterization because of time consuming tests with a high number of specimens. In the last few years, great efforts have been made to develop a number of methods aimed at reducing testing time and, subsequently, the cost of the experimental campaign. In the process, thermographic methods have shown to be a useful tool for the rapid evaluation of fatigue damage and fatigue limit. Referring to the results the paragraph 5.1 deals with the application of threshold method for the evaluation of fatigue limit and the monitoring of damage in GFRP material by means of thermography. Although damage mechanisms in composite materials are difficult to understand, the proposed procedure allows us to obtain a number of parameters providing information relating to the onset of failure phenomena. It will be showed also, that, presented results are in good agreement with those attained by the standard test methods.

In section 5.2, the phase of thermoelastic signal, associated with intrinsic dissipation processes occurring in the material, has been used to localize and assess the damaged areas in a quantitative manner.

In addition, this parameter, the thermoelastic phase analysis, leads to an evaluation of the endurance limit of composites. In fact, by comparing the results with those provided by the standard test methods, the potential has been shown of the proposed procedure firstly as a non-destructive technique for continuous monitoring of damage in composite structures undergoing fatigue loadings, and secondly, as a fatigue limit index.

### **5.1. Thermographic Signal Approach for studying fatigue in Composites**

### 5.1.1. Introduction

Composite materials are nowadays used to produce large structures in many applications ranging from boating-yachting to aeronautical or aerospace [1]. In this regard, wind turbine blades are made from polymer composites since a highly specific rigidity is required, in addition to strength and good mechanical behaviour [2]. In particular, the fatigue performances imposed by Standards have to be verified by means of experimental campaigns in laboratory on sample specimens or directly on large components.

Classical procedures for evaluating the fatigue limit of material involves expensive and time-consuming tests because of the high number of specimens being tested [3] as previously explained.

In recent years, with an aim to reduce testing times and costs of fatigue tests, different techniques and methods have been proposed in order to study the various damage phenomena rapidly and consistently [4-7]. In particular, Infrared Thermography Technique (IRT) represents a reliable support for investigating fatigue damage in metallic and composite materials [8-11]. The great interest in IRT is due to the possibility it provides for the assessment of information about fatigue behaviour by studying the heat sources generated during tests [12-16].

Luong [17] and Risitano [18] proposed a graphical method to assess the fatigue limit of metallic materials by monitoring the superficial temperature of the specimen during an incremental stepwise procedure. The same approach has been employed in Montesano's work [12] for determining the fatigue limit of polymer matrix composites (PMC). In this case, the lifespan curve has been determined by means of IRT and an excellent correlation with the conventional stress-life curve was obtained. Two different approaches (passive and active) have been applied in the work of Steinberger et al. [13]. In particular, a quantitative characterization of damage has been performed by calculation of the loss factor via hysteretic heating.

In another approach, different authors [19,20] use a specific data processing of recorded infrared sequences to investigate the damage phenomena in the material. In this case, the temperature signal is analyzed in the time domain so that the first and the second order harmonics of the signal can be used to describe the nonlinear thermal signal component, due to the thermomechanical coupling phenomena. This approach has been used in the work of Kordatos et al. [21] to study the fatigue behaviour of aluminum grade 1050 H16 and SiC/BMAS ceramic matrix composite cross-ply specimens by combining lock-in thermography (dissipative heat source analysis) and acoustic emission techniques. In this case, as well, IRT provides a good estimation of the material life in the finite life region.

As explained in Chapter 2, several authors [22-26], dealt with the use of TSA the potential to identify minimal damage, demonstrating the potentiality of such the technique.

The potential of TSA for analyzing composite materials has been reported in the works of Emery et al. [14] and Fruehmann et al. [15].

The first investigates various polymer-matrix composites with different laminate types, while the second highlights the possibility of using the phase signal for evaluation of fatigue damage, even at low stress.

In particular, in these works it has been demonstrated how damage mechanisms affect inner material producing a redistribution of strains/stresses with consequent stiffness degradation. Moreover, during damage phenomena a departure from adiabatic conditions occurs in the through-the thickness direction. These phenomena lead to a thermoelastic signal variation both in amplitude and phase. As shown in Palumbo et al. [27], in presence of damage, a significant thermal signal occurs at twice the loading signal related to the dissipative heat sources.

In the present section the application of procedure, algorithms and analysis methods adopted for metals, will be presented for illustrating the fatigue behaviour of GFRP composites and providing a rapid evaluation of the fatigue limit of material.

Moreover, the capability of the Thermoelastic Phase Analysis (TPA) both to evaluate the fatigue limit and to study the damage behaviour of GFRP composites. To date, no information is present in literature referring to the use of TPA for the aforementioned purposes since the capability of TPA to detect damage, has been mostly discussed for metals. The proposed approach is “passive”, since no external heat sources are used for exciting the material. In this case, the material is subjected to an external loading in order to assess the dissipative phenomena related to the damage. The main advantage with respect to the “active” approach is the opportunity to investigate the material (component) under actual loading conditions.

The strong point of the proposed method is the possibility to obtain with a single analysis of thermographic data, information about dissipative heat sources and thermoelastic heat sources, so that to obtain information about dissipative heat sources correlated to damage phenomena. The ability to localize the damaged areas has also been presented. In this regard, the main advantage is represented by the simple application and the much reduced processing time of the proposed algorithm, which makes it very useful for the automatic scanning of large composite structures.

By resuming, the analysis for determining the fatigue limit on composites will concerns the thermal indexes ( $S_0$ ,  $S_1$ ,  $S_2$ ) and as just said, the thermoelastic phase shift  $\phi$ . In this case, it will be considered the standard deviation of phase data as parameter to study fatigue

behaviour since it allows for a further reduction in the processing time, since the subtraction of the phase map of initial loading level as a reference for undamaged conditions, is not required.

This analysis has been applied for several fatigue tests on five standard specimens made of GFRP composite material. Each test has been monitored at regular intervals with a cooled infrared camera.

Conventional fatigue tests performed on the samples offer a comparison values for validating the adopted technique.

Moreover, since no difference between imposed sub-steps of specimens have been registered, several considerations lead to a validation of the test procedure for the tests on composites:

- The stepwise loading procedure is perfectly repeatable
- The stepwise loading procedure can be performed in less time, the time required to complete the first sub-step, without achieving 20,000 cycles.

### **5.1.2. Recall of basic concepts of TSA applied to Orthotropic Materials**

Generally, the two thermal effects are generated during a cyclic loading are: thermoelastic heat sources and intrinsic dissipations. The first represents the well-known thermoelastic coupling while, intrinsic dissipation is thermodynamically irreversible and is due to various factors including the viscoelastic nature of the matrix material, matrix cracking, fibre fracture, and interface cracking/friction [12], as previously stated.

For an orthotropic material, under the hypotheses of adiabatic conditions, the classical thermoelastic equation, as specified in Chapter 2, relating temperature changes  $T_{the}$  and changes in stresses in the principal material directions is:

$$T_{the} = -\frac{\alpha}{\rho C_p}(\alpha_1 \Delta \sigma_1 + \alpha_2 \Delta \sigma_2) \quad (1)$$

where  $\alpha_1$  and  $\alpha_2$  are the coefficients of linear thermal expansion relative to the principal axes,  $C_p$  is the specific heat at constant pressure,  $\rho$  is the density,  $T_0$  is the absolute temperature and  $\Delta \sigma_2$ ,  $\Delta \sigma_1$  are the principal stresses.

The non-radiometrically calibrated S signal proportional to the peak-to-peak variation in temperature during the peak-to-peak variation of the sum of principal stress, is provided by the IRTA software presented in Chapter 3.

S is usually presented as a vector, where modulus is proportional to the change in temperature due to the thermoelastic effect and the thermoelastic phase  $\phi$  is the angular shift between the thermoelastic and the reference signal [14]. In this case, the following equation can be used:

$$A * S = (\alpha_1 \Delta \sigma_1 + \alpha_2 \Delta \sigma_2) \quad (2)$$

where  $A^*$  is a calibration constant, presented in Chapter 2.

The signal S can be expressed in time domain as follows:

$$S_{the} = \frac{S}{2} (\sin \omega t + \pi + \varphi) \quad (3)$$

where S is the non-calibrated thermoelastic signal.

In equation 3, appear the thermoelastic phase shift, apart from the dependence from thickness of the painting or the grips of the loading machine, the phase can slightly change through the area analysed due to non-perfect homogeneity of the surface conditions, and remains locally constant in presence of linear elastic behaviour of material and adiabatic conditions. In the event of damage occurring, non-linearity of thermoelastic signal and phase variations can be observed [15].

As shown in Equation 3, the thermoelastic signal varies at the same frequency as the loading during the test.

Beyond the phase, also the second order temperature signal variations have been considered for analysing the fatigue behaviour of composite. It was demonstrated that the intrinsic dissipations occurred at twice the frequency of mechanical loading and are two orders lower than the thermoelastic type [19,21]. The dissipative terms are irreversible sources unlike the thermoelastic type, causing the increase in the mean temperature of the specimen.

In effect, in presence of damage, a typical three-stage trend is reported in surface temperature measurement [16]; firstly, there is a mean temperature increase, secondly, it reaches an equilibrium

value due to balancing in elastic dissipative sources and heat exchange effect [28-29].

Following the temperature plateau achieved, in the eventuality of failure occurring at a certain loading step, temperature will increase abruptly, as reported in Ref. [16].

Considering dissipative heat sources, the related thermal signal can be modelled by means of the following equation:

$$S_d = S_{2\omega} (\sin \omega t + \pi + \varphi) \quad (4)$$



where  $S_d$  is the non-calibrated thermographic signal correlated with irreversible sources and  $S_{2\omega}$  is the amplitude signal of thermal sources.

### 5.1.3. Experimental Campaign

Twelve specimens were extracted from a laminate panel made of an epoxy-type resin reinforced with two internal layers of cross-plyed quasi-isotropic glass fiber  $+45^\circ/0^\circ/-45^\circ/90^\circ$  and two external layers of unidirectional fiber of the  $0^\circ/90^\circ$  type. The fiber volume fraction was 63% while the matrix volume fraction was 37%. The overall density of composite was  $175 \text{ g/cm}^3$  and the resin density was  $110 \text{ g/cm}^3$ .

The dimensions of specimens were fixed according to Standard ASTM D 3039 [30] which were 25 mm wide, 250 mm long and 2.5 mm thick. All the specimens were tested on machines presented in Chapter 3.

For fatigue testing MTS loading machine and the Infrared detector FLIR X6540 SC.

The specimens were firstly, statically tested, to assess mechanical ultimate tensile strength. The tests provided 440 MPa. Conventional procedure was applied to test seven of the produced twelve specimens, providing the S-N curve and estimate of the fatigue limit. In Table 1, the maximum stress applied adopting a stress ratio of 0.1 and a loading frequency of 7 Hz is shown.

Step	$\sigma_{\max}$ [MPa]	Number of cycles
1	380	400
2	270	2630
3	240	13521
4	200	52434
5	175	120540
6	150	351588
7	138,5	1189803

Table I. Stresses and number of cycles to failure obtained on seven specimens.

Table 2 shows the loading table, used for performing the just exposed self-heating procedure (Chapter 3).

The same fatigue test parameters were used for the thermographic tests on the five leftover specimens. The loading stepped procedure was performed by starting with nominal stress amplitude ( $\Delta\sigma/2$ ) of 30 MPa. At the end of each step (about 10,000 cycles of loading machine), the applied load was increased according to the values shown in Table 2.

N	$\Delta\sigma/2$	$\sigma_{\min}$ [MPa]	$\sigma_{\max}$ [MPa]	$\sigma_{\text{mean}}$ [MPa]
1	30	4	44	24
2	35	7	67	37
3	40	8	78	43
4	45	9	89	49
5	50	10	100	55
6	55	11	111	61
7	60	12	122	67
8	65	13	133	73
9	70	14	144	79
10	75	16	156	86
11	80	17	167	92
12	85	18	178	98
13	90	20	200	110
14	100	22	222	122

Table II. Number of loading steps and correspondent applied stresses.

The adopted experimental set-up for thermographic tests is shown in Figure 1.

FLIR X6540 SC acquired three thermographic sequences at fixed stress level, respectively at 2000, 6000 and 8000 cycles, to investigate the damage within each loading step. These sequences, hereafter, will be indicated as Substep 1 (2000 cycles), Substep 2 (6000 cycles) and Substep 3 (8000 cycles).

The adopted frame rate was 100 Hz. Each acquisition lasts 10 s, therefore 1000 frames were recorded.

The processing procedure has been implemented in Matlab® software.



Figure 1. Experimental set-up adopted for thermographic tests.

#### 5.1.4. Methods and data analysis

In this section it will be presented the methods and data analysis adopted for processing the raw thermographic sequences.

The procedure are the same as presented in Chapter 3 for metals, and also the mathematical model adopted for representing the thermal variations is the one previously presented in terms of non-calibrated temperature signal.

However a brief recall is provided:

$$S(t) = S_0 + at + S_1 \sin(\omega t + \varphi) + S_2(\sin 2\omega t) \quad (5)$$

where the term  $S_0 + at$  represents the increase in mean temperature during cyclic mechanical loading in terms of radiometric signal,  $\omega$  is angular frequency of the mechanical imposed load,  $S_1$  and  $\varphi$  are respectively related to the amplitude and the phase of the first harmonic component of the Fourier series while  $S_2$  represents the amplitude of the second Fourier harmonic component.

Therefore, the term  $S_1$  corresponds to the signal variation related to thermoelastic effect and  $S_2$  is proportional to the amplitude of intrinsic dissipation.

Equation (5) was integrated in the algorithm of IRTA® software providing images in the form of data matrix for each constant parameter. The phase  $\varphi$  of thermoelastic signal has not

been taken into account in this paper since it will be shown in a further work. The procedure for the processing of thermographic data was applied for each loading step and sub-step and provides:

- The acquisition of the thermographic sequence. About one thousand frames were acquired for each sequence.
- Assessing of the three thermal signals:  $S_0$ ,  $S_1$  and  $S_2$  pixel by pixel (IRTA® software).
- Application of a Gaussian 2D-smoothing on IRTA® data matrix for the purposes of noise reduction. In this regard, the Gaussian kernel provides a gentler smoothing and preserves edges better than a similarly sized mean filter.
- sizing of data matrix (area of analysis) to refer the analysis only to the area of gauge length. In this case, the area of analysis was the same for  $S_0$ ,  $S_1$  and  $S_2$  ( $A_1$  area, Figure 2), and includes  $405 \times 49$  pixels ( $\text{mm/pixel} = 0.4$ ).

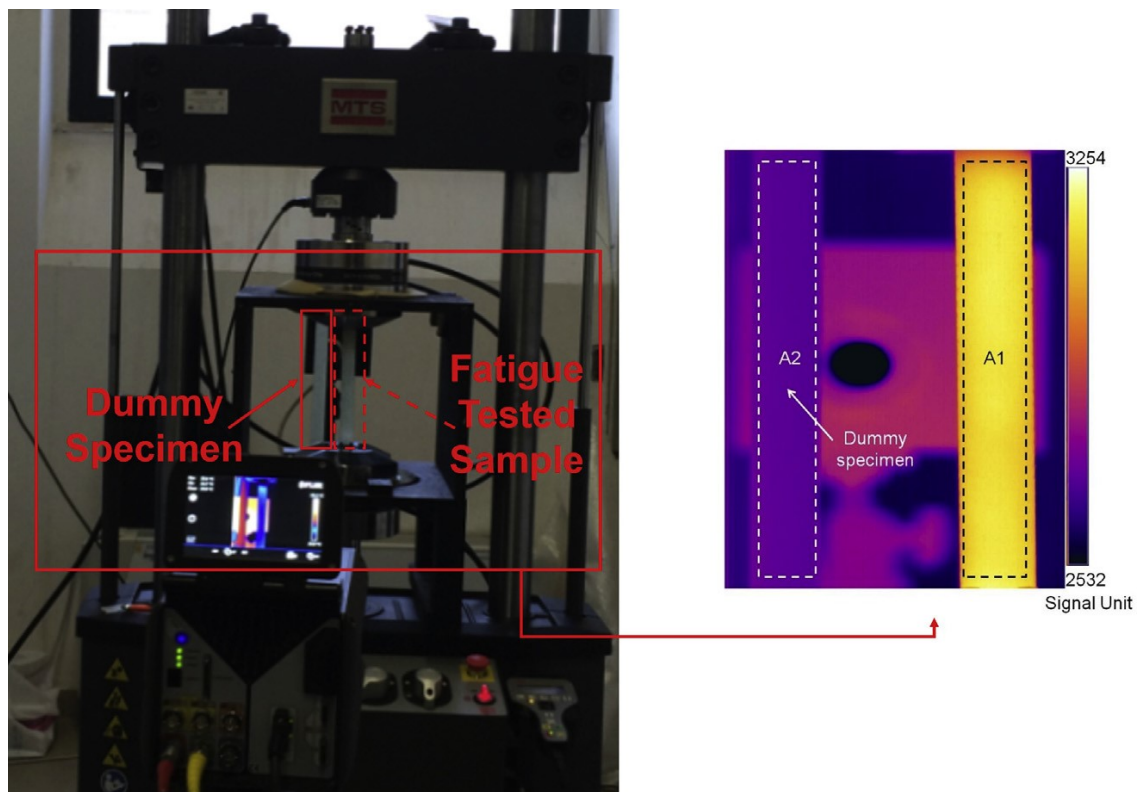


Figure 2. Area considered for the analysis ( $A_1$ ) and for evaluating of environmental temperature signal ( $A_2$ , dummy specimen).

For signal  $S_0$  (radiometric temperature signal), the processing steps are:

- Subtracting the environmental temperature influence on temperature signal  $S_0$  achieved during each step and sub-step ( $\Delta S_0$ ), which is required in order to obtain a good estimation of the temperature changes which are due to material damage.

Environmental temperature signal has been measured by using a dummy specimen (A<sub>2</sub> area in Figure 2).

- Evaluation of the 98th value of percentile to avoid outliers in temperature signal measurements ( $\Delta S_{0\_98perc}$ ) in the considered data matrix (A<sub>1</sub> area). As stated in [31], since the energy of damage is proportional to the dissipated energy as heat per cycle, in order to closely follow the dissipation phenomena, 98<sup>th</sup> percentile temperature value is chosen as a guideline.

For signal S<sub>1</sub> (thermoelastic signal), the analysis involves:

- Subtracting a thermoelastic amplitude data matrix of the first loading step when no damage occurred to provide a reference condition between damaged and undamaged situations. In this way, the thermoelastic variations are related to an undamaged reference condition ( $\Delta S_I$ ).
- Normalizing the thermoelastic data matrix with respect to the stress amplitude  $\Delta\sigma$  in order to detect the thermoelastic signal variation associated with damage ( $\Delta S_{I\_norm} = \Delta S_I / \Delta\sigma$ ).
- Evaluation of the maximum and the minimum values of the thermoelastic signal ( $\Delta S_I / \Delta\sigma$ ) in order to assess the  $\Delta S_{I\_norm} = S_{I\_norm\_max} - S_{I\_norm\_min}$  from the data matrix.

In order to avoid isolated bad pixels due for example, to “dead pixels”, values of 98th and 2nd percentile have been used as parameter for all thermographic quantities.

The processing of signal component S<sub>2</sub> (radiometric thermographic signal correlated to the intrinsic dissipations) refers to the:

- assessment of 98th percentile value of the S<sub>2</sub> signal ( $S_{2\_98perc}$ ). The choice of 98th percentile value is held up by the fact that signal variations are so low when compared to the other parameters, thus, the end of excluding the influence of isolated bad pixels in the analysis is pursued.

The procedure just explained for processing thermal parameters (S<sub>0</sub>, S<sub>1</sub>, S<sub>2</sub>) is shown in Figure 3 in a graphic flow-chart form.

From the sequence acquisition it descends the extraction pixels per pixels of the phase map the phase values. A double dimension Gaussian kernel filtering is provided for all the matrixes  $[\Phi]_{N,M}$ .

Hence the standard deviation is assessed in the last block of figure 4.

Just to analyse the phase maps another step of processing is required. The absolute value of phase signal varies between the loading steps and then, in order to compare the different phase maps, the mean value of the phase signal has been subtracted from each phase map (data matrix) according to the following equation:

$$[\Phi_m]_{N,M} = [\Phi]_{N,M} - \text{mean} \{ [\varphi_{N,M}] \} \quad (6)$$

Where  $[\varphi]_{N,M}$  is the phase data matrix of the  $A_1$  area and  $[\varphi_m]_{N,M}$ , is the same matrix after subtracting its mean value. The phase mean value which was calculated and subtracted from matrix, refers to the data matrix  $[\varphi]_{N,M}$  at fixed loading level.

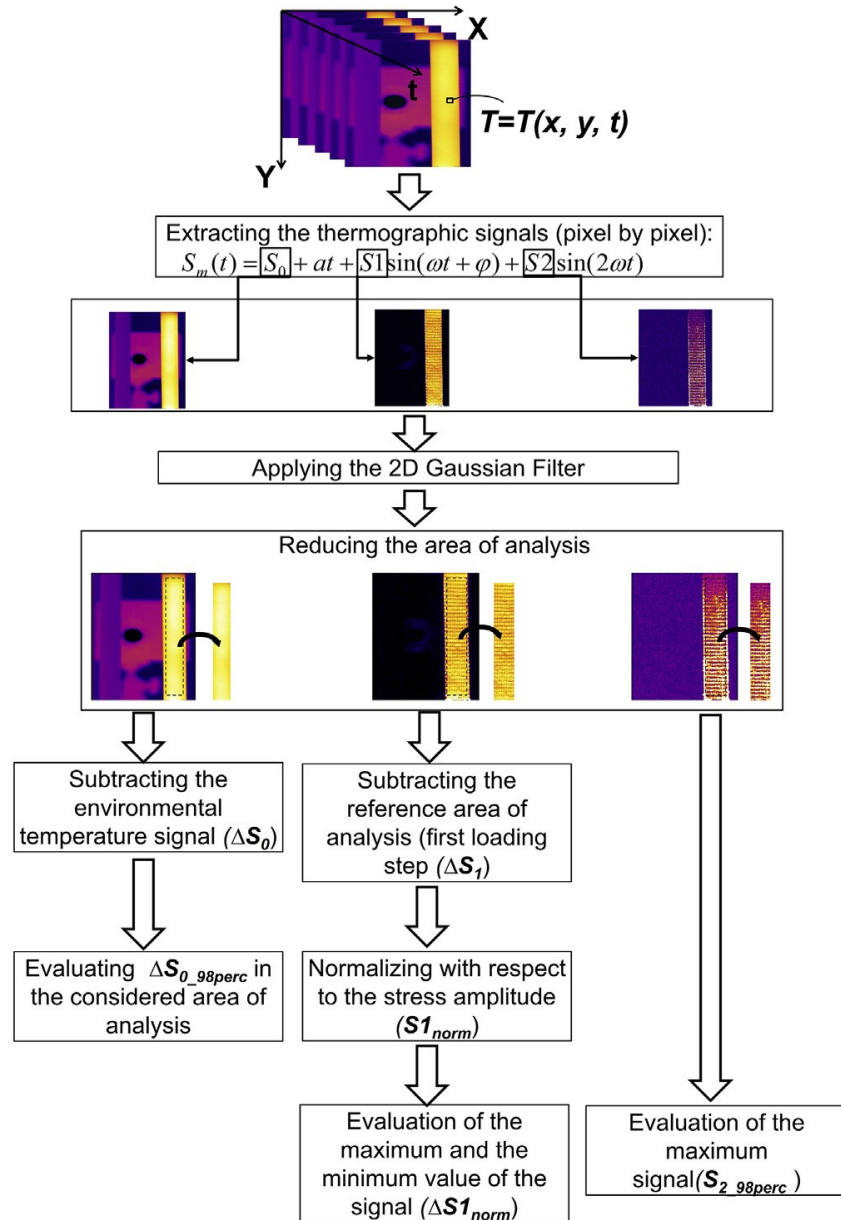


Figure 3. flow-chart of the proposed procedure for thermal indexes.

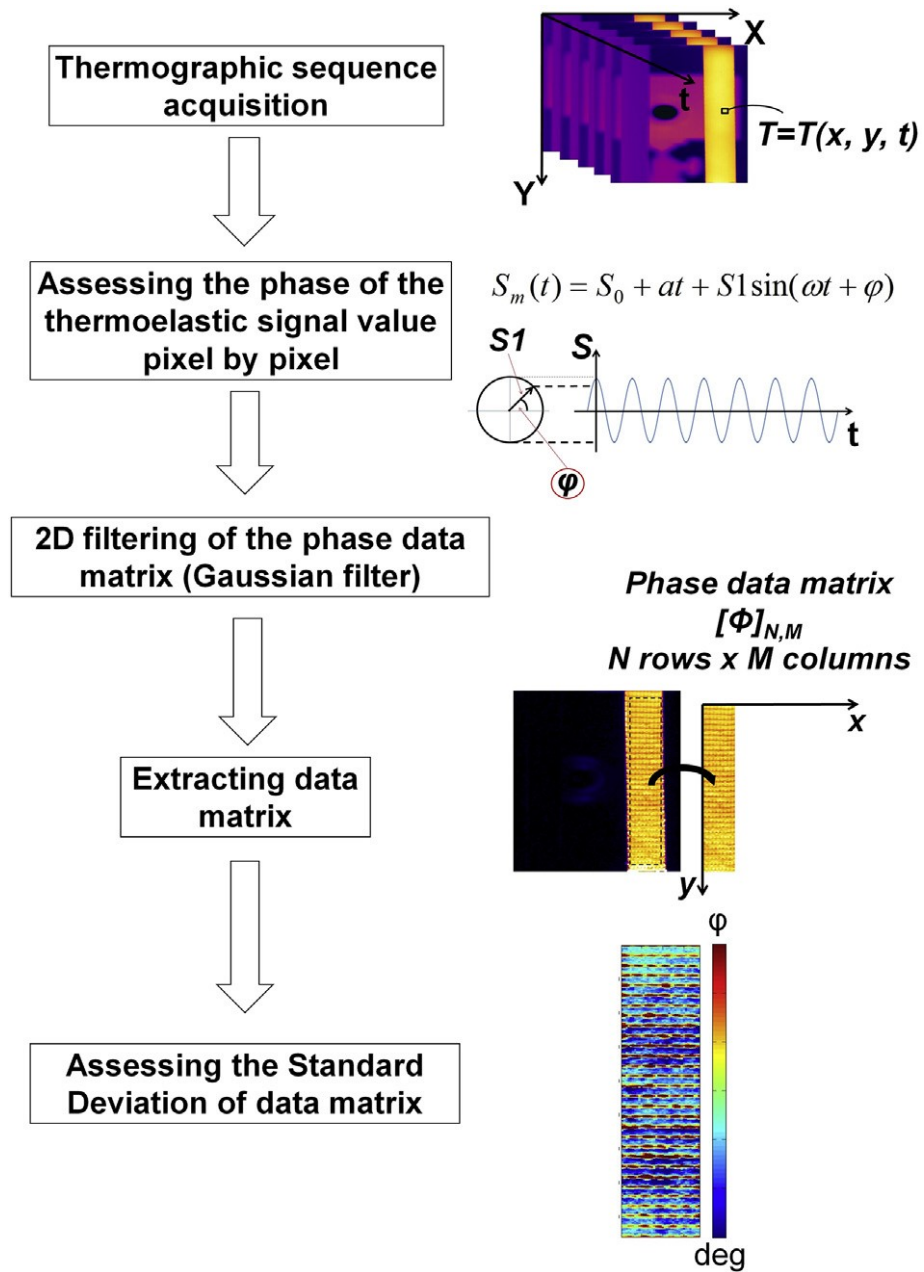


Figure 4. Flow chart of the proposed procedure for phase data.

## 5.2. A new rapid thermographic method to assess the fatigue limit in GFRP Composites.

In this section, the result for assessing the fatigue limit of GFRP composites by using the threshold method is presented together with a graphic analysis leading to obtain complementary information on the damage of composites.

Firstly the convectional curve S-N obtained is shown together with the data of Table 1 (seven of the specimens tested) which allows for the estimation of the fatigue limit of material for a conventional number of cycles. To derive an interval estimation of 'future' observation, it would be appropriate to include in the graph in Figure 5, a 90% survival probability (prediction straight lines) using a confidence interval of 95%, (dashed lines in Figure 5).

Considering a number of  $2 \cdot 10^6$  cycles as lifetime reference within High Cycle Fatigue as suggested by Standard Test Method [30], a value of 127.4 MPa is extracted by data series, representing the fatigue limit in terms of  $s_{max}$  and of 56.12 MPa in terms of stress amplitude ( $\Delta\sigma/2$ ).

Figure 6 shows the evolution of the temperature signal expressed as radiometric signal ( $\Delta S_0$ ) for Specimen 1 and for four different loading conditions (Substep 3). The depicted curve in Figure 6 refers to the mean temperature trend during the stepwise procedure and has been already discussed by several authors [16-18], [29]. A uniform increase of the signal is obtained in the whole gauge area and even in the last loading step (90 MPa) local differences of signal in correspondence to damage, are observed.

In the same way, in Figure 7, the maps of thermoelastic signal (Specimen 1, Substep 3) are reported.

Considering the reference stress condition of 30 MPa, thermoelastic signal experiences positive and negative value variations. As already demonstrated in other works [14-15], TSA allows for location

of the damaged areas of material and in particular, the thermoelastic signal variations are related to the redistribution of the stresses caused by stiffness degradation due to damage [15].

As confirmed by other authors [15], by analyzing stress maps, mechanical behaviour of fibers and matrix is indeed assessed.

In Figure 8, the maps of the thermal signal at twice the loading frequency are shown (Specimen 1, Sub step 3). In addition, in this case, a significant increase of the signal is obtained as the applied stress increases.

As demonstrated by parameter maps at a fixed stress level of 60 MPa, the failure appears on the right side of the gauge length as depicted in Figures 7 and 8 (Area A, crack initiation at



60 MPa). At 90 MPa, the occurrence of cracks hits most of the gauge length.

All maps seem to provide different and complementary information about the type of damage to material. In this regard, further works and other experimental techniques are necessary to relate the different damage mechanisms to the proposed thermographic signal procedure.

The trend of the signals evaluated with the proposed algorithm is shown in Figure 9 as a function of the amplitude stress for each substep.

In particular, the radiometric temperature signal increases for each loading step due to the viscoelastic nature of the matrix material until a significant increase is verified in correspondence with the presence of the damage mechanisms, while thermoelastic ( $S_1$ ) and double frequency signal ( $S_2$ ) show significant variations only for stress values above 60 MPa. Interesting considerations can be made by observing signal behaviour in correspondence with each sub-step, Figure 9. In fact, no appreciable signal differences are present among the three substeps excluding the last loading step coincident with the failure of the specimen.

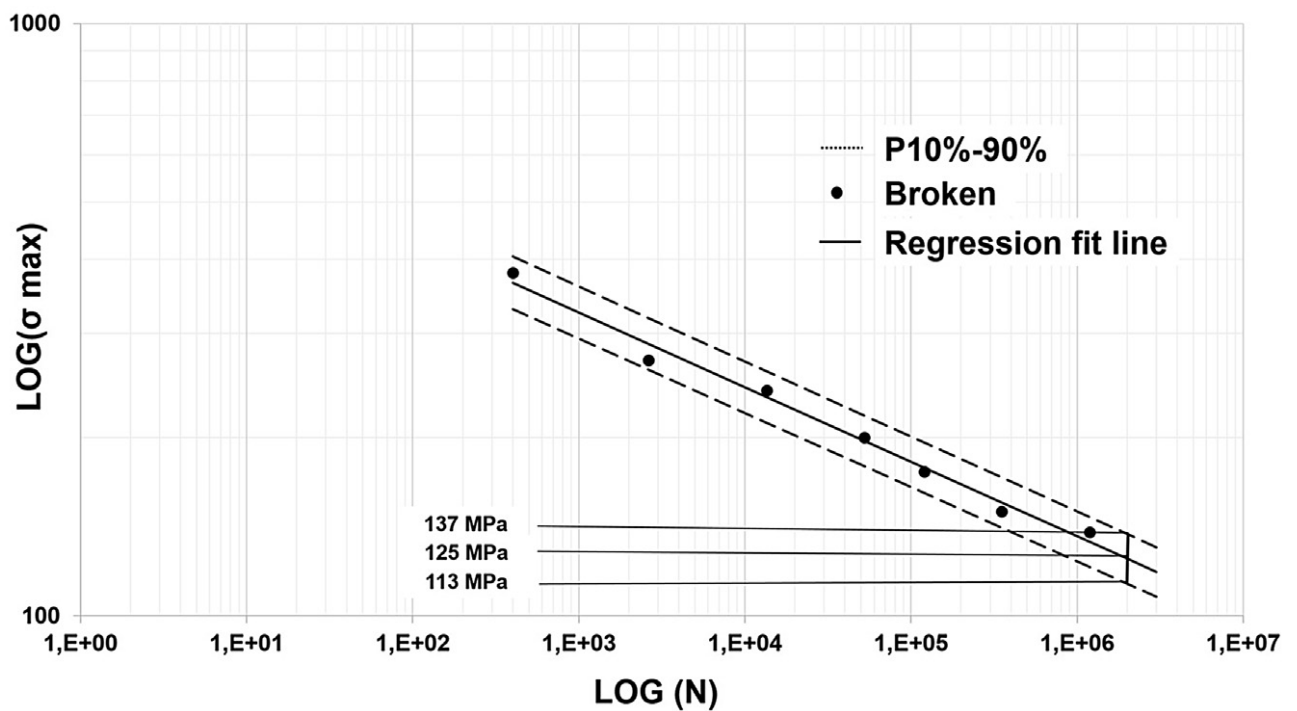


Figure 5. Conventional S-N curve and estimation of the fatigue limit in correspondence with a run-out limit of  $2 \times 10^6$  cycles.

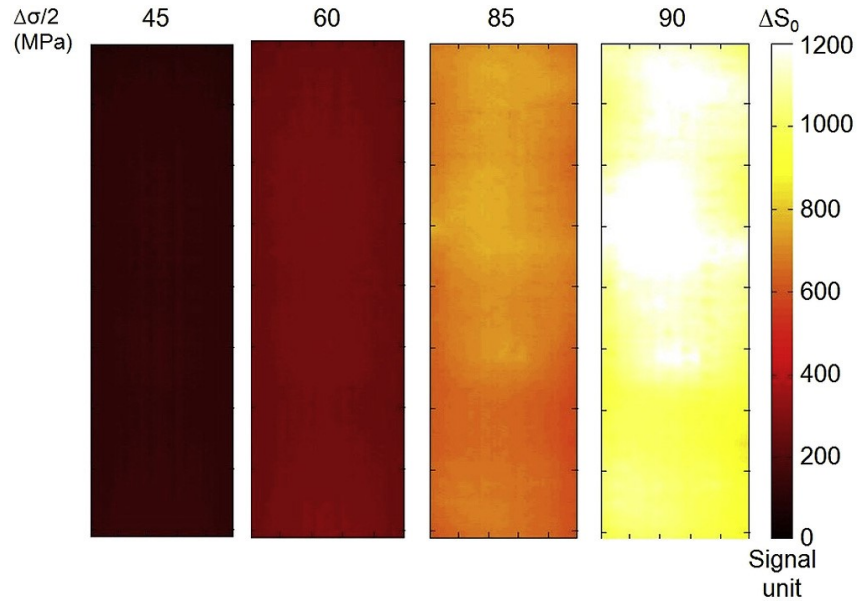


Figure 6. Maps of the radiometric signal obtained for four different loading steps, (Specimen 1, Sub-step 3).

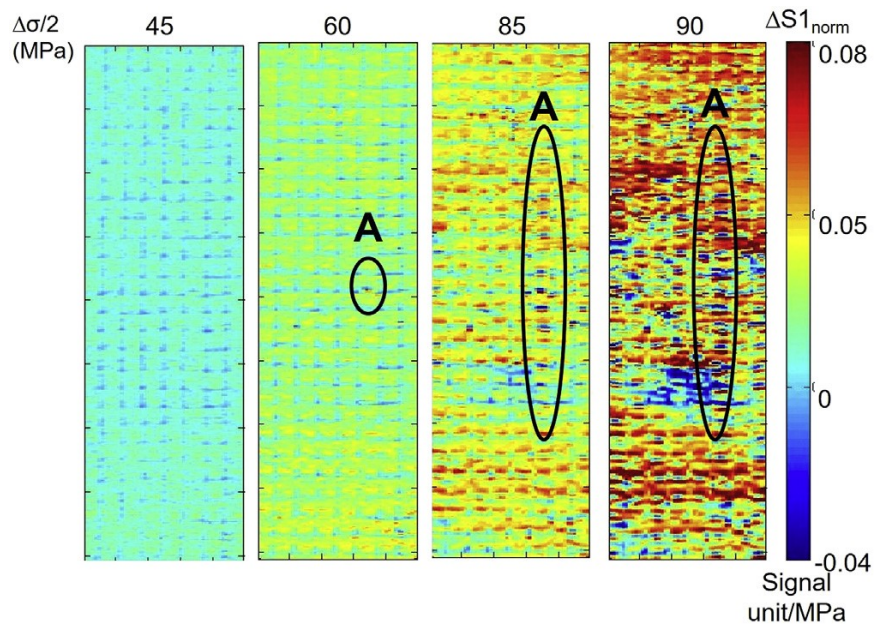


Figure 7. Maps of the thermoelastic signal obtained for four different loading steps, (Specimen 1, Sub-step 3).

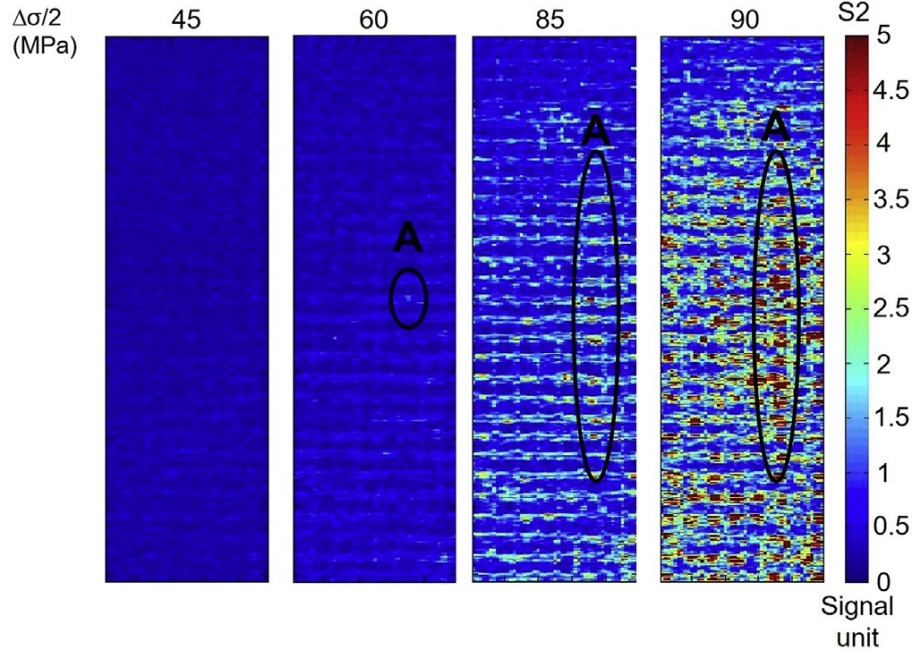


Figure 8. Maps of the thermographic signal at the twice the loading frequency obtained for four different loading steps, (Specimen 1, Sub-step3).

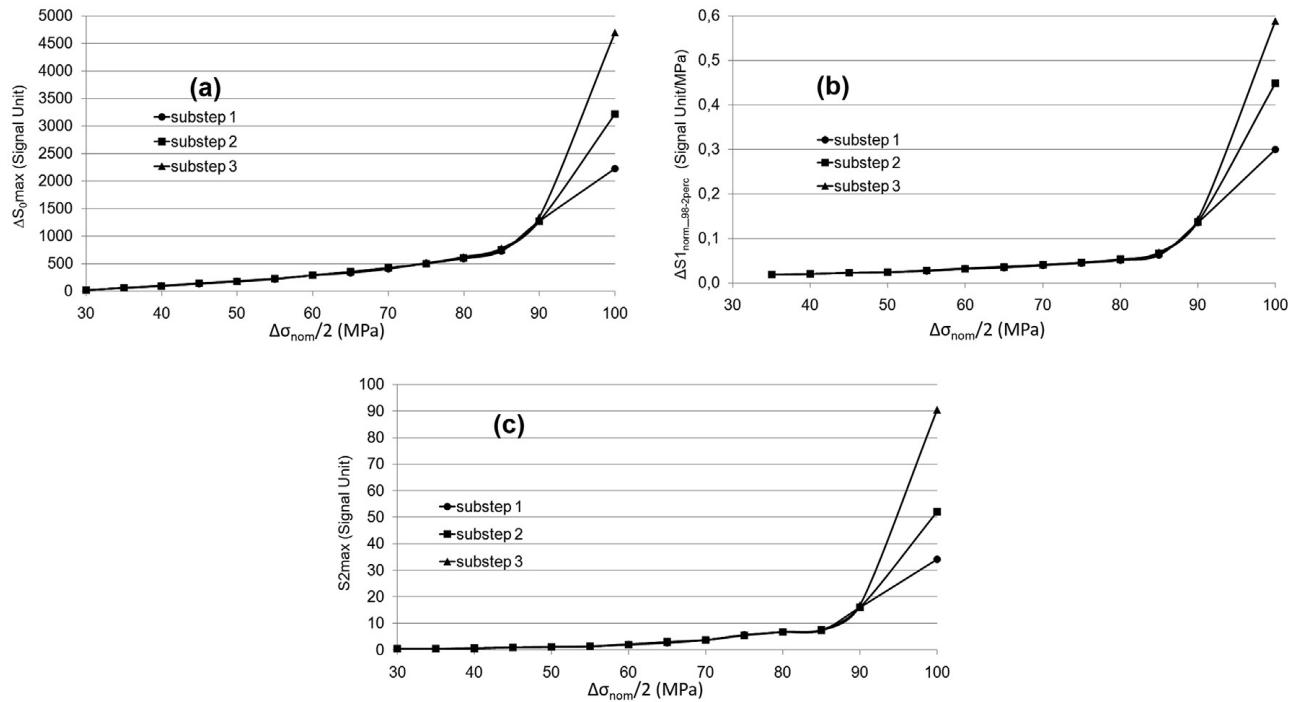


Figure 9. Thermographic signals obtained with proposed procedure as function of the amplitude stress for Specimen 1: comparison among the three sub-steps for the parameter (a)  $\Delta S_0$  (b)  $\Delta S_1$  (c)  $S_2$ .

The application of the threshold method on ( $\Delta S_0_{98\text{perc}}$ ,  $\Delta S_1_{98-2\text{perc}}$  and  $S_2_{98\text{perc}}$ ) involves considering just four initial data couples due to the small number of loading level in elastic regime provided by loading table (Table II).

For each specimen and for each substeps the results are represented in figure 10.

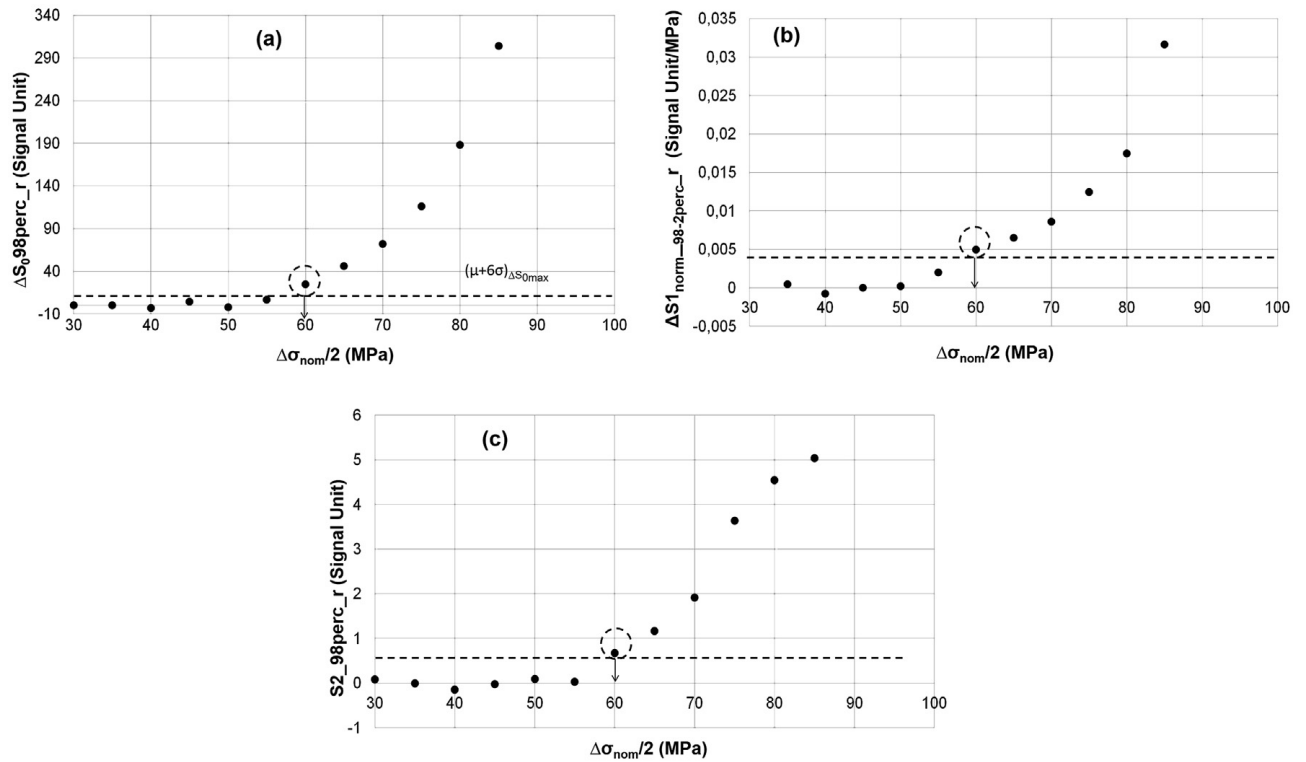


Figure 10. Estimation of the fatigue limit with method [16], (Specimen 1, Sub-step 3): comparison among residual of the three parameters (a)  $\Delta S_0$  (b)  $\Delta S_1$  (c)  $S_2$ .

Figure 10 (a, c) graphically illustrates the above procedure for Specimen 1 at Substep 3. In particular, the residuals are plotted versus the stress amplitude and the dotted line represents the threshold value adopted for the estimation of the fatigue limit. By using other methods it may be difficult to detect this point. The graphical approach [17,18], which involves separation of the data series for the assessment of the breakpoint, is not objective, and deduction and identification are hindered due to the noise affecting thermal measurements. In Table III, the results (fatigue limits in terms of stress semi-amplitudes) for each parameter ( $\Delta S_{0\_98perc}$ ,  $\Delta S_{1\_norm\_98-2perc}$  and  $S_{2\_98perc}$ ) at each sub-step are reported for five tested specimens.

As shown in Table III, referring to a single test, the results show good reproducibility and thus, the reliability of the technique is demonstrated.

This aspect is confirmed by Table IV in which overall results of five tests are compared with the standard test method. The results of thermal methods fit well with the S-N value reference as endorsed by the small standard deviation. In particular, referring to the analysis of three parameters the closest one to the reference value (56.12 MPa) is the  $S_{2\_98perc}$  parameter (~58 MPa), although the others provide a good estimation of fatigue limit.

As already shown in Fig. 9 (a, c), no difference exists among substeps and the adopted procedure for evaluating the fatigue limit provides the same value for each sub-step. Moreover, the considered thermographic parameters for low stress values seem independent

from the number of cycles at which the thermographic sequence was acquired. This means that an estimation of the fatigue limit could be obtained with the proposed procedure very rapidly since the thermographic data can be acquired at any time during the tests, whilst for the traditional procedure it is necessary to achieve steady state conditions before acquisition. Results obtained with thermography techniques are in good agreement with the fatigue limit obtained in the conventional manner by considering a run-out limit of  $2 \cdot 10^6$  cycles.

N° Specimen	Loading sub-step	$\Delta S_{0\_98perc}$ (MPa)	$ASI_{norm\_98-2perc}$ (MPa)	$S2\_98perc$ (MPa)
1	1	60.00	60.00	65.00
	2	60.00	60.00	60.00
	3	60.00	60.00	60.00
	Average	60.00	60.00	61.67
2	1	60.00	60.00	60.00
	2	60.00	60.00	60.00
	3	60.00	65.00	60.00
	Average	60.00	61.67	60.00
3	1	60.00	65.00	55.00
	2	60.00	70.00	55.00
	3	60.00	65.00	50.00
	Average	60.00	66.67	53.33
4	1	70.00	55.00	55.00
	2	65.00	55.00	70.00
	3	65.00	70.00	55.00
	Average	66.67	60.00	60.00
5	1	60.00	65.00	55.00
	2	55.00	65.00	50.00
	3	55.00	65.00	55.00
	Average	56.67	65.00	53.33

Table III. Comparison between overall results in sub-step, accomplished by adopting the thermographic technique.

N° Specimen	$\Delta S_{0\_98perc}$ (MPa)	$ASI_{norm\_98-2perc}$ (MPa)	$S2\_98perc$ (MPa)	<i>S-N curve</i> ( $2 \cdot 10^6$ cycles)
1	60.00	60.00	61.67	$\Delta \sigma / 2 = 56.12 \text{ MPa}$
2	60.00	61.67	60.00	
3	60.00	66.67	53.33	
4	66.67	60.00	60.00	
5	56.67	65.00	53.33	
Average	60.67	62.67	57.67	
Standard Deviation	3.65	3.03	4.01	

Table IV. Comparison between overall results accomplished by adopting the thermographic technique and conventional fatigue tests

### 5.3. Study of damage evolution in composite materials based on the Thermoelastic Phase Analysis (TPA) method

In this section, it will be presented the phase data compared with the mean temperature data, that is a global parameter and local parameter, in order to confirm the capability of TPA approach in the thermal signal analysis.

The Standard value are represented in figure 5 that is the convectional curve S-N.

Fig. 11 a, 12 a and 13 a show the evolution of the temperature signal expressed as radiometric signal ( $\Delta S_0$ ) for Specimens 2, 3 and 4 and for four different stress loading conditions (Sub-step 3). As stated in the previous section, this figure refers to the mean temperature trend during the stepwise procedure and has already been discussed by several authors [12] , [16-17].

In the same way, in Fig. 11 b, 12 b and 13 b the maps of thermoelastic phase signal (Specimens 2, 3 and 4, Sub-step 3) are reported.

Both temperature (Figs. 11a, 12a and 13a) and phase signal (figures 11 b, 12 b and 13 b) present a significant increase in damaged areas beyond the stress amplitude of 60 MPa. In particular, a correspondence is very evident between the damaged areas (dashed lines) comparing temperature and phase signal, even if the latter provides more details and information about damage. As clearly evident in all phase maps, with respect to the first loading steps, phase signal experiences positive and negative value variations due to different mechanisms involved during fatigue loading. In particular, there is a well distinguished ordered pattern of horizontal stripes in the phase signal maps, which is very likely related to the morphology of the fabric of the surface lamina. In fact, phase signal increases in correspondence with the stitched thermoplastic yarn used in these fabrics to prevent crimping or undulations that can lead to loss of performance in the finished laminate. It is worth noting that the stitched yarns are visible also for lower values of imposed stress since they provide a different thermoelastic response with respect to the remaining part of the specimen. These stitches are fibres

which are not aligned with the yarns and therefore, as also predicted by Eq. (1) and shown in Ref. [20], they give a different thermoelastic signal amplitude. In these areas, a different phase signal is probably due to a possible through-the-thickness heat leak between the stitches and the underlying fibre yarns due to very high temperature gradients. Consequently, the heat exchanges lead to the loss of adiabatic conditions and then to a positive phase shift over the stitches.

A phase signal delay characterizes (figures 11b, 12b,13b) the damaged areas of specimens as well illustrated in Palumbo's work [27]. This delay, as well as thermoelastic amplitude, is



correlated to the stiffness degradation with consequent strain redistribution in damaged areas. In fact, as described by other authors [32], the stiffness degradation is accompanied by an increase of the area of hysteresis loop and consequent phase lag between stress and strain. In particular, the strain is delayed with respect to stress and the phase lag increases as the fatigue damage increases.

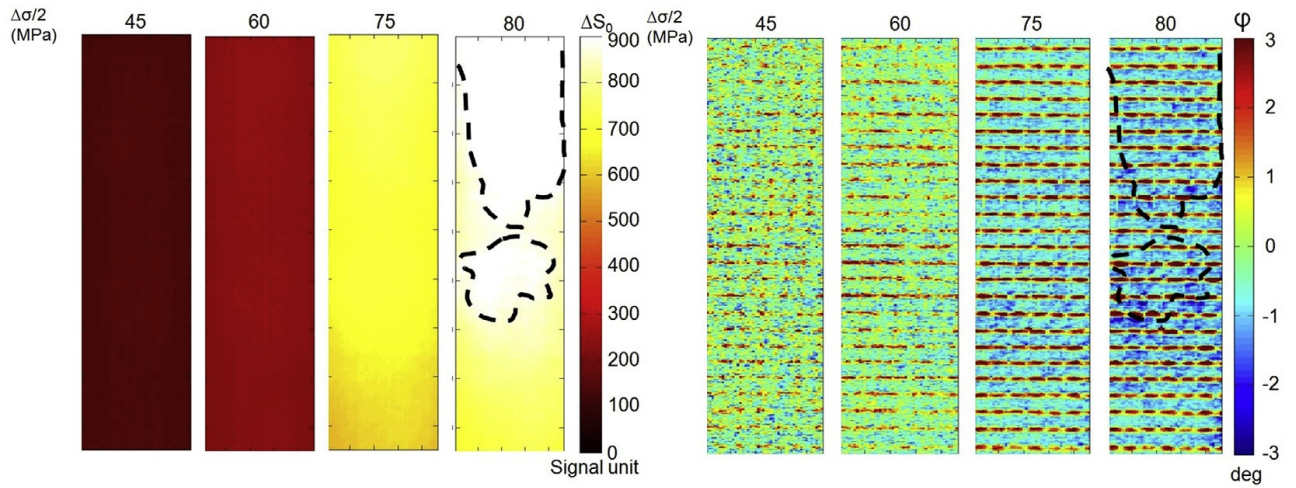


Figure 11. Maps of radiometric temperature signal (a) and phase signal (b) obtained for 4 different loading steps, (Specimen 2, Sub-step 3).

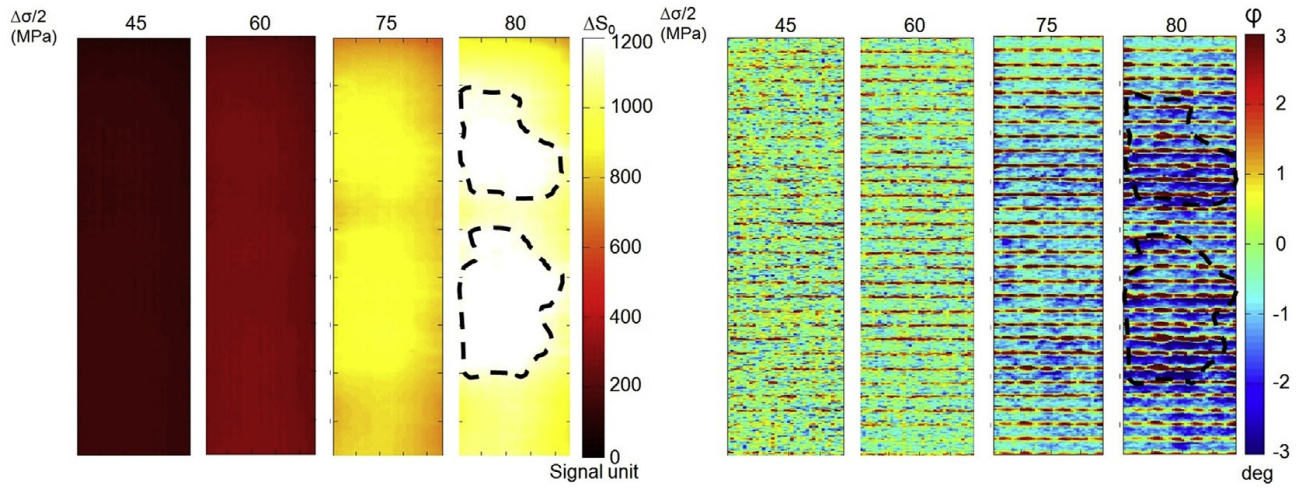


Figure 12. Maps of radiometric temperature signal (a) and phase signal (b) obtained for 4 different loading steps, (Specimen 3, Sub-step 3).

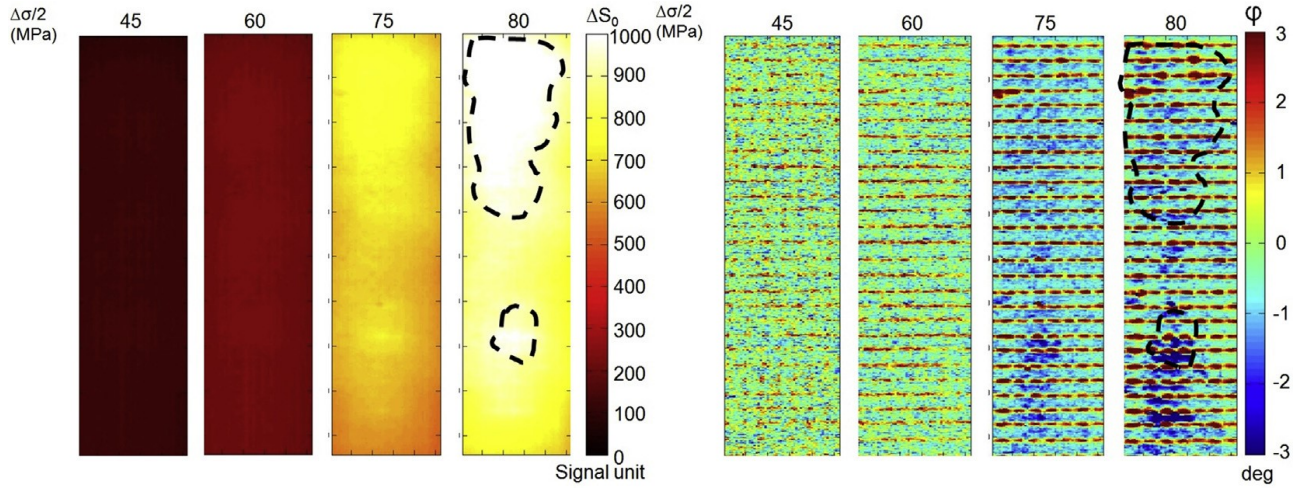


Figure 13. Maps of radiometric temperature signal (a) and phase signal (b) obtained for 4 different loading steps, (Specimen 4, Sub-step 3).

In this regard, further works and other experimental techniques are necessary to relate the different damage mechanisms to the proposed thermographic procedure based on the monitoring of the phase signal.

Moreover, it is clear that the phase signal variation is effectively due to the yarn damage rather than to the effect of motion of the specimen. In fact, there are not evident differences between the upper part of specimen fixed to the static grip and the lower portion fixed to the dynamic one.

The trend of the signals evaluated with the proposed algorithm is shown in figure 14 as a function of the amplitude stress for each substep. In particular, the radiometric temperature signal increases for each loading step due to the viscoelastic nature of the matrix material until a significant increase is verified in correspondence with the presence of the damage mechanisms, while the Standard Deviation of thermoelastic phase signal shows significant variations only for stress values above 55 MPa, Figure 15. In Figure 16, the same phase data are represented by omitting the last loading step. As already experimented for metallic materials [29], at first, the Standard Deviation of phase decreases as load increases and this is simply explained by a higher and better signal to noise ratio granted by higher load amplitudes. Subsequently, for a number of load steps, the phase is substantially stable. With the further increasing of loads, the Standard Deviation tends to increase due to the damage phenomena.

By considering this typical trend of phase data, the data have been processed by using the Slope method.

In this way, by considering Figure 16, the loading step that reaches the minimum value of Standard Deviation is considered to be the fatigue limit of material. Tables V-IX show the results obtained for all specimens in each sub-step.



Figs. 17 and 18 graphically illustrate the above procedures for Specimens 2, 3 and 4 at Sub-step 3. In particular, for the phase values, the slope values are plotted versus the stress amplitude and the dotted line represents the threshold value adopted for the estimation of the fatigue limit.

In Tables X and XI the results (fatigue limits in terms of stress semi-amplitudes) for each parameter for temperature and phase signal at each sub-step are reported for five tested specimens.

By comparing the fatigue limits obtained by using  $\Delta S_0$  and 4 data series, it is possible to observe that: temperature data allows for overestimation of the fatigue limit (60.67 MPa) with respect to the reference value 56.20 MPa, while the fatigue limit found by using 4 (52.00 MPa) seems to underestimate the value of S-N reference. Nevertheless, the difference between the fatigue limit found by using both temperature and phase are similar enough to the reference. It is therefore possible to conclude that the results fit well with the S-N value reference as endorsed by the small standard deviation. Moreover, the phase of thermoelastic signal (52 MPa) provides more conservative values of fatigue limit with respect to temperature data.

As already shown in Figs. 16 and 17, no difference exists between sub-steps. Hence, as shown in Ref. [20], an estimation of the fatigue limit could be very rapidly obtained with the proposed procedure

since the thermographic data can be acquired at any time during the tests, while for the traditional procedure it is necessary to achieve steady state conditions before acquisition.

Finally, the small scattering between thermal parameters suggests that fatigue estimations obtained using thermal methods provide accurate results. The parameters provided by thermal methods converge to close estimations of a fatigue limit since they are associated to a considerably high value of load cycles, specifically  $2 \cdot 10^6$ . This result makes such thermally derived fatigue limit estimations suitable for most engineering uses.

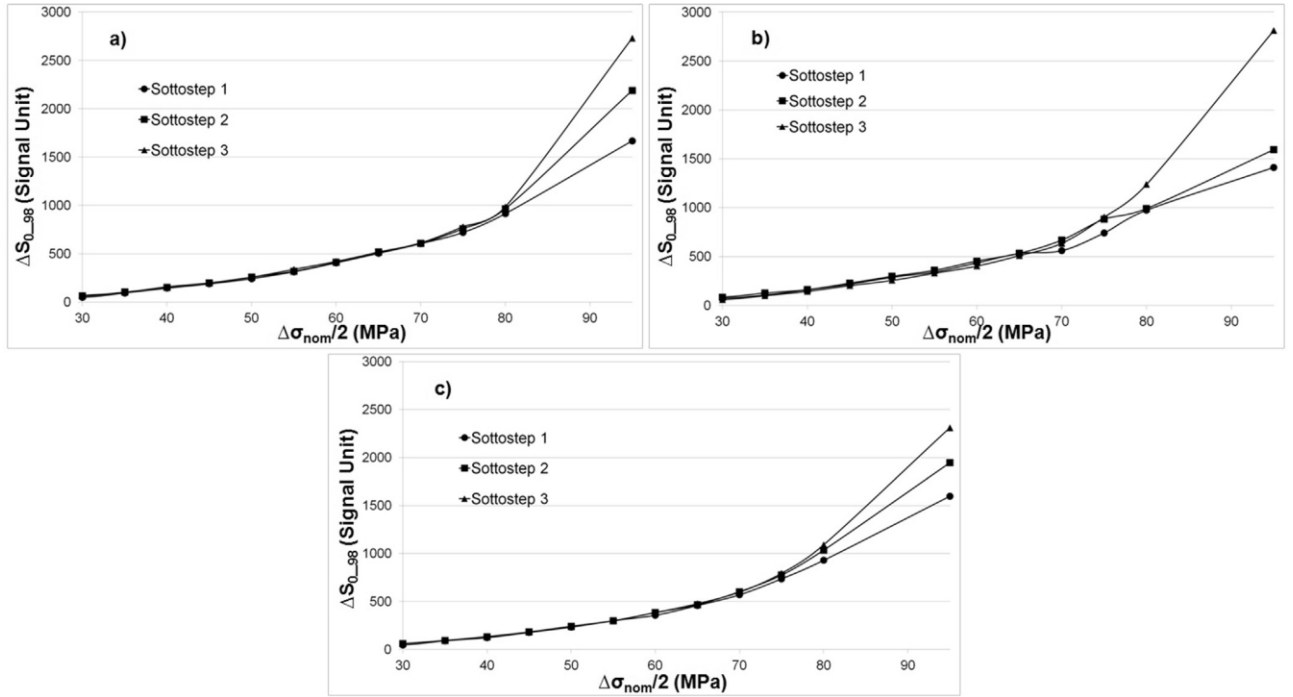


Figure 14. Thermographic signals expressed as radiometric uncalibrated signal obtained with proposed procedure as function of the amplitude stress for Specimens: a) 2, b) 3 and c) 4.

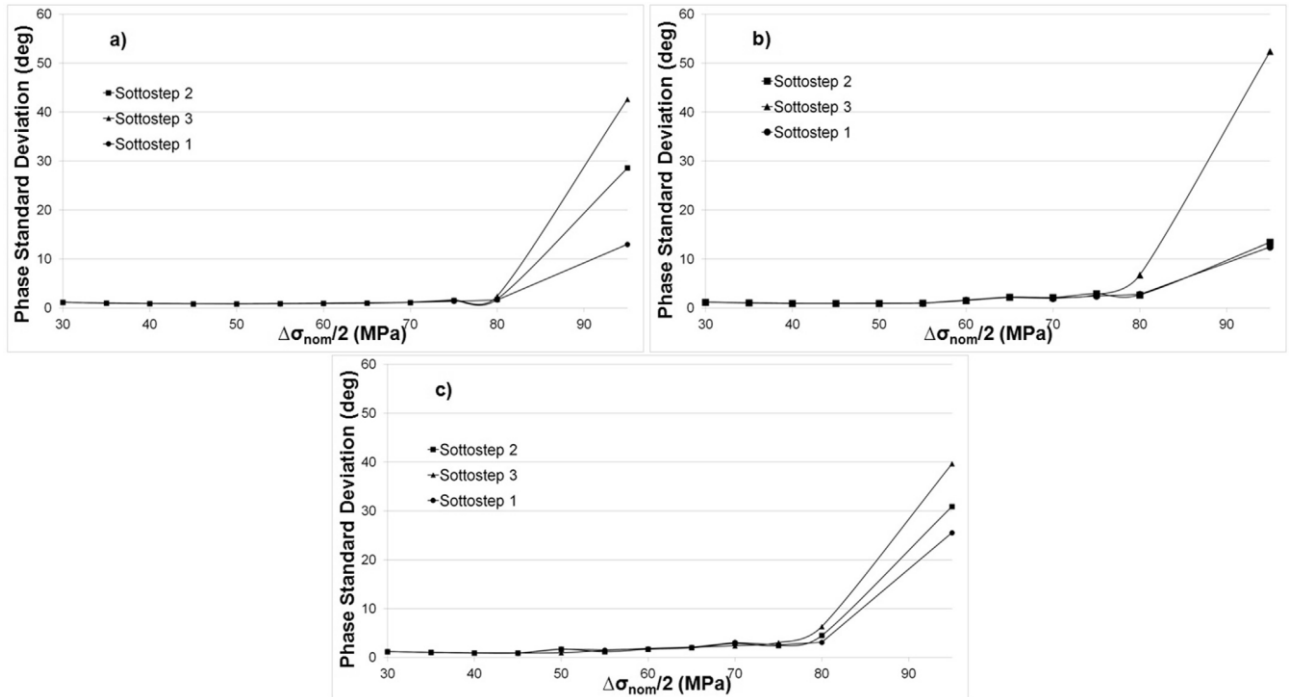


Figure 15. Standard Deviation of phase signal obtained with proposed procedure as function of the amplitude stress for Specimens: a) 2, b) 3 and c) 4.

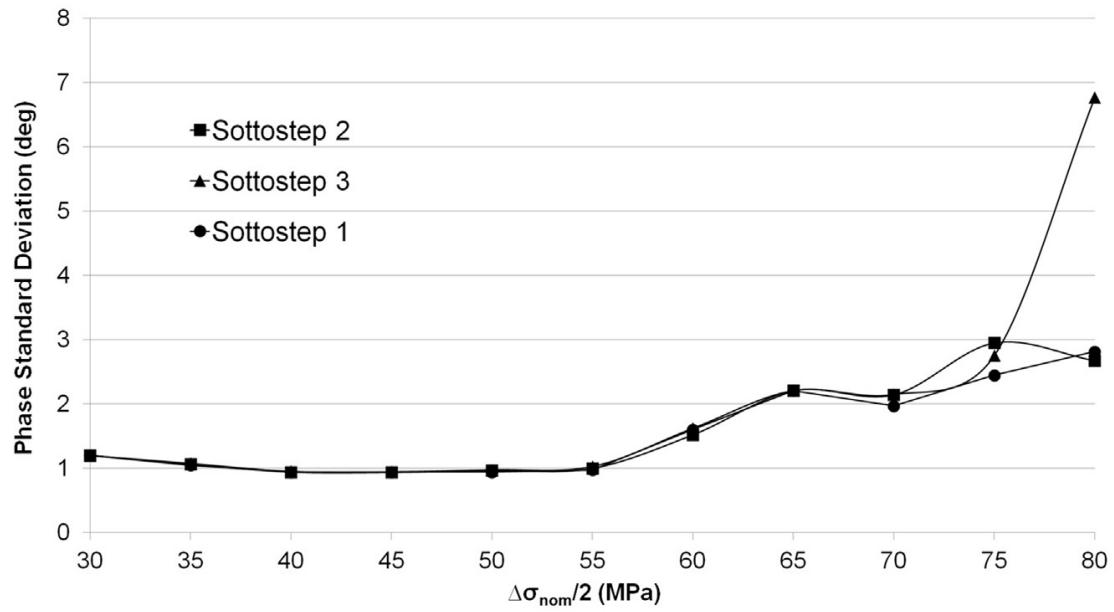


Figure 16. Standard Deviation of phase signal obtained with proposed procedure as function of the amplitude stress for Specimen 4.

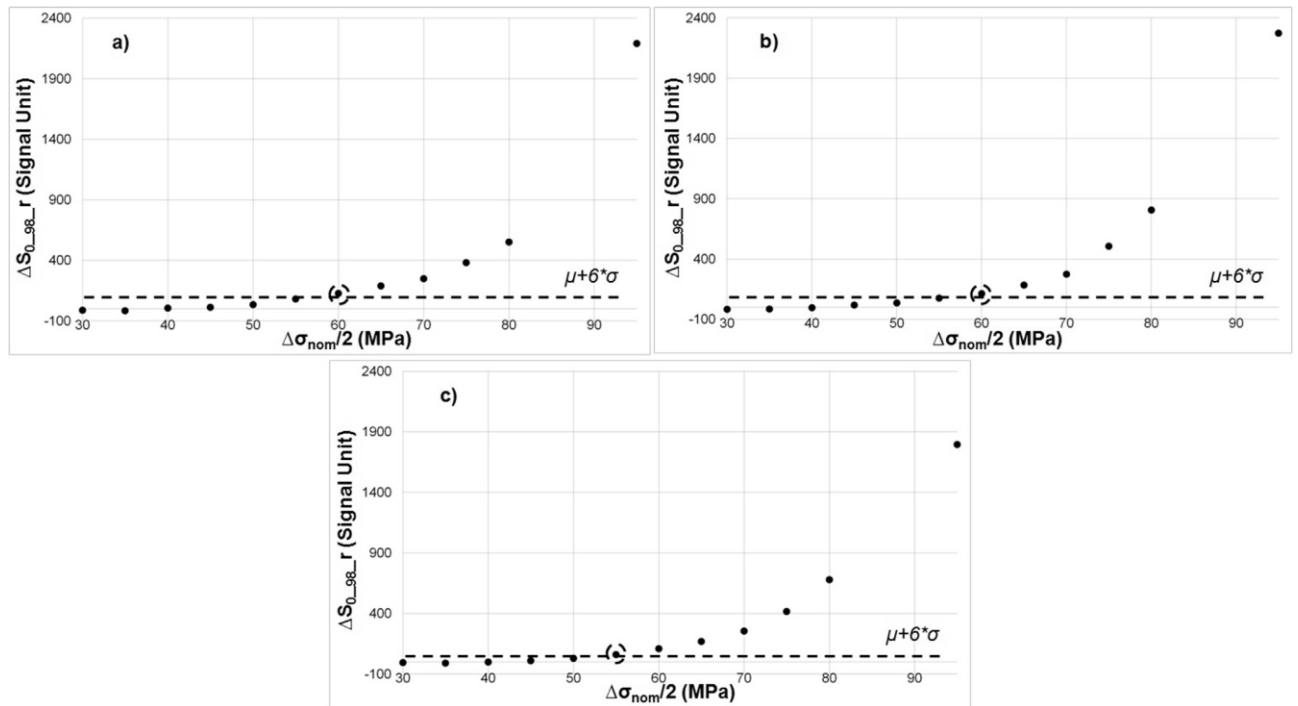


Figure 17. Estimation of the fatigue limit with the method [32] on temperature data, Sub-step 3, specimens: a) 2, b) 3 and c) 4.

		SUBSTEP 1		SUBSTEP 2		SUBSTEP 3	
N	$\Delta\sigma/2$	SD_ $\varphi_i$	M <sub>i</sub>	SD_ $\varphi_i$	M <sub>i</sub>	SD_ $\varphi_i$	M <sub>i</sub>
1	30	1,22	-	1,22	-	1,23	-
2	35	1,06	-0,03	0,92	-0,05	1,07	-0,03
3	40	0,95	-0,02	0,67	-0,02	0,93	-0,02
4	45	0,87	-0,01	<b>0,68</b>	0,01	0,88	-0,01
5	50	0,84	0	0,75	0,02	<b>0,87</b>	0,01
6	55	<b>0,86</b>	0,01	0,89	0,03	0,94	0,01
7	60	0,93	0,02	1,09	0,06	1,01	0,02
8	65	1,04	0,03	1,44	0,06	1,1	0,08
9	70	1,18	0,03	1,64	0,06	1,86	0,04
10	75	1,37	0,14	2	0,09	1,5	0,03
11	80	2,6	1,72	2,51	2,97	2,18	3,63
12	95	33,66	-	57,23	-	69,13	

Table V. Values of phase standard deviation (SD\_ $\varphi_i$ ) and slope (m) of each loading level and sub-step, capable of estimating the fatigue limit of material (Specimen 1). In bold, the m<sub>i</sub> values for which the condition in Point 3 is verified.

		SUBSTEP 1		SUBSTEP 2		SUBSTEP 3	
N	$\Delta\sigma/2$	SD_ $\varphi_i$	M <sub>i</sub>	SD_ $\varphi_i$	M <sub>i</sub>	SD_ $\varphi_i$	M <sub>i</sub>
1	30	1,17	-	1,17	-	1,15	-
2	35	1,00	-0,03	1,00	-0,03	1,01	-0,03
3	40	0,91	-0,02	0,91	-0,01	0,90	-0,02
4	45	0,85	-0,01	0,86	-0,01	0,85	0,00
5	50	0,82	0	0,85	0,00	0,86	0,00
6	55	<b>0,86</b>	<b>0,01</b>	<b>0,89</b>	0,01	0,90	0,01
7	60	0,91	0,01	0,96	0,01	0,98	0,02
8	65	1,00	0,02	1,04	0,02	1,06	0,02
9	70	1,12	0,04	1,15	0,05	1,19	0,06
10	75	1,38	0,5	1,53	0,06	1,68	0,12
11	80	1,65	0,62	1,79	1,45	2,43	2,19
12	95	13.02	-	28.58	-	42.62	-

Table VI. Values of phase standard deviation (SD\_ $\varphi_i$ ) and slope (m) of each loading level and sub-step, capable of estimating the fatigue limit of material (Specimen 2). In bold, the m<sub>i</sub> values for which the condition in Point 3 is verified.

		SUBSTEP 1		SUBSTEP 2		SUBSTEP 3	
N	$\Delta\sigma/2$	SD_ $\varphi_i$	M <sub>i</sub>	SD_ $\varphi_i$	M <sub>i</sub>	SD_ $\varphi_i$	M <sub>i</sub>
1	30	1,21	-	1,20	-	1,19	-
2	35	1,01	-0,03	1,05	-0,03	1,03	-0,03
3	40	0,92	-0,01	0,91	-0,02	0,93	-0,01
4	45	<b>0,87</b>	<b>0,08</b>	<b>0,90</b>	<b>0,08</b>	0,91	0,00
5	50	1,70	0,06	1,69	0,03	<b>0,95</b>	<b>0,05</b>
6	55	1,52	0,00	1,16	0,00	1,41	0,09
7	60	1,73	0,05	1,69	0,08	1,84	0,07
8	65	2,06	0,14	1,97	0,12	2,09	0,06

9	70	3.08	0,05	2.85	0,05	2.40	0,09
10	75	2.56	0,00	2.42	0,16	3.04	0,39
11	80	3.11	1.23	4.49	1,50	6.33	1.92
12	95	25.55	-	30.91	-	39.65	-

Table VII. Values of phase standard deviation ( $SD_{\varphi_i}$ ) and slope (m) of each loading level and sub-step, capable of estimating the fatigue limit of material (Specimen 3). In bold, the  $m_i$  values for which the condition in Point 3 is verified.

N	$\Delta\sigma/2$	SUBSTEP 1		SUBSTEP 2		SUBSTEP 3	
		$SD_{\varphi_i}$	$M_i$	$SD_{\varphi_i}$	$M_i$	$SD_{\varphi_i}$	$M_i$
1	30	1.20	-	1.20	-	1.20	-
2	35	1.04	-0.03	1.06	-0.03	1.07	-0.03
3	40	0.94	-0.01	0.94	-0.01	0.95	-0.01
4	45	<b>0.94</b>	<b>0.00</b>	<b>0.93</b>	<b>0.00</b>	<b>0.94</b>	<b>0.00</b>
5	50	0.94	0.00	0.96	0.01	0.97	0.01
6	55	0.97	0.07	1.00	0.06	1.03	0.07
7	60	1.60	0.12	1.60	0.12	1.62	0.12
8	65	2.21	0.04	1.52	0.06	2.21	0.05
9	70	1.97	0.02	2.21	0.07	2.15	0.05
10	75	2.45	0.08	2.95	0.05	2.75	0.46
11	80	2.81	0.53	2.67	0.57	6.77	2.61
12	95	12.47	-	13.43	-	52.40	-

Table VIII. Values of phase standard deviation ( $SD_{\varphi_i}$ ) and slope (m) of each loading level and sub-step, capable of estimating the fatigue limit of material (Specimen 4). In bold, the  $m_i$  values for which the condition in Point 3 is verified.

N	$\Delta\sigma/2$	SUBSTEP 1		SUBSTEP 2		SUBSTEP 3	
		$SD_{\varphi_i}$	$M_i$	$SD_{\varphi_i}$	$M_i$	$SD_{\varphi_i}$	$M_i$
1	30	1.20	-	1.20	-	1.19	-
2	35	0.98	-0.04	1.02	-0.03	0.94	-0.04
3	40	0.84	-0.02	0.85	-0.02	0.84	-0.01
4	45	0.76	-0.01	0.77	-0.02	0.81	-0.01
5	50	0.69	-0.01	0.69	0.00	0.71	-0.01
6	55	0.70	0.00	<b>0.73</b>	<b>0.01</b>	<b>0.74</b>	<b>0.01</b>
7	60	<b>0.74</b>	<b>0.01</b>	0.75	0.01	0.80	0.01
8	65	0.82	0.02	0.85	0.02	0.88	0.02
9	70	0.90	0.02	0.93	0.02	0.96	0.02
10	75	1.04	0.02	1.04	0.03	1.08	0.04
11	80	1.13	0.12	1.21	0.19	1.32	0.19
12	95	3.37	-	4.70	-	4.70	-

Table IX. Values of phase standard deviation ( $SD_{\varphi_i}$ ) and slope (m) of each loading level and sub-step, capable of estimating the fatigue limit of material (Specimen 5). In bold, the  $m_i$  values for which the condition in Point 3 is verified.

$\Delta S0\_98\text{perc}$ [MPa]				
N° sample	sub. 1	sub. 2	sub. 3	average for a sample
1	60,00	60,00	60,00	60,00
2	60,00	60,00	60,00	60,00
3	60,00	60,00	60,00	60,00
4	70,00	65,00	65,00	66,67
5	60,00	55,00	55,00	56,67
total average	60,67			
standard deviation	3,72			

Table X. Overall result for meant temperature data

Phase Standard Deviation [MPa]				
N° sample	sub. 1	sub. 2	sub. 3	average for a sample
1	50,00	50,00	50,00	60,00
2	55,00	55,00	55,00	55,00
3	45,00	45,00	50,00	46.67
4	55,00	55,00	50,00	51.67
5	60,00	55,00	55,00	56,67
total average	52.00			
standard deviation	4.14			

Table XI. Overall results accomplished by adopting the Standard Deviation of the phase signal.

## Conclusions

In this Chapter, the threshold and slope methods have been applied for evaluating the fatigue limit of GFRP composite materials.

They represent a useful tool for rapidly evaluating the fatigue limit with respect to the traditional thermographic method and the technique shows great potential as a non-destructive testing tool, thus, it could well be suitable for the monitoring of real and more complex components undergoing actual loading conditions.

Such the analysis interested twelve specimens extracted from a laminate panel: seven of them were tested to assess S-N curves while five of them were tested in an ‘accelerated’ manner by performing the stepwise loading procedure in which each specimen underwent incremental loading levels until failure and three thermal sequences were acquired during each step in correspondence with three different cycle numbers.

Moreover, it has been confirmed that the parameter related to mean temperature increase overestimates the fatigue limit (60.67 MPa) with respect the reference value 56.20 MPa, while the fatigue limit found by using  $\phi$  (52.00 MPa) seems underestimates the value of S-N reference.

Nevertheless, the difference between both the fatigue limit found by using temperature and phase are enough similar to the reference, then it's possible to conclude that the results fit well with the reference value.

The main considerations about the results obtained may be summarised as follows:

- the Standard Deviation of the phase signal can be used as a parameter to describe the fatigue damage in GFRP materials,
- no differences were observed between sub-steps (same loading step),
- results obtained with the proposed procedure show good agreement with those obtained by the S-N curve, an estimation of the fatigue limit may be obtained with the proposed procedure very rapidly since the phase data can be acquired at any time during the tests, in the same way as metallic materials, phase signal provides local and more detailed information about the damaged areas.

## References

- [66] M.K. Bannister. Development and application of advanced textile composites. Proceedings of the Institution of Mechanical Engineers, Part L: Journal of Materials Design and Applications, 218: 253-260, 2004.
- [67] D. Palumbo, R. Tamborrino, U. Galietti, P. Aversa, A. Tati , V.A.M. Luprano. Ultrasonic analysis and lock-in thermography for debonding evaluation of composite adhesive joints. NDT & E International, 78, 1-9, 2016.
- [68] B. Harris. Fatigue in composites. Cambridge: Woolhead Publishing Ltd, 2003.
- [69] V. Munoz, B. Valès, M. Perrin M, Pastor ML, Weleman H, Cantarel A. Damage detection in CFRP by coupling acoustic emission and infrared thermography. Composites: Part B, 85, 68-75, 2016.
- [70] C. Goidescu, H. Weleman , C. Garnier, M. Fazzini, R. Brault , E. Péronnet , S. Mistou. Damage investigation in CFRP composites using full-field measurement technique: Combination of digital image stereo-correlation, infrared thermography and X-ray tomography. Composites: Part B, 48, 95-105, 2013.
- [71] M. Naderi, A. Kahirdeh, M.M. Khonsari. Dissipated thermal energy and damage evolution of Glass/Epoxy using infrared thermography and acoustic emission. Composites: Part B, 2012;43:1613-1620.
- [72] E.Z. Kordatos, D.G. Aggelis, T.E. Matikas. Monitoring mechanical damage in structural materials using complimentary NDE techniques based on thermography and acoustic emission. Composites: Part B, 43, 2676-2686, 2012.
- [73] D. Palumbo, F. Ancona, U. Galietti . Quantitative damage evaluation of composite materials with microwave thermographic technique: feasibility and new data analysis. Meccanica, 50, 443-459, 2015.
- [74] U. Galietti, R. Dimitri , D. Palumbo, P. Rubino. Thermal analysis and mechanical characterization of GFRP joints. In: 15th European Conference on Composite Materials: Composites at Venice, ECCM 2012, Venice, Italy, 24-28 June, 2012.



- [75] R. Tamborrino, D. Palumbo, U. Galietti, P. Aversa, S. Chiozzi , V.A.M. Luprano. Assessment of the effect of defects on mechanical properties of adhesive bonded joints by using non destructive methods. *Composites Part B*, 91, 337-345, 2016.
- [76] J. Montesano, Z. Fawaz, H. Bougherara . Use of infrared thermography to investigate the fatigue behavior of a carbon fiber reinforced polymer composite. *Composite Structures*, 97, 76-83, 2013.
- [77] R. Steinberger, T.I. ValadasLeitão, E. Ladstätter,G. Pinter, W. Billinger,R.W. Lang. Infrared thermographic techniques for non-destructive damage characterization of carbon fibre reinforced polymers during tensile fatigue testing. *International Journal of Fatigue*, 28, 1340-1347, 2006.
- [78] T.R. Emery, J.K. Dulieu-Barton. Thermoelastic Stress Analysis of the damage mechanisms in composite materials. *Composites: Part A*, 41:1729-1742, 2010.
- [79] R.K. Fruehmann, J.M. Dulieu-Barton, S. Quinn. Assessment of the fatigue damage evolution in woven composite materials using infra-red techniques. *Composite Science and Technology*, 70:937-946, 2010.
- [80] R. De Finis, D. Palumbo, F. Ancona, U.Galietti. Fatigue Limit Evaluation of Various Martensitic Stainless Steels with New Robust Thermographic Data Analysis. *International Journal of Fatigue*,74, 88-96, 2014.
- [81] M.P. Luong. Infrared observation of thermomechanical couplings in solids. *Thermosense XXIV Conference*, part of SPIE's Aerosense 1-Orlando (Florida), 5 April, 2002.
- [82] G. La Rosa, A. Risitano. Thermographic methodology for the rapid determination of the fatigue limit of materials and mechanical components. *International Journal of Fatigue*, 22, 65-73, 2000.
- [83] J.K. Krapez, D. Pacou, G. Gardette.Lock-In Thermography and Fatigue Limit of Metals. *Quantitative InfraredThermography Journal*, 6, 277-282, 2000.
- [84] T. Ummenhofer, J. Medgenberg. On the Use of Infrared Thermography for the Analysis of Fatigue Damage Processes in Welded Joints. *International Journal of Fatigue*, 31, 130-137, 2009.
- [85] E.Z. Kordatos, K.G. Dassios , D.G. Aggelis, T.E. Matikas. Rapid evaluation of the fatigue limit in composites using infrared lock-in thermography and acoustic emission. *Mechanics Research Communications*, 54, 14-20, 2013.

- [86] N. Harwood , W. Cummings. Thermoelastic stress analysis. New York: National Engineering Laboratory; Adam Hilger, 1991.
- [87] G. Pittaresi, E.A. Patterson. A review of the general theory of thermoelastic stress analysis. *Journal of Strains Analysis*, 35, 35–39, 1999.
- [88] W.J. Wang , J.M. Dulieu-Barton, Q. Li. Assessment of Non-Adiabatic Behaviour in Thermoelastic Stress Analysis of Small Scale Components. *Experimental Mechanics*, 50:449-461, 2010.
- [89] D. Palumbo, U. Galietti. Data Correction for Thermoelastic Stress Analysis on Titanium Components. *Experimental Mechanics*, 56, 451-462, 2016.
- [90] D. Palumbo, U. Galietti. Characterization of Steel Welded Joints by Infrared Thermographic Methods. *Quantitative Infrared Thermography Journal*, 11(1), 29-42 , 2014.
- [91] U. Galietti, D. Palumbo. Application of thermal methods for characterization of steel welded joints. *EPJ Web of Conferences*, 6, 38012, 2010.
- [92] D. Palumbo, R. De Finis, P.G. Demelio, U. Galietti. A new rapid thermographic method to assess the fatigue limit in GFRP composites. *Compos Part B*, 103, 60-67, 2016.
- [93] F. Maquin, F. Pierron. Heat dissipation measurements in low stress cyclic loading of metallic materials: From internal friction to micro-plasticity. *Mechanics of Materials*, 41, 928-942, 2009.
- [94] G. Fargione, A. Geraci , G. La Rosa , A. Risitano. Rapid determination of the fatigue curve by the thermographic method. *International Journal of Fatigue*, 24, 11-19, 2002.
- [95] ASTM D 3039/D 3039M, standard test method for tension-tension fatigue of polymer matrix composite materials.
- [96] D. Palumbo, U. Galietti. Thermoelastic Phase Analysis (TPA): a new method for fatigue behaviour analysis of steels. *Fatigue Fract Eng Mater Struct* 2016. <http://dx.doi.org/10.1111/ffe.12511>. in press.
- [97] T. Baxter, K. Reifsnider. The application of the Load-Stroke hysteresis technique for evaluating fatigue damage development. In: *Proceedings of the American Society for Composites*. Newark: Delaware; September 20-22, 1994.

---

## ***Chapter 6: Thermographic Signal Analysis for Fracture Mechanics***

---

**I**n previous Chapters it was presented the application of thermal methods based on the detection of radiative emission to fatigue damage assessment, and their impact on scientific scenario.

The potentiality of these techniques to study mechanical behaviour of materials relies on the obtaining more information on damage as previously shown for both metals and composites. Referring to the damage assessment firstly the TSA, example of application of the IR technique for stress analysis evaluation on a cyclically loaded specimen, represented an evaluable tool to study the damage behaviour in the plastic region of cracked samples.

The recent developments in the field of the study of damage behaviour of materials involve the use of thermal signal analysis approach, which somewhat includes the benefits of the TSA, by proving different parameters to determine in comprehensive way the fatigue of materials, and as will be presented, the advantage of the proposed approach refers to the possibility of adopting the same parameters to discuss both fracture mechanics and fatigue behaviour. In particular,  $\phi$ ,  $S_d$  or  $T_d$ .

In this chapter, the analysis of  $\phi$  and  $S_d$  leads to crack propagation analysis: in fact, for the first time, the complementary use of  $\phi$  and  $S_d$  to localize the plastic zone and then to define crack propagation has been shown. The fact that two complementary indices could describe the mechanical behaviour of materials opens a wide discussion on fatigue damage assessment and on the localization of the crack tip of specimens undergoing a fracture mechanics test. It is worth noting that, in literature, only the phase shift of thermoelastic signal has been used to achieve the position of the crack tip (calculation of 'a' crack size) while the analysis of crack tip position may be improved by evaluation of both  $\phi$  and  $S_d$  indices.

The first results involves the assessment of the Paris Law in automatic way for AISI 422, ASTM

A182 grade F6NM, CF3M and CF8M.

Determination of the Paris Law constants implies the knowledge of both Stress Intensity Factor (SIF) and the crack growth rate ( $da/dN$ ). In this regard, the Standard proposes several method to assess the crack length and the SIF values, but most of them require an off-line

measurement of the crack with consequent high testing time and cannot be applied on actual structural components.

Based on the assessment of  $\phi$ , an automatic procedure based on the TSA technique was proposed for the continuous evaluation of the crack tip position and the SIF value. Advantages with respect to classical methods can be obtained in terms of reduction of: testing time, experimental set-up, data processing and data report.

Another result that will be presented refers to the assessment of energy dissipated in the plastic region by using the second order temperature variations index  $T_d$  in order to evaluate the heat dissipations.

Dissipated energy ahead of the crack tip represents a useful tool to study the fatigue crack growth. In this regard, different analytical and numerical models were proposed in literature to investigate the role of dissipated energy in fracture mechanics and experimental techniques were used to validate them. However, the experimental measurements of dissipated energy require an accurate equipment and suitable techniques that may restrict the applications only to laboratory tests.

Therefore, it will be shown that by monitoring the fatigue crack growth during a fracture mechanics tests, carried out on AISI 422, it is possible to obtain a similar Paris Law model based on the relation between the crack growth and the heat dissipated per cycle.

Finally, it will be confirmed the fourth power dependence of heat dissipated energy and Stress Intensity Factor (SIF) in agreement with numerical and analytical models presented in literature.

## 6.1 TSA for Fracture Mechanics: SIF and Crack Length

As presented in Chapter 2, the Thermoelastic Stress Analysis is useful to evaluate the Stress Intensity Factor derived by the amplitude of signal.

In fact, the following important relationship can be used for the thermoelastic signal obtained from a point  $(r, \theta)$  in a crack-tip stress field resulting from any combination of mode I and mode II loading [1]:

$$SA = \frac{2k_I}{\sqrt{2\pi r}} \cos \theta/2 - \frac{2k_{II}}{\sqrt{2\pi r}} \sin \theta/2 \quad (1)$$

And as it was showed, by considering a series of signal line plots taken parallel to the line of the crack ( $y=\text{constant}$ ), equation 1 can be developed by fixing  $K_{II}=0$  and by replacing  $r$  in the  $K_I$  term by using  $y/\sin \theta$ .

$$\frac{\partial S}{\partial \theta} = \frac{2k_I}{A\sqrt{2\pi y}} \left[ \left( \frac{\cos(\frac{\theta}{2}) \cos \theta}{\sqrt{\sin \theta}} \right) - \sin \theta/2 \sqrt{\sin \theta} \right] \quad (2)$$

it is simply observed that the partial derivative of  $S$  with respect to  $\theta$  is zero when  $\theta=60^\circ$  and thus it

follows that maximum signal ( $S_{max}$ ) in a line plot taken parallel to the crack occurs at  $\theta=60^\circ$ .

By

substituting this value of  $\theta$  [1]:

$$y = \left( \frac{3\sqrt{3}\Delta K_I^2}{4\pi A^2} \right) \frac{1}{S_{max}^2} \quad (3)$$

From equation 3, it is evident how  $y$  and  $1/S_{max}^2$  are linearly related and that, if the constant  $A$  is known,  $\Delta K_I$  can be obtained directly from the gradient of a graph of  $y$  versus  $1/S_{max}^2$ .

In the same way, the analysis for mode I loading can be based on signal plots along lines perpendicular to the crack and ahead of the crack tip ( $x=\text{constant}$ ), [1].

As an example, in Figure 1 the maximum signal  $S_{max}$  is plotted around the crack tip versus the vertical distance  $y$  from the crack tip growth direction. The angular coefficient of the best fit line of collected data provides the SIF value.

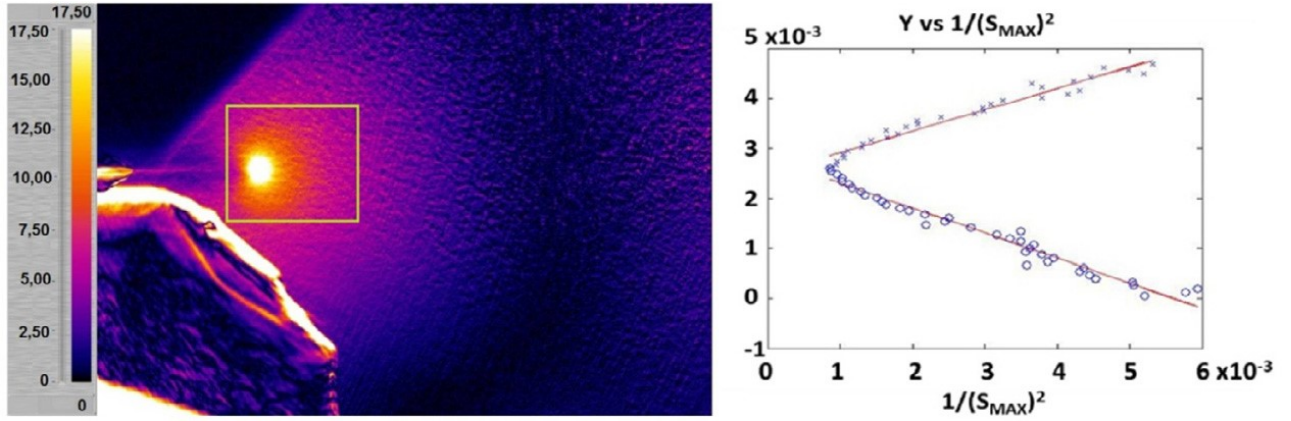


Figure 1. Typical Amplitude signal map (a) and evaluation of the signal around the crack tip in the selected area (b) for AISI 422 at 80,000 cycles.

The assessment of the crack length can be performed by considering the thermoelastic phase shift  $\Phi$ . As just explained, it depends on a number of parameters such as, for example, thickness of the painting or the grips of the loading machine, and it slightly change through the area analysed due to non-perfect homogeneity of surface conditions, it remains locally constant in presence of linear elastic behaviour of material and steady state conditions.

The considerable changes can occurs in presence of viscoelastic or plastic behaviour of material [2], [3-6], [7] and high stress gradient leading to heat conduction in material and to the loss of adiabatic conditions [8], occurring near the crack tip region.

It was stated that, around the crack tip, of notched samples for fracture mechanics the two phenomena lead to a lack of adiabatic conditions: the heat generation due to plastic work and the presence of high stress gradients [2], [9-11].

In correspondence of such the phenomena, phase signal can change in sign. In effect, by analysing the phase maps of the thermoelastic data, due to this change in sign, it is possible to determine the crack tip position. In Figure 2 (a), the typical phase map during a fracture mechanic test is shown.

Where adiabatic conditions were achieved, the phase signal should be constant; in fact thermoelastic and reference signal are set in phase. This condition is verified away from the crack tip where there are linear elastic conditions. Near the crack tip, adiabatic conditions were lost due to plasticity and high stress gradients [9-11]. The position of the crack tip can be extracted by plotting the phase values along a profile taken across the crack as shown in Figure 2b.

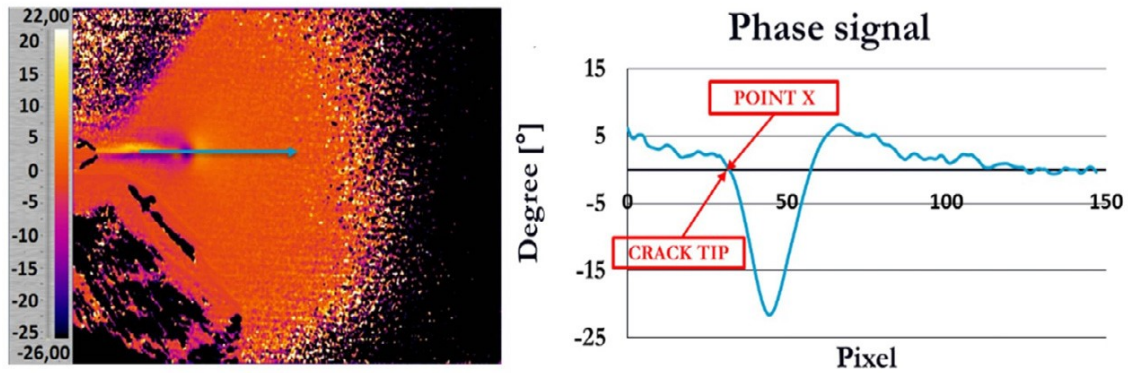


Figure 2. Typical Phase Map (a) and Phase profile along crack tip (b) for AISI 422 at 80,000 cycles.

Considering Figure 2 (b), starting from the right, there is a region where the phase value is approximately constant and equal to zero. In all these points, adiabatic conditions are achieved. In proximity of the crack tip, there is a positive increment of the phase value that indicates a loss of adiabatic conditions due to plasticity and high stress gradients. Then the phase changes in value from positive to negative, which indicates the presence of a reverse plasticity (phase inverted compared to the first region). The phase value returns to zero (Point X) and then it starts to assume various values (positive and negative) because of the contact between the crack faces and the background reflection [11]. Point X can be adopted for the estimation of the crack tip position and for the evaluation of crack growth during the tests [12].

One of the interestingly feature of the study of phase shift, in fracture mechanics is such that by assessing the zero-point at which the phase shift inverts its sign it is possible to separate the different phenomena occurring in the plastic zone.

In fact, in the study of fatigue crack propagation, crack closure has usually only been considered to occur under compressive loads [13]. Rice [14] has excluded the occurrence of crack closure under cyclic tension loading in the stress analysis of the crack tip.

This, however, applies only to an idealized crack which is not propagating. As a consequence of the permanent tensile plastic deformation left in the wake of a fatigue crack, one should expect partial crack closure after unloading the specimen [15]. A fatigue crack propagating under zero-to-tension loading was fully closed at zero load due to internal forces existing in the specimen. The common methods adopted for assessing the crack closure are based on the following two principles:

- (1) The net internal force acting across a section in a statically indeterminate structure can be obtained by cutting the section and measuring the force system required to reverse the displacement system produced by the cut.
- (2) A crack in a structural member is closed, when the stiffness of the member is the same as the stiffness of an identical untracked member under the same load system.

The crack closure phenomenon was first observed when a partially cracked sheet specimen with rectangular shape, was cut open in order to allow fractographic investigations of the fracture surfaces. This cutting was accompanied by deformations large enough to be observed by the naked eye. Figure 3 shows the areas of crack closure and plastic zone, separated by the crack tip.

Nevertheless, the study of such the phenomenon is not easy. For two main reasons [13]:

- The striation shape on the fracture surfaces is determined not only by the crack propagation process, but also by the crack closure stress, when these reach load maxima above the yield stress in compression.
- Under constant amplitude loading, the loading conditions at the crack tip cannot be determined solely by the stress intensity factor ( $\Delta K$ ) resulting from the whole stress increment ( $\Delta\sigma$ ).

So that the analysis of crack closure can be made by exploiting the features provided by TSA, in particular by using the thermographic signal analysis for assessing the thermoelastic phase shift. This latter, as explained above, can support in finding the separation point between plastic phenomena and crack closure area.

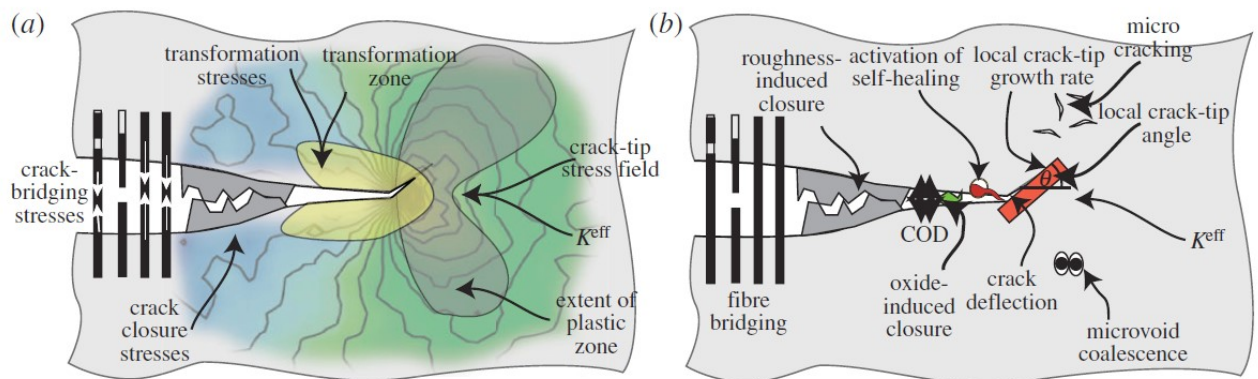


Figure 3. Schematic illustrating the wide range of qualitative and quantitative fracture mechanics information that can be obtained by (a) diffraction and (b) imaging. [16]

In this paragraph, two main features of TSA for fracture mechanics have been presented: the assessment of stress intensity factor and the assessment of phase-sign-inversion.

The stress intensity factor has been calculated by using the amplitude of thermoelastic signal according to approach described by Wong [17].

The phase signal inversion allows determining the crack tip localisation.

These evaluation of these quantities involves the Paris's Law calculation in automatic way, as will be shown in paragraph 6.3.

Another feature related to the analysis of phase maps is such that the crack closure region



can be assessed, in order to separate it from the plastic region zone.

The following 6.2 paragraph deals with the presentation of another feature of the presented approach: heat dissipations assessment by means of temperature variations of second order  $T_d$ . In effect,  $\Phi$  and  $T_d$  provide a complementary information to study intrinsic dissipations.

## **6.2 Temperature Variation for Assessing Dissipative Effects in the Plastic Zones**

The development of the fatigue crack involves three stages: nucleation and early growth, crack propagation within a plastic zone , and crack propagation through an elastic regime until failure results. The key to initiation of the processes and the continuation of crack propagation is cyclic plastic strain , whether it be at the tip of a propagating fatigue crack, at the root of a notch or fillet , or grossly over a large area of the structure. Cyclic plastic strain ranges from reversed slip of a few isolated surface grains in an otherwise elastically loaded component to some well-defined plastic zone containing a very large number of grains at the root of a notch or some other stress raiser. In the former case, where plastic deformation is highly isolated, crack initiation occurs after a very large number of cycles. This is referred to as high-cycle fatigue. It is very difficult to quantify the failure processes in terms plastic strain in such cases: rather, the elastically applied stress is only readily available basis for quantitative analysis of fatigue failure [18].

In most practical cases, particularly those dealing with failure and failure analysis, a plastic zone of finite size can be identified where the fatigue process has begun. Initiation of failure in such circumstances is the result of high cyclic strain, which can be referred to as high-strain or low-cycle fatigue.

The considered smooth hourglass test specimens, figure 4, have been used in this Thesis, for studying the processes of crack initiation and early growth, as presented in previous chapters for stainless steels and composites.

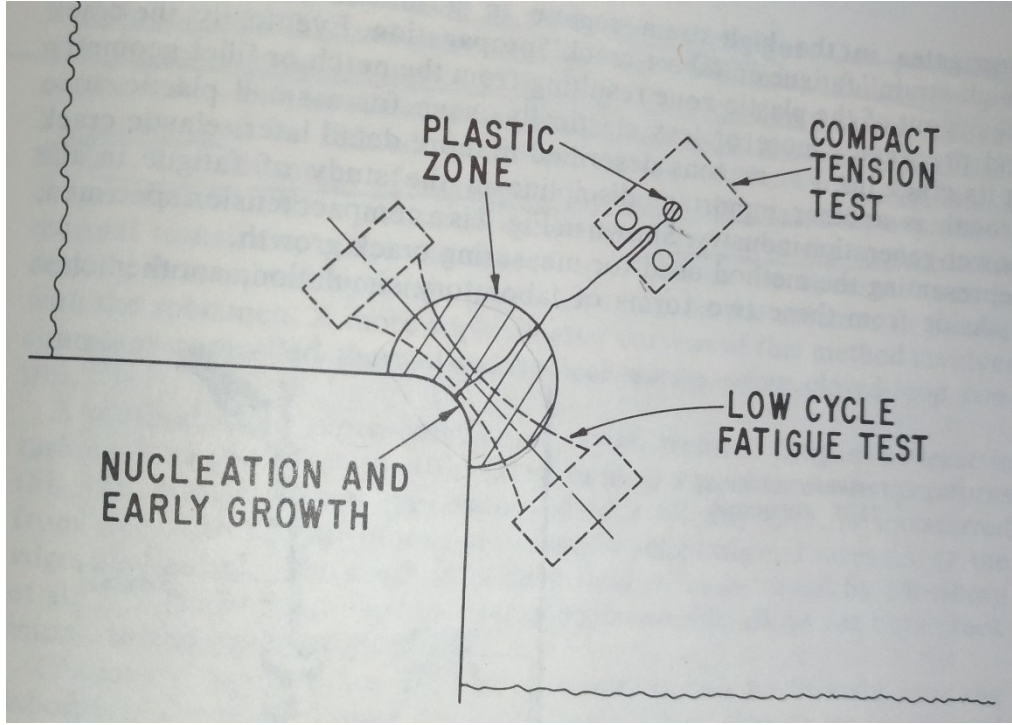


Figure 4. the multistage processes in fatigue [18].

Once the crack is formed, as the case of fracture mechanics, by continuing with the multistage nature of the fatigue process, it propagates in the high strain regime, in a manner characterised as ‘high-strain’ fatigue or ‘short crack’ propagation.

After the crack breaks out of the plastic zone resulting from the notch geometry and propagates more or less elastically, save for a small plastic zone at its crack tip.

The energy dissipated in such the zone is very important for estimating the fracture mechanics behaviour of the material, and in this thesis, it will be demonstrated as it can be studied by using the proposed thermographic approach.

In fact, in chapter 3, it has been presented the relation between the energy dissipated in the material as heat and the temperature variations of second order, furtherly the adopted model for determining such the variations has been presented.

By disregarding the thermoelastic temperature variations, since their presence is not influent in case of dissipative behaviour, the temperature variations can be supposed to be:

$$T(N) = T_0 + \frac{b}{f} N + A \cos(2\omega \left(\frac{N}{f}\right) + \varphi_{2\omega}) \quad (4)$$

Where the time is indicated in function of the number of cycles  $N$  and loading frequency  $f$ , and the phase shift between the first harmonic and the second harmonic components, previously indicated as  $\psi$ , is actually referred as  $\varphi_{2\omega}$ .

Adiabatic conditions are not easily guaranteed due to temperature gradient that arise during

cyclic loading so, the real condition should consider that  $Q \neq 0$  (heat exchanges cannot be neglected). In this case the relation between  $T_d$  and  $T_{2\omega}$  (chapter 3.3, equation 11) is not valid anymore but through the evaluation of the term  $A$ , a consistent  $E_d$  estimation can still be obtained since it is related to  $T_{2\omega}$  which in turn, produces  $\Delta T_d$ .

In fact, the idea is to assess  $E_d$  by determining  $\Delta T_d$ , through the ‘ $A$ ’ estimation.

As just said,  $E_d$  represents the energy dissipated as heat in a unit of volume and for cycles so, the total heat dissipated (J/cycles) can be expressed as:

$$Q_d = E_d V_p \quad (5)$$

where  $V_p$  is the plastic volume at the crack tip that can be estimated following Irwin [44] in plane stress conditions:

$$V_p = B r_p = \frac{B}{2\pi} \left( \frac{\Delta K}{\sigma_y} \right)^2 \quad (6)$$

and  $B$  is the specimen thickness. The model adopted for evaluating  $V_p$  refers to plane stress conditions. The shape and size of the plastic volume change through the thickness due to the plane strain conditions in the centre of the specimen which produces a little overestimation of  $V_p$  and then  $Q_d$  [19]. Nevertheless, as will be demonstrated furtherly by experimental data, this does not prejudice the quality of results.

### 6.3 On the Use of TPA for Crack Tip Measurement

Paris’s Law describes the behaviour of cracked materials subjected to dynamic loading and it implies the knowledge of both the stress intensity factor (SIF) and the crack growth rate ( $da/dN$ ) [20], [21]. In this regard, these parameters can be obtained by use of conventional methods according to Standards [22], by means of experimental and non-destructive techniques such as microscopy, extensometry, ultrasound, X-ray and DIC (Digital Image Correlation) [22], [23-29].

Saka *et al.*, [24] proposed a non-destructive method for evaluating a 3D surface crack based on a magnetic field induced in the air by DC current flow in materials. This method requires two probes for application of the DC current and cracks have to be extremely small in comparison with the distance between the probes. A 3D X-ray synchrotron tomography was used by Williams *et al.*, [25]

to obtain local measurements of crack growth in a 7075-T6 aluminium alloy. This

instrumentation allows for in situ measurements of crack opening displacement (COD) but requires a suited precision alignment fixture for *in situ* testing.

In Kainuma's work [26], a quantitative examination of the efficiency of micro-encapsulated dye mixing paint was performed. This method allows for an easily applicable inspection also on actual structural components. However, it presents difficulty when detecting initial crack and short fatigue

crack. The magnetic flux density around the fatigue crack was observed in the work of Tanabe *et al.*, [27]. The magnetic flux was measured by means of a Magneto-Impedance sensor and a strong correlation was found with the stress intensity factor. However, this technique does not allow for an accurate crack length measurement.

Infrared thermography (IRT) was also proposed for the study of the fracture behaviour of materials subjected to fatigue loading [30-35]. In particular, a temperature rise due to the heat dissipations can

be observed around the crack tip where the plastic zone is located. In this regard, Carrascal *et al.*, [30] used IRT for evaluating the Paris Law constants of a polymer (polyamide) with an experimental methodology. A good agreement was found with respect to traditional calculation methods. However, this procedure may find limitation in those cases in which temperature changes on material related to the plastic zone are very low (short cracks) and, moreover, high performance equipment and a difficult set-up are required. This is the case, for instance, with brittle materials (such as martensitic steels), welded joints and aluminium alloys [24-25].

On the other hand, the use of TSA is well-known for fracture mechanics, as previously said, in chapter 2. This paragraph in fact, presents the development of an automatable experimental procedure to characterize the fracture behaviour of steels and represents the completion of the works [34-35]. The proposed procedure allows for the on-line monitoring of crack growth during testing through a set-up which is simple compared to other techniques. Moreover, a simple specimen preparation is required, which makes the proposed procedure also suitable for the monitoring of actual structural components.

The tested stainless steels are AISI 422, ASTM A182 grade F6NM, CF3M, CF8M, a comparison with conventional methods was performed, in order to validate the procedure.

It will also presented the use of second order phase shift  $\varphi_{2\omega}$  for assessing the crack length and then determining the crack propagation behaviour compared to the well known  $\varphi$ .

### 6.3.1 Development of an Automatic Procedure for Paris Law Estimations

By referring to the experimental setup and procedure widely described in paragraph 3.4.4, the proposed procedure involves the acquisition of a series of thermographic sequences at constant regular intervals of cycles number by means of the Flir software RIR Max [36]. Amplitude and phase data were obtained for each sequence providing the data processing as described in the previous section (paragraph 3.3).

In order to obtain the Paris Law constants with the proposed procedure, firstly, the calibration constant  $A$  (eq. 2) needed to be assessed. In this regard, in this work, a “dog-bone” specimen was used made of the same material used for tests. In this way, the calibration constant  $A$  can be assessed by measuring the average thermoelastic signal  $S$  on the gauge length area of the “dogbone” specimen, Figure 5. Then, by knowing the stress field on the gauge length area of the specimen, the constant  $A$  is obtained by means of equation 1 [37].

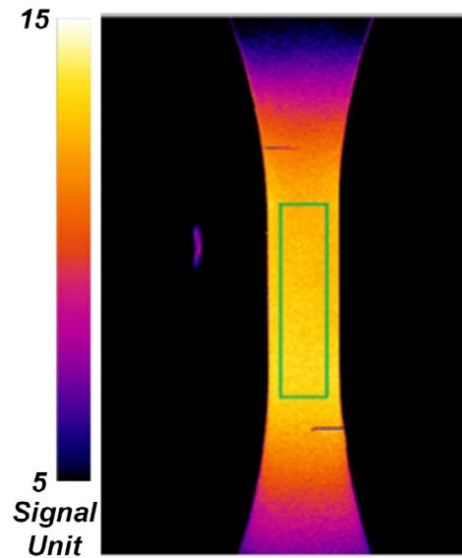


Figure 5. Amplitude signal map of a “dog-bone” specimen and area considered for the measuring of thermoelastic signal  $S$  (AISI 422 -  $\Delta\sigma = 275$  [MPa]).

Table I. shows the values of the calibration constant  $A$  obtained for the four stainless steels tested with the stress amplitude used for “dog-bone” specimens. It should be noted how these values can be very different with respect to those obtained by other commercial systems due to the different algorithms used to obtain amplitude of the TSA signal.

Material	$\Delta\sigma$ [MPa]	A [MPa/SU]
AISI 422	275	20,95
ASTM A 182	230	10,21
CF3M	120	24,54
CF8M	130	25,33

Table I. Calibration constant  $A$  and stress amplitude used for “dog-bone” specimens.

The proposed procedure can be summarized as follows:

- Thermographic sequence acquisition with infrared camera; Thermal sequences of about 10 seconds have been acquired at 123 frames/s and at regular intervals of 2000 cycles during the test.
- Thermoelastic phase and amplitude image assessing; About 2 minutes are required to extract the TSA data (phase and amplitude data) from each thermal sequence by means of the IRTA software.
- Evaluation of the maximum value of thermoelastic signal  $M(x,y)$  from the amplitude image; This value represents the maximum stress amplitude reached in proximity of the crack tip.
- Automatic detection of an analysis area (data matrix  $[A]_{ixj}$ ) around the maximum value of thermoelastic signal;  
 $[A]_{ixj}$  represents the area of interest for the following analysis and has dimensions  $i$ ,  $j$  with  $15 < i < 30$  and  $15 < j < 30$  pixel (the min values of  $i$ ,  $j$  were used during the first sequences on account of the presence of the test fixtures).
- Automatic extraction of the analysis area (data matrix  $[A]_{ixj}$ ) from the amplitude and phase maps in order to obtain the amplitude data matrix  $[S]_{ixj}$  and the phase data matrix  $[\Phi]_{ixj}$ ;
- Evaluation of the stress intensity factor  $\Delta K_I$  from the amplitude data matrix  $[S]_{ixj}$ , by using the procedure explained in section 6.1.
- Normalization of the selected phase area (data matrix  $[\Phi]_{ixj}$ ) in order to report the average phase data to zero away from crack tip. Normalized area  $[\Phi_n]_{ixj}$  is obtained by subtracting the average value of phase signal of the selected area  $[\Phi]_{ixj}$  ( $[\Phi_n]_{ixj} = [\Phi]_{ixj} - \text{mean}[\Phi]_{ixj}$ );
- Evaluation of the minimum value of phase signal  $m(x,y)$  in the selected normalized area (data matrix  $[\Phi_n]_{ixj}$ ) and identification of the crack growth direction; The crack growth direction is obtained by joining the minimum value of phase signal and the crack tip position obtained at the end of the pre-crack procedure.

- Plotting of the phase signal values along the crack growth direction;
- Automatic assessment of the crack tip position in terms of coordinates x and y in the local reference system (0, x, y) (local reference system of data matrix ([Φn]ixj));
- Evaluation of the crack tip growth rate; Plotting of the crack tip position in the main reference system (0, X, Y) versus the number of cycles and using the incremental polynomial method for evaluating the crack growth rate [22]; Automatic evaluation of the out-of-plane cracking limits [22].
- Evaluation of the constants m and C by plotting  $da/dN$  versus  $\Delta K_I$ .
- Accordingly, the Paris-Erdogan law is known:

$$da/dN = C\Delta K_I^m \quad (7)$$

The procedure is shown in Figure 6 in flow-chart form, and, in Figure 7 in graphic form. Matlab® code has been used for the processing of data from Step 3 to Step 12, but all routines can be easily adapted in equivalent open source software.



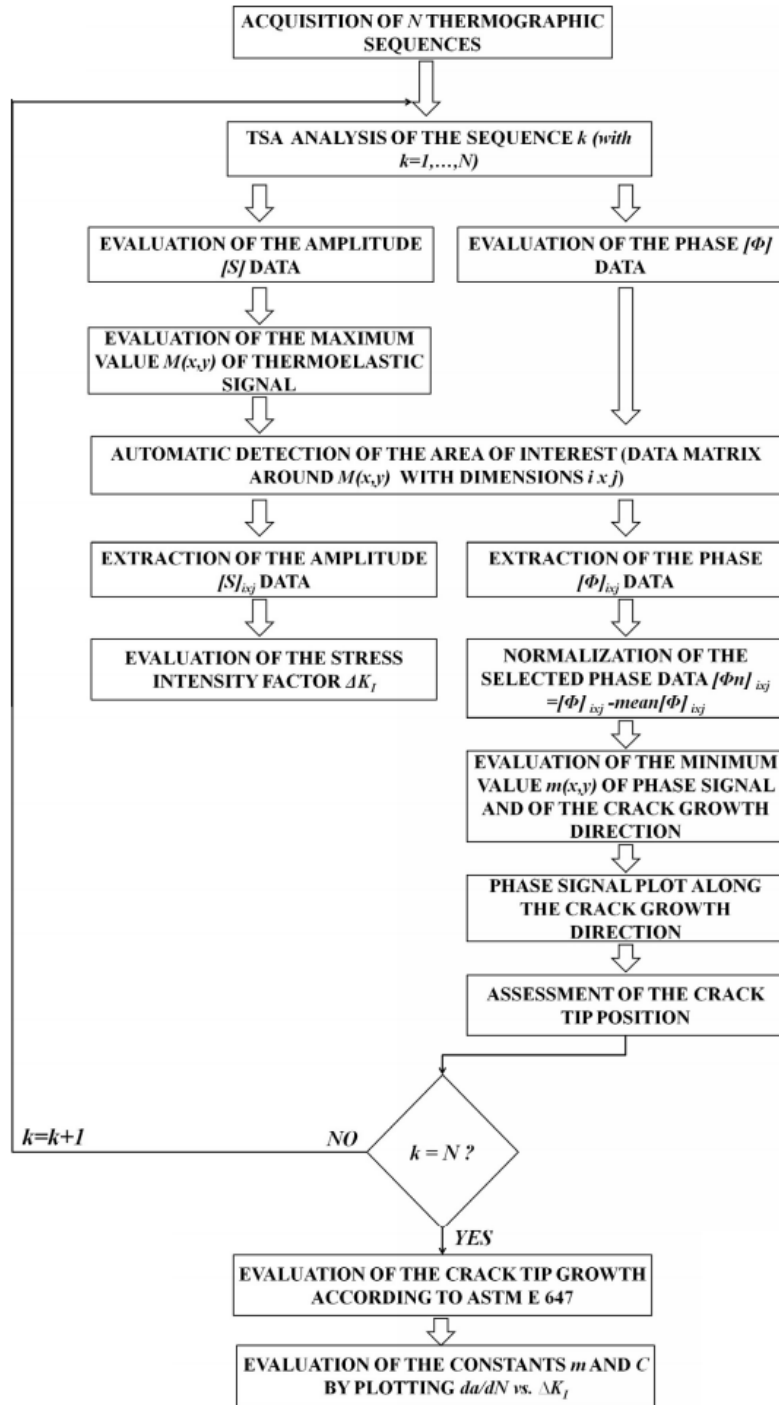


Figure 6. Flow chart of the proposed procedure for crack growth rate evaluation.

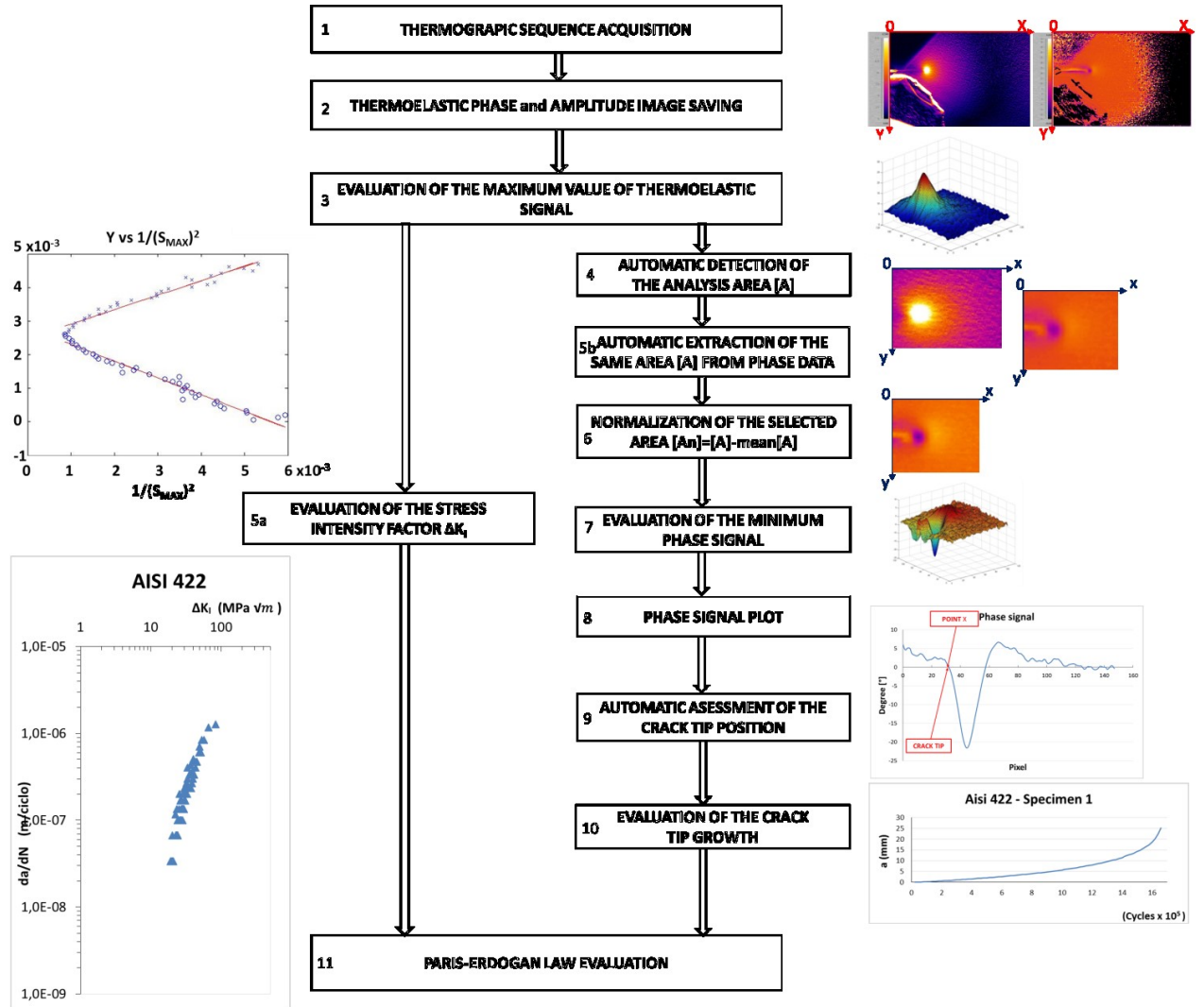


Figure 7. Graphical representation of proposed procedure.

In Figure 8, the phase maps and the phase data along the crack growth direction during the test are shown for AISI 422, Specimen 3. As illustrated in the previous section, these data are used to evaluate the crack length as the number of cycles increases.

For example, in Figure 8 (a), the crack length is of about 4 mm at 30,000 cycles. After 80,000 cycles, the crack grows to 8.5 mm (Figure 8 b) and in proximity of the failure (140,000 cycles) the crack reaches a length of about 19.5 mm (Figure 8 c).

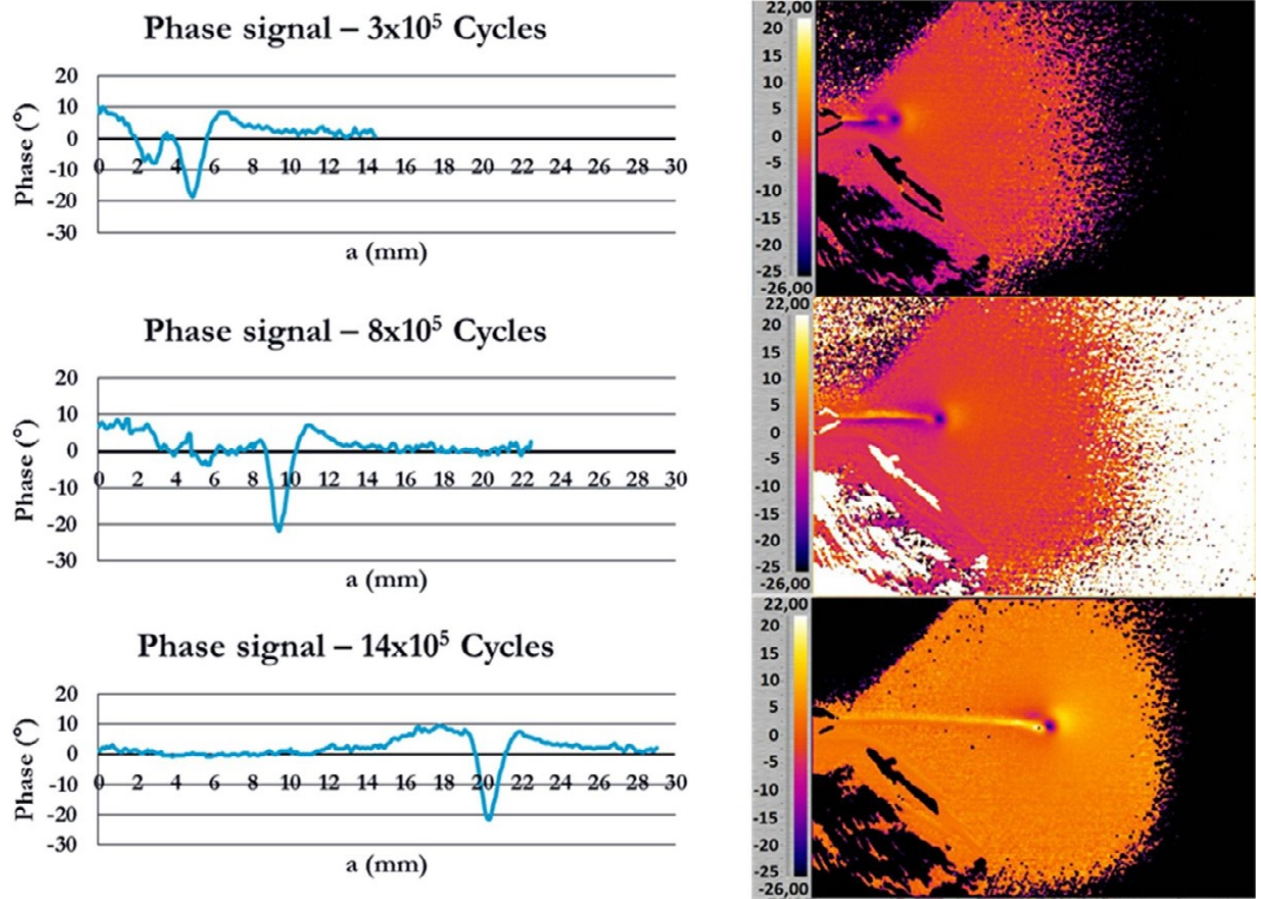


Figure 8. Phase map (right) and Phase profile along crack tip (left) at 30,000 cycles, 80,000 cycles and 140,000cycles for AISI 422 - Specimen 3.

In Figure 9, the crack tip growth trend is shown for Specimen 1 of each material as well as the fracture surfaces. Table II shows the constant load amplitude used for tests and the number of cycles performed until failure of specimens.

Material/sample	$\Delta P$ [kN]	Cycles
AISI 422		
1	10.8	166,000
2	10.8	124,000
3	10.8	134,000
ASTM A 182 grade F6NM		
1	12.4	146,000
2	12.4	142,000
3	12.4	138,000
CF3M		
1	9.9	186,000
2	9.9	164,000
3	9.9	214,000
CF8M		
1	9.45	138,000
2	9.45	198,000
3	9.45	164,000

Table II. Loads and number of cycles performed for all materials.

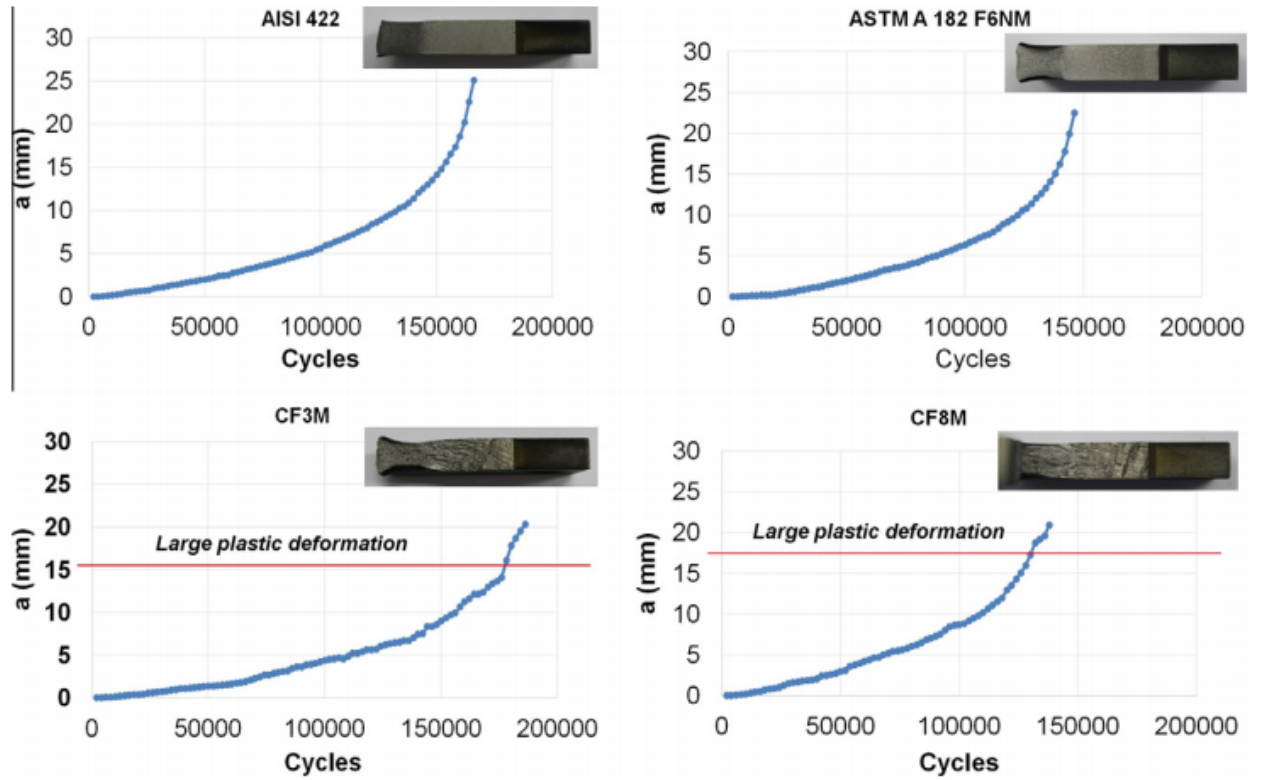


Figure 9. The crack tip growth trend for Specimen 1 of each material and fracture surfaces.

The different fracture mechanics behaviours for the presented stainless steel used in this work (martensitic and austenitic steel) are depicted in figures 9–11.

A comparison between the SIF values evaluated according to the Standard ASTM E 647 [22] and those obtained with the proposed procedure are shown in Figure 12 for Specimen 2 of the AISI 422.

In particular, ASTM E 647-00 provides the following equation for evaluating  $\Delta K_I$ :

$$\Delta K_I = \frac{\Delta P}{B\sqrt{W}} \frac{(2+\beta)}{\sqrt[3]{(1-\beta)^2}} (0.886 + 4.64\beta - 13.32\beta^2 + 14.72\beta^3 - 5.6\beta^4) \quad (8)$$

Where  $\beta=a/W$ ,  $a$  is the crack length,  $B=12.5 \text{ mm}$  and  $W=50 \text{ mm}$ , are two characteristic dimensions of the sample [22].



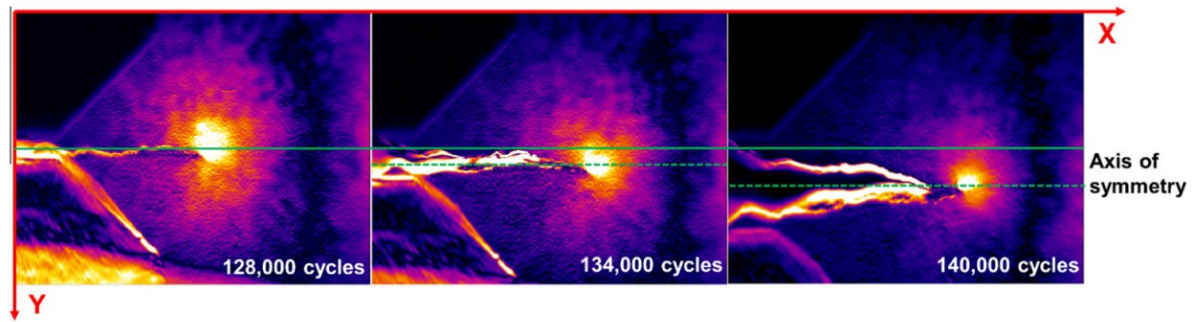


Figure 10. CF8M - Specimen 1, amplitude image at 128,000, 134,000 and 140,000 cycles.

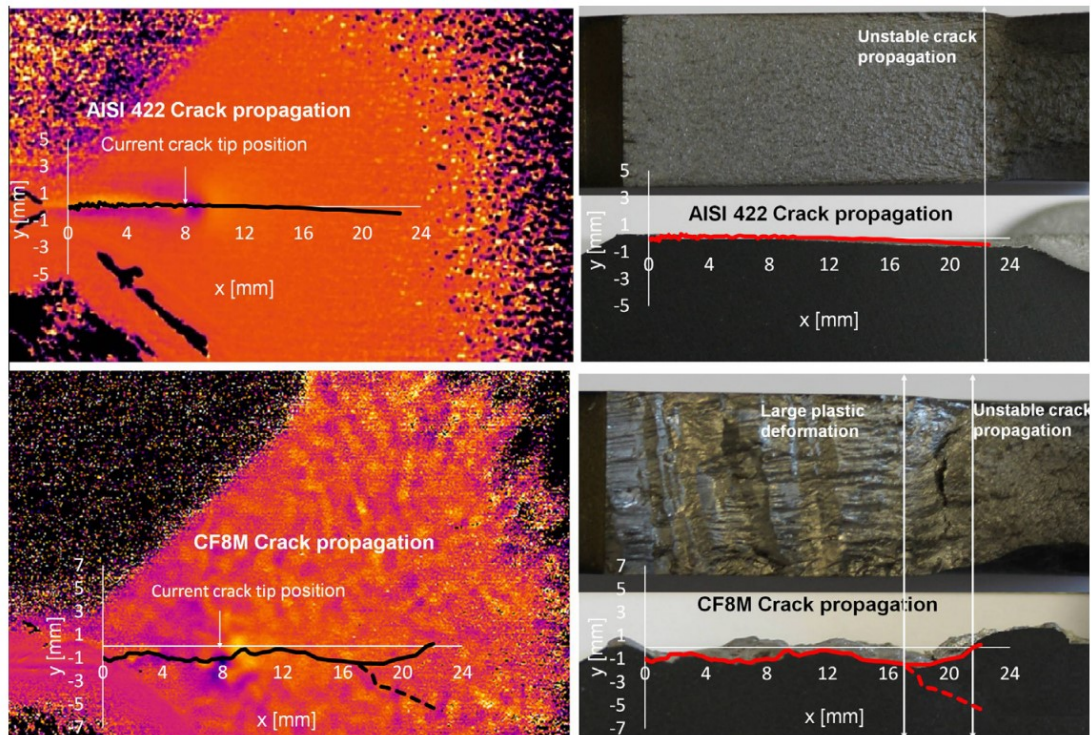


Figure 11. Crack propagation for martensitic (above, AISI 422 - Specimen 1 – 90,000 Cycles) and austenitic (below, CF8M - Specimen 1 – 100,000 Cycles) stainless steel by means of TSA technique on the left and real crack propagation surface on the right.

The austenitic steel (CF3M and CF8M specimens) in the last 10,000 cycles presents a more ductile behaviour compared to the martensitic. This behaviour produces considerable plastic deformation before the final failure and a downward movement of the crack tip with respect to the main reference system (0, X, Y), Figure 10. In Figure 11(a) the envelope of the crack tip position is shown for both stainless steels, AISI 422 and CF8M. For the latter, the dotted line represents the crack tip envelope obtained with the proposed algorithm. The effect of the rigid downward motion due to the characteristic behaviour of the material is clearly evident. In this case, a post-processing procedure was necessary in order to compensate the crack tip position along the coordinate Y. In Figure 11(b), the crack tip profile obtained with the proposed procedure (continuous red lines) is compared with the profile of the fracture

surface. The two profiles are practically superimposable. Figure 12 illustrates how the proposed procedure provides  $\Delta K_I$  values in good agreement with Standard ASTM.

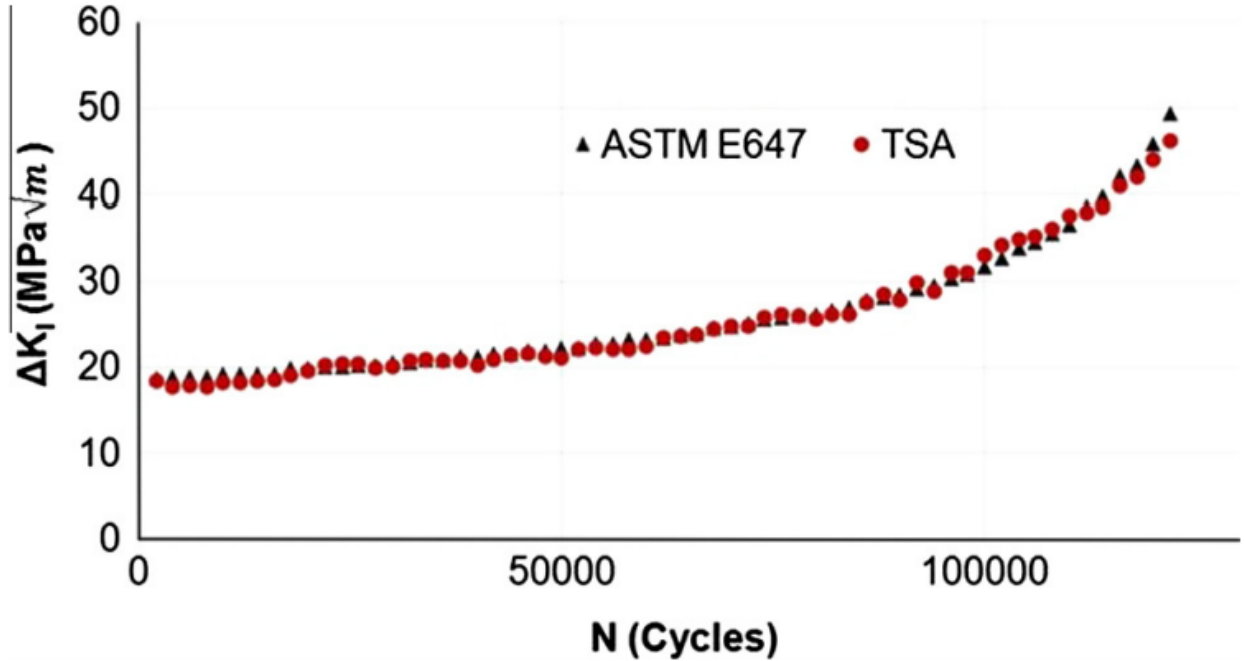


Figure 12. Comparison between the SIF values evaluated according to Standard ASTM E 647-00 and those obtained with the proposed procedure (AISI 422 - Specimen 2).

Figs. 13 and 14 summarize the data for both martensitic and austenitic steels respectively. In each graph, the results obtained from each specimen are reported in order to show the good repeatability of data. The coefficients of the Paris Law were evaluated considering the data deriving from the three specimens all together. In Table III, the results obtained by performing the linear fitting of data shown in Figures 13 and 14 are reported. These are in good agreement with indications in literature [38-39] for both martensitic and austenitic stainless steels. In particular, AISI 422 and ASTM A182 grade F6NM have a similar Paris equation and present a lower crack growth rate with respect to CF3M and CF8M.

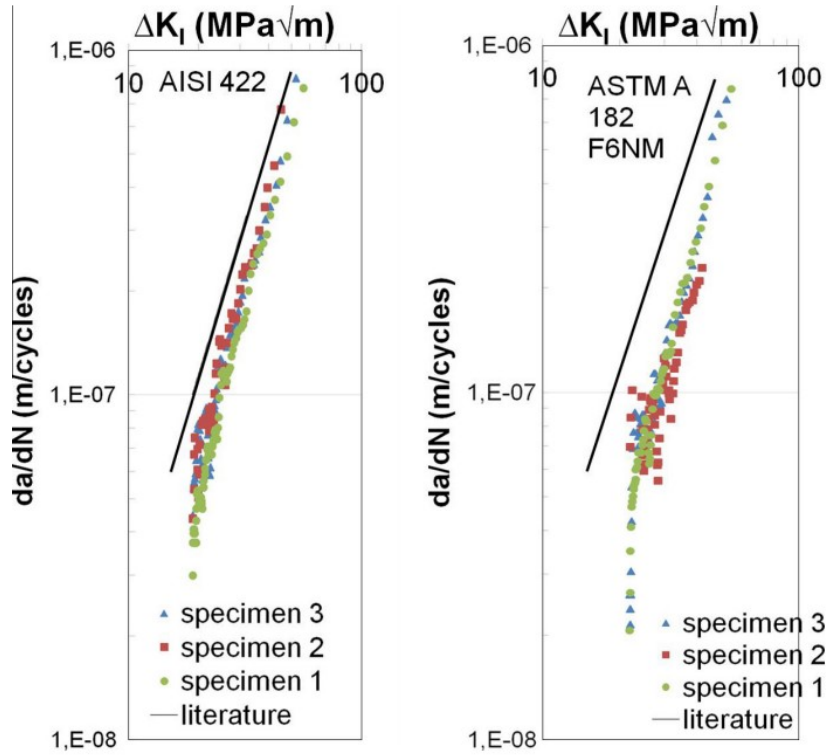


Figure 13. Crack growth rate obtained for martensitic stainless steels (AISI 422 and ASTM A182 grade F6NM) and comparison with literature [40].

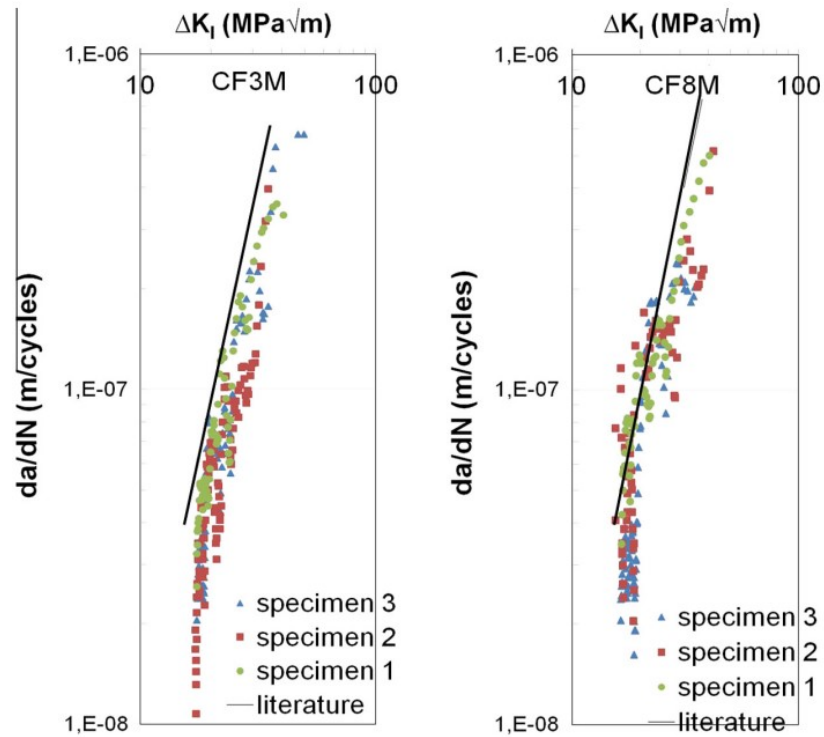


Figure 14. Crack growth rate obtained for austenitic stainless steels (CF3M and CF8M) and comparison with literature [39].



Material	m	C (m/cycles) (MPa * $\sqrt{m}$ ) <sup>-m</sup>
AISI 422	2.56	1.90E-11
ASTM A 182	2.66	2.02E-11
CF3M	3.01	5.99E-12
CF8M	3.37	2.66E-12

Table III. Paris Law coefficients m and C obtained for all materials.

Literature value for martensitic stainless steels class: m = 2.25, C = 1.67E10 [m/cycles], [38]; m = 2.25, C = 1.36E10 [m/cycles], [39]. Literature value for austenitic stainless steels class: m = 3.25, C = 7.62E12 [m/cycles], [38]; m = 3.25, C = 5.61E12 [m/cycles], [40]. 21

### 6.3.2 On the Use of Phase Shift of Second Harmonic for Crack Growth Length Assessment

Another feature of the presented approach is such that by the same analysis two phase parameters can be extracted from thermographic signal:  $\varphi$  discussed in previous section and  $\varphi_{2\omega}$ , capable to determine the crack growth length.

The use of  $\varphi$  has been widely discussed for assessing the crack tip position since it acts like a good indicator for determining the position of the crack [34], [40-41], and as said in paragraph 6.1, by assessing the inversion in sign. In particular, the point at which, the phase values invert the signal (from negative values to positive ones) represents the crack tip.

In this work, it has been considered  $\varphi_{2\omega}$  as parameter for evaluating the crack length, and its capability has been compared to the one provided by the thermoelastic phase data.

Also in this case, in order to determine the crack length 'a', the analysis of  $\varphi_{2\omega}$  maps is necessary. In figure 15, it is shown a  $\varphi_{2\omega}$  map and a phase signal profile extracted in correspondence of the crack propagation direction.

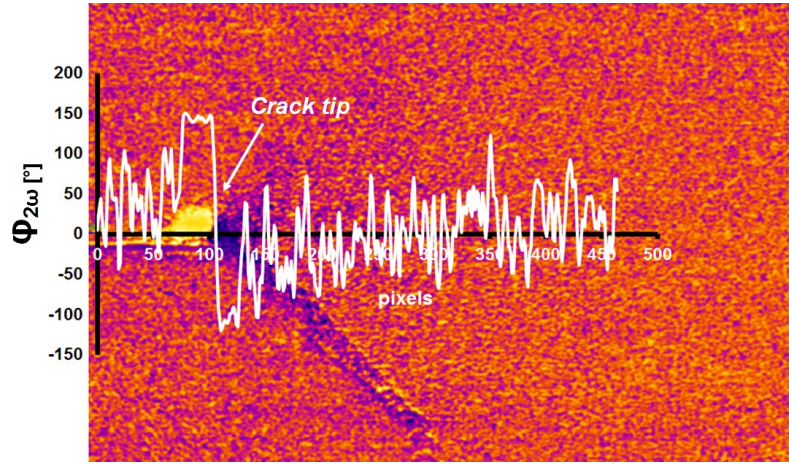
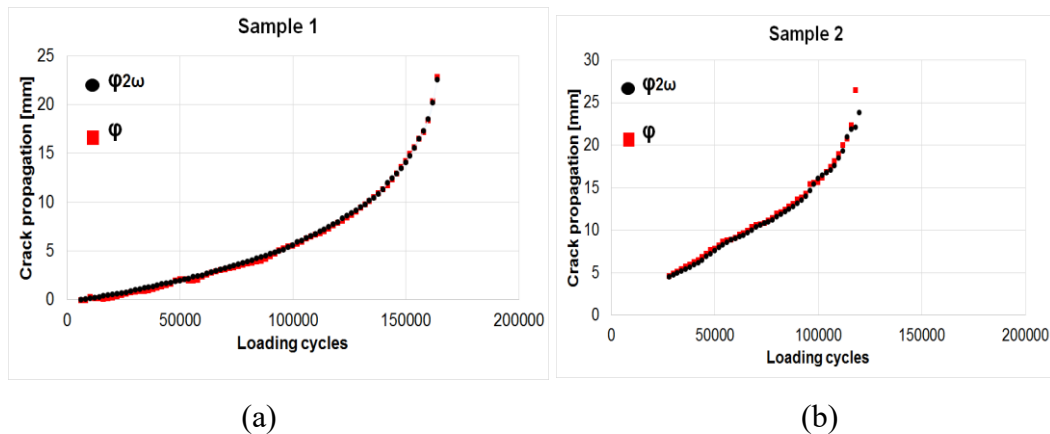
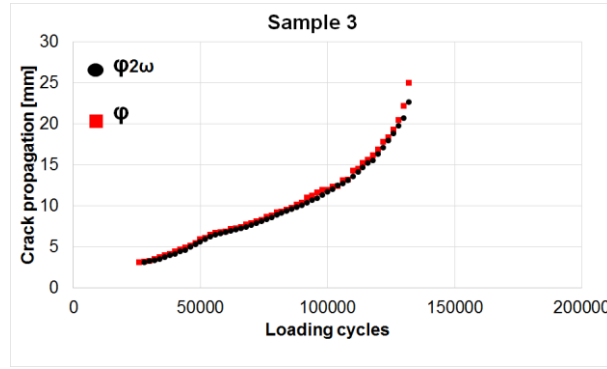


Figure 15. Phase map ( $\phi_{2\omega}$ ) to localise the crack tip.

It is possible to note that a signal inversion occurs, even in this case, between two regions: the crack closure effect zone and the plastic zone. The two different zones are clearly depicted in the phase maps since they are out of phase each other. The point in which the phase signal changes in sign, can be used for estimating the crack tip position

The determination of the position of the crack tip can be assessed by knowing the geometrical resolution in term of mm/pixel. This ratio is fixed since the infrared detector is setup at the beginning of the test and it depends on the dimension of the detector and on the lens system. By recording over time, the position (pixel) of the crack tip, the crack propagation can be assessed. In fact, in figure 16, the crack growth length 'a' of three samples is presented. The results of  $\phi_{2\omega}$  reported in figure 16, have been compared to thermoelastic phase results  $\phi$ .





(c)

Figure 16. Comparison between phase parameters ( $\phi$ ,  $\phi_{2\omega}$ ) for three samples (a) sample 1, (b) sample 2, (c) sample 3.

Two parameters are in fully agreement, and the curves demonstrate the capability of the phase parameter  $\phi_{2\omega}$  for evaluating the crack length.

It is worth noting that the data of  $\phi$  and  $\phi_{2\omega}$ , refer to a single test, and can be assessed by a single analysis. This is important since, at present to determine the crack propagation sophisticated experimental method are required (i.e. optical microscopy). By using thermography, the crack length 'a' can be assessed using different parameters, the methodology requires only a simple preparation of the specimen surface and can be easily automated.

#### 6.4 Development of a Different Form of Paris' Law Based on Dissipative Temperature Components.

Material fatigue behaviour in presence of crack depends on several factors related to the material and it is governed by different micro-mechanisms of damage at the crack tip. The first approach for describing the crack growth behaviour was proposed by Paris and Erdogan [20]. In their work the crack growth rate is expressed as a function of the stress intensity factor (SIF), [21]. In this regard, the constants of Paris's Law can be obtained by use of conventional methods according to Standards [22], by means of experimental and non-destructive techniques [2], [9], [10], [12], [23], [27-35].

In the last years, many works [42-46] have focused their attention to the energy dissipated at the crack tip and to a possible relation with the growth of cracks. The energy based approach, proposed firstly by Weertman [42], links the crack growth rate with the critical energy to create a unit surface area. Moreover, this approach predicts a fourth power dependence of the crack growth rate and Stress Intensity Factor (SIF). Similar results were obtained by Klingbeil [43], where the crack growth in ductile solids is governed by the total cyclic plastic

dissipation ahead of the crack. In [44] Mazari et al. starting from the Weertman's and Klingbeil's approach, developed a new model in which a similar Paris Law model was obtained between the crack growth and the heat dissipated per cycle.

The Dimensional Analysis approach was used in [45] to describe the fatigue crack growth rate as function of an energy parameter through a similar Paris-like model.

The experimental approaches used in literature aimed to determine the critical energy ( $U_c$ ) were based on the use of strain gages in the plastic zone [46-47], calorimetric measurements [48], and hysteresis loop evaluation [44]. However, these approaches require an off-line measurement and processing of data with consequent high testing time and cannot be applied on actual structural components.

In the work of Meneghetti et al. [49], experimental tests were performed for evaluating the specific heat energy per cycle averaged in a small volume surrounding the crack tip from temperature measurements.

These procedures as previously explained, may find limitation in those cases in which temperature changes on material related to the plastic zone are very low (short cracks) and, moreover, high performance equipment and a difficult set-up are required.

In this paragraph, the basis for a residual life estimation of a component in service conditions with a full field, contactless experimental technique able to determine the crack tip position and assess the dissipated energy per cycle is provided. In particular it will be showed the algorithm able to estimate the dissipated energy and define the crack tip position. Paris curve form thermographic data will allow a residual life estimation once the material is characterized.

The analysis involved three CT steel (AISI 422) specimens and a similar Paris Law model was obtained between the crack growth and the heat dissipated per cycle. Moreover, it was obtained a fourth power dependence of heat dissipated energy and Stress Intensity Factor (SIF) in agreement with numerical and analytical models present in literature.

As described in sections 3.4.4 and 3.4.5, thermographic sequences were acquired during constant load intervals of 2000 cycles and coefficients extracted from the algorithm presented in chapter 3.3 and object of study in this case are  $T_0$ ,  $b$  and  $A$  (which is proportional to  $T_{2\omega}$  and  $T_d$ ) were assessed through equation 14 of chapter 3.

The first two,  $T_0$ ,  $b$ , are related to the temperature rise ahead the crack tip due to the heat dissipated in the plastic volume. As already said, this heat can become difficult to assess due to heat exchanges for conduction, convection and radiation. The term  $A$  is more strictly related to dissipated energy.

Figure 17 shows  $T_0$  maps in correspondence of three different values of number of cycles (specimen 1). It is evident that a significant rise of temperature is only visible in proximity

of failure and for high values of  $\Delta K_I$ . This result is due to the prevalence of heat exchanges with respect to the heat dissipated related to plastic phenomena, as it was also pointed out in the work of Meneghetti et al. [49]. In the same figure, on the contrary, it can be seen that the thermal signal component that occurs at twice the mechanical frequency presents significant values from the first loading cycles.

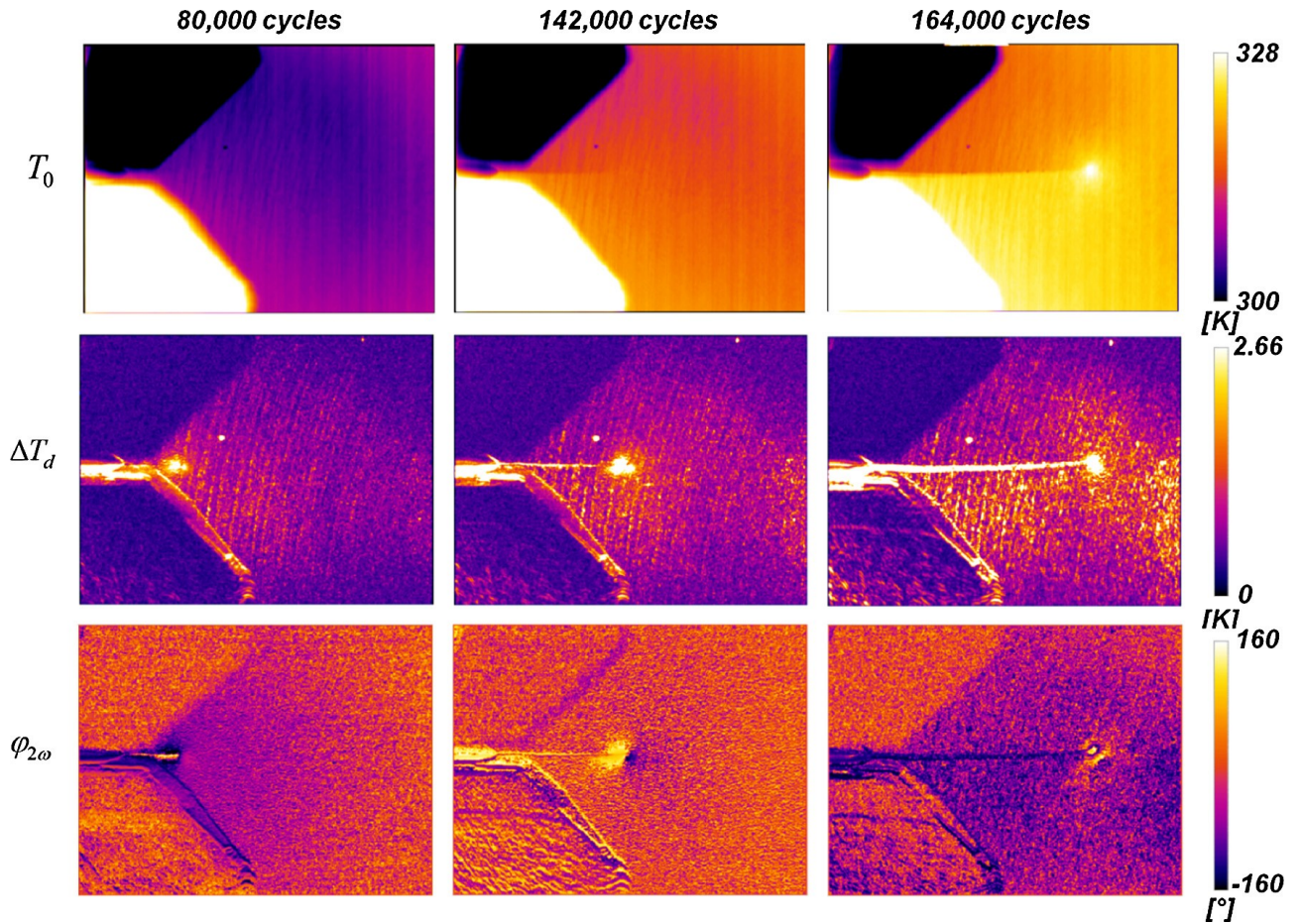


Figure 17. Maps of the absolute temperature  $T_0$ , the total temperature due to the heat dissipated ( $\Delta T_d$ ) and the phase signal of the temperature at twice of the loading frequency ( $\varphi_{2\omega}$ ), obtained in correspondence of three number of cycles (specimen 1).

This is more evident in figure 18, where it is possible to identify two zones ( $A_1$  and  $A_2$ ) characterized by a significant rise of the signal by considering the signal trend along the crack growth direction. This particular trend is due to two different effects: the crack closure effect [50] ( $A_1$ ) and the plastic conditions ahead of the crack tip ( $A_2$ ). In fact, as already described in literature [50], the crack closure can be induced by the plasticity at the crack tip, the contact of the fracture surfaces caused by the misfit of the microscopically rough fracture surfaces and the asperity contacts. The two different effects are also clearly described in the phase maps since they determine a

change of phase with opposite sign in respect to the sound area (Figure 17). It is worth to notice that the two zones  $A_1$  and  $A_2$  are clearly visible but the effect of the crack closure decrease with the increase of the crack length and SIF being this effect more and more negligible for high values of crack length and SIF.

In Fig. 8, it is reported the phase signal  $\varphi_{2\omega}$  that occurs at twice the mechanical frequency along the same profile used for assessing the behaviour of temperature signal. The phase changes in sign by passing through the  $A_2$  to the  $A_1$  zone and reaches the zero value in correspondence the relative minimum value of the  $\Delta T_d$  between  $A_2$  and  $A_1$ . This point represents the crack tip position and in this regard, the phase signal at the twice of loading frequency could be used for evaluating the crack growth in similar way to the thermoelastic phase signal [51]. However, this topic is out of aims of this work and it will be better investigated in further works.

In Figure 19 there are reported  $\Delta T_{d(max)}$  values as function of the number of cycles (specimen 1). These values represent the maximum values of  $\Delta T_d$  reached in the plastic zone ( $A_2$  area). As expected, the  $\Delta T_{d(max)}$  values increase as the number of cycles increase in similar way at the crack growth rate.

Equations (6, chapter 3.2), 5 and 6 of the present chapter, were used to assess the heat dissipated for cycle ( $Q_d$ ) by considering in equation 6 of chapter 3.2, the  $\Delta T_{d(max)}$  value.

In Fig. 20, the heat dissipated at the crack tip is reported versus the stress intensity factor (SIF) values for each specimen. It is very interesting to observe that the heat dissipated depends on the fourth power of the SIF. In this way, the relation between  $Q_d$  and  $\Delta K$  can be generally expressed by the following relation:

$$Q_d = n\Delta K^4 \quad (9)$$

with  $n$  equal to a constant value.

Equation 9 is in agreement with the equation obtained by Weertman [42] to describe the fatigue crack growth through an energy based approach:

$$\frac{da}{dN} = \frac{A_1 \Delta K^4}{\mu \sigma_c^2 U_c} \quad (10)$$

where  $da/dN$  is the crack growth rate,  $\mu$ , the shear modulus of the material,  $\sigma_c$ , the critical stress at fracture, and  $A_1$ , a constant.  $U_c$  is defined as the critical energy to create a unit surface:



$$U_c = E_{hl}/2b(da/dN) \quad (11)$$

Where  $E_{hl}$  is the hysteresis energy and  $b$  is the sample thickness.

Figure 21(a), shows the evolution of the crack growth rate with respect to the heat dissipated per cycle considering the data obtained with specimens 2 and 3. Also in this case, a linear relation can be determined between these two parameters:

$$\frac{da}{dN} = C_1 Q_d^{C_2} \quad (12)$$

A similar relation has been determined and verified by other authors by considering the dissipated hysteretic energy per cycle in place of the heat dissipated [45].

Equation 12 can be used to assess the crack growth rate by knowing the heat dissipated per cycle ahead of the crack tip. To do that, in this work, the thermographic data of the specimens 2 and 3 have been used for evaluating the coefficients  $C_1$  and  $C_2$  then, the linear model has been used for predicting the crack growth rate of the specimens 1.

In Figure 21(b) are shown the results obtained by applying the Equation 12 and the comparison with the crack growth rate measured by means of TSA previously explained.

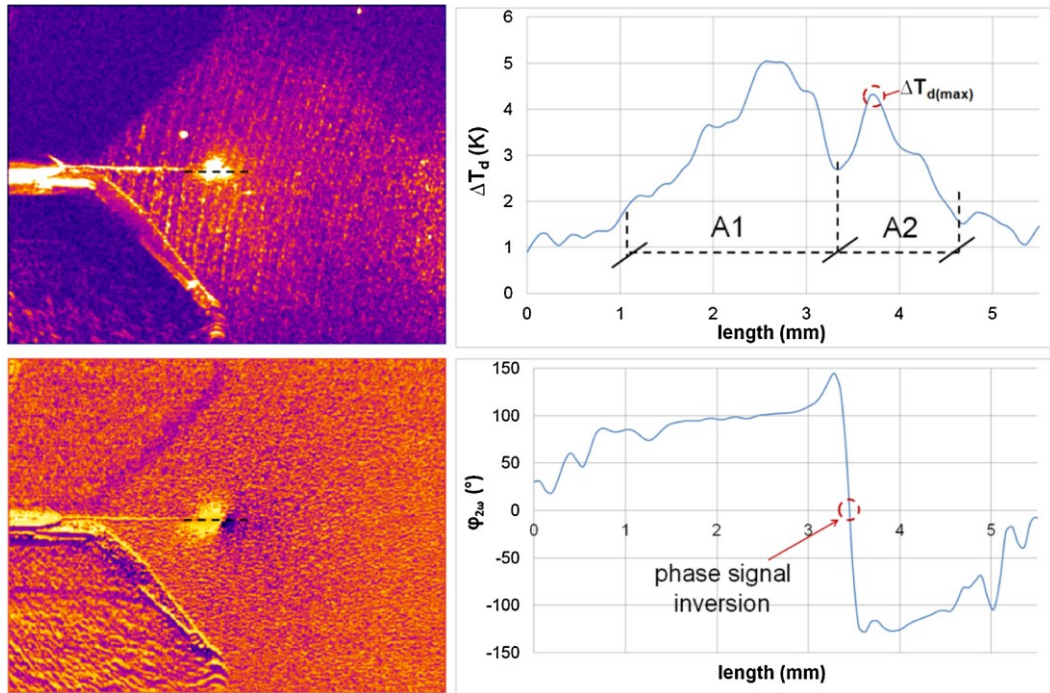


Figure 18. Total temperature and phase maps (142,000 cycles) and total temperature and phase profiles along the crack growth direction.

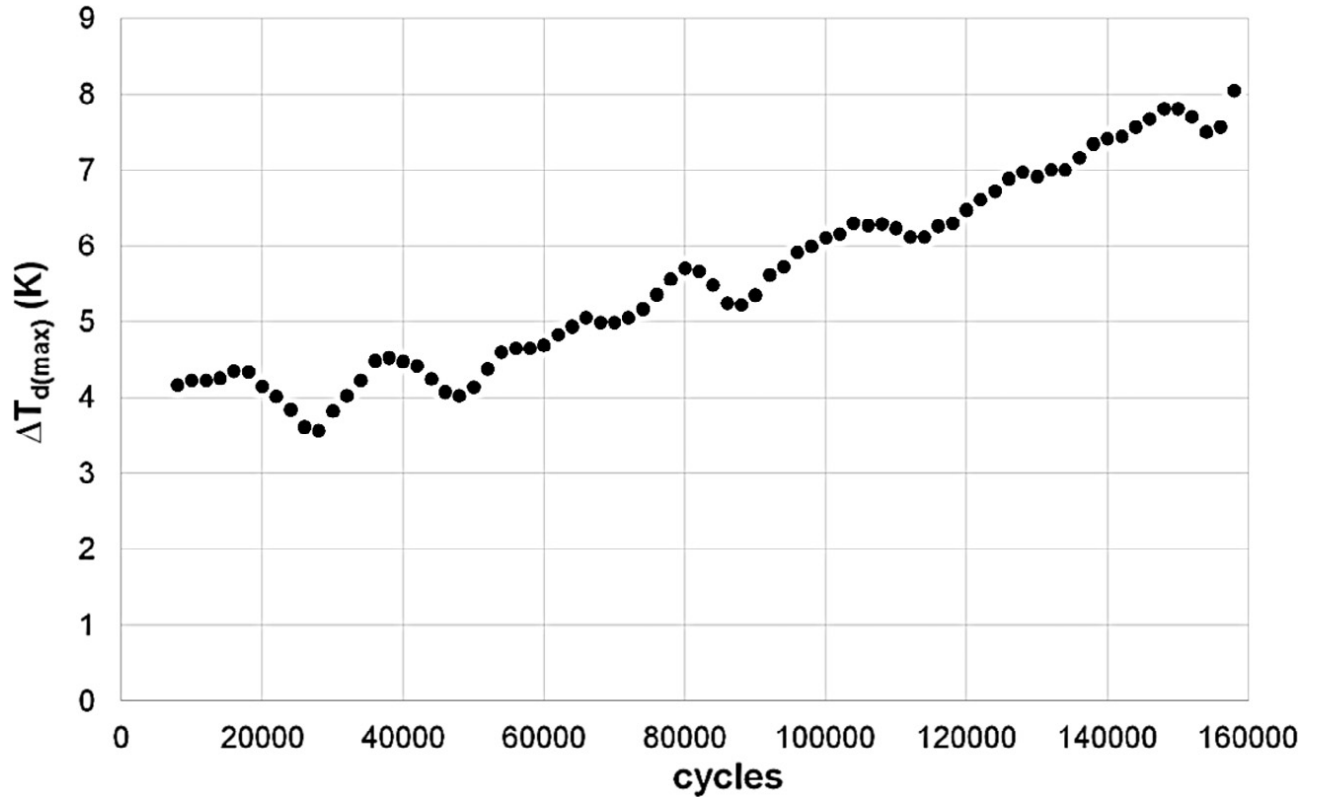


Figure 19.  $\Delta T_{d(max)}$  values as function of the number of cycles for specimen 1.

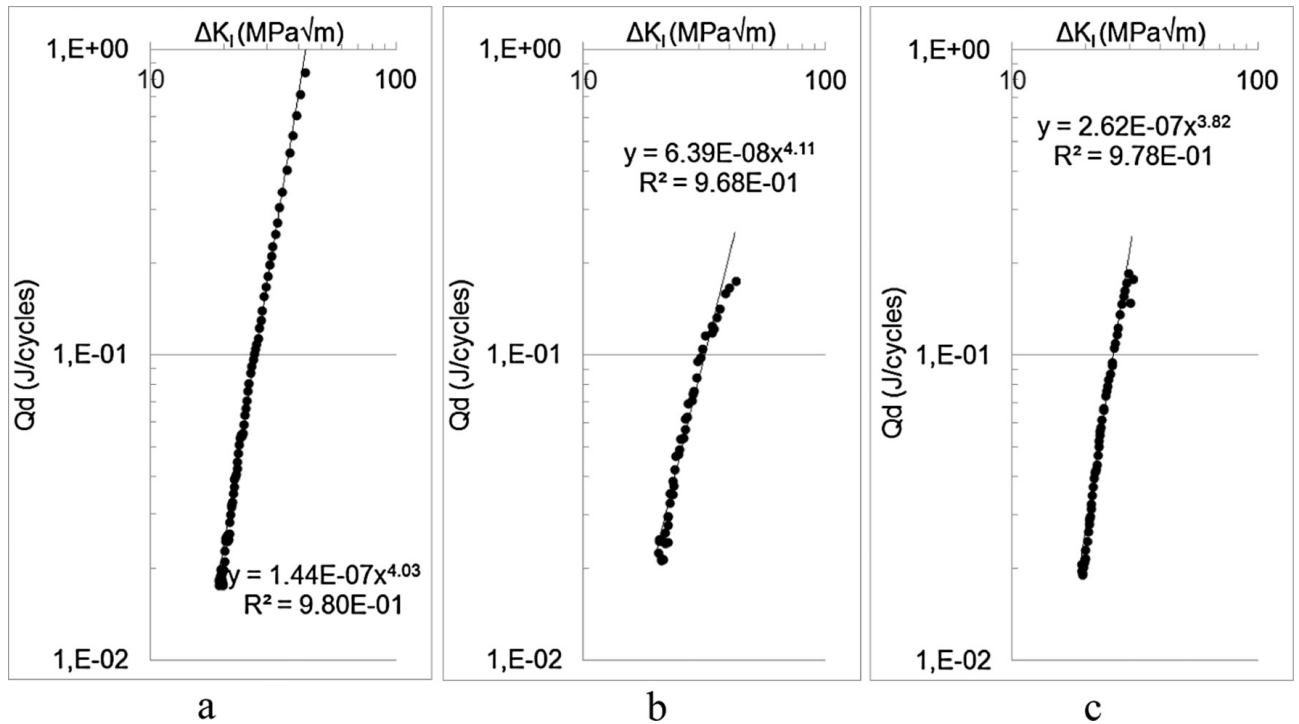


Figure 20. Estimated heat dissipated energy per cycle as function of the  $\Delta K_I$ , (a) specimen 1, (b) specimen 2, (c) specimen 3.



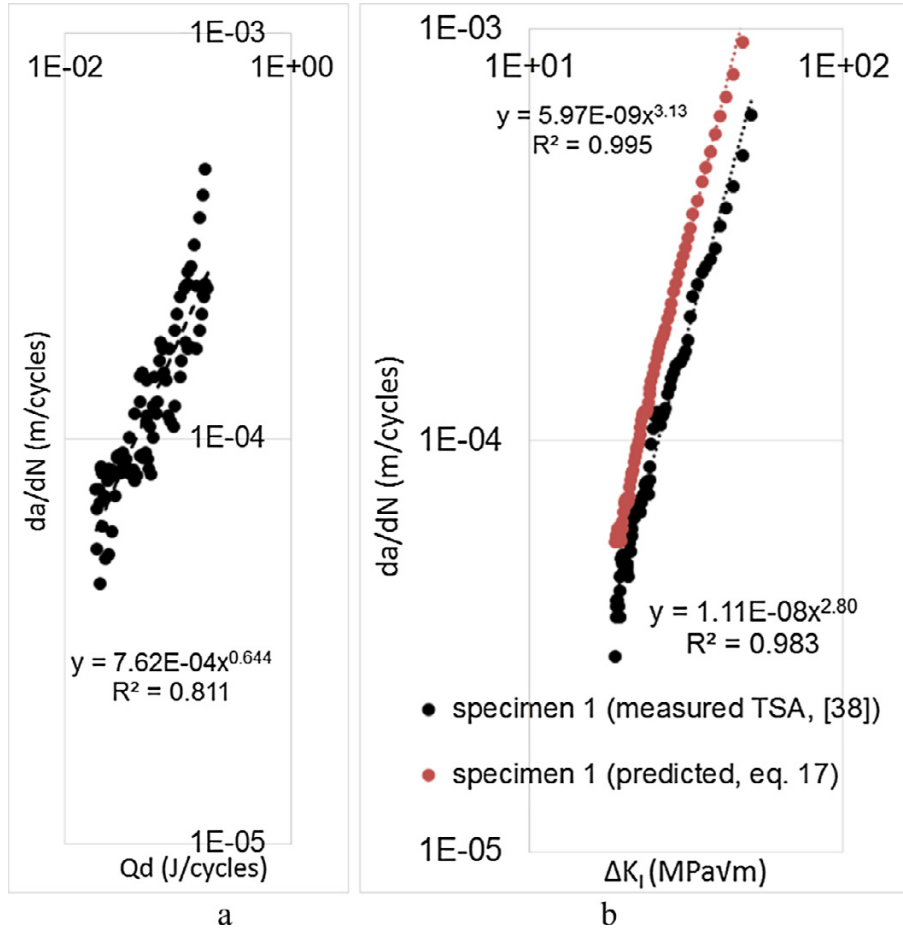


Figure 21. (a) Crack growth rate as function of the estimated heat dissipated energy per cycle and (b) comparison of predicted values obtained with the proposed procedure and measured values in [51].

It is worth to notice that the so called “predicted” and “measured” values have been obtained by using the same experimental set-up.

The SIF values were evaluated according to equation 8, of previous paragraph.

It can be seen in Figure 21(b) as the predicted values are in good agreement with measured ones. It is worth to highlight as the accuracy of the obtained results can be improved by increasing the number of data since data obtained only by two specimens (2 and 3) have been used to obtain the coefficients of the equation 12. Moreover, the scatter between the predicted and measured data can be due to the error in  $Q_p$  calculations (due to the oversized  $V_p$ ).

## Conclusions

In this chapter, an important application of the thermographic signal analysis has been presented in order to provide a good tool to study the fracture mechanics of the stainless steels.

In particular, on both martensitic and austenitic stainless steels an automatable procedure for determining the Paris's law has been presented based on the assessment of the amplitude and phase shift of thermoelastic signal assessed by using the thermographic signal analysis.

Results are in good agreement with those obtained by Standards and reported in literature. In particular, AISI 422 and ASTM A182 grade F6NM have a similar Paris equation and present a lower crack growth rate with respect to CF3M and CF8M. Main advantages when compared to traditional techniques are: a simple specimen preparation, a simple set-up, the online monitoring of the crack growth rate and an automatable procedure. The proposed method can also be used for the monitoring of damage or crack growth within real and more complex structures subjected to actual loading conditions.

Furtherly, in order to make automatic the study of fracture mechanics behaviour a new procedure based on the processing of thermographic data has been proposed for evaluating the crack growth rate through the assessment of heat dissipated at the crack tip during fracture mechanics tests continuously.

The index considered in the analysis was the double frequency temperature variations  $T_d$  of the martensitic steel AISI 422.

Such the temperature variations can be used for predicting the fatigue crack growth after a previous calibration procedure (energetic approach). Moreover, with respect to traditional experimental techniques, the proposed approach allows for the on-line monitoring of the crack growth automatically.

Others interesting results can be summarized as follows:

- the temperature rise in the plastic zone is only visible in proximity of failure and for high values of  $\Delta K_I$ ,
- the thermal signal component that occurs at twice the mechanical frequency presents significant values in the plastic zone from the first loading cycles and allows for evaluating also the crack closure effect,
- a similar Paris Law model was obtained between the crack growth and the heat dissipated per cycle,

- it was obtained a fourth power dependence of heat dissipated energy and Stress Intensity Factor in agreement with numerical and analytical models present in literature.

Finally, it is worth to underline as the proposed method can also be used for the monitoring of damage or crack growth within real and more complex structures subjected to actual loading condition

## References

- [223] N. Harwood, W.M. Cummings. Thermoelastic stress analysis. Bristol, Philadelphia and New York: Adam Hilger; 1991.
- [224] F.A. Diaz, E.A. Patterson, R.A. Yates. Some improvements in the analysis of fatigue cracks using thermoelasticity. *Int J Fatigue* 26(4), 365–76, 2004.
- [225] D. Palumbo, U. Galietti. Characterization of steel welded joints by infrared thermographic methods. *Quant Infrar Thermogr J*, 11, 42–52, 2014
- [226] U. Galietti, D. Palumbo. Application of thermal methods for characterization of steel welded joints. In: 14th International conference on experimental mechanics, ICEM 2014; Poitiers; France; 4–9 July 2010. *EPJ Web of conferences*, vol. 6, Article number 38012.
- [227] U. Galietti, D. Palumbo, R. De Finis , F. Ancona . Fatigue damage evaluation of martensitic stainless steel by means of thermal methods. In: National conference IGF XXII, 1–3 July, Rome; 2013. p. 80–90.
- [228] U. Galietti, D. Palumbo, R. De Finis , F. Ancona. Fatigue limit evaluation of martensitic steels with thermal methods. In: QIRT conference, 7–11 July, Bordeaux; 2014.
- [229] N. Connesson, F. Maquin , F. Pierron. Experimental energy balance during the first cycles of cyclically loaded specimens under the conventional yield stress. *Exp Mech*, 51, 23–44, 2011.
- [230] W.J. Wang, J.M. Dulieu-Barton, Q. Li. Assessment of non-adiabatic behaviour in thermoelastic stress analysis of small scale components. *Exp Mech*, 50, 449–61, 2010.
- [231] F.A. Diaz, E.A. Patterson, R.A. Tomlinson, R.A. Yates. Measuring stress intensity factors during fatigue crack growth using thermoelasticity. *Fract Eng Mater Struct*, 27(7), 571–83, 2004.
- [232] F.A. Diaz, E.A. Patterson, R.A. Yates. Application of thermoelastic stress analysis for the experimental evaluation of the effective stress intensity factor. *Frattura ed Integrità Strutturale* 25, 109–8, 2013.

- [233] F.A. Diaz, E.A. Patterson, R.A. Tomlinson, R.A. Yates. Differential thermography reveals crack tip behaviour? In: Proc SEM annual conf. on exp. app. mech., society for experimental mechanics. p. 1413–6, 2005.
- [234] R.A. Tomlinson, E.A. Patterson. Examination of crack tip plasticity using thermoelastic stress analysis. Thermomechanics and infra-red imaging. In: Proceedings of the society for experimental mechanics series, vol. 7, 123–129, 2005.
- [235] E. Wolf. Fatigue crack closure under cyclic tension. *Engineering Fracture Mechanics*, 2, 37-45, 1970.
- [236] J. R. Rice. Mechanics of crack tip deformation and extension by fatigue. *Fatigue Crack Propagation*, ASTM Spec. Tech. Publ. No. 4 15, 247. Am. Soc. Testing Mater, 1967.
- [237] W. Elber. Fatigue crack propagation. Ph.D. Thesis, Univ. of N.S.W., Australia, 1968.
- [238] P.J. Withers. Fracture mechanics by three-dimensional crack-tip synchrotron X-ray microscopy. *Philosophical Transactions A*, 373, 2-26, 2015.
- [239] A.K. Wong. Stress Distribution: Analysis Using Thermoelastic Effect, *Encyclopedia of Materials: Science and Technology (Second Edition)*, 8897-8901, 2001.
- [240] Fatigue and Microstructure. American Society for metals. Metals Park, Ohio. Papers presented at the 1978 ASM Material Science Seminar.
- [241] D. Palumbo, R. De Finis, F. Ancona, U. Galietti. Damage monitoring in fracture mechanics by evaluation of the heat dissipated in the cyclic plastic zone ahead of the crack tip with thermal measurements. *Engineering Fracture Mechanics* 181, 65–76, 2017.
- [242] P. Paris, F. Erdogan. A critical analysis of crack propagation laws. *Journal of Basic Engineering*, Transact Am Soc Mech Eng, D85(4), 528–37, 1963. DOI: 10.1115/1.3656900.
- [243] R.O. Ritchie. Mechanisms of fatigue-crack propagation in ductile and brittle solids. *Int J Fract*, 100, 55–83, 1999.
- [244] ASTM E 647–00. Standard test method for measurement of fatigue crack growth rates; 2004.
- [245] J. Réthore, N. Limodin, J.Y. Buffière, S. Roux, F. Hild. Three-dimensional analysis of fatigue crack propagation using X-ray tomography, digital volume correlation and extended finite element simulations. *Procedia IUTAM*, 4(4):151–8, 2012.
- [246] M. Saka ,I. Sato , H. Abè . NDE of a 3-D surface crack using magnetic field induced by DC current flow. *NDT&E Int*, 5, 325–8, 1998.
- [247] J.J. Williams, K.E. Yazzie, E. Padilla ,N. Chawla, X. Xiao, F. De Carlo. Understanding fatigue crack growth in aluminium alloys by in situ X-ray synchrotron tomography. *Int J Fatigue*, 57,79–85, 2013.

- [248] S. Kainuma, J.H. Ahn, Y.S. Jeong, H. Takahashi. Evaluation on estimation in characteristics of fatigue crack using micro-encapsulated dye mixing paint. *Engng Fail Anal*, 25, 1–12, 2015.
- [249] H. Tanabe , K. Kida , T. Takamatsu,N. Itoh, E.C. Santos. Observation of magnetic flux density distribution around fatigue crack and application to non-destructive evaluation of stress intensity factor. *Proced Eng*, 10,881–7, 2011.
- [250] Z.Q. Cui, H.W. Yang, X.W. Wang, Z.F. Yan, Z.Z. Ma,B.S. Xu, et al. Research on fatigue crack growth behavior of AZ31B magnesium alloy electron beam welded joints based on temperature distribution around the crack tip. *Engng Fract Mech*, 133, 14–23, 2015.
- [251] J.R. Yates, M. Zanganeh, Y.H. Tai. Quantifying crack tip displacement fields with DIC. *Engng Fract Mech*, 77, 2063–76, 2010.
- [252] I. Carrascal, J.A. Casado, S. Diego, R. Lacalle, S. Cicero, J.A. Álvarez. Determination of the Paris' law constants by means of infrared thermographic techniques. *Polym Testing*, 40, 39–45, 2014.
- [253] P.R. Guduru, A.T. Zehnder, A.J. Rosakis, G. Ravichandran. Dynamic full field measurements of crack tip temperatures. *Engng Fract Mech*, 68, 1535–56, 2001.
- [254] A.Y.U. Fedorova, M.V. Bannikov, O.A. Plekhov, E.V. Plekhova. Infrared thermography study of the fatigue crack propagation. *Frattura ed Integrità Strutturale*, 21, 46–8, 2012.
- [255] R.A. Tomlinson, E.J. Olden. Thermoelasticity for the analysis of crack tip stress fields – a review. *Strain*, 35, 49–55, 1999.
- [256] F. Ancona, R. De Finis, D. Palumbo, U. Galietti. Crack growth monitoring in stainless steels by means of TSA technique. *Proced Eng* ,109, 89–96, 2015.
- [257] D. Palumbo,F. Ancona, R. De Finis, U. Galietti. Experimental study of the crack growth in stainless steels using thermal methods. *Proced Eng*, 109, 338–45, 2015.
- [258] ResearchIR Max (RIR Max). FLIR System, Inc. Wilsonville, USA; 2015.
- [259] S.M. Dulieu-Smith SM. Alternative calibration techniques for quantitative thermoelastic stress analysis. *Strain*, 31, 9–16, 1995.
- [260] Damage Tolerance Assessment Handbook. Volume I: Introduction, fracture mechanics, fatigue crack propagation. U.S. Department of Transportation, Research and Special Programs Administration, Volpe National Transportation System Center, Kendall Square, Cambridge; October 1993.
- [261] L. Vergani. *Meccanica dei materiali*. Milano: McGraw Hill; 2001. ISBN:88 386 0860-1.

- [262] R. De Finis, D. Palumbo, F. Ancona , U. Galietti . Fatigue limit evaluation of various martensitic stainless steels with new robust thermographic data analysis. *Int. J. Fatigue*, 74, 88-96, 2015.
- [263] J.M. Dulieu-Barton. Introduction to thermoelastic stress analysis. *Strain*, 35, 35–39, 1999. Doi: 10.1111/j.1475-1305.1999.tb01123.x
- [264] J. Weertman. Theory of fatigue crack growth based on a BCS crack theory with work hardening. *Int J Fatigue*, 9, 125–31, 1973.
- [265] N.W. Klingbeil. A total dissipated energy theory of fatigue crack growth in ductile solids. *Int J Fatigue*, 117-12, 2003.
- [266] M. Mazari, B. Bouchouicha, M. Zemri , M.Benguediab, N. Ranganathan. *Comput Mater Sci* 2008;41:344–6.
- [267] P. Kucharski, G. Lesiuk , M. Szata . Description of fatigue crack growth in steel structural components using energy approach – influence of the microstructure on the FCGR. In: *Fatigue failure and fracture mechanics XXVI: proceedings of the XXVI Polish National Conference on Fatigue Failure and Fracture Mechanics*, (Dariusz Skibicki, ed.), AIP Publishing, 2016.
- [268] N. Ranganathan, F. Chalon, S. Meo. Some aspects of the energy based approach to fatigue crack propagation. *Int J Fatigue*, 30, 1921–8, 2008.
- [269] S. Ikeda, Y. Izumi, M.E. Fine. Plastic work during fatigue crack propagation in a high strength low alloy steel and in 7050 Al alloy. *Eng Fract Mech*, 9, 123–6, 1977.
- [270] T.S. Gross, J. Weertman. Calorimetric measurement of the plastic work of fatigue crack propagation in 4140 steel. *Metall Trans A*, 13A, 2165–72, 1982.
- [271] G. Meneghetti, M. Ricotta. Evaluating the heat energy dissipated in a small volume surrounding the tip of a fatigue crack, *92(2)*, 605–11, 2016.
- [272] R. Pippan, A. Hohenwarter. Fatigue crack closure: a review of the physical phenomena. *Fatigue Fract Eng Mater Struct*, 40(4), 471-25, 2017.
- [273] F. Ancona, D. Palumbo, R. De Finis, G.P. Demelio,U. Galietti. Automatic procedure for evaluating the Paris Law of martensitic and austenitic stainless steels by means of thermal methods. *Eng Fract Mech*,163, 206–14, 2016.

---

## Conclusions

---

In the present Thesis, a Thermography based approach has been developed capable of studying the fatigue of stainless steels and composites under different point of views.

The developed approach is based on an algorithm that allows to separate the temperature change components related to the energy production by different physical phenomena.

Each of the component of temperature evolution represents a signal: the linear part of the algorithm is related to the mean temperature increase (offset temperature ' $T_0$ ' ( $S_0$ ) and slope ' $b$ '), the first order harmonic components ( $T_{the}$  and  $\varphi$ ) are related to the thermoelastic temperature variations, the second order temperature variations ' $T_d$ ' ( $S_d$ ) and  $\varphi_{2\omega}$  leading to the study of intrinsic dissipations and energy of plastic deformations.

It was presented that the temperature  $T_0$  presents some peculiarities such as the strong dependence from the material properties (such as diffusivity) hence, the analysis requires accurate setups and smoothing procedures for extrapolating valid information on material behaviour. Moreover, the assessment of  $T_0$ , as it has been reported in literature, requires to reach a plateau condition of surface temperature evolution ( $T_{stab}$ ) in a fixed stress level. In some case, the plateau conditions is not achieved and then it becomes very difficult to study the fatigue behaviour of the material by simply analysing the linear part of temperature variations.

In the present Thesis, on one hand, it has been proposed a procedure to filtering out the 'thermal disturbances' from the linear temperature parameter, for a better estimating such the thermal component. On the other hand, algorithm has been proposed capable of assessing different parameters from  $T_{stab}$ . In particular the analysis of the slope ' $b$ ' of temperature increase in the first part of the loading procedure and the mean temperature increase  $T_{mean\_in}$  provide a valid tools for assessing the fatigue limit in case the steady-state temperature conditions are not achieved. However, another issue of the linear part of temperature variations is such that the temperature, is a 'global' parameter for describing the dissipative phenomena, specifically, it does not provide local information on damage processes.

The thermoelastic signal amplitude  $T_{the}$  loses its validity when adiabatic conditions are no longer present. In these conditions, it seems that also TSA is no longer valid, but due to the possibility to assess the phase shift between stress and temperature  $\varphi$ , TSA can be used and integrated in an approach for studying also irreversible processes. In effect,  $\varphi$  represents a valid tool for localising the crack initiation, monitoring the damage processes, and also for

separating, in particular in fracture mechanics field, the different physical phenomena associated to the crack propagation (plastic area and crack closure area). The literature, well knows such the approach of using phase data to assess fracture mechanics behaviour but in the present Thesis, the novelty is represented by the use, the complementary use of second order temperature variation information to study the fracture mechanics behaviour.

In effect, the amplitude  $T_d$  is related to the energy of plastic phenomena in the plastic zone and associated with the  $\varphi$ , surely supports in determining where the crack tip is. Otherwise, the  $\varphi_{2\omega}$  can be used in the same way as  $\varphi$ , for determining the crack propagation behaviour. However, all these parameters can be used for determining the fatigue limit of materials.

In this sense, two methods have been presented: the threshold method applied to the thermal indexes and the slope method applied to the phase data, completed by a specific processing procedure, as well.

A wide experimental campaign on martensitic (AISI 422, 17-4 PH, X 4 Cr-Ni-Si 16-5-1, ASTM A 182), austenitic (CF3M, CF8M), biphasic (A890 grade 4a), and composites GFRP, allowed the validation of these two methods, by calibrating the thresholds with respect to the specific microstructure properties.

The use of such the approach referring to the temperature modelling involves also an in-depth analysis of the physical processes determining the fatigue behaviour of the materials, in particular some considerations have been made on the relation between stress ratio-temperature parameters-fatigue behaviour. In this sense, in particular  $T_d$  and  $\varphi$ , exhibited a great sensitivity with respect the phenomenon by showing a specific range of variation for a specific stress ratio condition, this is important for separating any viscous or plastic behaviour of the lattice, and then discriminate the microstructure.

Even in fracture mechanics the use of  $\varphi$ , for determining the crack-tip, and then calculating the stress intensity factor, and the use of  $T_d$  for calculating the energy dissipated in the plastic zone, have been very useful for determining in a different way the Paris's Law.

The results presented, demonstrate the multistage characteristic of the adopted approach, from the data processing to the data analysis.

The temperature variation model and the analysis proposed, unify all the signals that previously has been treated separately in order to achieve:

- Experimental campaign testing time and costs reductions
- More understanding on specific damage process by assessing the temperature signals
- Detection and monitoring online/in-situ of damage processes by means of relatively simple setup.

The further development of the present work will involve:



- The introduction of a dumping parameter in the model of temperature, in order to determine directly the viscous behaviour, and then determining in a more accurate way the energy loss of material during fatigue processes;
- To quantify in a more accurate way the plastic region during fracture mechanics tests,
- To study also the mode II of fracture mechanics by using TSA approach, and its specificities.
- The study of thermal contribution by real and complex shaped components;
- The assessment of Wöhler curve by analysing temperature data for both stainless steel, composites and Friction Stir Welding aluminium H111-A5754 alloy;
- To correlate the temperature signal with the change in mechanical properties of biphasic stainless steels, by means of a suitable procedure of TSA data analysis.

## Appendix A: Loading Tables

In present appendix the imposed loading tables will be presented.

Each table presents the consecutive and incremental loading levels of stepwise loading procedure in terms of : stress semi amplitude  $\Delta\sigma/2$ , stress amplitude  $\Delta\sigma$ , stress ratio R, and respectively minimum, maximum and mean stresses.

The stresses have been imposed according to the procedure presented in Chapter 3.

ASTM A 890 grade 4a						
STEP	$\Delta\sigma/2$	$\Delta\sigma$	$R = \sigma_{\min}/\sigma_{\max}$	$\sigma_{\min}$	$\sigma_{\max}$	$\sigma_{\text{mean}}$
1	65,00	<b>130</b>	0,5	130	260	195
2	80,00	<b>160</b>	0,5	160	320	240
3	95,00	<b>190</b>	0,5	190	380	285
4	105,00	<b>210</b>	0,5	210	420	315
5	110,00	<b>220</b>	0,5	220	440	330
6	115,00	<b>230</b>	0,5	230	460	345
7	120,00	<b>240</b>	0,5	240	480	360
8	125,00	<b>250</b>	0,5	250	500	375
9	130,00	<b>260</b>	0,5	260	520	390
10	135,00	<b>270</b>	0,5	270	540	405
11	140,00	<b>280</b>	0,5	280	560	420
12	145,00	<b>290</b>	0,5	290	580	435
13	150,00	<b>300</b>	0,5	300	600	450
14	162,50	<b>325</b>	0,5	325	650	488
15	175,00	<b>350</b>	0,5	350	700	525

Table A1. Loading Table for biphasic material.

AISI 316						
STEP	$\Delta\sigma/2$	$\Delta\sigma$	$R = \sigma_{\min}/\sigma_{\max}$	$\sigma_{\min}$	$\sigma_{\max}$	$\sigma_{\text{mean}}$
1	35,00	<b>70</b>	0,5	70	140	105
2	45,00	<b>90</b>	0,5	90	180	135
3	50,00	<b>100</b>	0,5	100	200	150
4	55,00	<b>110</b>	0,5	110	220	165
5	60,00	<b>120</b>	0,5	120	240	180
6	65,00	<b>130</b>	0,5	130	260	195
7	70,00	<b>140</b>	0,5	140	280	210
8	75,00	<b>150</b>	0,5	150	300	225
9	80,00	<b>160</b>	0,5	160	320	240
10	85,00	<b>170</b>	0,5	170	340	255
11	90,00	<b>180</b>	0,5	180	360	270

12	95,00	<b>190</b>	0,5	190	380	285
13	100,00	<b>200</b>	0,5	200	400	300
14	105,00	<b>210</b>	0,5	210	420	315
15	115,00	<b>230</b>	0,5	230	460	345
16	125,00	<b>250</b>	0,5	250	500	375

Table A2. Loading Table for austenitic AISI 316 material.

AISI 316L						
STEP	$\Delta\sigma/2$	$\Delta\sigma$	$R = \bar{\sigma}_{\min}/\bar{\sigma}_{\max}$	$\bar{\sigma}_{\min}$	$\bar{\sigma}_{\max}$	$\bar{\sigma}_{\text{mean}}$
1	35,00	70	0,5	70	140	105
2	40,00	80	0,5	80	160	120
3	45,00	90	0,5	90	180	135
4	50,00	100	0,5	100	200	150
5	55,00	110	0,5	110	220	165
6	60,00	120	0,5	120	240	180
7	65,00	130	0,5	130	260	195
8	70,00	140	0,5	140	280	210
9	75,00	150	0,5	150	300	225
10	80,00	160	0,5	160	320	240
11	85,00	170	0,5	170	340	255
12	90,00	180	0,5	180	360	270
13	95,00	190	0,5	190	380	285
14	100,00	200	0,5	200	400	300
15	110,00	220	0,5	220	440	330
16	125,00	250	0,5	250	500	375

Table A3. Loading Table for austenitic AISI 316L material.

17-4PH						
STEP	$\Delta\sigma/2$	$\Delta\sigma$	$R = \bar{\sigma}_{\min}/\bar{\sigma}_{\max}$	$\bar{\sigma}_{\min}$	$\bar{\sigma}_{\max}$	$\bar{\sigma}_{\text{mean}}$
1	140,00	<b>280</b>	0,5	280	560	420
2	160,00	<b>320</b>	0,5	320	640	480
3	170,00	<b>340</b>	0,5	340	680	510
4	180,00	<b>360</b>	0,5	360	720	540
5	185,00	<b>370</b>	0,5	370	740	555
6	190,00	<b>380</b>	0,5	380	760	570
7	195,00	<b>390</b>	0,5	390	780	585
8	200,00	<b>400</b>	0,5	400	800	600
9	205,00	<b>410</b>	0,5	410	820	615
10	210,00	<b>420</b>	0,5	420	840	630
11	215,00	<b>430</b>	0,5	430	860	645
12	220,00	<b>440</b>	0,5	440	880	660
13	225,00	<b>450</b>	0,5	450	900	675
14	235,00	<b>470</b>	0,5	470	940	705
15	250,00	<b>500</b>	0,5	500	1000	750
16	275,00	<b>550</b>	0,5	550	1100	825

Table A4. Loading Table for precipitating hardening material.

ASTM A 182 F6NM						
STEP	$\Delta\sigma/2$	$\Delta\sigma$	$R = \sigma_{\min}/\sigma_{\max}$	$\sigma_{\min}$	$\sigma_{\max}$	$\sigma_{\text{mean}}$
1	25,00	<b>50</b>	0,5	50	100	75
2	45,00	<b>90</b>	0,5	90	180	135
3	65,00	<b>130</b>	0,5	130	260	195
4	85,00	<b>170</b>	0,5	170	340	255
5	100,00	<b>200</b>	0,5	200	400	300
6	115,00	<b>230</b>	0,5	230	460	345
7	130,00	<b>260</b>	0,5	260	520	390
8	140,00	<b>280</b>	0,5	280	560	420
9	150,00	<b>300</b>	0,5	300	600	450
10	160,00	<b>320</b>	0,5	320	640	480
11	170,00	<b>340</b>	0,5	340	680	510
12	175,00	<b>350</b>	0,5	350	700	525
13	180,00	<b>360</b>	0,5	360	720	540
14	185,00	<b>370</b>	0,5	370	740	555
15	190,00	380	0,5	380	760	570
16	195,00	390	0,5	390	780	585

Table A5. Loading Table for martensitic ASTM A182 F6NM material at R=0.5.

ASTM A 182 F6NM						
STEP	$\Delta\sigma/2$	$\Delta\sigma$	$R = \sigma_{\min}/\sigma_{\max}$	$\sigma_{\min}$	$\sigma_{\max}$	$\sigma_{\text{mean}}$
1	170,00	<b>340</b>	-0,1	-31	309	139
2	195,00	<b>390</b>	-0,1	-35	355	160
3	220,00	<b>440</b>	-0,1	-40	400	180
4	240,00	<b>480</b>	-0,1	-44	436	196
5	260,00	<b>520</b>	-0,1	-47	473	213
6	275,00	<b>550</b>	-0,1	-50	500	225
7	290,00	<b>580</b>	-0,1	-53	527	237
8	305,00	<b>610</b>	-0,1	-55	555	250
9	315,00	<b>630</b>	-0,1	-57	573	258
10	325,00	<b>650</b>	-0,1	-59	591	266
11	330,00	<b>660</b>	-0,1	-60	600	270
12	335,00	<b>670</b>	-0,1	-61	609	274
13	340,00	<b>680</b>	-0,1	-62	618	278
14	345,00	<b>690</b>	-0,1	-63	627	282
15	350,00	<b>700</b>	-0,1	-64	636	286
16	355,00	<b>710</b>	-0,1	-65	645	290

Table A6. Loading Table for martensitic ASTM A182 F6NM material at R=-0.1.

X4CrNiSi 16-5-1						
STEP	$\Delta\sigma/2$	$\Delta\sigma$	$R = \sigma_{\min}/\sigma_{\max}$	$\sigma_{\min}$	$\sigma_{\max}$	$\sigma_{\text{mean}}$
1	25	<b>50</b>	0,5	50	100	75

2	45	<b>90</b>	0,5	90	180	135
3	65	<b>130</b>	0,5	130	260	195
4	85	<b>170</b>	0,5	170	340	255
5	105	<b>210</b>	0,5	210	420	315
6	120	<b>240</b>	0,5	240	480	360
7	135	<b>270</b>	0,5	270	540	405
8	150	<b>300</b>	0,5	300	600	450
9	165	<b>330</b>	0,5	330	660	495
10	180	<b>360</b>	0,5	360	720	540
11	190	<b>380</b>	0,5	380	760	570
12	200	<b>400</b>	0,5	400	800	600
13	208	<b>415</b>	0,5	415	830	623
14	215	<b>430</b>	0,5	430	860	645
15	223	<b>445</b>	0,5	445	890	668

Table A5. Loading Table for martensitic X4CrNiSi 16-5-1 material.

---

## ***Appendix B: Matlab Routines***

---

In present appendix all the algorithms implemented in Matlab for processing parameters raw data, are presented.

### **THRESHOLD METHOD**

```
%CALCOLO DEI COEFFICIENTI DELLA RETTA DI REGRESSIONE LINEARE
for i=TIN:NUM

    Y_N=Y(TIN:NUM);
    X_N=X(TIN:NUM);
    y=polyfit(X_N,Y_N,1);
    m=y(1);
    q=y(2);

end

%CALCOLO DEI RESIDUI

for i=1:N

    RESIDUI(i)=(Y(i)-(X(i)*m)+q);
    R=RESIDUI';

end

save RESIDUI;
figure,
plot(X,R,'ko')
title('RESIDUI PARAMETRO')
xlabel('semiampiezza stress');
ylabel('Thermal Signal (°C)');
saveas(gcf,'RESIDUI','fig');
saveas(gcf,'RESIDUI','jpg');

%CALCOLO DELLA CARTA DI CONTROLLO PER I RESIDUI

%RESIDUI_N=R(1:N);
%save RESIDUI_N;

MEDIA=mean(mean(R(TIN:NUM)));
DEVST=std(std(R(TIN:NUM)));
Sth3=MEDIA+(3*DEVST);
Sth6=MEDIA+(6*DEVST);

save ('MEDIA','MEDIA');
save ('DEVST','DEVST');
save ('Sth3','Sth3');
save ('Sth6','Sth6');

%CREAZIONE DELLA TABELLA : STRESS/RESIDUI/SOGLIA

%for i=TIN:NUM

%Soglia3(i)=Sth3;
%Soglia6(i)=Sth6;
%R_S(i)=R(i);
%X_S(i)=X(i);
```

```

%end

%SOGLIA=Soglia';
%R_A=R_S';
%X_A=X_S';

%TABELLA = zeros(S,4);
%TABELLA(:,2)=R_A;
%TABELLA(:,3)=SOGLIA;

%save TABELLA;
%RICERCA DEL LIMITE DI FATICA: a partire dal primo punto sopra soglia. il
%punto trovato deve essere il minore dei successivi 3.

%for i=N+2:S
    %RPFL=R_A(R_A>SOGLIA);
%end

%RICERCA DEL LIMITE DI FATICA: PER LA SOGLIA 3SIGMA

    for i=NUM:N

        if Sth3>R(i)

            else
                LDF3=X(i);
                save('LDF3','LDF3');
                break
            end

        end

    for i=NUM:N
        if Sth6>R(i)

            else
                LDF6=X(i);
                save('LDF6','LDF6');
                break
            end

        end

    clear sth3;
    clear sth6;

end

%RICERCA DEL LIMITE DI FATICA: PER LA SOGLIA 6SIGMA

%v=size(RPFL);
%DIM=v(1);
%for i=1:DIM
%TRASP=RPFL(i);
%trasp(N+3,i+N+3)=TRASP;
%end
%T=trasp';
%T_T=T(:,8);
%TABELLA(:,4)=T_T;

%TABELLA(:,4)=RPFL;

%C=cat(2,X_A,R_A,SOGLIA,RPFL);
%C(1:8,:)=[];

%[stima,indice]=min(C(:,4));
%limitedifatica=C(indice,1);
%save limitedifatica;

```

%bisogna solo eliminare eventuali zeri nella serie finale.

## SLOPE COEFFICIENT b

%Routine di analisi del segnale term0oelastico : filtra il coefficiente %'b' (pendenza) dell'equ. Termoelastica, ne fa il filtro gaussiano sui dati del %primo sottostep.

```
clear all
close all
clc
```

% Fase di acquisizione delle immagini per quanti sono gli step di carico .txt o %.mat

```
flag=0;
while flag==0
    kind=input('Acquisire immagini da file .txt o da una file .mat: .txt (1) .mat (2) o
non acquisire (3) ','s');
    fprintf('\n\n')
    switch kind
        case '1'
            [MatDatib,s1,s2,s3,nomefile,n,nn]=Acq_imm_DT;    %funzione per %l'apertura dei
.txt del DeltaTherm
            flag=1;
        case '2'
            [MatDatib,s1,s2,s3,nomefile,n,nn]=Acq_imm_matb;    %funzione per %l'apertura dei
.mat
            flag=1;
        case '3'
            [MatDatib,s1,s2,s3,nomefile,n,nn]=estrazionemdam;    %funzione per caricare
direttamente tutta la matrice
            flag=1;
        otherwise
            fprintf('Inserimento non corretto')
            fprintf('\n\n')
    end
end
```

```
%Filtro immagini
flag=0;
while flag==0
    kind=input('Vuoi filtrare le immagini ?: SI (1) NO (2) ','s');
    fprintf('\n\n')
    switch kind
        case '1'
            [MatDatib_f,filt]=smoot_3D(MatDatib); %Funzione filtro immagini %caricata in
cartella
            flag=1;
        case '2'
            MatDatib_f=MatDatib;
            flag=1;
        otherwise
            fprintf('Inserimento non corretto')
            fprintf('\n\n')
    end
end
```

```
% Taglio delle immagini (scelta dell'area da analizzare)
flag=0;
while flag==0
    kind=input('Vuoi tagliare le immagini ?: SI (1) NO (2) ','s');
    fprintf('\n\n')
    switch kind
        case '1'
            [MatDatib_f_cut,x1,x2,y1,y2,s1_cut,s2_cut,s3_cut]=cut_imm(MatDatib_f,s1,s2,s3);
%Funzione taglio immagini
            flag=1;
        case '2'
            MatDatib_f_cut=MatDatib_f;
            s1_cut=s1;
            s2_cut=s2;
            s3_cut=s3;
            flag=1;
        otherwise
            fprintf('Inserimento non corretto')
```



```

        fprintf('\n\n')
    end
end

clear MatDatib; %Salvataggio delle immagini in un'unica matrice 3D

save MatDatib_f_cut; %Salvataggio delle immagini tagliate in un'unica matrice 3D
%clear MatDatib_f_cut;

%Ciclo per l'apertura delle immagini in Matlab
flag=0;
while flag==0
    kind=input('Vuoi aprire le immagini ?: SI (1) NO (2)    ','s');
    fprintf('\n\n')
    switch kind
        case '1'
            for i=1:s3_cut
                figure,
                imagesc(MatDatib_f_cut(:,:,i));
                num=int2str(i);
                n_tit=strcat(nomefile,num,'_',nn);
                title(n_tit)
            end
            flag=1;
        case '2'
            flag=1;
        otherwise
            fprintf('Inserimento non corretto')
            fprintf('\n\n')
        end
    end
end

Tab_load=xlsread('Carichi.xls'); %Apertura file dei carichi
Loads_1=Tab_load(1:s3_cut,3); % Estrapolazione del vettore dei carichi

% calcolo della media della deviazione standard del max e del min

for i=1:s3_cut
    Media(i)=mean(mean(MatDatib_f_cut(1:s1_cut-1,1:s2_cut-1,i)));
    d=MatDatib_f_cut(1:s1_cut-1,1:s2_cut-1,i);
    Dev_st(i)=std(d(:));
    Max(i)=max(max(MatDatib_f_cut(1:s1_cut-1,1:s2_cut-1,i)));
    Min(i)=min(min(MatDatib_f_cut(1:s1_cut-1,1:s2_cut-1,i)));
end

Max=Max(1:s3_cut);
Min=Min(1:s3_cut);
Media=Media(1:s3_cut);
Dev_st=Dev_st(1:s3_cut);

save Max; %Salvataggio dei vettori max, min e Delta
save Min;
save Media;
save Dev_st;

Loads=Tab_load(1:s3_cut,2); % Estrapolazione del vettore dei carichi

figure,
plot(Loads,Max,'ko');
title('Diagramma della pendenza (b) Max');
xlabel('Delta Sigma/2');
ylabel('b Max');
saveas(gcf,'b Max','fig');
saveas(gcf,'b Max','jpg');

figure,
plot(Loads,Min,'ko');
title('Diagramma del b Min');
xlabel('Delta Sigma/2');
ylabel('Segnale Min');
saveas(gcf,'b min','fig');

```

```

saveas(gcf,'b_min','jpg');

figure,
plot(Loads,Media,'ko');
title('Diagramma del b Medio');
xlabel('Delta Sigma/2');
ylabel('b Medio');
saveas(gcf,'b_medio','fig');
saveas(gcf,'b_medio','jpg');

figure,
plot(Loads,Dev_st,'ko');
title('Diagramma della Deviazione Standard');
xlabel('Delta Sigma/2');
ylabel('Segnale della Deviazione Standard');
saveas(gcf,'Deviazione Standard','fig');
saveas(gcf,'Deviazione Standard','jpg');

%Ciclo per l'apertura delle immagini in Matlab
flag=0;
while flag==0
    kind=input('Vuoi aprire e salvare le immagini ?: SI (1) NO (2) ','s');
    fprintf('\n\n')
    switch kind
        case '1'
            for i=1:s3_cut
                figure,
                imagesc(MatDatib_f_cut(:, :, i));
                num=int2str(i);
                n_tit=strcat(nomefile,num,'_',nn);
                title(n_tit)
                saveas(gcf,n_tit,'fig');
            end
            flag=1;
        case '2'
            flag=1;
        otherwise
            fprintf('Inserimento non corretto')
            fprintf('\n\n')
    end
end

save MatDatib_cut_f;
clear MatDatib_cut_f_n;

```

## T<sub>0</sub> PARAMETER ANALYSIS

```

% Fase di acquisizione delle immagini per quanti sono gli step di carico .txt o .mat
clc
clear all

flag=0;
while flag==0
    kind=input('Acquisire immagini da file .txt o da una file .mat: .txt (1) .mat (2) ','s');
    fprintf('\n\n')
    switch kind
        case '1'
            [MatDatiCN,s1,s2,s3,nomefile,n,nn]=Acq_imm_DTT; %funzione per l'apertura dei
            .txt del DeltaTherm
            flag=1;
        case '2'
            [MatDatiCN,s1,s2,s3,nomefile,n,nn]=Acq_imm_matR_t0; %funzione per l'apertura

```

```

dei .mat
    flag=1;
    case '3'
        [MatDatiCN,s1,s2,s3,nomefile,n,nn]=Acq_imm_mat_irtat0; %funzione per
l'apertura dei .mat
        flag=1;
        otherwise
            fprintf('Inserimento non corretto')
            fprintf('\n\n')
        end
    end

end

save MatDatiCN;

% Taglio delle immagini (scelta dell'area da analizzare)
flag=0;
while flag==0
    kind=input('seleziona area corpo nero ?: SI (1) NO (2) ','s');
    fprintf('\n\n')
    switch kind
        case '1'
            [MatDatiCN_cut,x1,x2,y1,y2,s1_cut,s2_cut,s3_cut]=cut_imm(MatDatiCN,s1,s2,s3);
%Funzione taglio immagini
            flag=1;
            case '2'
                MatDatiCN_cut=MatDatiCN;
                s1_cut=s1;
                s2_cut=s2;
                s3_cut=s3;
                flag=1;
            otherwise
                fprintf('Inserimento non corretto')
                fprintf('\n\n')
            end
        end
    end

end

save MatDatiCN_cut; %Salvataggio delle immagini tagliate in un'unica matrice %3D clear
MatDati_f_cut;

for i=1:s3_cut
    MatDatiCN_cut_mean(:, :, i)=mean(mean(MatDatiCN_cut(:, :, i)));
end
T_amb_mean=MatDatiCN_cut_mean(:); %la matdati3d diventa vettore

clear s1_cut;
clear s2_cut;
clear s3_cut;

% Fase di acquisizione delle immagini per quanti sono gli step di carico .txt o .mat
flag=0;
while flag==0
    kind=input('Acquisire immagini da file .txt o da una file .mat: .txt (1) .mat (2)
.avg(3) ','s');
    fprintf('\n\n')
    switch kind
        case '1'
            [T0MatDati,s1,s2,s3,nomefile,n,nn]=Acq_imm_DTT; %funzione per l'apertura dei
.txt del DeltaTherm
            flag=1;
            case '2'
                [T0MatDati,s1,s2,s3,nomefile,n,nn]=Acq_imm_matR_t0; %funzione per l'apertura
dei .mat
            flag=1;
            case '3'
                [T0MatDati,s1,s2,s3,nomefile,n,nn]=Acq_imm_mat_irtat0; %funzione per
l'apertura dei .mat
            flag=1;
            otherwise
                fprintf('Inserimento non corretto')
                fprintf('\n\n')
            end
        end
    end

end

% Taglio delle immagini t0 (scelta dell'area da analizzare)

```

```

flag=0;
while flag==0
    kind=input('seleziona area provino ?: SI (1) NO (2) ','s');
    fprintf('\n\n')
    switch kind
        case '1'
            [T0MatDati_cut,x1,x2,y1,y2,s1_cut,s2_cut,s3_cut]=cut_imm(T0MatDati,s1,s2,s3);
%Funzione taglio immagini
            flag=1;
            case '2'
                MatDatib_f_cut=MatDatib_f;
                s1_cut=s1;
                s2_cut=s2;
                s3_cut=s3;
                flag=1;
            otherwise
                fprintf('Inserimento non corretto')
                fprintf('\n\n')
        end
    end
end

save T0MatDati_cut; %Salvataggio delle immagini tagliate in un'unica matrice %3D clear
MatDati_f_cut;
% eliminazione della temperatura media del corpo nero da ogni pixel, di ogni matrice di
T0MatDati.

for i=1:s3_cut
    T0MatDati_cut_mCN(1:s1_cut,1:s2_cut,i)= T_amb_mean(i);
    T0MatDati_cut_m(:, :, i)= T0MatDati_cut(1:s1_cut,1:s2_cut,i)-
    T0MatDati_cut_mCN(1:s1_cut,1:s2_cut,i);
end
save T0MatDati_cut_m;

%Ciclo per l'apertura delle immagini in Matlab

for i=1:s3_cut
    figure,
    imagesc(T0MatDati_cut_m(:, :, i));
end

%funzione per eliminare il flusso termico della macchina di carico VIENE
%INIBITA IN CASO DI COMPOSITI

N=input('Indicare il numero di sequenze che si vuole acquisire: ');
r_mp=input('Inserire il rapporto mm/pixel verticale delle immagini: ');

%Filtro per eliminare riscaldamento dovuto alla macchina di carico

[T0MatDati_cut_mf,v_mm_t]=fl_termo3D_2_T0(T0MatDati_cut_m,r_mp);

save T0MatDati_cut_mf;

[MaxT0,mediaT0]=M_m_P_T0(T0MatDati_cut_mf,s3_cut);

```

## T<sub>thc</sub> PARAMETER ANALYSIS

```

%Routine di analisi del segnale term0oelastico (Immagini .txt provenienti da
%DeltaTherm o .mat)

clear all
close all
clc

% Fase di acquisizione delle immagini per quanti sono gli step di carico .txt o .mat
flag=0;
while flag==0

```

```

        kind=input('Acquisire immagini da file .txt o da una file .mat: .txt (1) .mat (2)
','s');
        fprintf('\n\n')
        switch kind
            case '1'
                [MatDati,s1,s2,s3,nomefile,n,nn]=Acq_imm_DT;    %funzione per l'apertura dei
.txt del DeltaTherm
                flag=1;
            case '2'
                [MatDati,s1,s2,s3,nomefile,n,nn]=Acq_imm_mat;    %funzione per l'apertura dei
.mat
                flag=1;
            otherwise
                fprintf('Inserimento non corretto')
                fprintf('\n\n')
        end
    end
end

% Taglio delle immagini (scelta dell'area da analizzare)
flag=0;
while flag==0
    kind=input('Vuoi tagliare le immagini ?: SI (1) NO (2) ','s');
    fprintf('\n\n')
    switch kind
        case '1'
            [MatDati_cut,x1,x2,y1,y2,s1_cut,s2_cut,s3_cut]=cut_imm(MatDati,s1,s2,s3);
%Funzione taglio immagini
            flag=1;
        case '2'
            MatDati_cut=MatDati;
            s1_cut=s1;
            s2_cut=s2;
            s3_cut=s3;
            flag=1;
        otherwise
            fprintf('Inserimento non corretto')
            fprintf('\n\n')
    end
end

clear MatDati; %Salvataggio delle immagini in un'unica matrice 3D

%Filtro immagini
flag=0;
while flag==0
    kind=input('Vuoi filtrare le immagini ?: SI (1) NO (2) ','s');
    fprintf('\n\n')
    switch kind
        case '1'
            [MatDati_cut_f,filt]=smoot_3D(MatDati_cut); %Funzione filtro immagini
            flag=1;
        case '2'
            MatDati_cut_f=MatDati_cut;
            flag=1;
        otherwise
            fprintf('Inserimento non corretto')
            fprintf('\n\n')
    end
end

save MatDati_cut; %Salvataggio delle immagini tagliate in un'unica matrice 3D
clear MatDati_cut;

Tab_load=xlsread('Carichi.xls'); %Apertura file dei carichi
Loads_1=Tab_load(1:s3_cut,3)'; % Estrapolazione del vettore dei carichi

%Normalizzazione dati
for i=1:s3_cut
    MatDati_cut_f_n(:, :,i)=MatDati_cut_f(:, :,i)/Loads_1(i);
end

save MatDati_cut_f; %Salvataggio delle immagini tagliate e filtrate in un'unica matrice 3D
clear MatDati_cut_f;

%Ciclo per l'apertura delle immagini in Matlab

```

```

flag=0;
while flag==0
    kind=input('Vuoi aprire le immagini ?: SI (1) NO (2)    ','s');
    fprintf('\n\n')
    switch kind
        case '1'
            for i=1:s3_cut
                figure,
                imagesc(MatDati_cut_f_n(:, :, i));
                num=int2str(i);
                n_tit=strcat(nomefile,num,'_',nn);
                title(n_tit)
            end
            flag=1;
        case '2'
            flag=1;
        otherwise
            fprintf('Inserimento non corretto')
            fprintf('\n\n')
    end
end

% Scelta dell'immagine di riferimento
flag1=0;
while flag1==0
    ss=input('Quale immagine vuoi usare come riferimento ? : ');

    if ss==0
        M_rif2=0;
        M_rif3=0;
    else
        M_rif1=medfilt2(MatDati_cut_f_n(:, :, ss));
        M_rif2=medfilt2(M_rif1); % L'immagine di riferimento viene filtrata 2 volte
        M_rif3=M_rif2(2:s1_cut-1,2:s2_cut-1);
    end

    % Sottrazione dell'immagine di riferimento e calcolo della media,
    % della deviazione standard del max e del min
    for i=1:s3_cut
        MatDati_cut_f_n_ss(:, :, i)=MatDati_cut_f_n(:, :, i)-M_rif2;
        Media(i)=mean(mean(MatDati_cut_f_n(2:s1_cut-1,2:s2_cut-1,i)-M_rif3));
        d=MatDati_cut_f_n(2:s1_cut-1,2:s2_cut-1,i)-M_rif3;
        Dev_st(i)=std(d(:));
        Max(i)=max(max(MatDati_cut_f_n(2:s1_cut-1,2:s2_cut-1,i)-M_rif3));
        Min(i)=min(min(MatDati_cut_f_n(2:s1_cut-1,2:s2_cut-1,i)-M_rif3));
    end

    Max=Max(ss+1:s3_cut);
    Min=Min(ss+1:s3_cut);
    Media=Media(ss+1:s3_cut);
    Dev_st=Dev_st(ss+1:s3_cut);

    save Max; %Salvataggio dei vettori max, min e Delta
    save Min;
    save Media;
    save Dev_st;

    Loads=Tab_load(ss+1:s3_cut,2)'; % Estrapolazione del vettore dei carichi

    figure,
    plot(Loads,Max,'ko');
    title('Diagramma del segnale Max');
    xlabel('Delta Sigma/2');
    ylabel('Segnale Max');
    saveas(gcf,'Segnale Max','fig');
    saveas(gcf,'Segnale Max','jpg');

    figure,
    plot(Loads,Min,'ko');
    title('Diagramma del segnale Min');
    xlabel('Delta Sigma/2');
    ylabel('Segnale Min');
    saveas(gcf,'Segnale min','fig');
    saveas(gcf,'Segnale min','jpg');

    figure,
    plot(Loads,Media,'ko');
    title('Diagramma del segnale Medio');

```

```

xlabel('Delta Sigma/2');
ylabel('Segnale Medio');
saveas(gcf,'Segnale medio','fig');
saveas(gcf,'Segnale medio','jpg');

figure,
plot(Loads,Dev_st,'ko');
title('Diagramma della Deviazione Standard');
xlabel('Delta Sigma/2');
ylabel('Segnale della Deviazione Standard');
saveas(gcf,'Deviazione Standard','fig');
saveas(gcf,'Deviazione Standard','jpg');

%Ciclo per l'apertura delle immagini in Matlab
flag=0;
while flag==0
    kind=input('Vuoi aprire le immagini ?: SI (1) NO (2) ','s');
    fprintf('\n\n')
    switch kind
        case '1'
            for i=ss+1:s3_cut
                figure,
                imagesc(MatDati_cut_f_n_ss(:, :, i));
                num=int2str(i);
                n_tit=strcat(nomefile,num,'_',nn);
                title(n_tit)
            end
            flag=1;
        case '2'
            flag=1;
        otherwise
            fprintf('Inserimento non corretto')
            fprintf('\n\n')
    end
end

% Possibilità di riscegliere l'immagine di riferimento
a=input('Vuoi ripetere la scelta dell immagine di riferimento ?: SI (1) NO (2) ');
if a==1
    flag1=0;
else
    flag1=1;
end
end

save MatDati_cut_f;
clear MatDati_cut_f_n;

```

## T<sub>D</sub> PARAMETER ANALYSIS

```

%NUOVA ROUTINE ANALISI DEI FILE CALIBRATI IN T plodeltaTt0 e deltat (si riferiscono a
MatdatiR normalizzata ma non divisa per MatdatiT)
%filese salvati come stepRx_y e stepTx_y
%ROUTINE TSA_SIGNAL_ANALYSISNEW
%Routine di analisi del segnale termOoelastico (Immagini .txt provenienti da
%DeltaTherm o .mat)
% questa routine calcola anche i percentili 98-2-95-5 del coefficiente
% termoelastico K

clear all
close all
clc

% Fase di acquisizione delle immagini per quanti sono gli step di carico .txt o .mat
flag=0;
while flag==0
    kind=input('Acquisire immagini da file .txt o da una file .mat: .txt (1) .mat (2)
','s');
    fprintf('\n\n')
    switch kind
        case '1'
            [MatDatiR,s1,s2,s3,nomefile,n,nn]=Acq_imm_DT; %funzione per l'apertura dei
.txt del DeltaTherm
            flag=1;

```

```

        case '2'
            [MatDatiR,s1,s2,s3,nomefile,n,nn]=Acq_imm_matR_t1;    %funzione per l'apertura
dei .mat
            flag=1;
            otherwise
                fprintf('Inserimento non corretto')
                fprintf('\n\n')
            end
        end

        % Fase di acquisizione delle immagini per quanti sono gli step di carico .txt o .mat
        flag=0;
        while flag==0
            kind=input('Acquisire immagini da file .txt o da una file .mat: .txt (1) .mat (2)
','s');
            fprintf('\n\n')
            switch kind
                case '1'
                    [MatDatiT,s1,s2,s3,nomefile,n,nn]=Acq_imm_DT;    %funzione per l'apertura dei
.txt del DeltaTherm
                    flag=1;
                case '2'
                    [MatDatiT,s1,s2,s3,nomefile,n,nn]=Acq_imm_matR_t0;    %funzione per l'apertura
dei .mat
                    flag=1;
                otherwise
                    fprintf('Inserimento non corretto')
                    fprintf('\n\n')
            end
        end

        %creazione matrice dati ottenuta da rapporto MATDATIR/MATDATIS

        for i=1:s3

            MatDatiT_K(:, :, i)=convtemp(MatDatiT(:, :, i), 'C', 'K');

            MatDati(:, :, i)=MatDatiR(:, :, i)./MatDatiT_K(:, :, i);

        end

        save MatDati;

        %Filtro immagini SU MATDATI
        flag=0;
        while flag==0
            kind=input('Vuoi filtrare le immagini su MATDATI ?: SI (1) NO (2) ','s');
            fprintf('\n\n')
            switch kind
                case '1'
                    [MatDati_f,filt]=smoot_3D(MatDati); %Funzione filtro immagini
                    flag=1;
                case '2'
                    MatDati_f=MatDati;
                    flag=1;
                otherwise
                    fprintf('Inserimento non corretto')
                    fprintf('\n\n')
            end
        end

        save MatDati_f;
        %Filtro immagini su MatDatiR

        flag=0;
        while flag==0
            kind=input('Vuoi filtrare le immagini di MatDatiR ?: SI (1) NO (2) ','s');
            fprintf('\n\n')
            switch kind
                case '1'
                    [MatDatiR_f,filt]=smoot_3D(MatDatiR); %Funzione filtro immagini

```



```

        flag=1;
        case '2'
            MatDatiR_f=MatDatiR;
            flag=1;
            otherwise
                fprintf('Inserimento non corretto')
                fprintf('\n\n')
        end
    end

end

% Taglio delle immagini (scelta dell'area da analizzare) SU MATDATI
flag=0;
while flag==0
    kind=input('Vuoi tagliare le immagini di Matdati ?: SI (1) NO (2) ', 's');
    fprintf('\n\n')
    switch kind
        case '1'
            [MatDati_f_cut,x1,x2,y1,y2,s1_cut,s2_cut,s3_cut]=cut_imm(MatDati_f,s1,s2,s3);
%Funzione taglio immagini
            flag=1;
            case '2'
                MatDati_f_cut=MatDati_f;
                s1_cut=s1;
                s2_cut=s2;
                s3_cut=s3;
                flag=1;
            otherwise
                fprintf('Inserimento non corretto')
                fprintf('\n\n')
        end
    end

end

clear MatDati; %Salvataggio delle immagini in un'unica matrice 3D

save MatDati_f_cut; %Salvataggio delle immagini tagliate in un'unica matrice 3D
%clear MatDati_f_cut;

% Taglio delle immagini (scelta dell'area da analizzare)MatDatiR
flag=0;
while flag==0
    kind=input('Vuoi tagliare le immagini di MatdatiR ?: SI (1) NO (2) ', 's');
    fprintf('\n\n')
    switch kind
        case '1'
            [MatDatiR_f_cut,x1,x2,y1,y2,s1_cut,s2_cut,s3_cut]=cut_imm(MatDatiR_f,s1,s2,s3);
%Funzione taglio immagini
            flag=1;
            case '2'
                MatDatiR_f_cut=MatDatiR_f;
                s1_cut=s1;
                s2_cut=s2;
                s3_cut=s3;
                flag=1;
            otherwise
                fprintf('Inserimento non corretto')
                fprintf('\n\n')
        end
    end

end

clear MatDatiR; %Salvataggio delle immagini in un'unica matrice 3D

save MatDatiR_f_cut; %Salvataggio delle immagini tagliate in un'unica matrice 3D
%clear MatDati_f_cut;

Tab_load=xlsread('Carichi.xls'); %Apertura file dei carichi
Loads_1=Tab_load(1:s3_cut,3)'; % Estrapolazione del vettore dei carichi

norm=input('Vuoi normalizzare i dati rispetto alla ampiezza di carico ? (3) Si, (4) No ');

if norm==3 %Normalizzazione dati su MATDATI e MATDATIR

```

```

for i=1:s3_cut
    MatDati_f_cut_n(:,:,i)=MatDati_f_cut(:,:,i)/Loads_1(i);
    MatDatiR_f_cut_n(:,:,i)=MatDatiR_f_cut(:,:,i)/Loads_1(i);

end

else
    for i=1:s3_cut
        MatDati_f_cut_n(:,:,i)=MatDati_f_cut(:,:,i)/1;
        MatDatiR_f_cut_n(:,:,i)=MatDatiR_f_cut(:,:,i)/1;

    end

end

save MatDati_f_cut; %Salvataggio delle immagini tagliate e filtrate in un'unica matrice 3D
save MatDatiR_f_cut; %Salvataggio delle immagini tagliate e filtrate in un'unica matrice
3D

clear MatDati_f_cut;
clear MatDatiR_f_cut;

%Ciclo per l'apertura delle immagini in Matlab di Matdati e MatdatiR
flag=0;
while flag==0
    kind=input('Vuoi aprire le immagini di Matdati e MatdatiR ?: SI (1) NO (2)
','s');
    fprintf('\n\n')
    switch kind
        case '1'
            for i=1:s3_cut
                figure,
                imagesc(MatDati_f_cut_n(:,:,i));
                num=int2str(i);
                n_tit=strcat(nomefile,num,'_',nn);
                title(n_tit)
                imagesc(MatDatiR_f_cut_n(:,:,i));
                num=int2str(i);
                n_tit=strcat('stepR',num,'_',nn);
                title(n_tit)

            end

            flag=1;

        case '2'

            flag=1;
            otherwise
                fprintf('Inserimento non corretto')
                fprintf('\n\n')
            end
    end
end

% Scelta dell'immagine di riferimento per MATDATI

flag1=0;
while flag1==0
    ss=input('Quale immagine vuoi usare come riferimento PER MATDATI ? : ');

    if ss==0
        M_rif2=0;
        M_rif3=0;
    else
        M_rif1=medfilt2(MatDati_f_cut_n(:,:,ss));
        M_rif2=medfilt2(M_rif1); % L'immagine di riferimento viene filtrata 2 volte
        M_rif3=M_rif2(1:s1_cut,1:s2_cut);

    end

    % Sottrazione dell'immagine di riferimento e calcolo della media,

```

```

% della deviazione standard del max e del min

for i=1:s3_cut
    MatDati_f_cut_n_ss(:, :, i)=MatDati_f_cut_n(:, :, i)-M_rif2;
    Media(i)=mean(mean(MatDati_f_cut_n(1:s1_cut, 1:s2_cut, i)-M_rif3));
    d=MatDati_f_cut_n(1:s1_cut, 1:s2_cut, i)-M_rif3;
    Dev_st(i)=std(d(:));
    Max(i)=max(max(MatDati_f_cut_n(1:s1_cut, 1:s2_cut, i)-M_rif3));
    Min(i)=min(min(MatDati_f_cut_n(1:s1_cut, 1:s2_cut, i)-M_rif3));
    e= MatDati_f_cut_n(1:s1_cut, 1:s2_cut, i)-M_rif3;
    vet_prctile98(i)=prctile(e(:), 98);
    vet_prctile2(i)=prctile(e(:), 2);
    vet_prctile95(i)=prctile(e(:), 95);
    vet_prctile5(i)=prctile(e(:), 5);

end

MaxK=Max(ss+1:s3_cut);
MinK=Min(ss+1:s3_cut);
MediaK=Media(ss+1:s3_cut);
Dev_stK=Dev_st(ss+1:s3_cut);
vet_prctile98=vet_prctile98(ss+1:s3_cut);
vet_prctile2=vet_prctile2(ss+1:s3_cut);
Delta2=vet_prctile98-vet_prctile2;
vet_prctile95=vet_prctile95(ss+1:s3_cut);
vet_prctile5=vet_prctile5(ss+1:s3_cut);
Delta3=vet_prctile95-vet_prctile5;

save MaxK; %Salvataggio dei vettori max, min e Delta
save MinK;
save MediaK;
save Dev_stK;
save MatDati_f_cut_n;
save Delta1;
save Delta2;
save vet_prctile98;
save vet_prctile2;
save Delta3;
save vet_prctile95;
save vet_prctile5;
save MatDati_f_cut_n_ss;

Loads=Tab_load(ss+1:s3_cut, 2); % Estrapolazione del vettore dei carichi

figure,
plot(Loads, Max, 'ko');
title('Diagramma del segnale Max-K');
xlabel('Delta Sigma/2');
ylabel('K Max');
saveas(gcf, 'Segnale Max-K', 'fig');
saveas(gcf, 'Segnale Max-K', 'jpg');

figure,
plot(Loads, Min, 'ko');
title('Diagramma del segnale Min-K');
xlabel('Delta Sigma/2');
ylabel('K Min');
saveas(gcf, 'Segnale min-K', 'fig');
saveas(gcf, 'Segnale min-K', 'jpg');

figure,
plot(Loads, Media, 'ko');
title('Diagramma del segnale Medio-K');
xlabel('Delta Sigma/2');
ylabel('K Medio');
saveas(gcf, 'Segnale medio-K', 'fig');
saveas(gcf, 'Segnale medio-K', 'jpg');

figure,
plot(Loads, Dev_st, 'ko');
title('Diagramma della Deviazione Standard-K');
xlabel('Delta Sigma/2');
ylabel('Segnale della Deviazione Standard');
saveas(gcf, 'Deviazione Standard-K', 'fig');
saveas(gcf, 'Deviazione Standard-K', 'jpg');

figure,

```

```

plot(Loads,Delta2,'ko');
title('Diagramma della differenza 98-2 perc-K');
xlabel('Delta Sigma/2');
ylabel('kpercentile');
saveas(gcf,'Delta2-K','fig');
saveas(gcf,'Delta2-K','jpg');

%Ciclo per l'apertura delle immagini in Matlab
flag=0;
while flag==0
    kind=input('Vuoi aprire e salvare le immagini di K?: SI (1) NO (2)
','s');
    fprintf('\n\n')
    switch kind
        case '1'
            for i=ss+1:s3_cut
                figure,
                imagesc(MatDati_f_cut_n_ss(:, :, i));
                num=int2str(i);
                n_tit=strcat('Kstep',num,'_',nn);
                title(n_tit)
                saveas(gcf,n_tit,'fig');
            end

            flag=1;

        case '2'
            flag=1;
        otherwise
            fprintf('Inserimento non corretto')
            fprintf('\n\n')
    end
end

% Possibilità di riscegliere l'immagine di riferimento
a=input('Vuoi ripetere la scelta dell'immagine di riferimento?: SI (1) NO (2) ');
if a==1
    flag1=0;
else
    flag1=1;
end
end

save MatDati_cut_f;
clear MatDati_cut_f_n;

% Scelta dell'immagine di riferimento per MATDATIR

flag1=0;
while flag1==0
    ss=input('Quale immagine vuoi usare come riferimento PER MATDATIR?: ');

    if ss==0
        M_rif2=0;
        M_rif3=0;
    else
        M_rif1=medfilt2(MatDatiR_f_cut_n(:, :, ss));
        M_rif2=medfilt2(M_rif1); % L'immagine di riferimento viene filtrata 2 volte
        M_rif3=M_rif2(1:s1_cut-1,1:s2_cut-1);
    end

    % Sottrazione dell'immagine di riferimento e calcolo della media,
    % della deviazione standard del max e del min
    for i=1:s3_cut
        MatDatiR_f_cut_n_ss(:, :, i)=MatDatiR_f_cut_n(:, :, i)-M_rif2;
        Media(i)=mean(mean(MatDatiR_f_cut_n(1:s1_cut,1:s2_cut,i)-M_rif3));
        d=MatDatiR_f_cut_n(1:s1_cut,1:s2_cut,i)-M_rif3;
        Dev_st(i)=std(d(:));
        Max(i)=max(max(MatDatiR_f_cut_n(1:s1_cut,1:s2_cut,i)-M_rif3));
        Min(i)=min(min(MatDatiR_f_cut_n(1:s1_cut,1:s2_cut,i)-M_rif3));
    end
end

```

```

MaxdeltaT=Max(ss+1:s3_cut);
MindeltaT=Min(ss+1:s3_cut);
MediadeltaT=Media(ss+1:s3_cut);
Dev_stdeltaT=Dev_st(ss+1:s3_cut);

save MaxdeltaT; %Salvataggio dei vettori max, min e Delta
save MindeltaT;
save MediadeltaT;
save Dev_stdeltaT;
save MatDatiR_f_cut_n;
save MatDatiR_f_cut_n_ss;

Loads=Tab_load(ss+1:s3_cut,2)'; % Estrapolazione del vettore dei carichi

figure,
plot(Loads,Max,'ko');
title('Diagramma del segnale Max-deltaT');
xlabel('Delta Sigma/2');
ylabel('delta T Max');
saveas(gcf,'Segnale Max-deltaT','fig');
saveas(gcf,'Segnale Max-deltaT','jpg');

figure,
plot(Loads,Min,'ko');
title('Diagramma del segnale Min-deltaT');
xlabel('Delta Sigma/2');
ylabel('delta T Min');
saveas(gcf,'Segnale min-deltaT','fig');
saveas(gcf,'Segnale min-deltaT','jpg');

figure,
plot(Loads,Media,'ko');
title('Diagramma del segnale Medio-deltaT');
xlabel('Delta Sigma/2');
ylabel('delta T Medio');
saveas(gcf,'Segnale medio-deltaT','fig');
saveas(gcf,'Segnale medio-deltaT','jpg');

figure,
plot(Loads,Dev_st,'ko');
title('Diagramma della Deviazione Standard-deltaT');
xlabel('Delta Sigma/2');
ylabel('delta T- Deviazione Standard');
saveas(gcf,'Deviazione Standard-deltaT','fig');
saveas(gcf,'Deviazione Standard-deltaT','jpg');

%Ciclo per l'apertura delle immagini in Matlab MATDATIR
flag=0;
while flag==0
    kind=input('Vuoi aprire e salvare le immagini MATDATIR ?: SI (1) NO (2)
','s');
    fprintf('\n\n')
    switch kind
        case '1'
            for i=ss+1:s3_cut
                figure,
                imagesc(MatDatiR_f_cut_n_ss(:,i));
                num=int2str(i);
                n_tit=strcat('deltaTstep',num,'_',nn);
                title(n_tit)
                saveas(gcf,n_tit,'fig');
            end

            flag=1;

        case '2'
            flag=1;
        otherwise
            fprintf('Inserimento non corretto')
            fprintf('\n\n')
    end
end
end

```

```

        % Possibilità di riscegliere l'immagine di riferimento
        a=input('Vuoi ripetere la scelta dell immagine di riferimento ?: SI (1) NO (2) ');
        if a==1
            flag1=0;
        else
            flag1=1;
        end
    end

end

save MatDatiR_cut_f;
clear MatDatiR_cut_f_n;

```

## Φ PARAMETER ANALYSIS

```

%Routine di analisi dei dati di fase (Immagini .txt provenienti da
%DeltaTherm o .mat)

clear all
close all
clc

% Fase di acquisizione delle immagini per quanti sono gli step di carico .txt o .mat
flag=0;
while flag==0
    kind=input('Acquisire immagini da file .txt o da una file .mat: .txt (1) .mat (2)
    ','s');
    fprintf('\n\n')
    switch kind
        case '1'
            [MatDati,s1,s2,s3,nomefile,n,nn]=Acq_imm_DT;    %funzione per l'apertura dei
            .txt del DeltaTherm
            flag=1;
        case '2'
            [MatDati,s1,s2,s3,nomefile,n,nn]=Acq_imm_mat;    %funzione per l'apertura dei
            .mat
            flag=1;
        otherwise
            fprintf('Inserimento non corretto')
            fprintf('\n\n')
    end
end

%Filtro immagini
flag=0;
while flag==0
    kind=input('Vuoi filtrare le immagini ?: SI (1) NO (2) ','s');
    fprintf('\n\n')
    switch kind
        case '1'
            [MatDati_f,filt]=smoot_3D(MatDati); %Funzione filtro immagini
            flag=1;
        case '2'
            MatDati_f=MatDati;
            flag=1;
        otherwise
            fprintf('Inserimento non corretto')
            fprintf('\n\n')
    end
end

save MatDati_f;    %Salvataggio delle immagini tagliate in un'unica matrice 3D

%clear MatDati_f;

% Taglio delle immagini (scelta dell'area da analizzare)
flag=0;
while flag==0
    kind=input('Vuoi tagliare le immagini ?: SI (1) NO (2) ','s');
    fprintf('\n\n')

```

```

switch kind
case '1'
[MatDati_f_cut,x1,x2,y1,y2,s1_cut,s2_cut,s3_cut]=cut_imm(MatDati_f,s1,s2,s3);

%Funzione taglio immagini
flag=1;
case '2'
MatDati_f_cut = MatDati_f;
s1_cut=s1;
s2_cut=s2;
s3_cut=s3;
flag=1;
otherwise
fprintf('Inserimento non corretto')
fprintf('\n\n')
end
end

%clear MatDati_f_cut; %Salvataggio delle immagini in un'unica matrice 3D

Tab_load=xlsread('Carichi.xls'); %Apertura file dei carichi
Loads_1=Tab_load(1:s3,3)'; % Estrapolazione del vettore dei carichi

%Calcolo e sottrazione del valore medio

for i=1:s3_cut
m=mean(mean(MatDati_f_cut(1:s1_cut-1,1:s2_cut-1,i)));
MatDati_f_cut_m(:, :,i)=MatDati_f_cut(:, :,i)-m;
end

save MatDati_f_cut_m; %Salvataggio delle immagini tagliate e filtrate in un'unica matrice
3D

%clear MatDati_f;

%Ciclo per l'apertura delle immagini in Matlab
flag=0;
while flag==0
kind=input('Vuoi aprire le immagini ?: SI (1) NO (2) ','s');
fprintf('\n\n')
switch kind
case '1'
for i=1:s3
figure,
imagesc(MatDati_f_cut_m(:, :,i));
num=int2str(i);
n_tit=strcat(nomefile,num,'_',nn);
title(n_tit)
end
flag=1;
case '2'
flag=1;
otherwise
fprintf('Inserimento non corretto')
fprintf('\n\n')
end
end

for i=1:s3
d=MatDati_f_cut_m(1:s1_cut-1,1:s2_cut-1,i); %calcolo dev.std
vet_dv(:, :,i)=std(d(:));
end

vet_dv2=vet_dv(:);
figure,plot(vet_dv2);
title('Diagramma della deviazione standard');
xlabel('Step');
ylabel('Deviazione Standard');
saveas(gcf,'Deviazione_standard','fig');
saveas(gcf,'Deviazione_standard','jpg');
save vt_dv2;

% Scelta dell'immagine di riferimento
flag1=0;
while flag1==0

```

```

ss=input('Quale immagine vuoi usare come riferimento ?: ');

if filt==1
    M_rif1=medfilt2(MatDati_f_cut_m(:,:,ss));
    M_rif2=medfilt2(M_rif1); % L'immagine di riferimento viene filtrata 2 volte
elseif filt==2
    filtro1=fspecial('average');
    M_rif1=imfilter(MatDati_f_cut_m(:,:,ss),filtro1);
    M_rif2=imfilter(M_rif1,filtro1); % L'immagine di riferimento viene filtrata 2
volte
elseif filt==3
    filtro1=fspecial('gaussian');
    M_rif1=imfilter(MatDati_f_cut_m(:,:,ss),filtro1);
    M_rif2=imfilter(M_rif1,filtro1); % L'immagine di riferimento viene filtrata 2
volte
elseif filt==4
    M_rif1=wiener2(MatDati_f_cut_m(:,:,ss));
    M_rif2=wiener2(M_rif1); % L'immagine di riferimento viene filtrata 2 volte
elseif filt==5
    M_rif1=AdpDirSm(MatDati_f_cut_m(:,:,ss));
    M_rif2=AdpDirSm(M_rif1); % L'immagine di riferimento viene filtrata 2 volte
elseif filt==6
    M_rif2=0;
end

% Sottrazione dell'immagine di riferimento e calcolo del Delta_fase
% max e del Delta_fase min
for i=1:s3_cut
    MatDati_f_cut_m_ss(:,:,i)= MatDati_f_cut_m(:,:,i)-M_rif2;
    Max(i)=max(max(MatDati_f_cut_m(1:s1_cut-1,1:s2_cut-1,i)-M_rif2(1:s1_cut-
1,1:s2_cut-1)));
    Min(i)=min(min(MatDati_f_cut_m(1:s1_cut-1,1:s2_cut-1,i)-M_rif2(1:s1_cut-
1,1:s2_cut-1)));
    e= MatDati_f_cut_m(1:s1_cut-1,1:s2_cut-1,i)-M_rif2(1:s1_cut-1,1:s2_cut-1);
    vet_prctile98(i)=prctile(e(:),98);
    vet_prctile2(i)=prctile(e(:),2);
end

Max=Max(ss+1:s3_cut);
Min=Min(ss+1:s3_cut);
Delta1=Max-Min;
vet_prctile98=vet_prctile98(ss+1:s3_cut);
vet_prctile2=vet_prctile2(ss+1:s3_cut);
Delta2=vet_prctile98-vet_prctile2;

save MatDati_f_cut_m; %Salvataggio delle immagini tagliate, filtrate a cui è stata
sottratta la media in un'unica matrice 3D

save Max; %Salvataggio dei vettori max, min e Delta
save Min;
save Delta1;
save Delta2;
save vet_prctile98;
save vet_prctile2;
save MatDati_f_cut_m_ss;

Tab_load=xlsread('Carichi.xls'); %Apertura file dei carichi

Loads=Tab_load(ss+1:s3_cut,2); % Estrapolazione del vettore dei carichi

%[Limite_di_fatica_M,r2_serie1_M,r2_serie2_M]=limite_di_fatica_man(Loads,Max);
%Funzione per la valutazione del limite di fatica con il metodo delle due rette
%[Limite_di_fatica_m,r2_serie1_m,r2_serie2_m]=limite_di_fatica_man(Loads,Min);
%[Limite_di_fatica_D,r2_serie1_D,r2_serie2_D]=limite_di_fatica_man(Loads,Delta);

%Ciclo per l'apertura delle immagini in Matlab
flag=0;
while flag==0
    kind=input('Vuoi aprire e salvare le immagini ?: SI (1) NO (2) ','s');
    fprintf('\n\n')
    switch kind
        case '1'
            for i=ss+1:s3_cut
                figure,
                imagesc(MatDati_f_cut_m_ss(:,:,i));
                num=int2str(i);

```



```

        n_tit=strcat(nomefile,num,'_',nn);
        title(n_tit)
        saveas(gcf,n_tit,'fig');
    end
    flag=1;
    case '2'
        flag=1;
    otherwise
        fprintf('Inserimento non corretto')
        fprintf('\n\n')
    end
end

% Possibilità di riscegliere l'immagine di riferimento
a=input('Vuoi ripetere la scelta dell immagine di riferimento ?: SI (1) NO (2) ');
if a==1
    flag1=0;
else
    flag1=1;
end
end

%clear MatDati_f_cut_m;

```

## THRESHOLD METHOD

```

%x stress vector
%y phase vector

function [Limite_di_fatica,r2_serie1,r2_serie2]=limite_di_fatica_auto(x,y)

sx=size(x);
sy=size(y);
if sx(1)>sx(2)
    x=x';
end
if sy(1)>sy(2)
    y=y';
end

figure,
plot(x,y,'ko'),
grid on;
xlim([min(x)-5, max(x)+5]);
ylim([min(y)-0.5, abs(max(y))+0.5]);
title('Fatigue limit evaluation');
xlabel('Delta Sigma/2');
ylabel('Delta Signal');

%pd=input('Indicate the point of the onset of damage');

%serie1x=x(1:pd-1);
for i=1:sy(1)-3
    sy_1_p=sy(1:3+t);
    sy_2_p=sy(3+t+1:sy(1));

serie1y=y(1:pd-1);

serie2x=x(pd:sx(2));
serie2y=y(pd:sx(2));

y_serie1=mean(serie1y);
r2_serie1 = 1 - sum((serie1y-y_serie1).^2) / sum((serie1y - mean(serie1y)).^2);

coeff_serie2=polyfit(serie2x,serie2y,1);
y_serie2=coeff_serie2(1,1)*serie2x+coeff_serie2(1,2);
r2_serie2 = 1 - sum((serie2y-y_serie2).^2) / sum((serie2y - mean(serie2y)).^2);

```

```

Limite_di_fatica=(y_seriel-coeff_serie2(1,2))/coeff_serie2(1,1);

figure,
x_fit1=[serielx Limite_di_fatica+10];
y_fit1=(ones(size(x_fit1,2)))*y_seriel;
x_fit2=[Limite_di_fatica-10 serie2x];
y_fit2=coeff_serie2(1,1)*[Limite_di_fatica-10 serie2x]+coeff_serie2(1,2);
plot(x,y,'ko'), hold on, plot(x_fit1,y_fit1,'b'), hold on, plot(x_fit2,y_fit2,'g'),
hold on,
plot([Limite_di_fatica, Limite_di_fatica], [y_seriel 0], 'k', Limite_di_fatica, 0,
'ro', 'MarkerSize', 7, 'MarkerFaceColor', 'red');
grid on;
xlim([min(x)-5, max(x)+5]);
ylim([min(y)-0.5, abs(max(y))+0.5]);
title('Fatigue limit evaluation');
xlabel('Delta Sigma/2');
ylabel('Delta Signal');
end

```

---

## Acknowledgements

---

The work presented in this document would not have been possible without the guidance, assistance, and support of others.

First, I would like to thank Prof. Galietti for choosing me as a collaborator in research and helping to scope a suitable research project which tapped both my interest and expertise. In addition, his technical guidance and contributions throughout the project were invaluable. It was truly an honor to work with such a leader in the field of Thermography.

Next I'd like to thank is Dr. Davide Palumbo for his guidance and support throughout my research, he was instrumental in leading me through the details necessary to complete this work and my degree. It was a privilege to work side by side with him, even if sometime it was difficult due to the different point of views, I believe that the debate is fundamental for researchers.

I'd also like to thank all the Francesco Ancona, my computer geek colleague and friend, we started the way together, and I hope will proceed again together.

I'd like to thank Dr. Rosa Di Mundo my woman academic inspiration, and all the guys of my research team for the support given to me.

Finally, a special thanks to Prof. Margareth Maria da Silva for her guidance and support during my foreign period of study at Instituto Tecnológico de Aeronáutica (ITA) at São José dos Campos (SP)-Brazil.

Every look that I crossed, every word I was told, every smile I received, represented for me an impulse of enthusiasm for my job.

Every occasion in research was for me an interesting experiment to increase my knowledge by crossing new horizons.

Research is where open minded people are.